



Canadian Nuclear Society
Société Nucléaire Canadienne



ÉCOLE
POLYTECHNIQUE



CA9700527-
ca9700527

18^e CONFÉRENCE ÉTUDIANTE ANNUELLE ANC/SNC
18th ANNUAL STUDENT CONFERENCE CNA/CNS

2 - 3 avril 1993 / April 2nd-3rd 1993

INSTITUT DE GÉNIE ÉNERGÉTIQUE
ÉCOLE POLYTECHNIQUE
Montréal, Québec

COMPTES RENDUS
PROCEEDINGS



CANATOM INC.

AECL

AECL

EAACL

EAACL

EAACL CANDU

EAACL CANDU



Atomic Energy
Control Board

Commission de contrôle
de l'énergie atomique



Hydro-Québec



Association des
Diplômés de
Polytechnique

C.D.T.
Centre de développement
technologique

18^e CONFÉRENCE ÉTUDIANTE ANNUELLE ANC/SNC
18th ANNUAL STUDENT CONFERENCE CNA/CNS

2 – 3 avril 1993 / April 2nd–3rd 1993
INSTITUT DE GÉNIE ÉNERGÉTIQUE
ÉCOLE POLYTECHNIQUE
Montréal, Québec

COMPTES RENDUS
PROCEEDINGS

ÉDITEUR / *EDITOR*: PETER TYE

INSTITUT DE GÉNIE ÉNERGÉTIQUE
ÉCOLE POLYTECHNIQUE
Montréal, Québec
1993

18^e CONFÉRENCE ÉTUDIANTE ANNUELLE ANC/SNC
18th ANNUAL STUDENT CONFERENCE CNA/CNS

2 – 3 avril 1993 / April 2nd–3rd 1993
INSTITUT DE GÉNIE ÉNERGÉTIQUE
ÉCOLE POLYTECHNIQUE
Montréal, Québec

COMITÉ ORGANISATEUR
ORGANIZING COMMITTEE

SOLANGE LABERGE
BENOIT ARSENAULT
PETER TYE

REMERCIEMENTS

Les membres du comité organisateur tiennent à remercier tous ceux et celles qui ont contribué au succès de la 18^e conférence étudiante annuelle de l'ANC/SNC.

Nous tenons à remercier tout particulièrement les principaux commanditaires soit l'Association Nucléaire Canadienne et la Société Nucléaire Canadienne. Nous aimerions également remercier Énergie Atomique du Canada Limitée-CANDU, Énergie Atomique du Canada Limitée, la Commission de Contrôle de l'Énergie Atomique, Canatom Inc., Hydro-Québec, l'Association des diplômés de Polytechnique, l'École Polytechnique, sa direction de la recherche et des études supérieures, son centre de développement technologique, l'Institut de génie énergétique et son laboratoire de thermohydraulique pour leur contribution financière.

Nous tenons à exprimer notre reconnaissance aux présidents de sessions, aux membres du jury, au Dr Daniel Rozon pour avoir accepté d'être le conférencier invité lors du banquet, au Dr Monique Lacroix de l'institut Armand-Frappier pour nous avoir permis de visiter le centre d'irradiation du Canada.

Un merci spécial à Gaby Roy pour son aide administrative, à Céline Labelle et Karen Côté pour la réalisation des tâches de secrétariat.

ACKNOWLEDGEMENTS

The members of the organizing committee would like to thank all those who have contributed to the success of 18th annual CNA/CNS student conference.

We would like to thank the major sponsors, the Canadian Nuclear Association and the Canadian Nuclear Society for their financial assistance. We also wish to thank Atomic Energy of Canada Limited, Atomic Energy of Canada Limited - CANDU, the Atomic Energy Control Board, Canatom Inc., Hydro-Québec, École Polytechnique, the Direction de Recherche et d'études supérieurs de l'École Polytechnique, the Association des Diplômés de Polytechnique, the Centre de développement technologique de l'École Polytechnique, l' Institut de génie énergétique and its thermalhydraulics laboratory for their financial contributions.

We wish to express our gratitude to all the session chairmen and the jury. We also wish to thank Dr. Daniel Rozon for agreeing to be our guest speaker for the banquet and Dr. Monique Lacroix of the Institut Armand-Frappier for giving us the opportunity to visit the Canadian Irradiation Centre.

A very special thank you also goes to Gaby Roy, Céline Labelle and Karen Côté for their help with all the administrative and secretarial work.

LE COMITÉ ORGANISATEUR
THE ORGANIZING COMMITTEE



Association des
Diplômés de
Polytechnique

La section des jeunes de l'Association des Diplômés de Polytechnique représente les cinq dernières promotions de diplômés. Avec un dynamisme qui lui est propre, la section des jeunes supporte les actions de l'École et organise des activités d'intérêt pour ses membres, favorise les liens avec les futurs diplômés et s'implique envers l'action communautaire.

La section des jeunes de l'ADP est fière de s'associer à la 18ème conférence étudiante annuelle de l'Association nucléaire canadienne et de la Société nucléaire canadienne qui favorise le rapprochement entre les chercheurs et l'avancement des connaissances dans le domaine du nucléaire.

Le conseil d'administration de la section des jeunes est formé de jeunes diplômés comme vous. N'hésitez donc pas à vous y impliquer! Pour tout renseignement sur votre association et ses activités, contactez le secrétariat de l'ADP au 340-4764.

**La voix des diplômés,
l'affirmation de leur volonté**

Le nucléaire au Québec - des racines profondes

Saviez-vous que Montréal a été, en 1942, le point de départ de la technologie nucléaire au Canada? En effet, il y a 50 ans qu'une équipe de chercheurs s'établissait dans des locaux de l'Université de Montréal pour s'attaquer au défi de maîtriser la fission de l'atome. Ils allaient former le noyau de l'entreprise qui porte maintenant le nom d'EACL.

Cette grande aventure s'est soldée par maintes découvertes. La médecine nucléaire a reculé les frontières du diagnostic des maladies et de la lutte contre le cancer. L'énergie nucléaire contribue à l'amélioration de notre niveau de vie : Hydro-Québec exploite une centrale de 680 mégawatts à Gentilly depuis 1983.

Nombre de Québécois se distinguent dans le génie nucléaire ou la fabrication de composantes spécialisées - systèmes de commande des centrales, calandres, simulateurs, ponts roulants, tuyauterie et robinetterie, entre autres. Ils participent aussi à la construction de centrales nucléaires CANDU à l'étranger, en Corée du Sud par exemple.

Les établissements de haut savoir québécois continuent de fournir des spécialistes en génie nucléaire fort en demande. Des recherches se poursuivent aussi à l'IREQ en vue de maîtriser la fusion, cette technologie de demain qui pourrait nous assurer des réserves d'énergie quasi-inépuisables au siècle prochain.

Le nucléaire au Québec - des racines profondes, un présent fier et un avenir prometteur.

EACL CANDU
1155, rue Metcalfe
Montréal (Québec) H3B 2V6
Téléphone : (514) 871-1116
Télécopieur : (514) 934-1322

Nuclear power deeply rooted in Québec

Did you know that it was in Montréal that nuclear power technology first developed in Canada, in 1942? It was fifty years ago that a team of scientists started work to control the nuclear fission process at the Université de Montréal facilities. They were to become the nucleus of the company now known as AECL.

This venture led to numerous discoveries. Nuclear medicine has provided us with better diagnostic techniques for identifying diseases and with radiation therapy devices for fighting cancer. Nuclear energy also enhances our standard of living : Hydro-Québec has been operating a 680 MW nuclear power station at Gentilly since 1983.

A number of Québécois are recognized specialists in the fields of nuclear engineering or manufacturing of specialized components such as nuclear power plants control systems, calandrias, simulators, overhead cranes, piping and valves. They are also involved in the construction of CANDU nuclear stations overseas, for example in South Korea.

Québec universities are a much valued breeding ground for professionals in nuclear engineering. Ongoing research is underway at IREQ focusing on nuclear fission, the technology of tomorrow that could enable us to have nearly inexhaustible energy resources in the next century.

Nuclear energy is a technology deeply rooted in the province. It is a source of pride for today's generation of Québécois and it is full of promise for tomorrow.

AECL CANDU
2251, rue Speakman
Mississauga (Ontario) L5K 1B2
Téléphone : (416) 823-9040
Télécopieur : (416) 823-1290



EACL

AECL

EACL CANDU

AECL CANDU



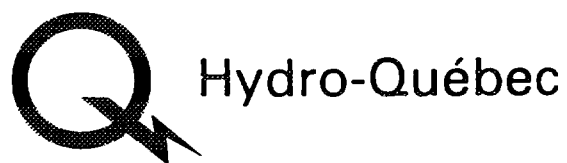
**Atomic Energy
Control Board**

**Commission de contrôle
de l'énergie atomique**

The Atomic Energy Control Board's mission is to ensure that the use of nuclear energy in Canada does not pose undue risk to health, safety, security and the environment.

La Commission de contrôle de l'énergie atomique a pour mission de s'assurer que l'utilisation de l'énergie nucléaire au Canada ne pose pas de risque indu pour la santé, la sécurité, la sécurité matérielle et l'environnement.

Canada



Le meilleur de nous-mêmes

Our Commitment Is To You

Région Mauricie



CANATOM INC.

2020 University
22e étage /22nd Floor
Montréal, Québec
H3A 2A5

Canatom, la plus grande société privée d'ingénierie oeuvrant exclusivement dans le domaine nucléaire, a joué un rôle clé dans le succès de la filière CANDU face à la concurrence mondiale. Cette réussite n'aurait pas été possible sans la prescience dont ont fait preuve les dirigeants des trois sociétés fondatrices (la Société d'ingénierie Montréal, la Société d'ingénierie Shawinigan et Surveyer, Nenniger & Chênevert - maintenant SNC-Lavalin Inc. et Monenco-AGRA Inc.) lorsqu'elles décidèrent de regrouper leurs ressources nucléaires en une même organisation. Cette dernière pouvait alors profiter de l'expérience combinée acquise par les trois sociétés en électricité et autres domaines connexes, expérience remontant au tournant du siècle. Par ailleurs, le fait que les années antérieures aient été couronnées de succès tient beaucoup aux étroites relations de travail développées entre Canatom et l'Énergie Atomique du Canada Limitée, promoteur et concepteur de la filière CANDU.

Au cours des années le nom de Canatom s'est propagé aux quatre coins du monde, notamment dans les pays suivants: Afrique-du-Sud, Arabie Saoudite, Argentine, Australie, Corée-du-Sud, Egypte, États-Unis, Grèce, Hong-Kong, Inde, Indonésie, Iran, Italie, Japon, Malaisie, Mexique, Nouvelle-Zélande, Pakistan, Roumanie, Royaume-Uni, Taïwan, Thaïlande, Turquie et Yougoslavie.

La réussite de la société sur la scène mondiale est un tribut à ses employés, à leur savoir-faire et expérience diversifiés, à leur ingéniosité et leur dévouement. Nos succès passés augurent bien de l'avenir.

Canatom is the largest Canadian private-sector engineering company operating exclusively in the nuclear field and has been a key player in enabling the CANDU nuclear power system to compete successfully on the world scene. This achievement would not have been possible without the foresight of the principals of the three founding engineering companies (Montréal Engineering, Shawinigan Engineering and Surveyer, Nenniger & Chênevert - now SNC-Lavalin Inc. and Monenco-AGRA Inc.) in bringing together their nuclear expertise under one umbrella organization. This organization then had the back-up provided by the combined resources of these companies in the electric power and related fields dating back to the beginning of this century. The other key ingredient to success was the close working relationship between Canatom and Atomic Energy of Canada Limited, the developer and designer of the CANDU reactor.

Over the years, the Canatom name has been carried to many parts of the world, including Argentina, Australia, Egypt, Greece, Hong Kong, India, Indonesia, Iran, Italy, Japan, Malaysia, Mexico, New Zealand, Pakistan, Philippines, Romania, Saudi Arabia, South Africa, South Korea, Taiwan, Thailand, Turkey, U.K., U.S.A and Yugoslavia.

The company's achievements throughout the world have been due to its people and their diverse skills and experience, the originality of their thinking, and their dedication to the work in hand. Our successes to date augur well for the future.

HORAIRE DE LA CONFÉRENCE
CONFERENCE SCHEDULE
VENDREDI 2 AVRIL, 1993
FRIDAY APRIL 2nd, 1993

- 8:30 – 11:45: Visite du CENTRE D'IRRADIATION DU CANADA / *Tour of The CANADIAN IRRADIATION CENTRE*
 (N.B. Départ des hôtels et Retour à l'École Polytechnique / *Note: Departure from the hotels and return to École Polytechnique*)
- 11:30 - 13:00: Inscription à l'hôtel suivi de l'inscription à la conférence au 6^{ième} de l'École Polytechnique/ *Registration at the hotel and conference registration 6th floor École Polytechnique*
- 13:00: Mot de bienvenue et ouverture de la conférence '93 dans l'Amphithéâtre Bell par le directeur de l'École Polytechnique, Dr. A. Bazergui (à confirmer) / *Welcoming Address and opening of the Conference by Dr. A. Bazergui director of École Polytechnique*
- 13:25 - 15:05: Sessions 1A & 1B
- 15:05 - 15:35: Pause / *Break*
- 15:35 - 16:55: Sessions 2A & 2B
- 16:55 - 18:00: Visite des laboratoires de l'I.G.E. / *Tour of the I.G.E. Laboratories*
- 18:00: Inscriptions tardives à l'hôtel / *Late registration at the hotel*
- 18:30 - 19:30: Apéro à la verrière de la cafétéria de l'École Polytechnique / *Cocktails, Baywindow area of the École Polytechnique cafeteria*
- 19:30: Banquet à la mezzanine de la cafétéria de l'École Polytechnique / *Banquet, mezzanine of the École Polytechnique cafeteria*
 Orateur invité / *Guest speaker: Dr. D. Rozon, Directeur / Chairman I.G.E.*
 "Perspectives de l'énergie nucléaire au Canada et au Québec pour les 20 prochaines années"

SAMEDI 3 AVRIL, 1993
SATURDAY APRIL 3rd, 1993

- 8:30 - 10:10: Sessions 3A & 3B
- 10:10 - 10:40: Pause / *Break*
- 10:40 - 12:00: Sessions 4A & 4B
- 12:00 - 13:30: Dîner à la galerie Rolland de l'École Polytechnique, au 6^{ième} / *Lunch, galerie Rolland of École Polytechnique 6th floor*
- 13:30 - 15:30: Session 5
- 15:30 - 16:00: Pause et délibération du jury / *Break and jury deliberation*
- 16:00 - 16:30: Remise des prix et clôture de la conférence '93 par Dr. H. Bonin C.R.M./ *Presentation of the prizes and closing of the conference by Dr. H. Bonin R.M.C.*

(Vendredi 2 avril 13:25 → 15:05)

(Friday April 2nd 13:25 → 15:05)

SESSION 1A: THERMOHYDRAULIQUE-1 / THERMALHYDRAULICS-1

Président / Chairman: Dr. A. Tapucu, I.G.E. École Polytechnique

Salle / Room: C-630

- P.Tye I.G.E., École Polytechnique
Determination of the Counter-Current Flooding Limit In Tubes Containing Orifices
- I.F. Obinelo McMaster University
Development of a Two-Fluid Model for Reflux Condensation and Flooding in a Vertical Tube
- A. Olekhnovitch I.G.E., École Polytechnique
Flux de chaleur critique pour des écoulements verticaux à faibles pressions
- D. Dormuth University of Manitoba
A Study of the Thermalhydraulic Factors Affecting Pressure Tube Rupture

SESSION 1B: SANTÉ & ENVIRONNEMENT / HEALTH & ENVIRONMENT

Président / Chairman: Dr. L. Zikovsky, I.G.E. École Polytechnique

Salle / Room: B-620.2

- K. Hammad University of Toronto
Iodine Behaviour and Measurement in the Canadian Shield Environment
- N. Thompson† Royal Military College
and J.Olsen† Integration of Radiation Monitoring for Nuclear Emergency Response Teams
- R. Quan University of Toronto
The Radiolysis of Aqueous Organic Systems and Their Influence on Iodine Volatility
- P. Gokhale University of New Brunswick
An Inverse and Adjoint Photon Transport Calculation in Radiotherapy Planning

† Denotes Undergraduate student
Indique un(e) étudiant(e) au Baccalauréat

(Vendredi 2 avril 15:35 → 16:55)
(Friday April 2nd 15:35 → 16:55)

SESSION 2A: THERMOHYDRAULIQUE-2 / THERMALHYDRAULICS-2

Président / Chairman: Dr. A. Teyssedou, I.G.E. École Polytechnique

Salle / Room: C-630

- P. Busono McMaster University
 An Experimental Investigation of Steam-Water Two-Phase Flow Regimes In a Horizontal Pipe
- P. Tye I.G.E., École Polytechnique
 The Representation of the Various Intersubchannel Transfer Mechanisms and Their Effects on the Predictions of the ASSERT-4 Subchannel Code
- J. Wang McMaster University
 Experimental Investigations of Counter-Current Flow Limitations in Vertical Two-Phase Flow Under Both Steady State and Pulsed Gas Flow
- P. Han University of New Brunswick
 Effect of Internal Metallic Structure on Void Fraction Measurement Using Neutron Scattering

SESSION 2B: MATÉRIAUX NUCLÉAIRES-1 NUCLEAR MATERIALS-1

Président / Chairman: Dr. Brent Lewis, Royal Military College

Salle / Room: B-620.2

- A. Harnden-Gillis Queen's University / Royal Military College
 Fission Product Release from Slowpoke-2 Reactors
- C.A. Deir University of Toronto
 Iodine Retention on Stainless Steel
- H.M. Pak† Royal Military College
 Damage Analysis of Polymer Composite Epoxies in High Radiation Environments
- R. Sahney Carleton University
 Potential Drop Crack Measurements System for CANDU Components

(Samedi 3 avril 8:30 → 10:10)
(Saturday April 3rd 8:30 → 10:10)

SESSION 3A: GESTION DES DÉCHETS & NEUTRONIQUE / WASTE MANAGEMENT & NEUTRONICS

Président / Chairman: Dr. M. Beaudet, Hydro Québec

Salle / Room: C-632

- G.F. Naterer University of Waterloo
 Species Redistribution During Solidification of Nuclear Fuel Waste Metal Castings
- B. Arsenault I.G.E., École Polytechnique
 Calculation of the Negative Reactivity Inserted by Shutdown System Number Two (SDS2) of a CANDU Reactor
- J. Whitlock McMaster University
 Dependence of Calculated Void Reactivity on Film Boiling Representation in a CANDU Lattice

SESSION 3B: DÉTECTION & ACTIVATION NEUTRONIQUE-1 DETECTION AND ACTIVATION-1

Président / Chairman: Dr. G. Evans, University of Toronto

Salle / Room: C-630

- M. Samri Université Laval
 Système multidétecteur pour l'identification et la mesure des énergies des ions lourds aux énergies intermédiaires
- P. Roy Université de Montréal
 Étude de la réponse d'un détecteur Si irradié par des neutrons de 1 Mev
- M.E. Abdelbaky University of New Brunswick
 Design of Intermediate Energy Filters for Neutron Beams
- M. Gourde Université Laval
 Développement et performances de détecteurs de particules chargées appliqués à l'étude des réactions avec ions lourds

(Samedi 3 avril 10:40 → 12:00)
(Saturday April 3rd 10:40 → 12:00)

SESSION 4A: MATÉRIAUX NUCLÉAIRES-2 NUCLEAR MATERIALS-2

Président / Chairman: M.A. Petrelli, Hydro Québec

Salle / Room: C-632

- S. Gong University of Toronto
 Mass Spectrometric Studies of Cluster Formation of Radon Progeny
- N.V. Arendtsz University of New Brunswick
 Material Density Differentiation: A Nonintrusive Method Using High Energy Gamma Rays
- T. Dhoum† University of Toronto
 Radiolytic Abatement of NO_x from Flue Gas
- M. M. Oskui University of Toronto
 Measurement of Interfacial Transfer of Iodine Species

SESSION 4B: DÉTECTION & ACTIVATION NEUTRONIQUE-2 DETECTION AND ACTIVATION-2

Président / Chairman: Dr. M. Gagnon, Fondateur du C.I.C.

Salle / Room: C-630

- D. Freed Massachusetts Institut of Technology
 Time-Resolved Luminescence Spectroscopy of Trace Uranyl in Wet Sand
- P. Bekeris† University of Toronto
 Iodine Behaviour in the Slowpoke Reactor
- M.S. Fila University of Toronto
 Neutron Activation Measurements of Submicron Aerosol Deposition onto a Cylinder Energized with an Alternating Electric Field
- V. Awafo Institut Armand Frappier
 Effect of Gamma Irradiation on the Structure of Corn Stalks and Their Subsequent Bioconversion into Protein-Rich Mycelial Biomass of Pleurotus Sajor-CAJU

(Samedi 3 avril 13:30 → 15:30)
(Saturday April 3rd 13:30 → 15:30)

SESSION 5: RÉACTEUR À SUSPENSION DE PARTICULES / PELLET SUSPENSION REACTOR

Président / Chairman: Dr. A. Harms, McMaster University

Salle / Room: C-631 (AMPHITHÉÂTRE BELL)

- C.W. Baetsen McMaster University
Fuel Pellet Considerations for the PSR (Pellet Suspension Reactor)
- J. Whitlock McMaster University
Core Physics Analysis of a Pellet Suspension Reactor (PSR)
- D. Kingdon McMaster University
Pellet Suspension and Fluidization Considerations in a Pellet Suspension Reactor (PSR)
- G. Rose† McMaster University
Pellet Dynamics in a Fluidized Bed Reactor Core
- W. Fundamenski McMaster University
Pellet Entrapment in LOCA Scenerio for the PSR Reactor
- S. Day McMaster University
Fission Product Management and Fuel Reprocessing in a Pellet Suspension Reactor

TABLE DES MATIERES / TABLE OF CONTENTS

HORAIRES / <i>SCHEDULE</i>	xix
TABLE DES MATIERES / <i>TABLE OF CONTENTS</i>	xxv

SESSION 1A: THERMOHYDRAULIQUE-1 / THERMALHYDRAULICS-1

P.Tye "Determination of the Counter-Current Flooding Limit In Tubes Containing Orifices"	2
I.F. Obinelo "Development of a Two-Fluid Model for Reflux Condensation and Flooding in a Vertical Tube"	3
A. Olekhnovitch "Flux de chaleur critique pour des écoulements verticaux à faibles pressions"	4
D. Dormuth "A Study of the Thermalhydraulic Factors Affecting Pressure Tube Rupture"	16

SESSION 1B: SANTÉ & ENVIRONNEMENT / HEALTH & ENVIRONMENT

K. Hammad "Iodine Behaviour and Measurement in the Canadian Shield Environmental"	18
N. Thompson† and J.Olsen† "Integration of Radiation Monitoring for Nuclear Emergency Response Teams"	20
R. Quan "The Radiolysis of Aqueous Organic Systems and Their Influence on Iodine Volatility"	30
P. Gokhale "An Inverse and Adjoint Photon Transport Calculation in Radiotherapy Planning"	32

SESSION 2A: THERMOHYDRAULIQUE-2 / THERMALHYDRAULICS-2

P. Busono "An Experimental Investigation of Steam-Water Two-Phase Flow Regimes In a Horizontal Pipe"	34
P. Tye "The Representation of the Various Intersubchannel Transfer Mechanisms and Their Effects on the Predictions of the ASSERT-4 Subchannel Code"	35
J. Wang "Experimental Investigations of Counter-Current Flow Limitations in Vertical Two-Phase Flow Under Both Steady State and Pulsed Gas Flow"	51
P. Han "Effect of Internal Metallic Structure on Void Fraction Measurement Using Neutron Scattering"	52

SESSION 2B

MATÉRIAUX NUCLÉAIRES-1 / NUCLEAR MATERIALS-1

A. Harnden-Gillis "Fission Product Release from Slowpoke-2 Reactors"	54
C.A. Deir "Iodine Retention by Stainless Steel"	78
H.M. Pak† "Damage Analysis of Polymer Composite Epoxies in High Radiation Environments"	80
R. Sahney "Potential Drop Crack Measurements System for CANDU Components"	88

† Denotes Undergraduate student
Indique un(e) étudiant(e) au Baccalauréat

SESSION 3A
GESTION DES DÉCHETS & NEUTRONIQUE / WASTE MANAGEMENT & NEUTRONICS

- G.F. Naterer "Species Redistribution During Solidification of Nuclear Fuel Waste Metal Castings" 102
 B. Arsenault "Calculation of the Negative Reactivity Inserted by Shutdown System Number Two (SDS2) of a CANDU Reactor" 112
 J. Whitlock "Dependence of Calculated Void Reactivity on Film Boiling Representation in a CANDU Lattice" 125

SESSION 3B
DÉTECTION & ACTIVATION NEUTRONIQUE-1 DETECTION AND ACTIVATION-1

- M. Samri "Système multidétecteur pour l'identification et la mesure des énergies des ions lourds aux énergies intermédiaires" 136
 P. Roy "Étude de la réponse d'un détecteur Si irradié par des neutrons de 1 Mev" 146
 M.E. Abdelbaky "Design of Intermediate Energy Filters for Neutron Beams" 156
 M. Gourde Université Laval
 "Développement et performances de détecteurs de particules chargées appliqués à l'étude des réactions avec ions lourds" 157

SESSION 4A
MATÉRIAUX NUCLÉAIRES-2 NUCLEAR MATERIALS-2

- S. Gong "Mass Spectrometric Studies of Cluster Formation of Radon Progeny" 168
 N.V. Arendtsh "Material Density Differentiation: A Nonintrusive Method Using High Energy Gamma Rays" 178
 T. Dhout "Radiolytic Abatement of NO_x from Flue Gas" 179
 M. M. Oskui "Measurement of Interfacial Transfer of Iodine Species" 181

SESSION 4B
DÉTECTION & ACTIVATION NEUTRONIQUE-2 DETECTION AND ACTIVATION-2

- D. Freed "Time-Resolved Luminescence Spectroscopy of Trace Uranyl in Wet Sand" 184
 P. Bekerist "Iodine Behaviour in the Slowpoke Reactor" 193
 M.S. Fila "Neutron Activation Measurements of Submicron Aerosol Deposition onto a Cylinder Energized with an Alternating Electric Field" 198
 V. Awafo "Effect of Gamma Irradiation on the Structure of Corn Stalks and Their Subsequent Bioconversion into Protein-Rich Mycelial Biomass of *Pleurotus Sajor-CAJU*" 204

SESSION 5:
RÉACTEUR À SUSPENSION DE PARTICULES / PELLET SUSPENSION REACTOR

- C.W. Baetsen "Fuel Pellet Considerations for the PSR (Pellet Suspension Reactor)" 215
 J. Whitlock "Core Physics Analysis of a Pellet Suspension Reactor (PSR)" 216
 D. Kingdon "Pellet Suspension and Fluidization Considerations in a Pellet Suspension Reactor (PSR)" 217
 G. Rose "Pellet Dynamics in a Fluidized Bed Reactor Core" 219
 W. Fundamenski "Pellet Entrapment in LOCA Scenerio for the PSR Reactor" 220
 S. Day "Fission Product Management and Fuel Reprocessing in a Pellet Suspension Reactor" 221

(Vendredi 2 avril 13:25 → 15:05)
(Friday April 2nd 13:25 → 15:05)

SESSION 1A

THERMOHYDRAULIQUE-1 / THERMALHYDRAULICS-1

Président / Chairman: Dr. A. Tapucu, I.G.E. École Polytechnique

Salle / Room: C-630

- P. Tye I.G.E., École Polytechnique
Determination of the Counter-Current Flooding Limit In Tubes Containing Orifices
- I.F. Obinelo McMaster University
Development of a Two-Fluid Model for Reflux Condensation and Flooding in a Vertical Tube
- A. Olekhnovitch I.G.E., École Polytechnique
Flux de chaleur critique pour des écoulements verticaux à faibles pressions
- D. Dormuth University of Manitoba
A Study of the Thermalhydraulic Factors Affecting Pressure Tube Rupture



DETERMINATION OF THE COUNTER-CURRENT FLOODING LIMIT IN TUBES CONTAINING ORIFICES

*P. Tye,⁽¹⁾ M. Davidson,⁽¹⁾ A. Teyssedou,⁽¹⁾
A. Tapucu,⁽¹⁾ A. Matuszkiewicz,⁽¹⁾ and W. Midvidy⁽²⁾*

*(1) Institut de Génie Énergétique
École Polytechnique de Montréal
Montréal, Québec, Canada H3C 3A7
(2) Ontario Hydro*

ABSTRACT

For certain hypothetical loss of coolant accidents in nuclear reactors, the rapid reflooding of the core is essential. In CANDU reactors the emergency cooling water is injected into the headers which are connected to the fuel channels by the feeder pipes. These pipes consist of vertical and horizontal runs; in some feeders, orifices and/or venturi flow meters are installed for flow adjustments and measurements respectively. For certain postulated accident scenarios steam coming from the fuel channels and/or generated by the hot feeders may flow in the direction opposite to that of the cooling water thereby, creating a vertical or horizontal counter-current two-phase flow. Under these conditions, the rate at which emergency cooling water can enter the fuel channels is limited by the flooding phenomena. This phenomena is greatly affected by the geometry of the feeder pipes, shape and number of fittings, and the flow area restrictions located in the feeders.

In this paper the influence that orifice type flow area restrictions have on the counter-current flooding limit (CCFL) in a vertical tube is examined. The data collected on the counter-current flooding limit in a vertical tube both with and without flow area restrictions is compared against some of the most commonly used correlations that are available in the open literature.



CA9700529

Development of a Two-Fluid Model For Reflux Condensation and Flooding in a Vertical Tube

I.F. Obinelo

**Department of Mechanical Engineering
McMaster University
Hamilton, Ontario. L8S 4K1**

Supervisors: Dr. J.S. Chang and Dr G.F. Round

In certain situations involving a small-break loss of coolant accident in the primary loop of a nuclear reactor, reflux condensation is known to be the only means available for heat removal at low primary coolant inventories. In such situations, a reliable safety analysis to predict the heat removal capability of reflux condensation must involve a detailed knowledge of the flow and heat transfer characteristics of the phenomenon, including the steam/condensate flow regimes, the void fraction and temperature distributions, the pressure drop across the tubes, and most importantly the exact nature of the flooding phenomenon which marks the point of departure from stable counter-current flow. In a typical experimental test on reflux condensation, flooding in the steam generator tubes results in the formation of a single-phase water column on top of the condensing region, resulting in a cyclic build-up of a single-phase water column which is periodically carried over the top of the tube. In such situations the condensing region length, and hence one boundary of the solution domain, is neither fixed in time or space and is not known *a priori*.

This paper discusses a high resolution two-fluid model for reflux condensation developed with the aim of obtaining a better assessment of the heat removal capability of the phenomenon over simple models or the more general reactor safety codes. As the boundary of the solution domain is unknown and time-dependent, a special time-dependent grid adaptation technique is built into the solution algorithm in order to track boundary of the condensing region, and the exact location of this boundary with time is determined from the overall energy conservation of the system. Sample results are obtained and compared with experimental measurements.



FLUX DE CHALEUR CRITIQUE EN ECOULEMENTS VERTICAUX AUX PRESSIONS FAIBLES

A.Olekhnovitch

Institut de génie énergétique

École Polytechnique, Université de Montréal

Montréal, CANADA

1. INTRODUCTION

L'un des paramètres les plus importants du transfert de chaleur dans des conditions d'ébullition est le flux de chaleur critique (FCC) qui indique d'une façon générale une situation dans laquelle une détérioration du mécanisme de transfert de chaleur a lieu à cause de la perte du contact entre la paroi chauffée et le liquide. Dans les systèmes où on contrôle le flux de chaleur à la paroi, cette détérioration entraîne une augmentation substantielle de la température de la surface chauffée jusqu'à sa destruction.

Le flux de chaleur critique pour les écoulements verticaux a été étudié pour une grande gamme de paramètres (Groeneveld [1], Collier [2], Katto [3]). Certains modèles mécanistiques ont été élaborés pour les écoulements à titre faible et à titre élevé. Pour les écoulements où l'ébullition sous-refroidie ou saturée à titre faible prédomine, ces modèles sont principalement basés sur l'échange de masse qui a lieu entre le noyau de liquide et la couche de bulles à la paroi (Weisman & Pei [4] et Ying & Weisman [5]). Pour les conditions de titre élevé, où la configuration d'écoulement est annulaire, ces modèles sont basés sur la supposition que le FCC correspond au tarissement du film de liquide sur la paroi (Whalley et al. [6]). Cependant, ces modèles ne sont valides que pour une configuration d'écoulement donnée et pour les cas où les hypothèses utilisées sont encore valables. Une autre approche générale de la prédiction du FCC est basée sur l'utilisation des corrélations empiriques. La région d'application de celles-ci est limitée au domaine des données expérimentales sur lesquelles elles ont été établies.

Récemment, pour prédire le flux de chaleur critique, des tables des valeurs du FCC ont été proposées (Groeneveld et al. [7], Doroshchuk et al. [8], Académie de Science de l'U.R.S.S. [9]). Ces tables fournissent des valeurs du FCC pour une large gamme de pressions, de vitesses massiques et de

titres d'écoulement. Les données incluses dans ces tables ont été obtenues pour des tubes cylindriques chauffés uniformément; des facteurs de correction ont été proposés pour tenir compte des paramètres géométriques différents, des distributions des flux de chaleur non-uniformes et des orientations de l'écoulement. Néanmoins, pour des pressions faibles ($P \leq 30 \text{ bars}$), il n'existe presque pas de données et les valeurs du FCC dans la table [7] pour ce domaine ont été obtenues par une extrapolation des données de hautes pressions. C'est pourquoi, des erreurs substantielles de l'estimation du FCC peuvent avoir lieu. D'autre part, la connaissance des flux de chaleur critique aux pressions faibles est très importante pour des situations accidentelles occasionnées par une baisse de pression subite due à une perte de caloporteur. Afin d'améliorer les tables, une série d'expériences a été menée pour les régions où les données sont rares ou non-existantes.

2. INSTALLATION EXPERIMENTALE

Cette étude a été produite avec la boucle thermique de l'institut de génie énergétique de l'Ecole Polytechnique. Pour les écoulements en régime permanent, cette boucle permet les marges d'opération suivantes:

puissance appliquée 10 - 400 kW,
 pression d'opération 3 - 40 bars,
 débit massique 0.05 - 1.7 kg/s,
 sous-refroidissement à l'entrée 0 - 100° C.

La boucle thermique est constituée d'un ballon de vapeur, d'un condenseur, d'une pompe, d'un échangeur de chaleur, de deux préchauffeurs, d'une section d'essai et d'un système de contrôle de puissance (*Figure 1*). Les paramètres principaux de la boucle et de la section d'essai (la puissance, le débit, les températures et les pressions aux points-clés dans les lignes et les composants de la boucle) sont contrôlés et maintenus constants par des systèmes de contrôle, d'alarme et d'interruption du système.

La section d'essai est fabriquée à partir d'un tube cylindrique en INCONNEL 600 d'une longueur de 2.2 m et de diamètre interne de 8 mm. La chaleur est produite par effet Joule en appliquant un courant continu à la paroi, et en choisissant une longueur chauffée donnée. La longueur chauffée peut être modifiée par la position des barres de chauffage faites en cuivre reliant la section d'essai à la source de puissance (voir la *Figure 1*).

Pour la détection du commencement du FCC un certain nombre de thermocouples de Chromel-Alumel gainés de diamètre externe de 0.5 mm sont soudés par contact sur la surface de la section d'essai. La *Figure 2* montre l'arrangement de la section d'essai telle qu'utilisée pour les expériences effectuées à la longueur chauffée de 1.8 m . Afin de protéger le tube, un thermocouple à la sortie de la section d'essai et deux groupes de cinq thermocouples connectés en parallèle, et distribués le long du tube, sont utilisés pour interrompre la puissance. Les signaux des thermocouples ont été enregistrés en temps réel sur une bande graphique et quelques températures principales ont été collectées par le système d'acquisition de données (DAS) pour l'analyse ultérieure.

Par ailleurs, d'autres paramètres de l'écoulement ont aussi été mesurés et enregistrés. Les températures à la sortie et à l'entrée de la section d'essai sont mesurées par un thermomètre à résistance de type RTD ayant une précision de $\pm 1^\circ\text{C}$. dans le domaine d'intérêt ($100\text{-}200^\circ\text{C}$). La pression absolue à l'entrée et à la sortie de la section d'essai a été mesurée sur la bride inférieure et sur le collier de prise de pression se trouvant à 80 mm en aval de la barre de chauffage supérieure respectivement. Ces mesures ont été prises par deux capteurs de pression de marque "Sensotec" dont la précision est de $\pm 0.1\%$ à pleine échelle. Le débit volumique d'eau a été mesuré avec un débitmètre à turbine dont la précision est de $\pm 1\%$.

Les expériences principales ont été menées à une pression au condenseur, un débit volumique et une température à l'entrée de la section d'essai fixes. Quand ces paramètres étaient établis, la puissance appliquée à la section d'essai était graduellement augmentée (tout près du FCC les paliers d'augmentation de puissance étaient moins que 0.5 kW) jusqu'à l'apparition des premières fluctuations de température de la paroi.

Pour le FCC de type assèchement, c'est-à-dire pour des titres d'écoulement élevés, ces premières fluctuations de température (habituellement de $2\text{ à }4^\circ\text{C}$) étaient considérées comme le début du FCC. Ce critère a été choisi selon la considération suivante: pour des pressions faibles ($P_s \leq 10\text{ bars}$) et des vitesses massiques de $G \leq 2000\text{ kg m}^{-2}\text{ s}^{-1}$ les fluctuations de température de la paroi s'accroissent assez lentement, lorsque la puissance appliquée augmente. L'amplitude de ces fluctuations peut atteindre $20\text{ - }40^\circ\text{C}$ par rapport à une valeur moyenne sans qu'une excursion de température soudaine se produise. Un comportement pareil a été décrit par Groeneveld [10] et a été nommé comme étant l'assèchement instable ("unstable dryout"). Dans ce cas, une telle procédure pour déterminer le début du FCC est plus logique et plus objective parce qu'il n'y a pas de points de repère pour caractériser la

début de la crise. Pour des FCC ayant lieu dans des conditions d'écoulement à titre faible (grand sous-refroidissement à l'entrée) la température de la paroi varie brusquement. Dû à ce fait, la différence de puissance observée entre l'apparition de la première fluctuation de température et celle qui déclenche l'arrêt du système de puissance est très faible ($\leq 3kW$). Pour ne pas perdre la généralité, ce critère a été utilisé aussi pour les cas où on relie le FCC avec une augmentation brusque de la température de paroi. Pour le FCC de type caléfaction, l'excursion soudaine de la température de paroi détermine uniquement le FCC.

3. RESULTATS EXPERIMENTAUX

Les *Figures 4a-c* présentent la dépendance du FCC au sous-refroidissement à l'entrée pour la pression de sortie de 5, 10 et 30 *bars* respectivement. Le sous-refroidissement représente l'état thermodynamique à l'entrée de la section d'essai et il est donné par:

$$\Delta h_{sre} = h_{sat}(P_e) - h_e(P_e, T_e). \quad (1)$$

Comme on peut le voir sur ces figures, la dépendance du FCC au sous-refroidissement est presque linéaire et le FCC augmente lorsque Δh_{sre} s'accroît. Ce fait correspond aux tendances présentées dans la littérature. Cependant, pour des pressions ≤ 10 *bars* et des vitesses massiques ≥ 2000 *kg m⁻²s⁻¹*, il n'était pas possible de maintenir une pression présélectionnée. A partir d'une puissance appliquée, c'est-à-dire d'un titre d'écoulement donné, la pression à la sortie de la section d'essai restait constante même après la diminution de la pression au condenseur jusqu'à 3 *bars*. D'autre part, cette pression s'accroissait lorsque la puissance était augmentée. Cette situation est très semblable aux écoulements critiques où le débit de l'écoulement diphasique sortant d'un réservoir de haute pression reste limité et indépendant de la pression. Un comportement pareil a été supposé par Fauske [11] dans l'analyse des données sur le FCC de Lowdermilk et al. [12] et exige, bien sûr, une étude plus détaillée. Présentement, on peut seulement supposer que la vitesse de vapeur à la sortie de la section chauffée, ou quelque part tout près du changement de la section de passage de conduit, atteint la vitesse de propagation des perturbations faibles ou, autrement dit, celle du son.

Les courbes présentées sur les *Figures 3a-c* montrent clairement les tendances suivantes:

- pour un sous-refroidissement et une vitesse massique constants, le FCC augmente lorsque la longueur chauffée diminue, et

- pour un sous-refroidissement et une longueur chauffée fixes, le FCC augmente avec une augmentation de vitesse massique.

Présentement, il existe deux approches ou, plus correctement, deux hypothèses sur le phénomène du FCC: L'hypothèse locale qui détermine le FCC par une combinaison des paramètres dans une certaine section du tube, et l'hypothèse globale qui suppose que tous les facteurs influençant l'écoulement à partir de l'entrée de la section chauffée jusqu'à l'endroit où le FCC a lieu ont un effet sur le FCC. Ces deux approches ont leurs côtés forts et faibles, mais si le FCC ne dépend que des conditions locales, la longueur et la forme de distribution de la puissance le long du tube n'affecteraient pas le FCC. Le traitement des données représente dans ce cas la recherche d'une fonction de type: $q_{cr} = f(P_s, G, x, d)$, où P_s est la pression de saturation, G est le flux ou la vitesse massique, x est le titre d'écoulement, d est le diamètre interne du tube. Les Figures 4a-c comparent le FCC en fonction du titre pour des vitesses massiques et des longueurs chauffées différentes. Le titre d'écoulement à la sortie de la section d'essai est calculé à partir du bilan thermique.

La Figure 4a montre que pour des pressions de 5 à 8 bars le FCC est affecté par la longueur chauffée. Pour des longueurs de 1.0 et 1.4 m et des vitesses massiques de 2000 et 3000 $kg\ m^{-2}\ s^{-1}$, une chute considérable du FCC à titre presque constant est observée. On observe aussi que cette chute commence à avoir lieu à partir des titres correspondant aux enthalpies à l'entrée de la section chauffée égales ou plus élevées que l'enthalpie du liquide saturé correspondant à la pression de saturation à la sortie. Cette indépendance du FCC en fonction du titre a été déjà observée par des chercheurs russes (Levitan & Lantsman [13]), et le titre correspondant a été nommé "titre-limite". Selon Doroshchuk [14], dans cette région, les gouttelettes d'eau entraînées dans le noyau de vapeur n'atteignent pas le film de liquide sur la paroi à cause d'un flux de vapeur transversal, et le FCC a lieu au moment où le film de liquide sur la paroi tarit naturellement. Cette condition n'est déterminée que par la vitesse massique et par la pression absolue. Dans ce cas le FCC perd son sens physique, et une seule valeur - le titre-limite - définit entièrement l'assèchement. Doroshchuk a nommé ce type de FCC la crise de deuxième type. Néanmoins, une influence de la longueur chauffée sur le FCC telle que nous observons (pour des sous-refroidissement assez élevés) semble démontrer que le titre-limite n'est pas un phénomène général. Ceci est probablement relié aux mécanismes de l'assèchement spécifiques ayant lieu aux pressions faibles.

En général, des tendances semblables sont aussi présentes pour les données obtenues aux pressions

de 10 - 12 bars (*Figure 4b*). L'effet de la longueur chauffée commence à disparaître lorsque la pression à la sortie de la section d'essai augmente (*Figure 4c*). Ceci s'applique seulement à partir d'une longueur de 1.4 m ($L/D \geq 175$). Pour une longueur chauffée 1 m le FCC est plus élevé que ceux correspondant à des longueurs plus grandes.

Une comparaison des Figures 4a-c permet de déterminer les tendances paramétriques suivantes:

- le flux de chaleur critique diminue lorsque le titre d'écoulement à la sortie augmente, cependant une généralisation globale de ce comportement n'est pas possible, car dans certains cas une région de titre-limite se développe,
- pour un titre constant le FCC diminue avec l'augmentation de la longueur chauffée, toutefois cet effet a tendance à disparaître aux hautes pressions (30 bars).

4. COMPARAISON AVEC DES CORRELATIONS EXISTANTES

Un bon nombre de corrélations disponibles pour la prédiction du FCC existent présentement dans la littérature (Bergles [15]). Afin de comparer les données, trois corrélations les plus utilisées, celles de Biasi et al. [16], de Bowring [17], de Katto & Ohno [18], et la table des valeurs du FCC de Groeneveld [7], ont été sélectionnées. Des résultats de cette comparaison pour une longueur de 1.4 m sont présentés sur la *figure 5*. En général, les écarts entre les valeurs mesurées et celles prédites sont assez élevés, et la différence peut atteindre dans certains cas de 200 -300 %. Probablement ceci est relié au fait que ces corrélations sont basées principalement sur des données obtenues aux hautes pressions. Selon les figures, pour les pressions faibles, la table de Groeneveld donne la meilleure prédiction du FCC. D'autre part, pour des pressions moyennes (30 bars) et des vitesses massiques élevées ($4000 \text{ kg m}^{-2}\text{s}^{-1}$), les écarts entre la corrélation de Katto & Ohno et les données obtenues sont moindres.

5. CONCLUSION

Le but principal de cette étude a été de collecter des données sur le FCC pour une plage large des titres d'écoulement dans le domaine des paramètres où ces données sont rares ou non-existantes (pressions faibles). Les expériences ont été produites sur une section d'essai verticale constituée d'un tube cylindrique de diamètre interne de 8 mm et pour trois longueurs chauffées différentes: 1, 1.4 et 1.8 m. En général, les données obtenues corroborent les tendances déjà décrites dans la littérature (Groeneveld [1], Collier [2], Carey [19]). Cependant, nous avons observé que pour des pressions faibles

le FCC semble dépendre de la longueur chauffée. Cet effet commence à disparaître pour des pressions de 30 bars. Pour des pressions faibles (de 5 à 10 bars) et des vitesses massiques plus grandes que $2000 \text{ kg m}^{-2} \text{ s}^{-1}$, dans un domaine de petits sous-refroidissements, le FCC semble ne pas dépendre du titre d'écoulement, et un titre-limite a lieu. Des expériences supplémentaires sont présentement en cours pour confirmer ce comportement.

Les données expérimentales ont été comparées avec les prédictions des corrélations de Biasi [16], de Bowring [17], de Katto & Ohno [18] et avec les données de la table des valeurs du FCC de Groeneveld [7]. Selon cette comparaison, aucune des ces corrélations ne prédit précisément le FCC dans toute la gamme étudiée, et on peut dire seulement qu'une corrélation plutôt qu'une autre s'applique à une certaine région donnée de la plage des types d'écoulement étudiés.

Remerciements

Ce travail a été partiellement subventionné par AECL/COG (contract # C64036) et par NSERC-CRD (contract # 116727).

REFERENCES

- [1] D.C. Groeneveld, Thermohydraulic Problems Related to LWR Safety, ISPRA (1980).
- [2] J.C. Collier, Convective Boiling and Condensation (McGraw-Hill, New York, 1981).
- [3] Y. Katto, Critical heat flux, in: Advances in Heat Transfer, ed. T.F. Irvine, Jr. and J.P. Harnett, (Academic Press, Orlando, 1985) Vol. 17, pp. 1-64.
- [4] J. Weisman and B.S. Pei, Prediction of critical heat flux in flow boiling at low qualities, Int. J. Heat Mass Transfer, 26 (1983) 1463-1477.
- [5] S.H. Ying and J. Weisman, Prediction of the critical heat flux in flow boiling at intermediate qualities, Int. J. Heat Mass Transfer, 29, No. 11 (1986) 1639-1648.
- [6] P.B. Whalley, P. Hutchinson and G.F. Hewitt, The calculation of critical heat flux in forced convection boiling, Report AERE-R7520, Harwell, U.K., (1973).
- [7] D.C. Groeneveld, S.C. Cheng and T. Doan, AECL-UO critical heat flux look-up table, Heat Transfer Engng., Vol.7, No. 1-2 (1986) 46-62.
- [8] V.E. Doroshchuk et al., Recommendations for calculating burnout in a round tube with uniform heat release, Thermal Engng., Vol. 22, No. 12 (1975) 66-70.

- [9] U.S.S.R. Academy of Science, Recommendations for the calculation of the heat transfer crisis at boiling of water in round tubes, Institut of High Temperatures of the Academy of Science (in Russian), Preprints 1-57 (1980) 67.
- [10] D.C. Groeneveld, The onset of dry sheath condition - A new definition of dryout, Nuclear Eng. and Design, Vol. 92, (1986) 135-140.
- [11] H.K. Fauske, Compressibility affects flow instability and burnout, Power Reactor Technology, Vol. 9, No. 2 (1966) 65-68.
- [12] W.H. Lowdermilk et al., Investigation of boiling burnout and flow stability in tubes, Report NACA-TN-4382, National Advisory Committee for Aeronautics (1958).
- [13] L.L. Levitan and F.P. Lantsman, Investigating burnout with flow of steam water mixture in a round tube, Thermal Engng., (U.S.S.R.), English trans., Vol. 22, No. 1 (1975) 102-105.
- [14] V.E. Doroshchuk, Heat Transfer Crisis at Boiling of Water in Round Tubes, (in Russian - Energoatomizdat, Moscow, 1983)
- [15] A.E. Bergles, Burnout in boiling heat transfer: High-quality forced convection systems, in: Two-Phase Flow and Heat Transfer, China-U.S. Progress, ed. X.-J. Chen and T.N. Veziroglu (Hemisphere, New York 1985) pp. 177-206.
- [16] L. Biasi, G.C. Gariloben, S. Sala and A. Tozzi, Studies on burnout, Part 3, A new correlation for round ducts and uniform heating and its comparison with world data, Energia Nucleare, Vol. 14, No. 9 (1967) 530-536.
- [17] R.W. Bowring, A simple but accurate round tube uniform heat flux correlation over the pressure range 0.7-17 MN/m² (100-2500 psia), Br. Report AEEW-R789, Winfrith, U.K. (1972).
- [18] Y. Katto and H. Ohno, An improved version of the generalized correlation of critical heat flux for the forced convective boiling in uniformly heated vertical tubes, Int. J. Heat Mass Transfer, Vol. 27 (1984) 1641-1648.
- [19] V.P. Carey, Liquid-vapor phase-change phenomena (Hemisphere Publishing Corporation, Washington, (1992) pp. 524-539.

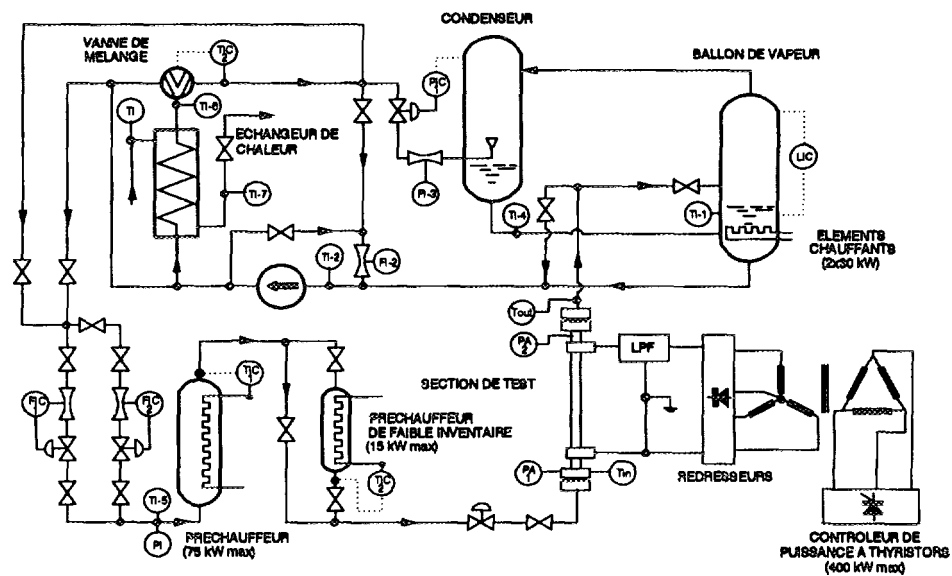


Figure 1. Boucle thermique

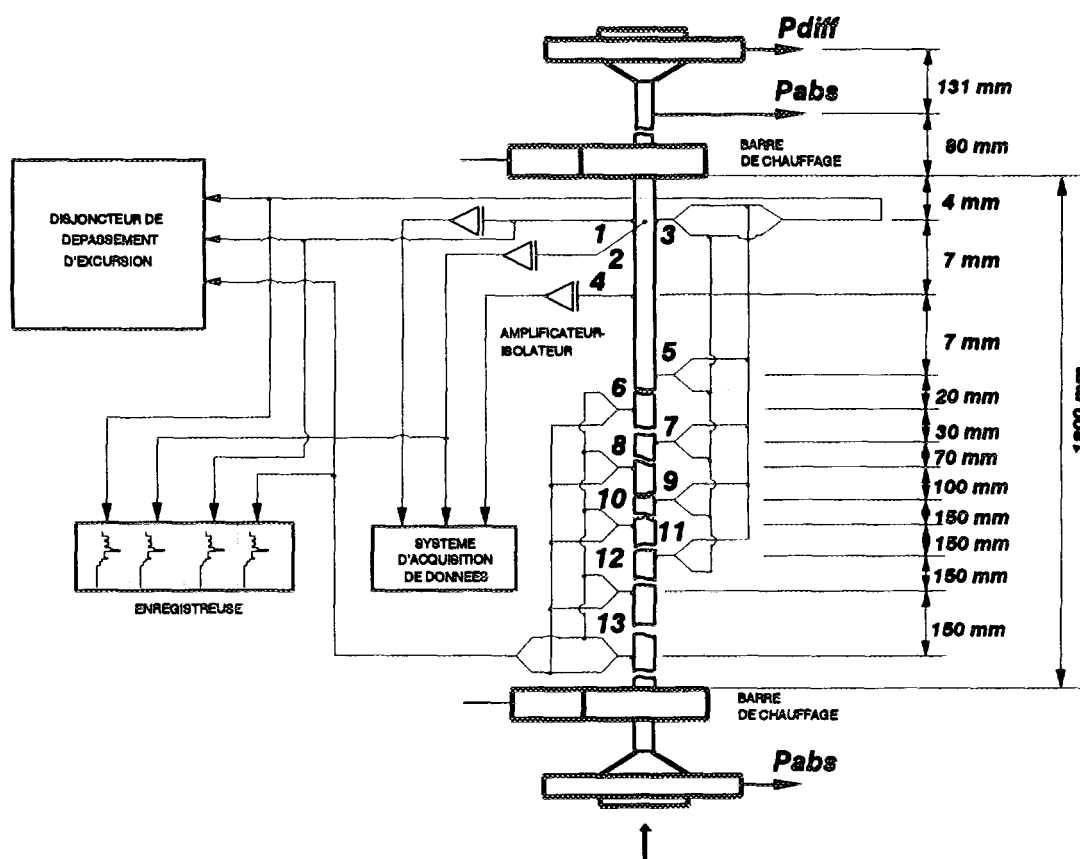


Figure 2. Section d'essai

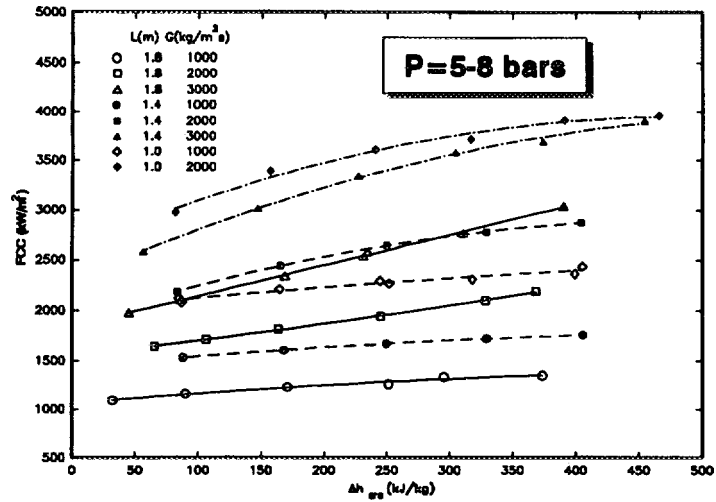


Figure 3a. FCC en fonction du sous-refroidissement à l'entrée (P=5-8 bars)

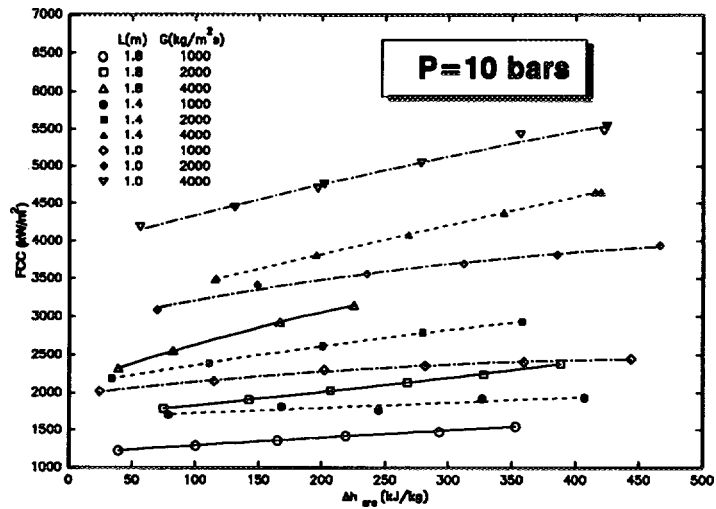


Figure 3b. FCC en fonction du sous-refroidissement à l'entrée (P=10 bars)

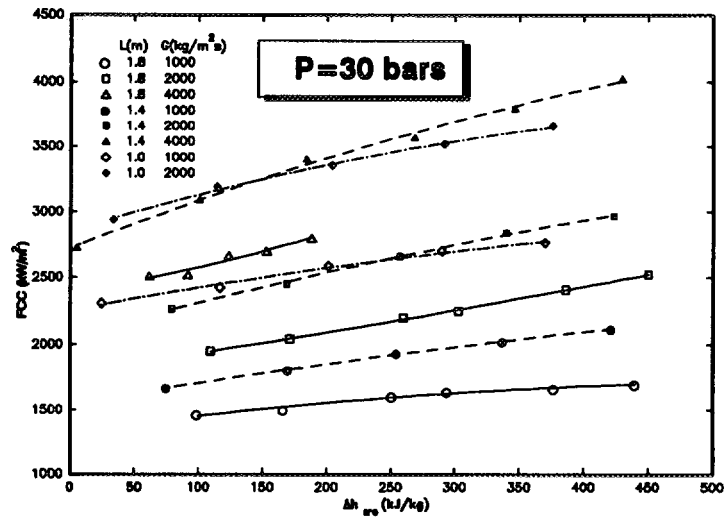


Figure 3c. FCC en fonction du sous-refroidissement à l'entrée (P=30 bars)

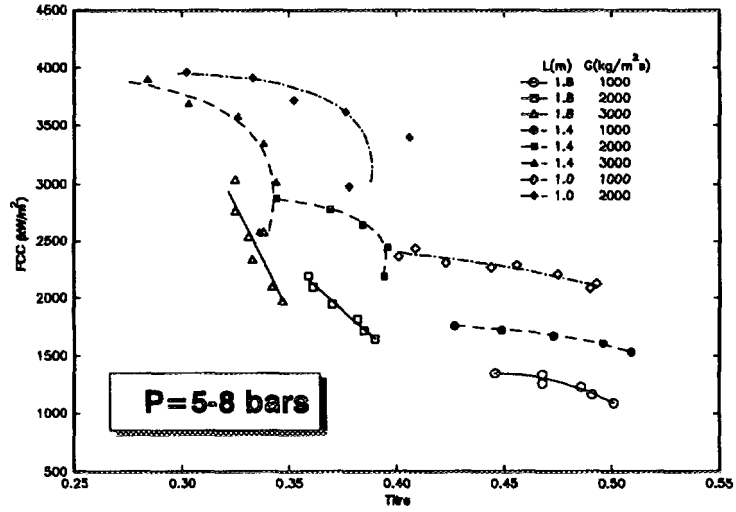


Figure 4a. FCC en fonction du titre (P=5-8 bars)

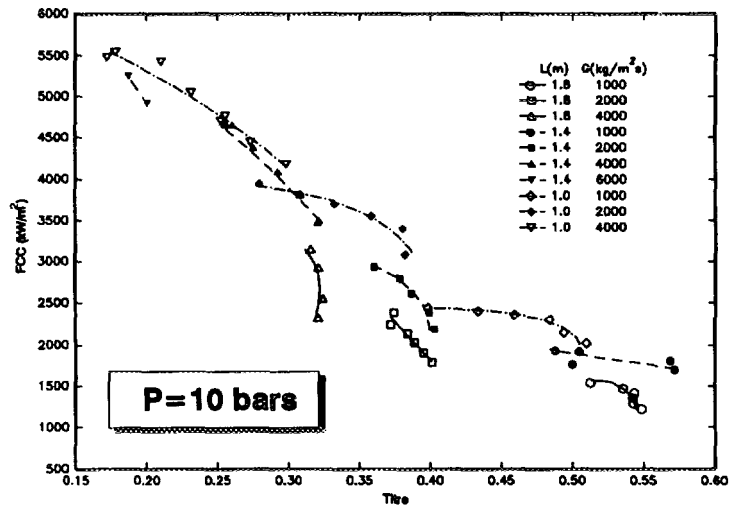


Figure 4b. FCC en fonction du titre (P=10 bars)

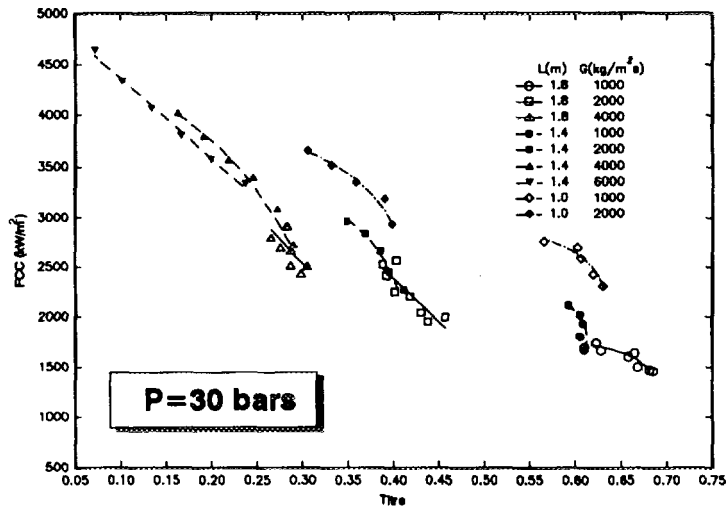


Figure 4c. FCC en fonction du titre (P=30 bars)

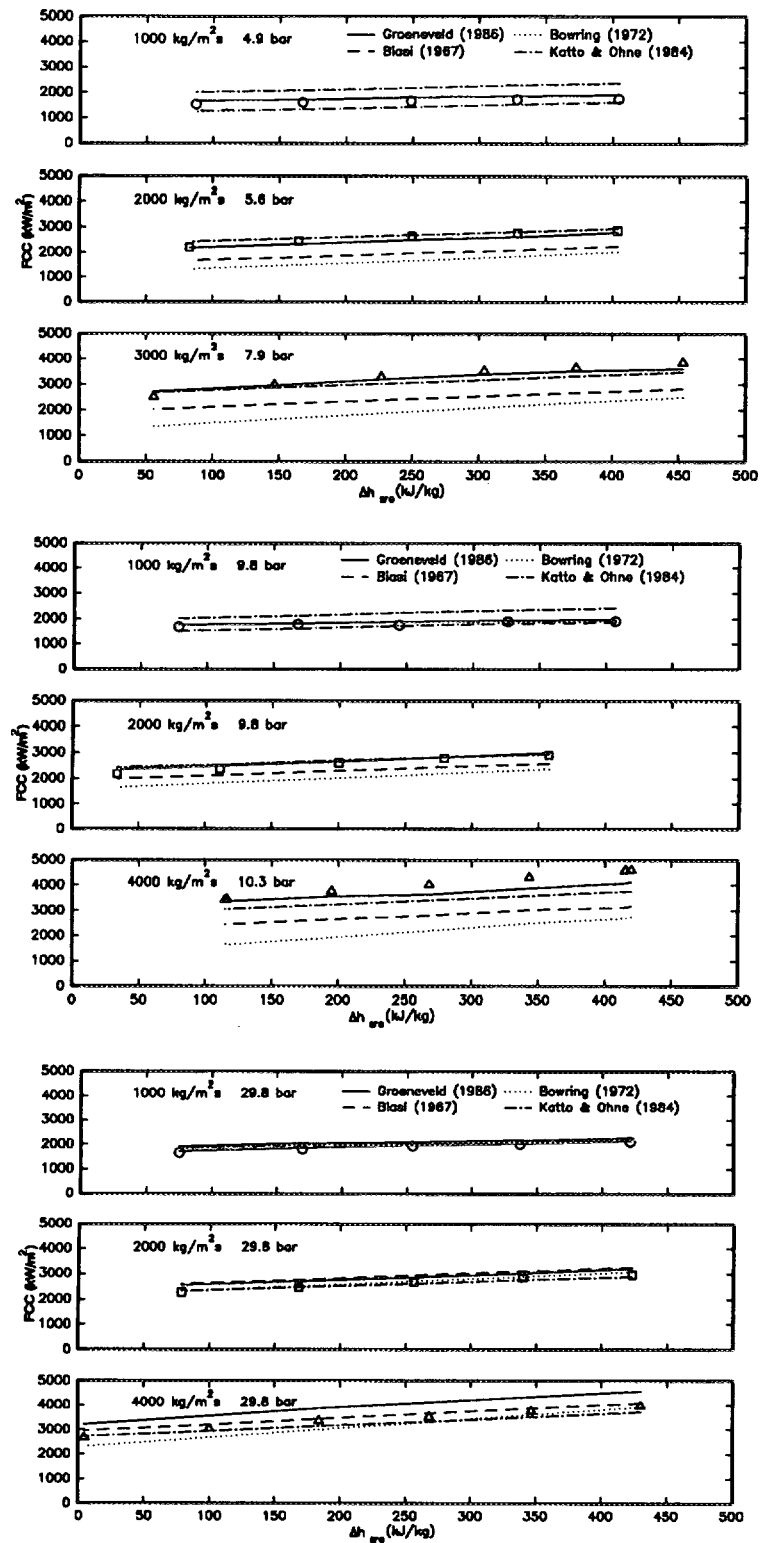


Figure 5. Comparaison des données expérimentales avec les prédictions de différentes corrélations



A STUDY OF THERMALHYDRAULIC FACTORS
AFFECTING PRESSURE TUBE RUPTURE

by

D.W. Dormuth and B.H. McDonald

ABSTRACT

Observation of experiments conducted at Stern Laboratories to investigate the effects of cracks in bursting pressure tubes has led to an in-depth analysis of the mechanical behaviour of this phenomenon. Part of this analysis comprises simulating a bursting pressure tube using a finite-element model that requires thermalhydraulic boundary conditions as input. This report focuses on using a multidimensional thermalhydraulics model to supply these boundary conditions. In particular, parameters that could influence the internal pressure during a burst transient are studied in a sensitivity analysis using statistical techniques. The results of this sensitivity study indicate that the break opening rates and the vapour generation rates are very important in properly determining the internal pressure distribution. However, because statistical techniques are employed in this study it has been found that these two parameters cannot be modified without examining the effect of other parameters. This study provides a detailed summary of concerns to be addressed when refining the thermalhydraulic model and concludes that further analysis on the thermalhydraulics of a bursting pressure tube would be useful, especially if focused on developing an interactive simulator containing both the mechanical and thermalhydraulic models.

In response to the statistical parameter study, a dynamic volumes model was incorporated into the thermalhydraulic model to represent the movement of the pressure tube wall during tube deformation and an adjustable parameter was added to fine tune the vapour generation rate to represent experimental situations. Results are presented indicating that the thermalhydraulic model does compare quite well to experimental data. Future directions to this research are also discussed.

(Vendredi 2 avril 13:25 → 15:05)
(Friday April 2nd 13:25 → 15:05)

SESSION 1B
SANTÉ & ENVIRONNEMENT / HEALTH & ENVIRONMENT
Président / Chairman: Dr. L. Zikovsky, I.G.E. École Polytechnique
Salle / Room: B-620.2

- K. Hammad University of Toronto
Iodine Behaviour and Measurement in the Canadian Shield Environmental
- N. Thompson† Royal Military College
and J.Olsen† Integration of Radiation Monitoring for Nuclear Emergency Response Teams
- R. Quan University of Toronto
The Radiolysis of Aqueous Organic Systems and Their Influence on Iodine Volatility
- P. Gokhale University of New Brunswick
An Inverse and Adjoint Photon Transport Calculation in Radiotherapy Planning

† Denotes Undergraduate student
Indique un(e) étudiant(e) au Baccalauréat



CA9700532

IODINE BEHAVIOUR AND MEASUREMENT IN THE CANADIAN SHIELD ENVIRONMENT

K. A. Hammad
FACULTY ADVISOR: Dr. G. J. EVANS

Department of Chemical Engineering and Applied Chemistry
University of Toronto
200 College St., Toronto, ONT.

ABSTRACT

Proper and safe management of radioactive waste from the nuclear power industry, as well as from other industries, is a major concern. The Canadian concept of the disposal of highly radioactive waste is based on permanent geological burial of wastes in concrete vaults. To ensure a permanently safe disposal of these wastes, knowledge of the behaviour of certain fission products, and modelling of their potential movement into the geosphere and biosphere are crucially important. Iodine is one of the radionuclides of greatest concern in these wastes, and the objective of this research is to model its transport in the environment.

Modelling of iodine behaviour depends on the prediction of possible transfer pathways and environmental processes, the development of certain parameters and transfer coefficients contained in the models describing these pathways, and finally the analysis of the models performance. Although some studies have dealt with iodine behaviour and the parameters affecting its transfer, there remains many uncertainties and variations in their findings, especially because most of the parameters of concern are site specific and dependant on the prevailing environmental conditions.

Although the radioactive iodine 129 is the isotope of concern, the investigation of iodine 127 can give a very good prediction of I-129 chemistry and behaviour in the environment. Both isotopes behave chemically the same, and as any potential release of I-129 is predicted to take place over a very long period of time, the long term distribution and behaviour pattern of I-129 should follow that of I-127. Evaluating I-127 in the environment gives the advantage of analysing an isotope that is many orders of magnitude more abundant compared to I-129.

Iodine chemical speciation is one of the several factors that have a significant effect on its behaviour and transport. A method for

differentiating the speciation of iodine between iodate (IO_3^-) and iodide (I^-) in different environmental waters has been examined. Other parameters of concern include soil to plant concentration factors and sediment/soil - water distribution coefficients K_d . Due to the inherently low iodine concentration, analysis of relevant samples has required NAA coupled with preconcentration techniques. Laboratory tracer experiments on the sediment-water K_d , type of bonding, and its relation to the iodine chemistry have been conducted. This presentation will include the above general aspects of research, and some of the preliminary results and techniques being used.



INTEGRATION OF RADIATION MONITORING FOR NUCLEAR EMERGENCY RESPONSE TEAMS

OCdt J.T. Olsen and OCdt N.Y. Thompson

Royal Military College of Canada
Kingston, Ontario
Dr. LGI Bennett, Major WS Andrews

INTRODUCTION

The Canadian Forces have established Nuclear Emergency Response Teams (NERTs), using military personnel under the direction of an officer, to act as on-site monitors and controllers if a nuclear accident occurred. The teams are primarily oriented towards responding to a nuclear accident occurring on a military base; their principal concern being the consequences of a large scale release of radioactive material into the environment. A secondary task is assistance to civil authorities in the event of an accident in the civilian sector.

Presently, NERTs are able to detect only gamma and high energy beta radiation by means of radiation survey instruments. Realizing that this is inadequate, new radiation sampling, detection and analysis equipment were acquired. Air samplers with filters for trapping the airborne radionuclides and beta counters, to provide gross beta counts that would be initial indicators of contamination in the area, were purchased. To complement these, and to provide definitive identification of the contaminants and their concentrations, new high purity germanium (HPGe) gamma ray detectors, Multi-Channel Analyzers (MCAs) and software (GammaVision), to analyze gamma ray spectra were purchased. This recent acquisition of new equipment enhances detection abilities and enables the identification of radionuclides present and their relative concentrations. However, a means of integrating this equipment and the results of the analysis is lacking.

The purpose of this design project is to propose a way of using the new equipment, to analyze the results from the gamma and beta detectors, to design a shielding castle for the beta detector, and to integrate the results into a format for decision making. Integration is accomplished through the creation of a computer program, Radiation Integration Program (RIP). This program analyzes gross beta counts and uses these counts to estimate the relative danger to the thyroid. As well, the results from GammaVision are converted from becquerels to dose rate for several parts

of the body. Overall gamma results affecting the thyroid are compared to the beta results to verify the initial estimations.

In short, this design project will enable the NERTs to estimate the radionuclides present in the plume or fallout from a reactor accident using results from the beta and gamma detectors. Information obtained from GammaVision will be used to calculate the length of time to exceed dangerous dose levels, and indicate which organs are in most danger.

METHODS AND EQUIPMENT

Gross Beta and Gamma Radiation Counters

The beta counter consists of an Eberline model MS-2 Mini Scaler and a RDA3A plastic beta scintillation detector with an aluminum housing. The detector will be located in a shielding castle (a design of a prototype was part of this project). Two forms of analysis can be performed. Filters from the air sampler can be analyzed by the beta counter to determine the gross beta count of airborne radionuclides, and ground contamination activity can be determined by counting smear samples in the castle. It is assumed that the ASP-1 portable radiation measuring instrument, with the HP260 beta gamma contamination detector, can be used to monitor beta activity at ground level by extending the detector on a probe through a window of the recce vehicle. It is also assumed that gross gamma radiation will be measured by the ASP-1 (at 1 m height) with the HP270 gamma exposure detector to monitor the radiation field to which the team members are exposed.

GammaVision, MCA, and Gamma Detector

The gamma spectroscopy system consists of an EG&G ORTEC MCA in an IBM PS/2 Model P70 portable computer, an EG&G ORTEC 92X Spectrum Master with GammaVision software, and an EG&G ORTEC Pop Top Gamma X detector in a lead shielding castle. The MCA, used in conjunction with the gamma ray detector, is an instrument that counts and sorts data, viz. gamma rays, by energy. The basis of the MCA is similar to a mail room. Many different mail boxes, or channels exist at specific energy levels and a running tally is kept on the number of times pulses have been sorted into a channel, and this count, coupled in ascending order of energies with all the counts of the other channels, establishes the spectrum's shape and location of its peaks. An MCA's greatest benefit is its ability to present a graphical representation of the spectrum of gamma ray energies. This ability linked with GammaVision's analysis capability makes a very powerful combination.

The GammaVision software package allows the combination of MCA emulation and analysis of gamma ray spectra gathered by the germanium detector. GammaVision is user friendly and provides analytical accuracy. GammaVision analyzes spectra recorded by the MCA and has the option of direct analysis of a spectrum, as it is recorded, or of analyzing past spectra saved on disk. GammaVision is presently made for Microsoft Windows, which provides an environment in which functions may be quickly and easily accessed in menu form. Future versions of GammaVision will be made for OS/2, an even more versatile package. Acquisition and analysis functions can be easily activated to perform tasks such as calibration, library editing, setting parameters and providing graphical displays.

The outputs of GammaVision are radionuclide activities in becquerels; it does not produce dose rate information. Without dose rates and a comparison to dose limits, the concentration results are not useful to the officer in charge. The GammaVision results must be converted into a gross dose rate, and the relative danger to the organs and body must be determined by using conversion factors for each radionuclide. Manually converting the GammaVision results would not only be extremely time consuming, it could be less accurate and more error prone than a computer program. Developing software for these calculations is the main goal of this thesis.

Excel Spreadsheet

To facilitate the manipulation and entry of data, it was decided to use a spreadsheet. Spreadsheets are basically large grids of cells, with each cell bearing an address in column/row form that allows it to be referenced by other cells, or by programs known as macros. Individual cells can hold either text, numbers or formulae. Text and numbers are simply entered into a cell and remain constant until a different value is entered. Formulae, on the other hand, have variable values which change as the values contained in the cells that they reference change. Formulae can be as simple as $cellA + cellB$, or they can be complex with functions and exponents as necessary. Macros are programs that are written in a format similar to that of a spreadsheet. Each line of a macro is written into a cell with an address that is referred to instead of a line number. The primary purpose of a macro is to manipulate spreadsheets, performing specific operations and placing results in specific addresses.

Microsoft Excel was the spreadsheet acquired for the NERTs and was used for this project. It is a user friendly spreadsheet, with macro capabilities, and able to convert files from other spreadsheet or text files into an Excel spreadsheet format. An example of this was the transferal of a spreadsheet written in Supercalc, containing a list of radionuclides, their conversion factors, and the formulae necessary to convert becquerels to dose rate, to Excel. An extremely useful function found in Excel is the

Record function. This function, when enabled, allows the programmer to perform the tasks desired, recording the commands the computer followed in macro form. After disabling the recorder, the user is able to display this macro that has all the commands they utilized beforehand. This greatly increases the rate of programming, by decreasing the time spent referring to a command manual for unknown commands.

Proposed Radiation Integration Program (RIP)

In order to accomplish the task of integrating the new NERT equipment, and to ensure the proposed monitoring procedures be easily implemented, a computer program must be designed. Ideally, the program would follow a sequence involving two sections, a beta section, and a gamma section.

In the beta section of the program, the gross beta counts obtained by the recce vehicles are used to estimate the thyroid dose rate. It is assumed that part of the gross beta count is due to radioiodine which is the most radiosensitive nuclide in the plume and is attracted to the thyroid. Note that the number of gross beta reports will depend on the number of team members, beta counters available and the duration of the accident. Data, that would identify the sample, the time and location at which it was taken and analyzed, the means of sample analysis, the gross beta count, and the volume of air sampled, must be entered by the user. This information would be entered into an Excel spreadsheet that had already been prepared, and the necessary calculations would be performed by the spreadsheet. The spreadsheet with the results would be printed out, and ideally be saved for future reference. This would allow further comparison between gamma and beta results. Since the times at which the gross beta count was taken from the recce vehicle and the GammaVision analysis was performed in the shelter are known, the thyroid dose rate from the beta results should be recalculated with the time lag taken into account.

The gamma section of the program must be able to access a report file prepared by GammaVision. The report file must be searched for pertinent nuclide peaks, and these peaks will be compared to a list of probable nuclides present in a nuclear accident on board a submarine. The counts of peaks found in the report file and on the spreadsheet will be transferred from the report file to the spreadsheet for conversion from becquerels to dose rate for the different body parts listed on the spreadsheet. Final results should list the time to exceed an action level, in hours, in chart form. As well, it would be at this point that the beta result concerning the thyroid would be entered in its recalculated form into the chart. This chart would also be available for print out. Data required for the smooth running of the gamma section of the program would be the name of the report file, which would also enable access to the beta result for this sample, and the volume of air sampled.

Creation of the Radiation Integration Program

The Radiation Integration Program (RIP) was created using the Microsoft Excel spreadsheet program. Two spreadsheets were created: a beta count results sheet and a spreadsheet containing the gamma spectroscopy results. The first spreadsheet allows for entry of the gross beta counting data reported from the recce vehicles and calculates the time to exceed the recommended dose rate. The second spreadsheet uses the peak areas of each radionuclide detected by gamma spectroscopy and their conversion factors to perform the same type of calculation to give the time to exceed the recommended dose rate.

For the second spreadsheet, the radionuclides that may be present in a radioactive plume, their conversion factors for various body parts and the action levels for these body parts were made available in a Supercalc spreadsheet. This information was transferred to Excel. The conversion factors were taken as the absorbed dose integrated over a fifty year time period for adults. If there was no factor listed for a particular nuclide over fifty years because of a short half life, the last factor listed that was closest to fifty years was used. The reason for choosing a fifty year time span was to imitate the span of a lifetime if a person had been exposed when they were young. The organs of interest were the thyroid, the bone marrow, the lungs, the digestive tract, and finally a full body dose. The conversion factors are used with the results of GammaVision (that are transferred to the spreadsheet by RIP) to convert the concentrations in becquerels to a dose rate in millisieverts per hour and then to a time to reside in the area, in hours.

Cs-137 and Uranium Solution Experiments

The purpose of these experiments was to test the validity of RIP in the comparison of beta and gamma results. Initially, the Cs-137 experiment was performed, using a Cs-137 solution with a radioactive concentration of 4.672 kilobecquerels per gram of solution. Although this sample does not have any iodine present, this initial test was just to pass a result from GammaVision through RIP. However, the beta analysis is quite incorrect in estimating the amount of iodine affecting the thyroid. Therefore, a sample of a 1000 ppm uranium solution which would contain iodine after irradiation in the SLOWPOKE-2 reactor was tested. Both experiments used similar procedures.

DISCUSSION

Explanation of RIP

The program is divided into two parts, a beta analysis, and a gamma spectrum analysis, with a report format for each. Initially, the program asks the user which analysis to perform. Assuming that the user chooses a beta analysis, the program then asks a series of questions which provide it with the necessary data for an estimate of the dose rate in the area. Data requested are: the sample identification number; date, time and location of sampling; the level on which the sample was placed in the castle for counting; the gross beta count; and the volume of the air sampled. These data are entered onto a spreadsheet created expressly for the calculation of the dose rate. Data are entered into specific cells, which are then used to find the sample gross activity estimate, the gross air concentration estimate, the iodine concentration estimate, the estimated thyroid dose rate, and ultimately the time to exceed the maximum recommended dose. Once the results are displayed, the user is asked whether a printout of the results spreadsheet is wanted. The user is alerted to retain the spreadsheet, or to copy down the time to exceed recommended dose, as this result will be necessary in the second part of the program. Finally, the program asks whether the user wishes to quit. If the user answers 'n', the program returns to the beginning and offers the choice of gamma spectrum or beta analysis again.

Assuming the user now wishes to perform gamma spectrum analysis, the program requests the report file name. Once given the name, the program opens the file and opens the spreadsheet into which the results will be copied. The volume of air sampled is then requested, and the user must now wait for the results to be displayed. The program first searches the report file for the start of the list of nuclides. It then parses the line, splitting the individual pieces of information into separate cells. Next the program checks whether the nuclide's peak on the spectrum was large enough for GammaVision to be certain of its existence. Finally, the program enters the spreadsheet and determines whether that specific nuclide is listed on the spreadsheet. If it is, the number of disintegrations recorded (the peak count) for the nuclide is entered into the spreadsheet. If the nuclide was not present on the spreadsheet, the program advances to the next nuclide, repeating the process. Peak counts that are entered into the spreadsheet are then entered into calculations which determine the dose of radiation affecting certain organs and the body as a whole. All doses affecting an organ, or the body, are summed, and this sum is converted to mSv/hr. Finally, the time to exceed the maximum recommended dose is found by dividing the action level by the dose rate and is displayed in a chart.

At this point in the program, the beta results for the sample are requested. These results are entered by the user and serve as a comparison to the 'time to exceed' result for the thyroid gland derived by the spreadsheet from the GammaVision report. Another opportunity is given for the user to quit and exit the program, or to return to the beginning and start again.

RIP has several redeeming properties. First, and most importantly, it successfully processes information and produces easily understood output. RIP accomplishes this by accepting user input and converting it to dose rates. For the beta analysis, the program uses the information provided by the beta counter along with specific formulae to estimate the thyroid dose rate due to beta emitting iodine nuclides. For the gamma analysis, it matches nuclides found in a report file from GammaVision to a master library of nuclides present in the spreadsheet utilized by RIP. The spreadsheet manipulates the various peak counts of the nuclides found in the spectrum of the sample to reach dose rates for the thyroid, lungs, bone marrow, digestive tract and the body as a whole. Secondly, this program requires a minimal amount of input from the user, thereby decreasing the probability of human error when entering the data. This simplicity also allows virtually anyone to run this program, without extensive training. Thirdly, RIP is equipped with several safety checks to ensure that proper data are being entered. Examples of this are a check on several of the questions that require a response of 'y' or 'n', and a check to ensure that information is entered in a specific format, i.e., not allowing letters or text to be entered when the answer should be in numbers. The checks allow the user to return to the original question and resubmit a response.

The user has many choices available in terms of which analysis to perform, and type of output desired. After RIP is opened and started, it asks which of the types of analysis the user wishes to perform, beta or gamma. Once the selected analysis has been completed, the program offers first a printout, then an opportunity to quit the program. Should the user decide to continue, the user is again offered a choice of which analysis he/she wishes to perform.

In addition to ease of entering data, amount of choice and simplicity, the program is inherently neat and easy to read. Screen clutter is avoided by hiding windows that are not being used directly. Hiding windows also prevents accidental entry of data into the various spreadsheets, and speeds up the overall process of transferring data from one window to another. The output of RIP is another strength. The output is short, concise, and does not require interpretation. The user simply has to read down a column to realize how long people may remain in the area before the action level radiation dose is reached.

One difficulty is the necessity of a manual link between the beta and the gamma analysis. Since one of the objectives behind producing this program was the reduction of human/computer interfacing, the necessity of having the user record or retain a printout of the beta results should be eliminated in future versions of RIP. Extra paper means greater possibilities of incorrect data entry and, therefore, misinterpretation of results. Furthermore, since the gross beta counts and the analysis of the sample by GammaVision will take place at different times, to determine accurately the relation between the two, the time difference must be taken into account. Another point to note is that once the program has commenced, it is impossible to exit, short of using a Break command, until the selected analysis is complete. Finally, input formats other than via the keyboard could be included, such as mouse buttons with optional keyboard commands. Again, these problems could have been solved if not for unfamiliarity with the language and lack of time.

One point that requires addressing is the uncertainties in the gamma ray counts. GammaVision provides a list of nuclides, including the uncertainties associated with each peak. RIP, however, chooses all real peaks with their uncertainties but does not take into account these uncertainties. A reason behind this omission was the fact that some peaks displayed extremely high uncertainty, i.e., ~50%, and this would provide a range of values too wide to be of any use. Uncertainty when dealing with radionuclide decay, statistically speaking, is the square root of the counts recorded by the detector. This uncertainty is due to the relationship between counts and the Gaussian curve associated with the distribution of counts.

Uncertainties which are found in the spreadsheet used in the calculation of dose rates from the GammaVision results pertain to weather and the people that would be found in the plume area. First, the spreadsheet assumed that the weather conditions would be conducive to a small, narrow plume with little dispersion. These are ideal conditions, and it is more than likely the plume would not behave this way. Moreover, it would require many man-hours of tedious work and research to produce even the simplest model of one harbour. Note that the conversion factors used in RIP are for PWR's and may not be valid for other reactors. In terms of people affected by the plume, it was assumed, for reasons explained in Chapter 3, that the best representation of contamination of the populace by radioactivity would be to take the conversion rates for adults over a fifty year period. If a value for fifty years was not available, due to a short half life for the nuclide, it was assumed that the value for the longest period of time available, was used.

Programming Challenges

In terms of programming, the first difficulty, and the difficulty that plagued the project was the unfamiliarity with the language used to write the macro. This problem manifested itself in the project from the beginning. Simple commands to accomplish the smallest task had to be looked up in the manual, costing valuable time and causing frustration. There were the inevitable endless loops entered when "if" statements did not perform as expected, and some difficulty was encountered in using the print command for the output.

GammaVision has the capability of outputting several variations of report files. Since each type of report is laid out slightly differently and since the start/save report has only the summary peaks, RIP was programmed specifically to use this report file format.

CONCLUSIONS

The completion of this project is a solid start to an integrated procedure, providing a foundation upon which to build a more complete analysis. Conclusions on the various aspects of the project are as follows.

Radiation Integration Program

RIP was designed for the purpose of integrating monitoring data to provide usable results for decision-making, and it accomplishes this goal to a large extent. The program successfully imports data from GammaVision into an Excel spreadsheet, where the data is converted to dose rates. It then provides a short and concise report that allows the officer in charge to make decisions regarding countermeasures quickly. A minimum of input from the user is required, and further improvements on the program can further decrease the amount of data input by hand. Gross beta counts are manipulated into a spreadsheet, and provide an initial estimate of danger levels facing the NERTs and the population in the area. Both results are easily printed out for hard copy, and the beta count results are present on the GammaVision output, for easy reference. The program is the only alternative to the calculation of dose rates from reports by hand, an impossible, time consuming process with possible human error.

The program should be improved so that, after each run, beta reports will be saved, matched and opened with their respective GammaVision report files. This would eliminate the need for manual entry of 'time to exceed thyroid action levels'. Secondly, the inability to exit the program at any point at any time during its execution could cause difficulty should incorrect data be entered. Thirdly, inputs requiring one of

two possible answers could be improved on by using on screen 'buttons' along with keyboard commands instead of only using keyboard commands.

RECOMMENDATIONS

To further the usefulness of this project, the following recommendations are suggested:

1. Modifications to RIP to decrease user input should be made, i.e., the saving of beta reports, taking the time lag between beta and gamma counting, and making RIP an application like GammaVision or Excel that has an icon in the main menu for entry into the program. A means of stopping the program once started, and mouse buttons could also be added.
2. The conversion factors used in RIP should be assessed with respect to variables such as weather, plume shape, people affected and reactor type.
3. More extensive testing possibly using fission products, should be attempted to verify the beta and gamma calculations.



The Radiolysis of Aqueous Organic Systems and Their Influence on Iodine Volatility

Raymond C. Quan

Department of Chemical Engineering and Applied Chemistry
University of Toronto

200 College St.
Toronto, Ont., CANADA
M5S 1A4

Faculty Advisor: Dr. G.J. Evans

Radioiodine (I-131) is one of the most important of the fission products which may be released from a nuclear reactor following an accident. This is because it has a high radiotoxicity and can assume many volatile (ie. airborne) forms, giving it the potential to be released from containment structures, resulting in significant environmental damage.

It is believed that certain organic compounds may enhance the formation of volatile iodine species. These compounds may exist in nuclear reactor containment structures in the form of paints, wiring, lubricants, and water chemistry control chemicals, for example.

This study was done in two parts. The first of these was a scoping study, aimed at identifying specific organic compounds which may enhance or suppress iodine volatility. The second part consisted of detailed studies which looked at the effect of related factors such as solvent concentration, iodide concentration, and pH.

A group of some 30 organic compounds was chosen for the scoping study. The choice of candidates was based on the need to cover a wide range of classes of organic compounds. It was also important to pick compounds representative of those actually expected in reactor containment.

The experiments involved the Co-60 γ -irradiation (dose rate: 0.3 kGy/hr) of aqueous 10^{-5} M CsI solutions containing a small amount (10^{-3} to 10^{-1} M) of an organic compound. These conditions were selected so as to approximate the post-accident environment expected in a CANDU reactor containment structure. The solutions were irradiated in flasks which allowed for a liquid volume of 10mL, with a gas phase of 50mL.

Many of the compounds were found to contribute to the formation of volatile iodine. The iodine partition coefficient (H = iodine concentration in the liquid phase/iodine concentration in the gas phase) varied, from as low as 300 for aqueous chloroform solutions, to as high as 1×10^5 for aqueous phenol solutions. As a reference, a partition coefficient of 10^4 is often used in safety analysis.

The increase in iodine volatility appeared, in most cases, to be related to the reduction in aqueous pH, believed to be due to the radiolytic conversion of the organic compounds to carboxylic acids. Most of the compounds tested followed this trend, with one group producing low H values and low pH, and the other high H and high pH. A third group deviated from this general trend, showing a reduction in pH.

but maintaining high H.

Compounds in the first group (low H, low pH) included chloroform, 1,2-dichloroethane, methanol, ethylene glycol, diethyl ether, butyl acetate, acetone, and methyl ethyl ketone. Examples from the second group (high H, high pH) were toluene, xylene, hexane, n-heptane, pentene, chlorophenol, polyethylene, polypropylene, teflon, and poly vinyl chloride. Deviations (high H, low pH) from this general relationship of increasing H with pH were seen in phenol, formaldehyde, chlorobenzene, cyclohexylamine, and diethylamine.

Detailed studies were performed on five of the compounds tested in the scoping studies: chloroform, MEK, paraldehyde, phenol, and toluene. These compounds were chosen based either on their ability to contribute to iodine volatility (the first three), or on their ability to suppress volatility (in the last two). These experiments were performed at a dose rate of 12.5kGy/hr, with smaller flasks, with a liquid volume of 5mL, and a gas volume of 10mL.

The first of these tests concerned the effect of organic solute concentration. Experiments were performed at the following concentrations : $10^{-6}M$, $10^{-4}M$, $10^{-2}M$, and $1M$. As the solute concentration was increased, the partition coefficient decreased in the case of chloroform, MEK, and paraldehyde. There was no significant change in H for phenol and toluene.

In experiments conducted over a range of CsI concentrations ($10^{-8}M$, $10^{-5}M$, and $10^{-4}M$), different compounds showed different behaviour. In the case of chloroform, the partition coefficient dropped as the concentration was increased. In the case of phenol and toluene, little change was seen in the partition coefficient over the range of CsI concentrations.

Studies concerning pH were performed using buffered solutions at pH3, 5, 7, 9, and 11. Results from these tests showed a similar trend to those observed in the scoping studies, in that the partition coefficient increased with an increase in pH. At every pH level, phenol and toluene produced a higher partition coefficient than that seen in chloroform, MEK, and paraldehyde.

A final group of studies was performed in which a group of bromine-containing organic compounds was irradiated (bromoform, bromobutane, bromobenzene, and bromophenol). It was found that in most of the bromine compounds, the partition coefficients produced were similar to those seen in their chlorine counterparts, except in the case of bromoform, which produced a partition coefficient roughly two orders of magnitude higher than that seen in chloroform.



AN INVERSE AND ADJOINT PHOTON TRANSPORT CALCULATION IN RADIOTHERAPY PLANNING

Prasad Gokhale

Department of Mechanical Engineering
University of New Brunswick

In radiotherapy planning, the tumour is usually treated using an arrangement of multiple beams. The selection of beam orientations in multitumour and complex geometry cases is particularly difficult. This paper presents a computer-assisted method for determining optimal beam orientations in a one-step procedure which enables simultaneous evaluation of beam directions.

Two techniques are proposed. Both rely on determining the "path of least resistance" to radiation travelling from the tumour location to the surface of the section. An inverse approach is proposed which employs a fictitious monoenergetic isotropic source placed at the tumour site, for which the dose distribution on the patient surface is calculated. The direction from the tumour to the location of high dose on the patient surface then indicates the optimal beam orientation. To account for radiation collisions more appropriately, an adjoint approach is developed. This technique considers a fictitious source at the tumour site and upscatters the photons backward in energy. The source is given as an energy spectrum, typical of that deposited in a tumour. The optimal beam orientation is then evaluated by directly monitoring the flux distribution of photons with energy equivalent to that of the treatment beam.

The inverse and the adjoint calculations for three tumour cases were performed using a two-dimensional discrete ordinates transport code, DOT-IV. The "proposed" treatment plans from DOT-IV calculations for the three tumour cases were verified against "standard" treatment plans using the Theraplan planning system. The new method clearly resulted in an improvement in the dose distribution in the treated section. Apart from assessing the beam orientations in current treatment plans, the method effectively deals with sections with multitumours and/or with complex geometries. The methods can be potentially useful in 3-D planning systems and also in selecting beam orientations in rotational and conformal therapy.

(Vendredi 2 avril 15:35 → 16:55)
(Friday April 2nd 15:35 → 16:55)

SESSION 2A
THERMOHYDRAULIQUE-2 / THERMALHYDRAULICS-2
Président / Chairman: Dr. A. Teyssedou, I.G.E. École Polytechnique
Salle / Room: C-630

- P. Busono McMaster University
An Experimental Investigation of Steam-Water Two-Phase Flow Regimes In a Horizontal Pipe
- P. Tye I.G.E., École Polytechnique
The Representation of the Various Intersubchannel Transfer Mechanisms and Their Effects on the Predictions of the ASSERT-4 Subchannel Code
- J. Wang McMaster University
Experimental Investigations of Counter-Current Flow Limitations in Vertical Two-Phase Flow Under Both Steady State and Pulsed Gas Flow
- P. Han University of New Brunswick
Effect of Internal Metallic Structure on Void Fraction Measurement Using Neutron Scattering



CA9700536

AN EXPERIMENTAL INVESTIGATION OF STEAM-WATER TWO-PHASE FLOW REGIMES IN A HORIZONTAL PIPE

Pratondo Busono

Supervisor : J.S. Chang and V.S. Krishnan

Department of Engineering Physics

McMaster University

Hamilton, Ontario L8S 4M1

Abstract

An experimental study has been conducted to investigate the air-water and steam-water two phase flow regimes in a concurrent horizontal pipe under near atmospheric pressure. The liquid flow rate and vapor flow rate were varied experimentally from 0.1 to 1 kg/s and from 0.001 to 0.01 kg/s respectively. The work was also emphasized on the study of void fraction, liquid level and vapor velocity along the tube.

To identify the flow regimes, two methods were used in the present experiment. The first was the direct investigation through the transparent window and the second was the ultrasonic pulse echo method. The latter has capability to identify the flow regimes inside metallic pipe. The liquid level was measured by using the ultrasonic pulse echo methods which attached at the bottom of the pipe. The void fraction was measured using the ring type capacitance void meter.

The experimental results were then compared to the numerical calculations. The results show that the liquid level data can be satisfactorily correlated using a Martinelli parameter. The flow regime maps based on the superficial liquid and vapor velocities, and based on dimensionless parameters were also presented.



The Representations of the Various Intersubchannel Transfer Mechanisms
and their Effects on the Predictions of the ASSERT-4 Subchannel Code

P. Tye

*Institut de Génie Énergétique
Ecole Polytechnique de Montréal
Montréal, Québec, Canada H3C 3A7*

ABSTRACT

In this paper, effects of that the constitutive relations used to represent some of the inter-subchannel transfer mechanisms have on the predictions of the ASSERT-4 subchannel code for horizontal flows are examined. In particular the choices made in the representation of the gravity driven phase separation phenomena, which is unique to the horizontal fuel channel arrangement seen in CANDU reactors, are analyzed. This is done by comparing the predictions of the ASSERT-4 subchannel code with experimental data on void fraction, mass flow rate, and pressure drop obtained for two horizontal interconnected subchannels. ASSERT-4, the subchannel code used by the Canadian nuclear industry, uses an advanced drift flux model which permits departure from both thermal and mechanical equilibrium between the phases to be accurately modeled. In particular ASSERT-4 contains models for the buoyancy effects which cause phase separation between adjacent subchannels in horizontal flows. This feature, which is of great importance in the subchannel analysis of CANDU reactors, is implemented in the constitutive relationship for the relative velocity required by the conservation equations.

In order to, as much as is physically possible, isolate different inter-subchannel transfer mechanisms, three different subchannel orientations are analyzed. These are: the two subchannels at the same elevation, the high void subchannel below the low void subchannel, and the high void subchannel above the low void subchannel. It is observed that for all three subchannel orientations ASSERT-4 does a reasonably good job of predicting the experimental trends. However, certain modifications to the representation of the gravitational phase separation effects which seem to improve the overall predictions are suggested.

1. INTRODUCTION

In CANDU-PHW reactors, the rod bundles are contained in horizontal pressure tubes which run through the calandria vessel. The coolant flowing through the fuel bundles may boil during normal operating conditions thus creating a horizontal two-phase flow. The thermal-hydraulic analysis of the fuel bundles requires detailed information on the conditions prevailing in each subchannel, i.e., pressure, liquid and gas mass flow rates, quality, void fraction, enthalpy, etc. This information may be obtained by using subchannel codes. In these codes, the complex geometry of the rod bundle is divided into smaller sections called "subchannels." The one dimensional conservation equations of mass, momentum and energy are written for each subchannel while taking into account the possible inter-subchannel interactions as source terms to these 1-D equations. These interactions as identified by Lahey and Moody [1], and Tahir and Carver [2] are:

i) Diversion Crossflow: is the directed flow caused by pressure differences between the subchannels. These differences may be induced by the subchannel geometries, the variation of heat flux from one subchannel to the other, incipient boiling in one of the subchannels or by flow section variations caused by blockages.

ii) Turbulent Interchange: in turbulent flow, the velocity and pressure at a fixed point do not remain constant but display random fluctuations. These fluctuations promote the exchange of mass, momentum and energy. In single phase flows, there is momentum and energy transfer between the subchannels but there is no net mass transfer. In two-phase flows, in addition to momentum and energy transfer there is usually a substantial net mass transfer. In the discussion of the void fraction data, this mechanism will be identified as "turbulent void diffusion."

iii) Void Drift: this mechanism accounts for the tendency of the vapor phase to shift to higher velocity channels.

iv) Buoyancy Drift: in horizontal channels, the void is pushed upwardly normal to the major flow direction due to the difference in the densities of the two phases.

There are several codes capable of performing the subchannel analysis of rod bundles, among the best known are COBRA-IV (Stewart et al. [3]) which handles vertical flows and ASSERT-4 (Carver et al. [4]) which handles both vertical and horizontal flows. Once the subchannel codes are developed their ability to predict the thermal-hydraulic behaviour must be checked against experimental data and in most cases the constitutive relations used to close the set of conservation equations require some "tuning" so as to best represent the physically observed phenomena. Most constitutive relations contain one or more "parameters" that were determined by a best fit with a given experimental data base. When these constitutive relations are applied outside the range of the original data base used in their development they may require some slight modification to best represent the observed trends. To this end a large number of experiments have been carried out at École Polytechnique on two laterally interconnected subchannels in a geometry identical to some of the subchannel pairs seen in a CANDU fuel bundle so as to check and if necessary modify the constitutive relations used to represent the inter-subchannel transfer mechanisms applied in ASSERT-4. In this paper ASSERT-4 predictions are compared with experimental data obtained in horizontal subchannels in order to evaluate the effect of the buoyancy drift correlation on the predictions.

2. ASSERT-4 SUBCHANNEL CODE

ASSERT-4 uses an advanced drift flux model which permits cases involving mechanical and thermal non-equilibrium to be considered. ASSERT-4 is, at the level of the individual subchannels

a one dimensional two-phase flow code, however, at the level of the fuel bundle it has a three dimensional nature. This quasi three-dimensional representation of the fuel bundles is arrived at by the representation of the affects of the crossflow as source terms in the 1-D form of the conservation equations of mass, axial momentum and energy, and by the addition of a transverse momentum equation. Some of the simplifying assumptions required to obtain the subchannel conservation equations used in ASSERT-4 include:

- 1) the flow is predominantly in the axial direction;
- 2) one dimensional equations
- 3) mixture properties only; eliminates interfacial terms and reduces the number of equations that must be solved;
- 4) no turbulent velocities, intersubchannel turbulent mixing only;
- 5) for transverse momentum consider the partial transverse momentum equation given below,

$$\frac{\partial \rho \overbrace{v}^{\delta}}{\partial t} + \frac{\partial \rho \overbrace{u \cdot v}^{1 \cdot \delta}}{\partial x} + \frac{\partial \rho \overbrace{v \cdot v}^{\delta \cdot \delta}}{\partial y} + \frac{\partial p}{\partial y} = \dots \quad (1)$$

where we use the x direction as the direction of the axial flow, and the y as the crossflow direction. From assumption (1) we will also consider that, u , the axial velocity is of order 1 and, v , the transverse velocity to be of order δ by retaining terms of order 1 and δ only and discarding terms of order δ^2 the transverse momentum equation can be greatly simplified.

In the axial direction the control volume used to write the conservation equations is defined by the flow area A (Figure 1) of the subchannel and the axial node length Δx .

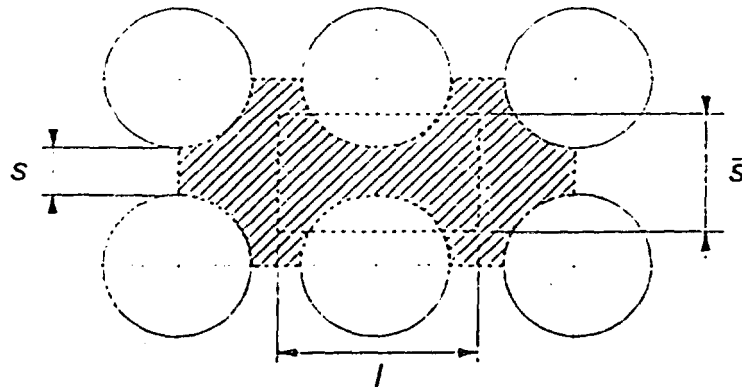


Figure 1. Subchannel Axial and Transverse Control Volumes

In the transverse direction the control volume has dimensions of \bar{s} by ℓ by Δx where \bar{s} is the effective gap clearance between two adjacent fuel rods and ℓ is usually taken to be the centroid to centroid distance between adjacent subchannels i and j . The effective gap clearance, \bar{s} , is not necessarily equal to the actual gap clearance, s , but is defined so as to preserve the volume of the lateral momentum computational cell (Carver et al. [5]). The volume of the lateral momentum cell is taken to be the average of the volumes of the two subchannels communicating through this cell.

The volume of the transverse cell is thus defined as:

$$\bar{s} \times \ell \Delta x = \frac{1}{2} [A_i + A_j] \Delta x \quad . \quad (2)$$

The effective gap clearance, \bar{s} , is therefore defined as:

$$\bar{s} = \frac{[A_i + A_j]}{2\ell} \quad . \quad (3)$$

Thus the resulting equations of conservation of mass, and axial momentum written for the i^{th} subchannel, and transverse momentum equation written for the transverse momentum control volume as applied in the ASSERT-4 subchannel code, are:

i) Conservation of Mass for subchannel i :

$$A_i \frac{\partial}{\partial t} \rho_{mi} + \frac{\partial}{\partial x} m_i + \sum_{j=1}^n W_{ij} = 0 \quad . \quad (4)$$

ii) Conservation of Axial Momentum for subchannel i :

$$\begin{aligned} & \frac{\partial}{\partial t} m_i + \frac{\partial}{\partial x} m_i u_{mi} + \frac{\partial}{\partial x} A_i \frac{\alpha_i (1 - \alpha_i) \rho_{\ell} \rho_g}{\rho_{mi}} u_{ri}^2 + \sum_{j=1}^n W_{ij} u_m^* \\ & + \sum_{j=1}^n s \frac{\alpha^* (1 - \alpha^*) \rho_{\ell}^* \rho_g^*}{\rho_m^*} v_{rij} u_r^* = -A_i \frac{\partial}{\partial x} p_i - \mathcal{F}_{ai} - A \rho_{mi} g \cos \theta \quad , \end{aligned} \quad (5)$$

with: $u_{mi} = \frac{m_i}{A_i \rho_{mi}}$, $W_{ij} = s \rho_m^* v_m$, and $\rho_{mi} = \alpha_i \rho_{gi} + (1 - \alpha_i) \rho_{\ell i}$.

iii) Conservation of Transverse Momentum:

The transverse momentum control volume $\bar{s} \ell \Delta x$ where \bar{s} is the effective gap clearance as defined in equation (2) can be split into two parts, as shown below:

$$\bar{s} \ell \Delta x = \overbrace{s \ell \Delta x}^A + \overbrace{(\bar{s} - s) \ell \Delta x}^B \quad . \quad (6)$$

Part A represents the portion of the control volume through which mass may be transferred. Part B contains the fictitious part of the effective gap clearance ($\bar{s} - s$). This is a solid boundary (see Figure 1) thus no flow can pass through this section. Therefore terms in the equation of conservation of transverse momentum that involve the transfer of mass between the two subchannels will be expressed using the actual gap clearance, s , and terms involving forces will be expressed using \bar{s} . This yields:

$$\begin{aligned} & \frac{\partial}{\partial t} W_{ij} + \frac{\partial}{\partial x} W_{ij} \bar{u}_m + \frac{\partial}{\partial x} s \left[\frac{\alpha^* (1 - \alpha^*) \rho_{\ell}^* \rho_g^*}{\rho_m^*} \right] \bar{u}_r v_{rij} = \\ & - \frac{\bar{s}}{\ell} (p_j - p_i) - \frac{\bar{s}}{\ell} \mathcal{F}_{tij} - \bar{s} \bar{\rho}_m g \sin \theta \cos \phi \quad , \end{aligned} \quad (7)$$

where θ represents the bundle orientation, and ϕ is the angle of the inter-subchannel gap.

Since, in this paper the experimental data used for comparison was obtained for adiabatic air-water two-phase flows the equation of conservation of energy is omitted. The equations are

solved using a method that is an extension of the I.C.E. (Implicit Continuous-fluid Eulerian) algorithm (Harlow and Amsden [6]), details on the solution scheme as applied in ASSERT-4 are given by Webb and Rowe [7].

3.0 CONSTITUTIVE RELATIONS

In developing the equations used in ASSERT-4 a large number of simplifying assumptions were made. Each of these simplifying assumptions costs us some fundamental information which must then be replaced by closure relations. Closure relationships for the inter-subchannel interchange mechanisms are required. These include relations for: 1) the transverse relative velocity, 2) the buoyancy drift, 3) the turbulent void diffusion, and 4) the void drift. Items 2, 3, and 4 are represented as contributions to item 1, the transverse relative velocity. The general form of the relative velocity is given by :

$$\vec{V}_r = \frac{(C_0 - 1)\vec{j}}{(1 - \alpha)} + \frac{\vec{V}_{gj}}{(1 - \alpha)} - \frac{\epsilon}{\alpha(1 - \alpha)} \vec{V}(\alpha - \alpha_{eq}) \quad , \quad (8)$$

where the first term represents the effect of cross sectional averaging, the second term is the buoyancy drift, and the third term represents a combination of both turbulent void diffusion and void drift.

3.1 Axial Relative Velocity

Since in the axial direction the diffusion is negligible, the axial relative velocity is modelled using only the first two terms of equation (8). For horizontal flow buoyancy is absent in the axial direction and the axial relative velocity is given by:

$$u_r = \frac{(C_0 - 1)j}{(1 - \alpha)} \quad . \quad (9)$$

3.2 Transverse Relative Velocity

The phase distribution coefficient, C_0 , in the transverse direction is assumed to be equal to 1, which eliminates the first term of Equation (8). The drift velocity, v_{gj} , used to represent the buoyancy drift mechanism is expressed using Wallis's [8] model for the terminal rise velocity of a bubble which is:

$$v_{gj} = \bar{\alpha}(1 - \bar{\alpha})^n K_1 \left(\frac{\rho_l - \rho_g}{\rho_l^2} \sigma g \right)^{0.25} \cos \phi \quad , \quad (10)$$

where the recommended values of K_1 are 1.414 – 1.56; the term $\cos \phi$ represents the orientation of the inter-subchannel gap, and $\bar{\alpha}(1 - \bar{\alpha})^n$ is used to take into account the presence of other bubbles. A point that should be made about the drift velocity is that v_{gj} should tend to zero as $\alpha \rightarrow 0$ and also as $\alpha \rightarrow 1$. In ASSERT-4 the recommended value of the coefficient n is 0 and the remaining $\bar{\alpha}$ is raised to the power of 0.1. A consequence of using $n = 0$, is that the drift velocity does not go to zero as $\alpha \rightarrow 1$. It is thus necessary to introduce an additional term that drives v_{gj} to zero as the void fraction tends towards one. Thus the drift velocity as applied in ASSERT-4 is given by:

$$v_{gj} = 1.5F(\bar{\alpha})^{0.1} \left(\frac{\rho_l - \rho_g}{\rho_l^2} \sigma g \right)^{0.25} \cos \phi \quad , \quad (11)$$

where F is the Ohkawa-Lahey [9] correction factor used to drive $v_{gj} \rightarrow 0$ as $\alpha \rightarrow 1$. It is given by:

$$F = \left[1 - \left(\frac{\bar{\alpha} - \chi}{1 - \chi} \right) \right]^m, \quad (12)$$

with $\chi = 0.588 - 1.817\Psi + 2.0\Psi^2 - 3.343\Psi^3$, and $\Psi = \sqrt{\frac{\rho_g}{\rho_l}}$, for $\bar{\alpha} > \chi$, otherwise $F = 1$. The recommended value of m is 1.5.

As part of this work Wallis's [8] model for the drift velocity was implemented in ASSERT-4. As this expression automatically has the correct trend as $\alpha \rightarrow 1$ the Ohkawa-Lahey [9] correction factor F was no longer needed. The test of the full Wallis model for the drift velocity in ASSERT-4 involved simply replacing Equation (11) by Equation (10) where values of $K_1 = 1.5$ and $n = 2$ were used. Figure (2) shows a comparison of the leading terms of equations (10) and (11) which are given by $1.5 * \bar{\alpha}(1 - \bar{\alpha})^2$ and $1.5F(\bar{\alpha})^{0.1}$ respectively, as a function of the average void fraction. It is clear that the use of equation (10) significantly reduces the magnitude of the drift velocity. The effect that this has on the predicted results will be examined later on in the paper.

The turbulent void diffusion coefficient, ϵ , in Equation (8) is specified using a correlation with the inverse turbulent Peclet number, and is given by:

$$\frac{\epsilon}{\bar{u}_m \bar{D}_h} = a Re^b, \quad (13)$$

where \bar{u}_m is the average velocity and \bar{D}_h the average hydraulic diameter in the two subchannels under consideration, the recommended values of a and b are 0.05 and 0 respectively.

The void diffusion and void drift for two subchannels i and j are calculated using the model presented by Lahey and Moody [1], which is given by:

$$\frac{\epsilon}{\bar{\alpha}(1 - \bar{\alpha})} \nabla(\alpha - \alpha_{EQ})_{ij} = \frac{\epsilon}{\bar{\alpha}(1 - \bar{\alpha})} \left[\frac{[\alpha_j - \alpha_i] - [\alpha_j - \alpha_i]_{EQ}}{\ell} \right], \quad (14)$$

where α_{EQ} is the void fraction at equilibrium. It is calculated using a weighting of the individual subchannel mass fluxes to the average mass flux in the two subchannels. For the i^{th} subchannel the equilibrium void fraction is calculated as:

$$\alpha_{iEQ} = \left[\frac{\bar{\alpha}}{\bar{G}_m} \right] G_{mi}, \quad (15)$$

the average void fraction $\bar{\alpha}$ and the average mass flux \bar{G}_m are calculated using subchannel flow area weighting which results in the following expressions:

$$\bar{\alpha} = \frac{(\alpha A)_i + (\alpha A)_j}{A_i + A_j}, \quad (16)$$

and,

$$\bar{G}_m = \frac{m_{mi} + m_{mj}}{A_i + A_j}. \quad (17)$$

4.0 COMPARISON OF DATA AND ASSERT-4 PREDICTIONS

In this paper three of the horizontal Tapucu et al. [10] experiments are analyzed. All three cases have inlet void fractions of approximately 30% at the inlet of the high void subchannel and 0% at the inlet of the low void subchannel. The three experiments differ in that different subchannel orientations were used: high void subchannel above low void subchannel, high void subchannel below low void subchannel, and both subchannels at the same elevation. In the remainder of the text these three cases will be referred to as: $\frac{HV}{LV}$, $\frac{LV}{HV}$, and $HV = LV$, respectively. These experiments were chosen in such a way as to separate the inter-subchannel transfer mechanisms and allow their effects on void fraction and mass flow rate to be evaluated independently. In the equal elevation case, the inter-subchannel transfer is due to a combination of the diversion crossflow, turbulent void diffusion and void drift. In the other two cases gravity plays a role in the transfer mechanisms. In the case where the high void subchannel is above low void subchannel the gravity acts in such a way as to oppose the void transfer by the net influence of the void diffusion and void drift while in the case where the high void subchannel is below low void subchannel it acts in the same direction.

Figures (3 to 7) and (8 to 12) show the ASSERT-4 predictions and the experimental results for the void fraction and mass flow rate respectively in the two horizontal interconnected subchannels. Details on the experimental facility used to collect the data presented in this paper are given in a companion paper by Tapucu et al. [11].

4.1 Comparison with Void Fraction Data

Figures (3 to 7) show the experimental results for the void fraction profiles in the two interconnected subchannels for the three different subchannel orientations.

Figure (3) shows the results of a comparison between the void fraction data and the predictions of ASSERT-4 for case $HV = LV$. ASSERT-4 was run with two different values of the constant, a , used in equation (13) to calculate the diffusion coefficient. These values were $a = 0.05$ (default) and $a = 0.01$. We can see that the default value overpredicts the void fraction in the low void subchannel and underpredicts the void fraction in the high void subchannel. The use of $a = 0.01$ slightly overpredicts the void fraction in the low void subchannel but does a very good job for the high void subchannel. This equal elevation case was used to find the optimum value of the constant, a , in equation (13) in the absence of gravitational effects. Having done so, this value will be used for the other cases where gravitational effects are present. It should be pointed out that a value of $a = 0.01$ for the constant used in equation (13) to calculate the void diffusion coefficient is not an optimum value for all cases but only for this set of experiments. It has been shown elsewhere (Tye et al. [12] and Tapucu et al. [11]) that the constant a is dependent on the void fraction. Here its value has simply been optimized for the void fraction being examined so that an analysis of the constitutive relations used for the buoyancy drift could be carried out without the representation of the void drift and void diffusion interfering with this analysis. The experimental results show the tendency towards an equilibrium void fraction difference between the two subchannels. This clearly shows the need for an equilibrium void difference model of the type given by equations (14) to (17).

Figures (4 and 5) show the results of the comparison between the ASSERT-4 predictions and the experimental results for the $\frac{HV}{LV}$ case, two slightly different representations of the buoyancy drift mechanism were tested. The first was the one given by equation (11) which is the representation currently used in ASSERT-4. The second was the one given by equation (10) with $K_1 = 1.5$ and $n = 2$. Figure (4) shows the predicted and experimental void fraction profiles with the use

of equation (11) (ASSERT-4) for the representation of the buoyancy drift. For the high void subchannel the void fraction is quite well predicted. However no void is seen in the low void subchannel. Figure (5) shows the results of the predictions with the use of equation (10) (Wallis [8]) for the representation of the buoyancy drift. Here we see that the void fraction in the high void subchannel is slightly underpredicted and the void fraction in the low void subchannel is slightly overpredicted.

Figures (6 and 7) show the experimental and predicted void fraction profiles in both subchannels for the $\frac{LV}{HV}$ case. Figure (6) shows the predicted and experimental void fraction profiles with the use of equation (11) for the representation of the buoyancy drift. It can be seen that the void fractions were predicted to cross something not seen in the experimental data. Figure (7) shows the results of the predictions with the use of equation (10) for the representation of the buoyancy drift. It can be seen that this results in an almost perfect prediction of the void fraction in the high void subchannel and a very slight overprediction of the void fraction in the low void subchannel.

Examining Figure 2 which shows the leading terms in the constitutive relation used for the drift velocity we can see that using equation (10) (Wallis [8]) instead of equation (11) (ASSERT-4) significantly reduces the importance of the buoyancy drift as an inter-subchannel transfer mechanism. If turbulent void diffusion and void drift are correctly represented in a case without gravitational affects, as was done using the equal elevation case, we may then use this representation in cases where gravity is present to try and improve the constitutive relation used to estimate the buoyancy drift.

4.1 Comparison with Mass Flow Rate Data

Figures (8 to 12) show the predicted and experimental results for the mass flow rate for the three cases being analyzed.

Figure (8) shows the results of a comparison between the mass flow rate data and the predictions of ASSERT-4 for the $HV = LV$ case. Here we see that the use of the default value of a in equation (13) underpredicts the mass flow rate in the low void subchannel and overpredicts it in the high void subchannel. It can also be seen that the use of $a = 0.01$ leads to a good prediction of the mass flow rates in both subchannels. The data shows that the high void subchannel transfers a significant amount of liquid to the low void subchannel in the first $1/3^{rd}$ of the interconnected region. This initial transfer is due to the diversion crossflow caused by the pressure differences between the two subchannels. The significance of the diversion crossflow does not continue for any great length along the interconnected region.

Figure (9) shows the comparison of the predicted and experimental mass flow rates in both subchannels for the $\frac{HV}{LV}$ case where equation (11) (ASSERT-4) was used for the representation of the buoyancy drift. It can be seen that this leads to an overprediction of the mass transferred from the high void subchannel to the low void subchannel. Figure (10) shows the comparison of the predicted and experimental mass flow rates in both subchannels for the same case with the use of equation (10) (Wallis [8]) for the representation of the buoyancy drift. We can see that this leads to an almost perfect prediction of the mass flow rates in both the high and low void subchannels.

Figure (11) shows the comparison of the predicted and experimental mass flow rates in both subchannels for the $\frac{LV}{HV}$ case where equation (11) (ASSERT-4) was used for the representation of the buoyancy drift. It can be seen that the mass flow rates are predicted to cross something that is not seen in the experimental results. Figure (12) shows the same case using equation (10) (Wallis [8]) for the buoyancy drift. We can see that this leads to a good prediction of the mass

flow rates in both subchannels.

CONCLUSIONS

By using a set of three horizontal two-phase flow experiments having the same inlet conditions but different subchannel orientations we have been able to separate the void diffusion and void drift mechanisms from the buoyancy drift mechanism. Using a case where the two subchannels were at the same elevation the constitutive relation used to represent the combined effects of void diffusion and void drift was optimized for a given set of inlet conditions. This optimized representation was then used in cases where buoyancy drift was present as an inter-subchannel transfer mechanism. Two slightly different forms of the constitutive relation used to represent this mechanism were tested.

It was found that for both cases analyzed the use of the buoyancy drift based on the correlation due to Wallis [8] results in better agreement between the predictions and the experimental results than correlation for the buoyancy drift mechanism implemented in ASSERT-4. Further, our suggested representation eliminates the need for the Ohkawa-Lahey [9] correction factor.

References

- [1] R.T. Lahey Jr. and J.F. Moody, *The Thermal-hydraulics of a Boiling Water Nuclear Reactor*, (American Nuclear Society., N.Y., 1979) pp 122-138.
- [2] A. Tahir and M.B. Carver, Comparison of ASSERT subchannel code with Marviken bundle data, AECL Report, AECL-8352 (1984).
- [3] C. Stewart, C. Wheeler, R. Cena, C. McMonagle, J. Cuta and D. Trent, COBRA-IV: The model and the method, BNWL-2214, NRC-4 (1977).
- [4] M.B. Carver, R.A. Judd, J.C. Kiteley and A. Tahir, The drift flux model in the ASSERT subchannel code, *Nucl. J. of Canada*, Vol. 1 No. 2 (1987) 153-165.
- [5] M.B. Carver, A. Tahir, D.S. Rowe, A. Tapucu and S.Y. Ahmad. Computational analysis of two-phase flow in horizontal bundles, *Nucl. Engng. Des.* 82 (1983) 215-226.
- [6] F.H. Harlow and A.A. Amsden, A numerical fluid dynamics calculation method for all flow speeds, *J. of Comp. Physics*, Vol. 8, No. 2. (1971) 197-213.
- [7] S.W. Webb and D.S. Rowe, Modeling techniques for dispersed multiphase flows, in: *Encyclopedia of Fluid Mechanics*, (Gulf Publishing Company, 1986) pp. 909-968.
- [8] G.B. Wallis, *One Dimensional Two-Phase Flow*, (McGraw Hill, N.Y., 1969) pp 248-255.
- [9] K. Ohkawa, and R.T. Lahey Jr., The analysis of CCFL using drift-flux models, *Nucl. Engng. Des.* 61 (1980) 245-255.
- [10] A. Tapucu, M. Geçkinli, N. Troche, and R. Girard, Experimental investigation of mass exchanges between two laterally interconnected two-phase flows, *Nucl. Engng. Des.* 105 (1988) 295-312.
- [11] A. Tapucu, A. Teyssedou, P. Tye, N. Troche, The Effect of Turbulent Mixing Models on the Predictions of Subchannel Codes, paper submitted to NURETH-6, (Grenoble, 1993) to appear.
- [12] P. Tye, A. Tapucu and S. Gençay An Analysis of the Lateral Void Transfer Mechanisms in the ASSERT Subchannel Code, *CNS/ANS Proc. 3rd Int. Conf. on Simul. Meth. in Nucl. Engng.* (Montréal, 1990) 115-139.

Nomenclature

A	Subchannel flow area (m^2)
D_h	Hydraulic diameter (m)
\mathcal{F}_a	Axial friction pressure loss (N/m)
\mathcal{F}_t	Transverse friction and form pressure loss (N/m^2)
\bar{G}	Area weighted average axial mass flux in subchannels (kg/m^2s)
Re	Reynold's number
\bar{V}_{gj}	Drift velocity (m/s)
\bar{V}_r	Relative velocity (m/s)
W	Mixture cross-flow per unit length of interconnection (kg/ms)
a	void diffusion constant
\bar{j}	volumetric flux of the mixture (m/s)
ℓ	Effective mixing length or centroid-to-centroid distance between adjacent subchannels (m)
m	Axial mass flow rate (kg/s)
p	Pressure (N/m^2)
s	Gap clearance (m)
\bar{s}	Effective gap clearance (m)
u	Axial velocity (m/s)
u_r	Axial relative velocity; $u_g - u_\ell$ (m/s)
v_r	Transverse relative velocity; $v_g - v_\ell$ (m/s)
α	Void fraction
$\bar{\alpha}$	Area weighted average void fraction in subchannels
ϵ	Eddy diffusivity (m^2/s)
ρ_i, ρ_g	Phasic density (kg/m^3)
ρ_m	Mixture density (kg/m^3)

Subscripts

i, j	subchannel identifiers
EQ	Equilibrium void fraction difference

Superscripts

- average over interconnected subchannels
- * denotes donor assignment

Acknowledgement

ASSERT-4 was made available to Ecole Polytechnique by agreement with the CANDU OWNERS GROUP, Fuel Channel Critical Power Working Party.

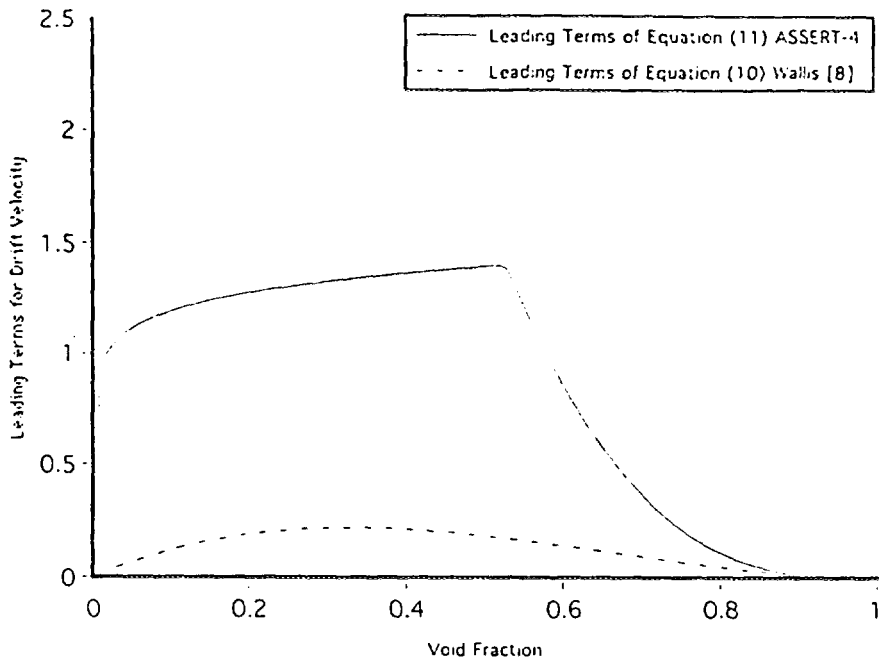


Figure 2: Leading Terms for the Drift Velocity

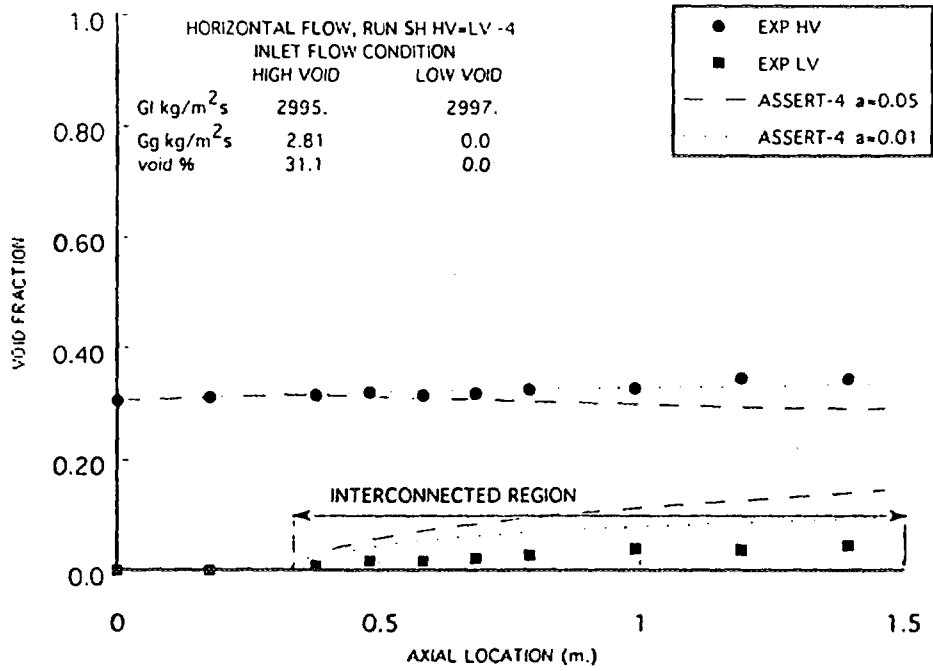


Figure 3: Void Fraction ASSERT-4 (Optimization of "a" in Equation 13)

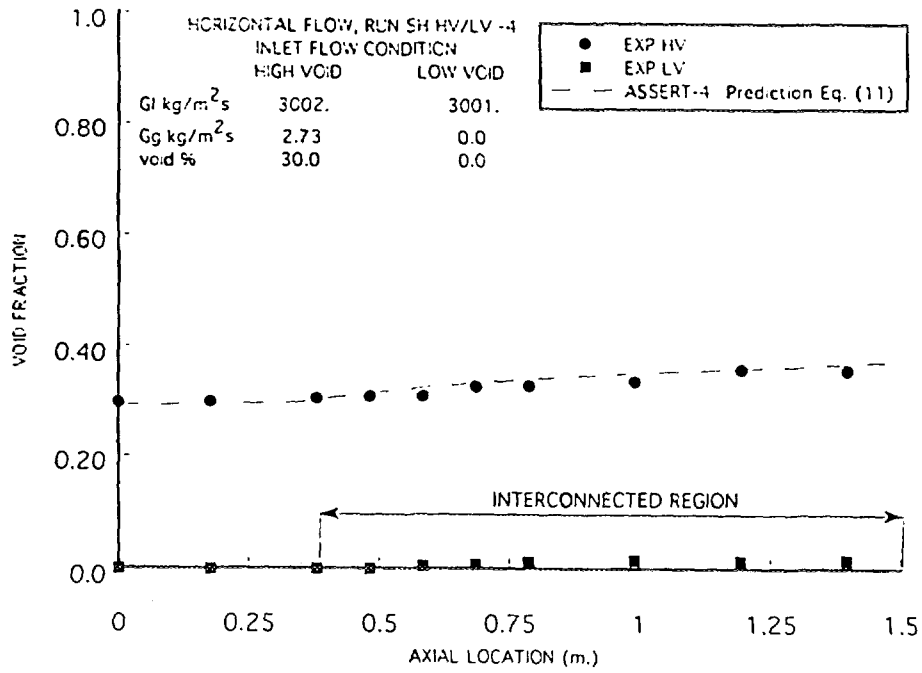


Figure 4: Void Fraction ASSERT-4 (v_{gj} Equation 11)

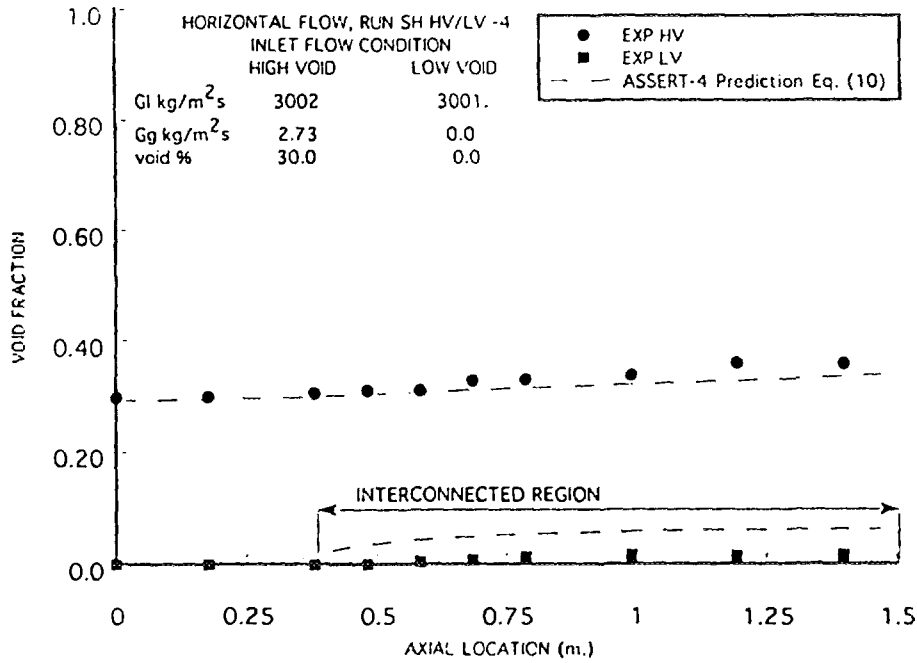


Figure 5: Void Fraction ASSERT-4 (v_{gj} Equation 10)

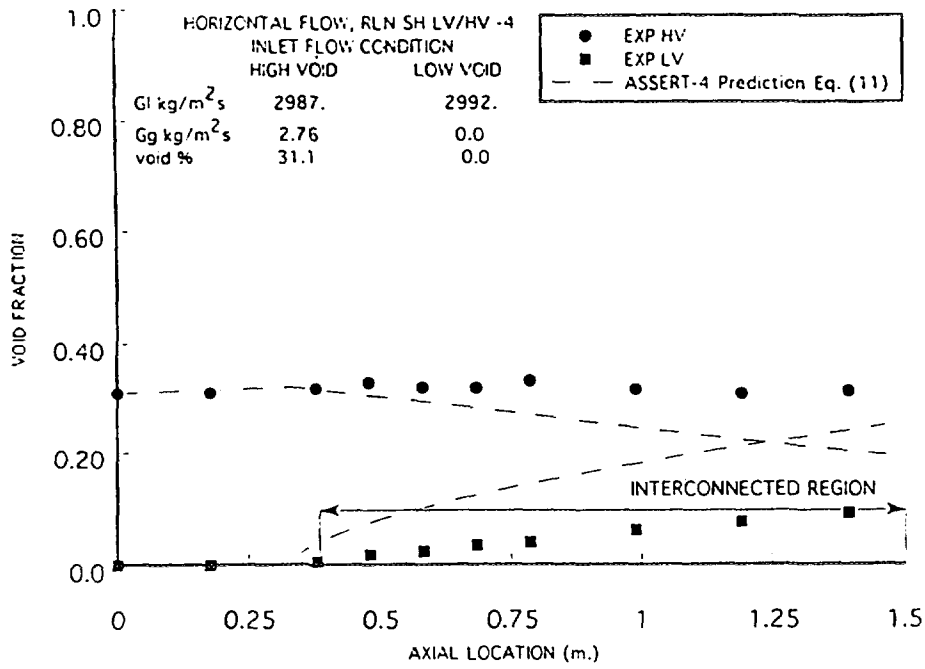


Figure 6: Void Fraction ASSERT-4 (v_{gj} Equation 11)

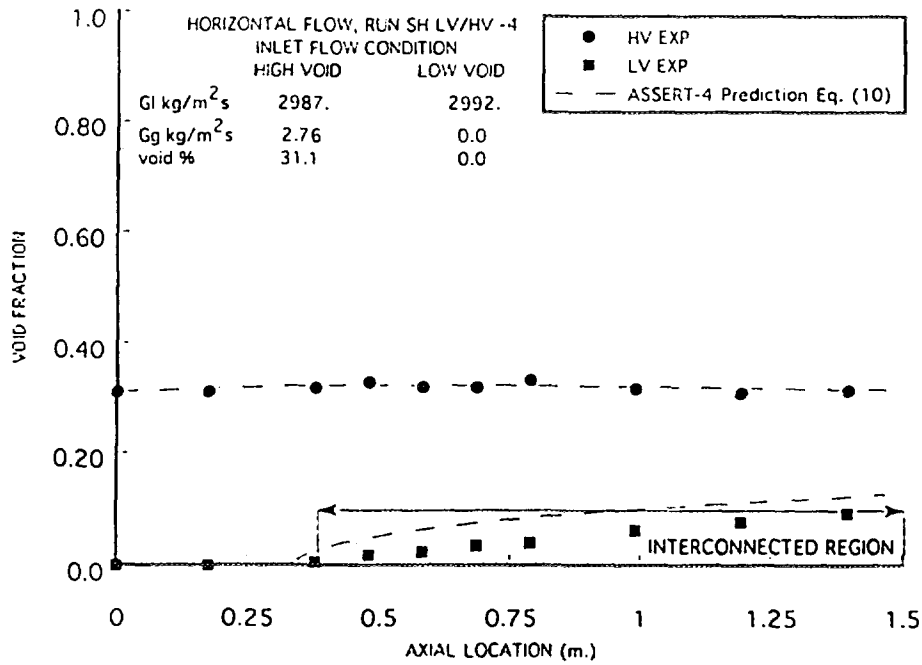


Figure 7: Void Fraction ASSERT-4 (v_{gj} Equation 10)

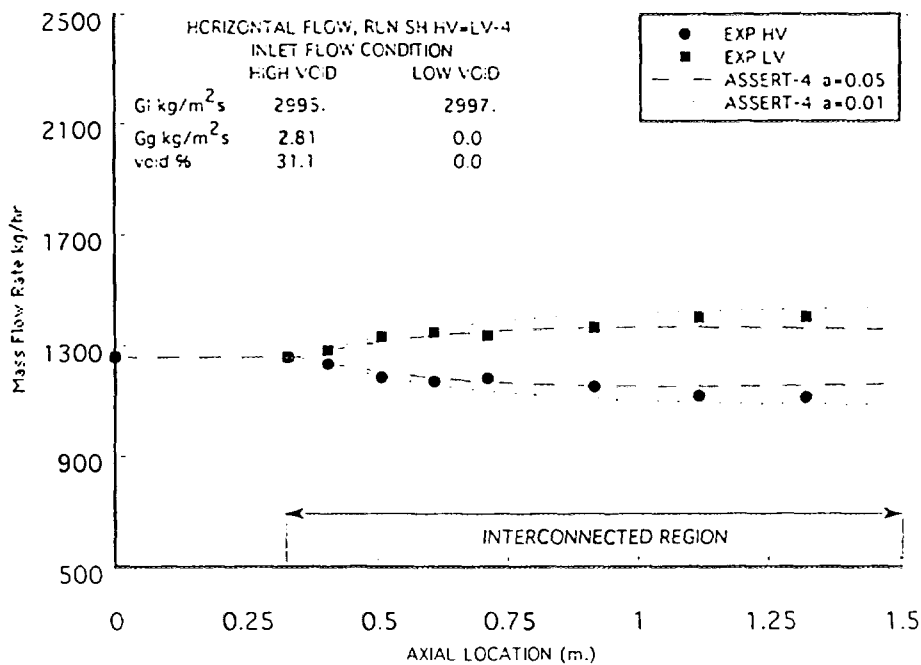


Figure 8: Mass Flow Rate ASSERT-4 (Optimization of "a" in Equation 13)

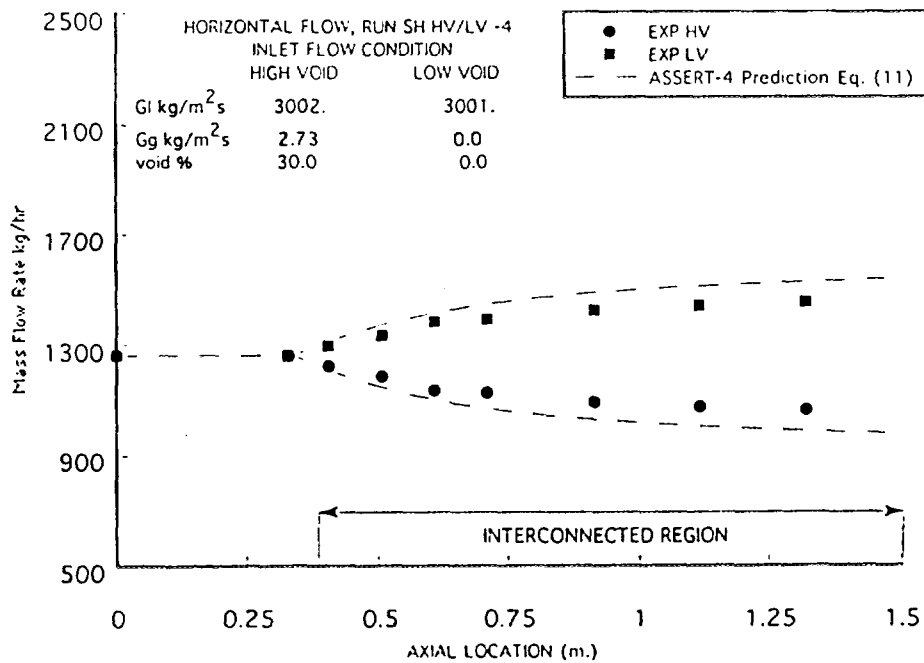


Figure 9: Mass Flow Rate ASSERT-4 (v_{gj} Equation 11)

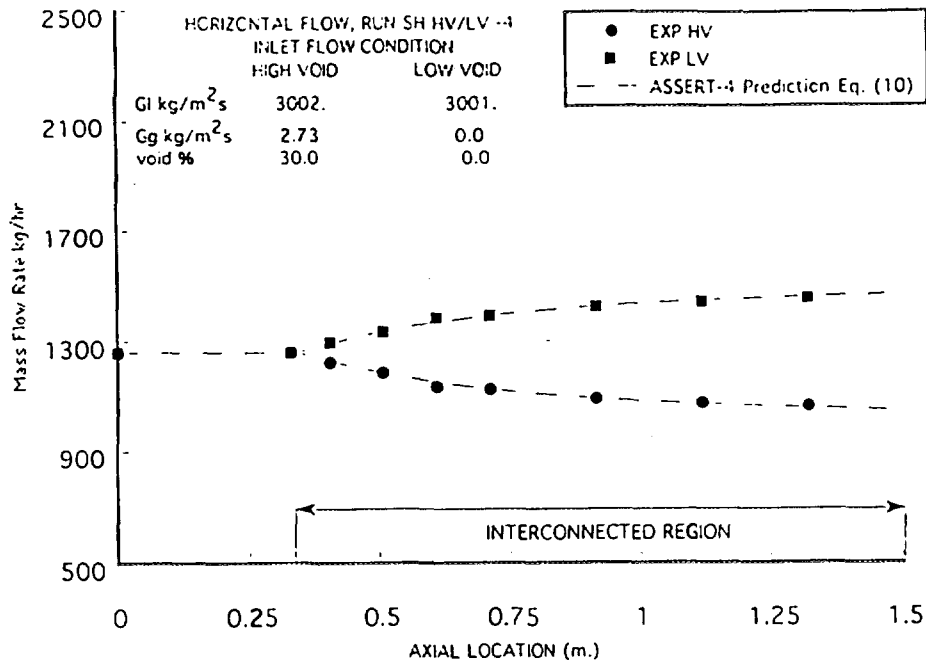


Figure 10: Mass Flow Rate ASSERT-4 (v_{gj} Equation 10)

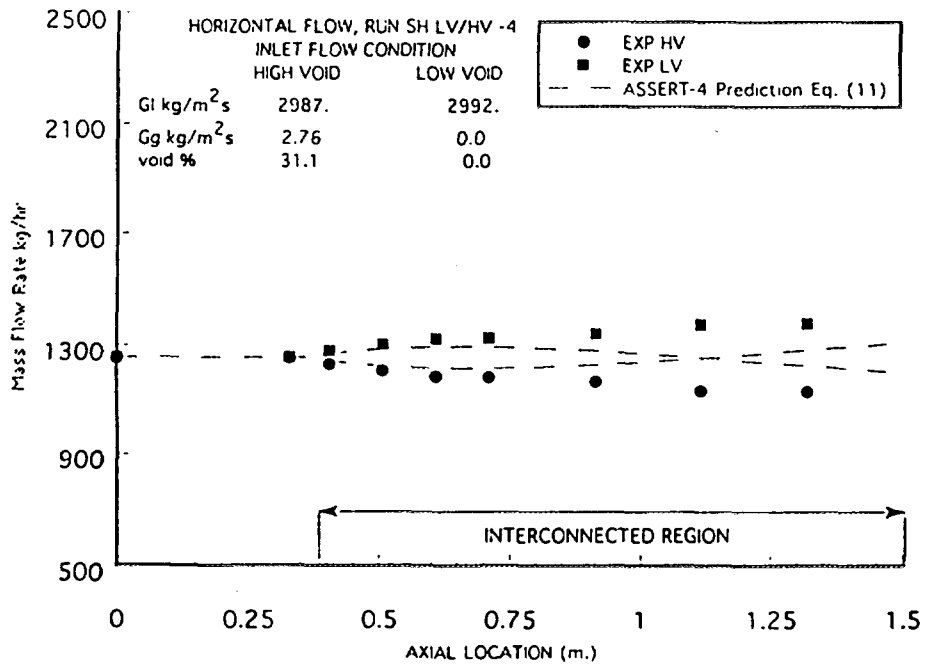


Figure 11: Mass Flow Rate ASSERT-4 (v_{gj} Equation 11)

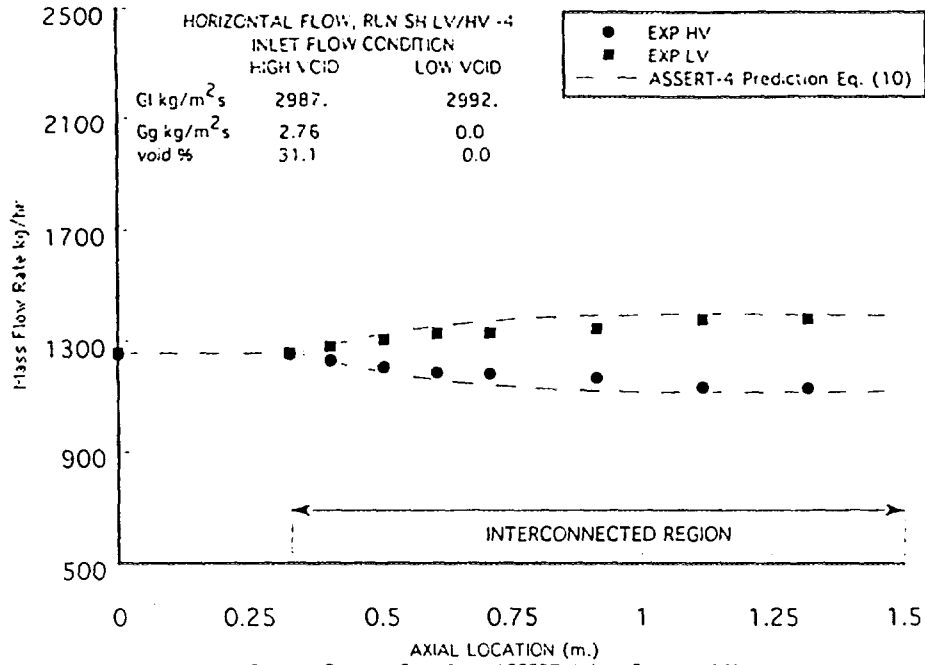


Figure 12: Mass Flow Rate ASSERT-4 (v_g , Equation 10)



1993 CNS STUDENT CONFERENCE
April 2nd & 3rd, 1993. MONTREAL

Experimental Investigations of Counter-Current Flow Limitations
in Vertical Two-Phase Flow Under Both Steady State and Pulsed Gas Flow

Jianwei Wang
Feb. 12, 1993

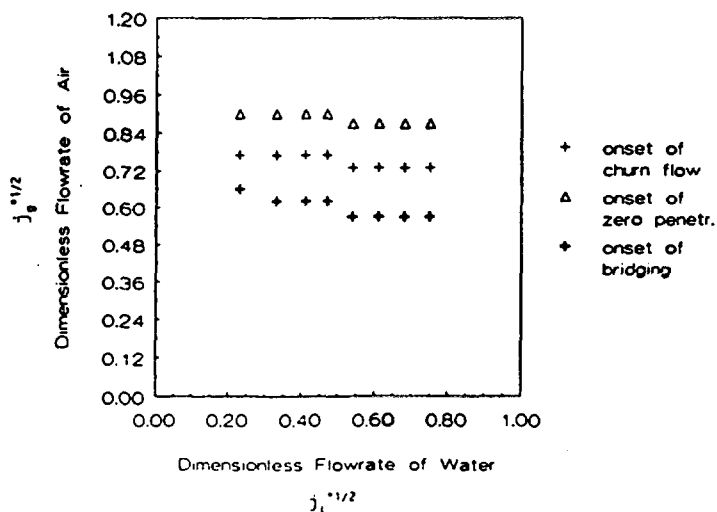
Supervisor: Dr. J.S. Chang
Dr. M. Shoukri

Dept. of Mechanical Engineering
McMaster University
Hamilton, Ontario

Abstract

Experimental investigations of counter-current flow limitations (CCFL) in vertical gas-liquid two-phase flow under the both steady state and pulsed gas flow conditions have been conducted in i.d. of 2.07 cm and length of 2.1 m pyrex glass tube. The results show that the pluse frequency of gas flow has an insignificant effect on the flooding point where the pulse frequencies examed are 0.8, 1.4 and 2.5 Hz. Comparison of flow regime transition observed for pulsed and steady state gas flow will be discussed in detail. Typical flow regime map is shown in fig.1.

Figure.1 Flooding Regimes in Plused Air Injection
Frequency of 0.14 Hz





EFFECT OF INTERNAL METALLIC STRUCTURE ON VOID FRACTION MEASUREMENT USING NEUTRON SCATTERING

Pinlian Han

Mechanical Engineering Department
University of New Brunswick
Fredericton, New Brunswick
E3B 5A3

ABSTRACT

Neutron scattering has been used for many years to measure void fraction of two-phase flow in a simple thick metallic pipe. However, the excessive metallic content and complex structure of some channels, such as those encountered in critical heat flux and nuclear reactor safety related experiments, may affect the performance of the scatterometer. Absorption of thermal neutrons by the metal reduces the count rate, while the same time scattering of epithermal neutrons from metal increases the count rate. All these effects need to be considered in the design of the scatterometer.

Monte Carlo simulation and the subsequent laboratory experiments were conducted to study the effects of metallic structures and contents on void fraction measurement using neutron scattering. The results will be discussed and recommendations for designing the scatterometer will be presented.

(Vendredi 2 avril 15:35 → 16:55)
(Friday April 2nd 15:35 → 16:55)

SESSION 2B
MATÉRIAUX NUCLÉAIRES-1 NUCLEAR MATERIALS-1
Président / Chairman: Dr. Brent Lewis, Royal Military College
Salle / Room: B-620.2

- A. Harnden-Gillis Queen's University / Royal Military College
Fission Product Release from Slowpoke-2 Reactors
- C.A. Deir University of Toronto
Iodine Retention by Stainless Steel
- H.M. Pak† Royal Military College
Damage Analysis of Polymer Composite Epoxies in High Radiation Environments
- R. Sahney Carleton University
Potential Drop Crack Measurements System for CANDU Components

† Denotes Undergraduate student
Indique un(e) étudiant(e) au Baccalauréat

Anne M.C. Harnden-Gillis
Department of Physics, Queen's University
Kingston, Ontario, K7L 3N6



CA9700540

ABSTRACT

Increasing radiation fields at several SLOWPOKE-2 reactors fuelled with highly enriched uranium aluminum alloy fuel have begun to interfere with the daily operation of these reactors. To investigate this phenomenon, samples of reactor container water and gas from the headspace were obtained at four SLOWPOKE-2 reactor facilities and examined by gamma ray spectroscopy methods.

These radiation fields are due to the circulation of fission products within the reactor container vessel. The most likely source of the fission product release is an area of uranium-bearing material exposed to the coolant at the end weld line which originated at the time of fuel fabrication. The results of this study are compared with observations from an underwater visual examination of one core and the metallographic examination of archived fuel elements.

INTRODUCTION

Following fabrication of the highly enriched uranium (HEU) fuel elements for the SLOWPOKE-2 research reactor, an external uranium contamination of the weld area was observed. This contamination occurred during the welding of end caps to the fuel pin meat, where some of the uranium aluminum alloy fuel was locally heated above its melting temperature and flowed out of the weld location. Although the weld area was machined later to remove this material, external contamination still remained (Figure 1) [1].

In subsequent operation of several HEU-fuelled SLOWPOKE-2 reactors, radionuclides have been observed in the reactor container water that surrounds the fuel. The gamma radiation fields around the reactor can generally be attributed to this buildup of radionuclides, although no radiological hazard has resulted. At present, the radiation fields at the higher-burnup facilities reach levels sufficient to activate the medium-level radiation alarms positioned above the reactor container after only a few hours of operation at high power. Although these alarms were initially installed to detect a maloperation of the control rod or a loss of pool water shielding, they are now being triggered during normal operation at which point the reactors must be shut down.

By measuring the fission product release from the fuel to the reactor container water, it is

possible to distinguish between release mechanisms and therefore to determine if the increase in radiation fields around the reactor is due to a loss of integrity of the fuel sheath.

This paper summarizes the results of studies conducted at the SLOWPOKE-2 facilities of the Royal Military College (RMC), the University of Toronto (U of T), Ecole Polytechnique (EP), and the Kanata Isotope Production Facility (KIPF). Although the reactor at RMC is the only one to be fuelled with a low-enriched uranium (LEU) core of uranium dioxide, it has provided a convenient location to commission the experimental equipment for fission product analysis. A visual examination of the uranium alloy core at EP with an underwater television camera has also been performed to provide additional information on the condition of the core.

SLOWPOKE-2 REACTOR DESIGN

The name SLOWPOKE is an acronym for Safe LOW Power (K) critical Experiment, a research reactor developed by Atomic Energy of Canada Limited. The reactor produces a flux of 1.0×10^{12} neutrons/cm²/s and 20 kW of thermal energy at full power. Six of these reactors are now operating across Canada and one is located at the University of the West Indies, in Kingston, Jamaica.

The SLOWPOKE-2 reactor is a tank-in-pool type of design with a light-water moderated core within a reactor container structure (see Figure 2) [2]. The surrounding pool of light-water serves as radiation shielding for research personnel and also as a secondary heat sink. Water purity is maintained by circulating the container water through a series of deionizer columns on a weekly basis. Radiation monitors are located just above the reactor container (reactor alarm), above the reactor on the ceiling of the room (area alarm), and beside the deionizer columns (low-level alarm). Generally, only the reactor alarm prohibits continuous full-power operation.

Fuel Design

Of the seven operating SLOWPOKE-2 reactors, seven were fuelled with 93% U-235 enriched uranium aluminum alloy fuel pins coextruded with a 1050-aluminum cladding. The most recently commissioned SLOWPOKE-2 reactor (which is operating at RMC) is fuelled with low enriched uranium oxide fuel (20 % U-235), clad in Zircalloy-4. Radiation fields associated with fission product release have been observed only at those reactors fuelled with the HEU core.

EXPERIMENTAL DETAILS

EQUIPMENT

An analysis of fission products in the reactor container water and gas headspace at four SLOWPOKE-2 reactors has been performed by gamma ray spectroscopy methods using a

**POOR QUALITY
ORIGINAL**

GMX high purity germanium detector with a thin beryllium window (EG&G Ortec). Radiation shielding of the detector was provided by a transportable ensemble consisting of a lead brick castle supported by an aluminum frame.

SAMPLING PROCEDURE

Due to the very low activity levels at the RMC reactor, it was necessary to count water samples for a minimum of four hours, and gas samples for eight hours. At the other reactors, gas and water samples were taken once per hour, and counted for 25 minutes to provide good counting statistics.

Gas Sampling

Each SLOWPOKE-2 reactor is equipped with a closed sampling line and pump (5 L/min) for the measurement of any hydrogen in the gas headspace above the reactor water. In order to obtain a uniform, well-mixed fission gas sample before counting, the pump was operated for ten minutes after which it was switched off and the sample counted. At RMC, a gas sample was obtained with a 50 mL syringe which was inserted into the hydrogen sampling port. For the other reactors, a 40 mL gas chamber was connected in line with the pump, and the sampling lines were then inserted into the gas headspace to form a closed system. The transport time from the headspace to the sample chamber was typically less than 30 s.

Water Sampling

The SLOWPOKE-2 reactor water purification system has a bypass loop through which one can obtain samples of reactor container water. The pump (with a flow rate of ~10 L/min), was run for two minutes in order to clear the dead space in the sampling line. At RMC, the water sample was obtained in an open graduated cylinder and then decanted into a Marinelli beaker. During this transfer, some degassing occurred. As such, the sampling procedure was modified for the U of T, EP and KIPF experiments with the use of a sealed, pressurized sample chamber (40 mL) connected in line with the sampling port.

EXPERIMENTAL DESCRIPTION

A brief summary of the operating parameters for each experiment is given in Table 1. The reactor in each experiment was run continuously at one-quarter power, producing a flux of 2.5×10^{11} neutrons/cm²/s for approximately 100 h to allow most of the long-lived fission products to reach equilibrium in the reactor. The reactor was operated at this low power to maintain an excess reactivity. The radiation alarm monitor levels were recorded throughout the week so that these levels could be correlated with the fission product inventory in the reactor water.

EXPERIMENTAL RESULTS AND ANALYSIS

Concentration Calculation

The concentration in the reactor medium (water or gas) of a given isotope as a function of time can be calculated from the gamma spectra. In this calculation, the area of the peak of interest is evaluated with the MicroSAMPO analysis program [3] with the use of an energy calibration file, the detector efficiency and a shape calibration of the expected photo-peaks. The peak-search algorithm in MicroSAMPO will search for all peaks of a height which is greater than or equal to a specified number of standard deviations (sigma) of the Compton background. Typical peaks observed in the fission-product spectra were greater than 10 sigma as required for quantitative determination [4]. The count rate for the peak (gamma/s) was incorporated into a Microsoft Excel spreadsheet where the activity concentration of the isotope was calculated given the absolute gamma ray abundance, the time lag between the collection and measurement of the sample, and the counting time.

A list of activation and fission products observed in the reactor container water and gas headspace at the U of T reactor are given in Table 2. These isotopes are typical of those observed at the other HEU reactors.

The most significant difference between the various reactors is the absolute activity concentrations of the reactor water and gas as shown in Table 3. This table gives the absolute activity concentration of ^{133}Xe after continuous reactor operation at one-quarter power. The activity at the LEU reactor (RMC), is at least three orders of magnitude less than that observed at the other HEU reactors. The fission products observed at RMC are most likely due to surface contamination from the original uranium traces deposited on the fuel pin external surfaces during fuel fabrication [6,7].

Transport Time Estimate

There is a delay between the creation of fission products in the core and their uptake at the sampling port. During this time, the activity of the short-lived fission products will have decayed. The transport time was therefore estimated by rapidly sampling the coolant at the start of a given experiment (i.e. every three minutes) and noting the time lag between the point at which the reactor had reached power and the first occurrence of the short-lived isotope, ^{133}Xe . (The reactor would generally reach the flux set point in one to two minutes.) Typical values obtained with this method for the various reactors ranged from about three to fourteen minutes, e.g. for the following analysis the transport time is taken to be six minutes at U of T and KIPF, and fourteen minutes at EP.

Release Rate Calculation

In order to determine the mechanism of release from the core, the release rate can be determined for the noble gas fission products. Based on mass balance considerations in the closed reactor container, the release rates of fission gases from the fuel into the water (R_w), and from the water into the gas headspace (R_g), can be calculated from the activity

concentration data [5]. The net rate of change of the number of atoms with respect to time of a given radioactive isotope in the water (N_w) is

$$dN_w/dt = R_{fw} - \lambda N_w - R_{wf} \quad (1)$$

where λ is the radioactive decay constant (s^{-1}). Similarly, the mass balance for the inventory in the gas headspace (N_g) is

$$dN_g/dt = R_{wg} - \lambda N_g \quad (2)$$

These inventories are related to the measured activity concentrations (C) as:

$$C = \lambda N/V \quad (3)$$

where V is the given volume of water above the core (1380 L) or the volume of the gas headspace (108 L) [2]. Hence, using the above relation, Eqs. (1) and (2) can be rewritten as

$$R_{fw} - R_{wf} = V_w \{ (1/\lambda) dC_w/dt + C_w \} \quad (4)$$

$$R_{wg} = V_g \{ (1/\lambda) dC_g/dt + C_g \} \quad (5)$$

In general, for the noble gas isotopes, the release rates from the fuel to the water (R_{fw}) are much greater than those from the water to the gas headspace (R_{wf}), i.e. $R_{fw} \gg R_{wf}$ [8]. In this case, Eqs. (4) and (5) can be decoupled such that:

$$R_{fw} = V_w \{ (1/\lambda) dC_w/dt + C_w \} \quad ,$$

which can be equivalently written as:

$$dC_w/dt = \lambda R_{fw}/V_w - \lambda C_w \quad (6)$$

If R_{fw} is relatively constant over the course of the experiment, the solution of Eq. (6) is given by

$$C_w(t) = (R_{fw}/V_w)(1 - \exp\{-\lambda t\}) + C_{w0} \exp\{-\lambda t\} \quad (7)$$

where C_{w0} is the initial (measured) concentration in the water at the start of the experiment.

Equation (7) was fit to the measured concentration data, using a Marquardt-Levenberg algorithm [9] where R_{fw} was the single fitting parameter (see Figure 3). For isotopes with relatively long-lived precursors (e.g. ^{133}Xe and ^{135}Xe), Equation (7) was generalized to account for precursor effects in the container water.

Iodine Activity Concentration

Although the release mechanism is best determined from the analysis of the noble gas activity concentration in the reactor container water, other fission products are present in the reactor container (see Table 2). As iodine is one of the most radiologically hazardous fission products, the modelling of the activity concentrations of its various isotopes present was undertaken.

The quantities of iodine present was at least one order of magnitude lower than expected based on the noble gas analysis. A model for the hold-up of iodine following release from the fuel was suggested to account for the low activity concentration. This model incorporates the idea of a constant release rate and introduces a generalized "hold-up" zone somewhere within the reactor container [8]. Mass balance equations were used to describe the release of the fission product iodine from the fuel into the hold-up zone. From the hold-up zone, the iodine is released into the circulating reactor container water through a first-order rate process as characterized by an escape-rate coefficient k (such as one might expect for a desorption process) [10]. This model was fit to the iodine concentration data for I-131, I-133 and I-135 using the release rates as determined from the noble gas analysis, where the escape-rate coefficient was the only fitting parameter. The excellent fit of this model (see Reference 8) to the data is shown in Figure 4.

Noble Gas Activity in the Headspace

An analysis of the fission product activity levels in the gas headspace is required to fully understand the transport of fission gases within the reactor container vessel. A model which is able to describe the time-dependent behaviour of the activity concentrations of the noble gas species in the reactor container headspace has been developed. This model builds on the ideas employed in studying the activity concentrations in the reactor container water.

A convection model has been employed to describe the transport of fission products within the reactor container water during the water sampling procedure. These currents carry water containing fission products from the core up to the intake pipe of the sampling station (located 15 cm below the water surface). The currents are generally localized; as such there is a boundary layer near the surface of the water column through which the noble gas atoms must diffuse for entry into the gas headspace. Fission products which have been carried up to this height fairly quickly must diffuse through this layer at the interface of the water and gas headspace. Since diffusion is a slow process, this becomes the rate determining step in the release to the headspace.

This model of combined convection/diffusion was applied to describe the time-dependent behaviour of the activity concentrations of the noble gases in the headspace [8]. As shown in Figure 5, the model is in excellent agreement with measurement for the isotopes of ^{85m}Kr , ^{86}Kr , ^{133}Xe and ^{135}Xe observed in the gas headspace at the UT reactor. For this modelling, one fitting parameter (the height of the boundary layer) was used to reproduce the data. For other long-lived noble gas fission products observed in the gas headspace, production is effectively delayed due to the long-lived nature of their precursors.

MODEL DEVELOPMENT

When a fission fragment is created from the splitting of a ^{235}U nucleus, it is highly energetic (average kinetic energy of about 80 MeV) and can therefore travel a finite range before coming to rest in the uranium aluminide fuel meat where it would normally be contained. If, however, the fission product is created near the surface of some exposed portion of the fuel (such as at the uranium-bearing end weld line), it can be ejected directly into the surrounding coolant. Such a release can therefore occur by direct fission recoil. Alternatively, a fission fragment created deep inside the fuel will lose its kinetic energy, following which it may slowly migrate or diffuse through the fuel matrix and escape once it reaches the exposed surface.

Since recoil release is an instantaneous process, the release rate (R_{rec}) (in atoms/s) from the fuel pin into the coolant is independent of the half-life of the fission product so that [6]:

$$(R_{\text{rec}}/Y)_{\text{rec}} = \frac{1}{4}\mu(\Delta S/V)F, \quad (8)$$

where $\Delta S/V$ = ratio of the exposed fuel surface to the total fuel pin volume (m^{-1})
 μ = average fission-fragment range in the fuel (m)
 Y = fission yield for a given radionuclide (atoms/fission)
 F = fission rate per rod (fissions/s).

On the other hand, for a diffusion process, the release rate (R_{dif}) will depend on the half-life of the isotope [11]:

$$(R_{\text{dif}}/Y)_{\text{dif}} = (\Delta S/S) 3(D_i'/\lambda)^{1/2}F, \quad (9)$$

where $\Delta S/S$ = fractional surface area of fuel exposed to the coolant per rod
 D_i' = effective diffusion coefficient for fission products in the fuel (s^{-1})
 λ = radioactive decay constant (s^{-1}).

For example, a diffusion model has been employed in the STARS fuel performance code for the prediction of fission gas release in metal fuels [12]. At lower fuel temperatures, resolution back into the fuel matrix will dominate so that if any gas bubbles are formed they will remain small, and gas release will therefore depend more on the behaviour of single gas atoms rather than on bubbles [12,13].

If both diffusion and recoil are important, Eqs. (8) and (9) yield

$$R_{\text{rec}}/Y = n\{(R_{\text{dif}}/Y)_{\text{dif}} + (R_{\text{rec}}/Y)_{\text{rec}}\} = a\lambda^{-1/2} + c, \quad (10)$$

where n is equal to the number of defective fuel pins, $c = \frac{1}{4}\mu(\Delta S/V)(nF)$ and $a = 3(\Delta S/S)(D_i')^{1/2}(nF)$. The model in Eq. (10) has been fit to the measured fuel to water release rate data for the noble gas fission products in the reactor container water (as shown in Figure 6). The measured values of the short-lived isotopes have been corrected for radioactive decay

during transport from the reactor core to the sampling port [8]. The fitting parameters (a and c) are listed in Table 4 for the HEU reactors. A relatively flat line in Figure 6 indicates that recoil is a dominant release mechanism for the short-lived isotopes.

FUEL-SURFACE EXPOSURE

The average fuel exposure per pin can be determined from the recoil component of the release (Table 4) through Eq. (8), where for a cylindrical pin of radius r and length l :

$$R_p/Y = \frac{1}{4}\mu(\Delta S)F_c/(\pi r^2 l) = c. \quad (11)$$

Assuming that all pins are contributing to the release, $F_c (=nF)$ can be estimated from the average fission rate for the core. If the reactor is operating at 5 kW, and each fission event liberates 200 MeV of energy, then $F_c = 1.56 \times 10^{14}$ fissions/s. The range (μ) of the noble gas precursors [14] in the uranium aluminide fuel is calculated to be $\sim 13 \mu\text{m}$ using the individual ion ranges and the Bragg combining law for the compound [15,16]. Using the fuel pin dimensions [1], and the values of c in Table 4, the fuel exposure ΔS (per pin) can be determined from Eq. (11). As seen in Figure 7, the exposed area has been increasing with the accumulated flux-hours. The increase in the fission-product release is associated with the core burnup rather than the physical age of the reactor; the higher burnup U of T reactor has radiation levels approximately one order of magnitude greater than those at the University of Alberta (U of A) reactor even though both cores were commissioned at about the same time.

The curve in Figure 7 also correlates well with the reactor alarm monitor levels given in Table 1 for the various reactors. Hence, the monitor levels serve as an indication of the "normal" progression of the fission product release and exposed fuel surface area.

The curve can be extrapolated back to zero burnup to determine the amount of fuel exposure for the unirradiated fuel pins. This implies that an average pin in Figure 1 would have $\sim 10 \text{ mm}^2$ of fuel exposure. This value can be compared to a metallographic examination of archive fuel elements [17]. A band is seen at the end weld line of the fuel pin (Figure 8) after excess uranium-bearing material had been removed by machining. Based on the metallographic examination, the average exposed surface of each unirradiated fuel pin is estimated to be 4.0 mm^2 [17]. This value is in good agreement with that determined from the fission product release study (10 mm^2), i.e. the metallographic examination provides a lower-bound value since one must consider the total surface area rather than the geometrical area due to surface irregularities.

Since the activity of the short-lived fission products have been increasing with core burn-up, it is apparent that a larger surface area of uranium-bearing material is being exposed to the coolant. For instance, corrosion at the contaminated end welds of the fuel pins may account for the increased release. The uniform corrosion rate of the aluminum cladding is sufficiently small ($0.76 - 1.53 \mu\text{m/yr}$ at operating temperatures) that the cladding should remain intact throughout the core lifetime [17]. However, corrosion at the end-weld line

could increase any surface irregularity thereby exposing more uranium-bearing material to the coolant. Unfortunately, limited data are available on the corrosion behaviour of uranium-aluminum alloys under conditions similar to those in the SLOWPOKE-2 reactor [13]. Aqueous corrosion of uranium-aluminum alloy fuel was observed in the Advanced Test Reactor (ATR) after the formation of a pit defect in the plate-type fuel; however, the coolant flow and temperature of the cladding of the ATR fuel were higher than those associated with the SLOWPOKE-2 reactor [18]. It has also been suggested [19] that the corrosion resistance of uranium-aluminum alloy fuels is drastically reduced by cold machining. It is therefore possible that in removing the uranium bearing material at the end welds of the HEU SLOWPOKE-2 fuel, the fuel may be more susceptible to attack by corrosion.

VISUAL EXAMINATION OF THE EP CORE

A visual examination of the high burnup SLOWPOKE-2 core at EP was performed on 24 September 1991. The core was lifted out of its resting position so that its entire length was exposed. A remote underwater television camera Westinghouse Model ETV 1250 with built-in light source and right-angle viewing attachment provided by Chalk River Laboratories (CRL), was lowered down beside the core. Direct observation of the entire outer ring of fuel pins and portions of some inner pins was possible.

This examination indicated that the core was in good condition with no evidence of gross failure, or any loss of structural integrity. The end welds of the fuel pins were visible with no significant evidence of corrosion (although the lighting and the resolution capability of the camera were limited). Some minor swelling was observed at the bottom section of ten to twelve peripheral fuel pins.

CONCLUSIONS

1. Highly enriched uranium (HEU) fuel elements for the SLOWPOKE-2 reactors have a band of uranium-bearing material (at the end-weld line) exposed to the coolant as a consequence of the fuel fabrication process. This band of exposed fuel is the initial source of fission products in the reactor container water.
2. Fission-product activity levels have been quantitatively measured by gamma spectroscopy methods in the reactor container water and gas headspace of SLOWPOKE-2 reactors fuelled with uranium alloy cores at the University of Toronto (U of T), Ecole Polytechnique (EP) and Kanata Isotope Production Facility (KIPF). Activity levels in the SLOWPOKE-2 reactor at the Royal Military College (RMC) (containing a uranium dioxide core) have also been measured.
3. The predominant radionuclides observed in the reactor container water after approximately 100 hours of operation at 5 kW include: the noble gases; and the alkali metals, cesium and rubidium. These metals are produced principally from the decay of the noble gases. Iodine and molybdenum were also observed. Only noble gases are present in the gas headspace of the reactor container.

4. The release of the shorter-lived noble gases from the HEU alloy cores to the reactor container water is due predominantly to a recoil process. Increased activity levels with time may be attributed to corrosion of the end weld area. The exposed surface area predicted from the fission-product release study is consistent with the results of a metallographic examination of several unirradiated fuel pins.
5. The extremely low levels of fission products measured at the low enriched uranium (LEU) fuelled reactor at RMC are due to tramp uranium contamination on the surface of the Zircalloy cladding. In comparison, the ^{135}Xe levels were five orders of magnitude less than those measured at U of T.
6. The measured alarm monitor levels and fission-product activities correlate with the burnup of the various HEU reactors. The exposed fuel surface area has increased by an order of magnitude with burnup in the U of T core.
7. An underwater visual examination of the outer fuel elements of the EP core was performed. The core appeared to be in good condition with no evidence of gross deterioration, or any loss of structural integrity. No evidence of corrosion of the cladding was observed.
8. No fission products were detected in the external pool water. In addition, the release of fission products into the reactor container water and gas headspace pose no immediate health or safety hazard.

REFERENCES

- [1]. A.D. SMITH and B.M. TOWNES, "Description and Safety Analysis for the SLOWPOKE-2 Reactor with LEU Oxide Fuel", Atomic Energy of Canada Limited - Chalk River Laboratories Report no. CPR-77, January 1985.
- [2]. M.E. WISE and R.E. KAY, "Description and Safety Analysis for the SLOWPOKE-2 Reactor", Atomic Energy of Canada Limited, Radiochemical Company, report no. CPR-26 (Rev.1), September 1983.
- [3]. "MicroSAMPO Advanced Gamma Spectrum Analysis Software - Version 2.0", User's Guide, Canberra Nuclear Products Group, CISE 511, September 1989.
- [4]. L.A. CURRIE, "Limits for Qualitative Detection and Quantitative Determination", Anal. Chem. 40 p. 587, 1968.
- [5]. B.J. LEWIS, R.G.V. HANCOCK, D. COLE and L.G.I. BENNETT, "A Preliminary Analysis of Fission Product Release in the HEU-Fueled SLOWPOKE-2 Reactor", Proceedings of the 11th Annual Conference of the Canadian Nuclear Society, Toronto, p. 6.29, 1990.

- [6]. B.J. LEWIS, "Fission Product Release from Nuclear Fuel by Recoil and Knockout", J. Nucl. Mater. 148 p. 28, 1987.
- [7]. B.J. LEWIS, "Fundamental Aspects of Defective Nuclear Fuel Behaviour and Fission Product Release", J. Nucl. Mater. 160 p. 201, 1988.
- [8]. A.M.C. HARNDEN, Fission Product Release from SLOWPOKE-2 Reactors, Queen's University, Department of Physics, Ph.D. Thesis, 1993.
- [9]. "SigmaPlot Scientific Graphing Software", User's Manual, Version 4, Jandel Scientific, Corte Madera, California, 1990.
- [10]. K. A. DINOV, "A Model of Crud Particle/Wall Interaction and Deposition in a Pressurized Water Reactor Primary System", Nucl. Technol. 94 p. 281, 1991.
- [11]. A.H. BOOTH, "A Suggested Method for Calculating the Diffusion of Radioactive Rare Gas Fission Products from UO₂ Fuel Elements and a Discussion of Proposed In-Reactor Experiments that May be Used to Test its Validity", Atomic Energy of Canada Limited report AECL-700, September 1957.
- [12]. M.C. BILLONE, Y.Y. LIU, E.E. GRUBER, T.H. HUGHES and J.M. KRAMER, "Status of Fuel Modeling Codes for Metallic Fuels", Proc. Int. Conf. Reliable Fuels for Liquid Metal Reactors, Tucson, Arizona, Sept. 7-11, 1986.
- [13]. J.M. BEESTON, R.R. HOBBS, G.W. GIBSON and W.C. FRANCIS, "Development and Irradiation Performance of Uranium Aluminide Fuels in Test Reactors", Nucl. Technol. 49 p. 136, 1980.
- [14]. C. WISE, "Recoil Release of Fission Products from Nuclear Fuel", J. Nucl. Mater. 136 p. 30, 1985.
- [15]. L.C. NORTHCLIFFE and SCHILLING, Nuclear Data Tables 7A p. 233, 1970.
- [16]. G. FRIEDLANDER, J. KENNEDY, E. MACIAS and J. MILLER, "Nuclear and Radiochemistry", 3rd Edition, John Wiley and Sons, New York, 1981.
- [17]. J.P. MURPHY, P.J. Valliant, E.G. McVey, and P.W. Reynolds, "Examination of SLOWPOKE-2 Reactor Fuel Elements at the Chalk River Laboratories", Chalk River Laboratories (Draft) Report RC-827, March 1992.
- [18]. K. VINJAMURI and R.R. HOBBS, "Aqueous Corrosion of Uranium Aluminide Fuel", Nucl. Technol. 62 p. 145, 1983.
- [19]. H.C. BOWEN and R.L. DILLON, "High Temperature Aqueous Corrosion of Aluminum-Uranium and Aluminum-Silicon-Uranium Alloys", Corrosion 17, no.7, Tech Topica 9-11, 9.

ACKNOWLEDGEMENTS

I would especially like to thank my supervisors Dr. B.J. Lewis and Dr. L.G.I. Bennett for their patience, advice and encouragement throughout this project.

As well, I would like to express my sincere gratitude to the staff of the Atomic Energy Control Board (AECB) for their support and guidance of the project. I am much indebted to the following SLOWPOKE-2 operators for their assistance during the weeks of experimentation: R.G.V. Hancock (U of T), G.G. Kennedy (EP), and G.A. Burbidge, M. Mueller and A. Anderson (NORDION). Many thanks are due to J.P. Murphy (CRL), G.A. Burbidge and A. Anderson (NORDION) for their work on the visual examination. I would also like to acknowledge the help of R.D. MacDonald, P.J. Fehrenbach, and P.J. Valliant (CRL) for the metallographic study. Finally, of considerable benefit have been helpful discussions with J.W. Hilborn (CRL), G.G. Kennedy (EP), J.R. Robertson (RNC), and B. Cox (U of T).

This work was jointly funded by the Atomic Energy Control Board (research contract 2.197.1), Atomic Energy Canada Limited, and the Academic Research Program of the Department of National Defence (allocation number 3705-902).

Table 1: Summary of SLOWPOKE-2 Fission Product Experiments

Reactor	Date of Experiment	Test Description	Reactor Power (kW)	Radiation Monitor Levels (mR/h)			Coolant Outlet Temp (°C)	Coolant pH
				Reactor	Deionizer (prestart-up)	Area		
RHC	5-9 Nov 90	Constant operation at 1/4 power	5	N/A	N/A	N/A	N/A	N/A
U of T	26-30 Nov 90	Constant operation at 1/4 power	5	8 - 10	N/A	0.08	28 - 33	N/A
	20-21 May 91	Transport time calculation at 1/4 power;	5	N/A	N/A	N/A	N/A	N/A
		Transport time and operation at full power.	20	40-100 (level recalibrated in Mar 91)	N/A	0.08 - 0.1	40 - 45	N/A
EP	25 Feb - 1 Mar 91	Transport time calculation; steady operation at 1/4 power; Power ramp at end of test.	5	N/A	4 - 6	N/A	27	N/A
			5	2 - 3		0.05 - 0.1	27 - 34	
			5	2 - 3		0.05 - 0.1	27 - 34	
			13	6		0.06 - 0.1	35 - 42	
			23	8 - 20		0.1 - 0.2	51 - 54	
KIPF	9 - 11 Apr 91	Transport time calculation; Power ramp at 1/4, 1/2, 3/4, and full power.	5	0.4 - 0.6	2 - 4	0.4	24 - 28	N/A
			5	0.6 - 1.0		0.2 - 0.4	29 - 32	N/A
			10	2 - 4		0.4 - 0.6	36 - 41	N/A
			15	N/A		N/A	45 - 47	N/A
			20	2 - 6		1 - 2	40 - 46	N/A
	13-17 May 91	Constant operation at 1/4 power; Water sampling at various heights in container (1-4 m) at end of test.	5	0.8 - 1.5	4 - 6	0.4 - 0.6	28 - 39	5.5 - 6
			5	0.8 - 1.5		0.4 - 0.6	39	

N/A: Not Available

Table 2: Observed Radionuclides at the U of T Reactor

A. Reactor Container Water	
<u>Fission Products</u>	
Noble Gases:	Kr-85m, -87, -88, -89 Xe-133, -133m, -135, -135m, -137, 138
Halogens:	I-131, -132, -133, -134, -135
Alkali Metals:	Rb-88, -89, Cs-138
Alkaline Earth:	Sr-91, Ba-140
Noble Metals:	Mo-99, Tc-99m
Rare Earths:	Y-91m, La-140, -142, Ce-141, -143, Nb-95, Zr-95
<u>Activation Products</u>	
Noble Gases:	Ar-41
Alkali Metals:	Na-24
B. Gas Headspace^(a)	
<u>Fission Products</u>	
Noble Gases:	Kr-85m, -87, -88, -89, -90 Xe-133, -133m, -135, -135m, -137, 138
Alkali Metals:	Rb-88, -89, Cs-138
<u>Activation Products</u>	
Noble Gases:	Ar-41
C. Deionizer Column^(b)	
Halogens:	I-131
Alkali Metals:	Cs-137
Alkaline Earth:	Ba-140
Rare Earths:	La-140, Nb-95, Zr-95

- (a) The alkali metals present in the sample vial are produced by the decay of the noble gas species.
 (b) From a previous gamma spectroscopy analysis [5].

Table 3: ^{135}Xe Concentration in the Reactor Container Water and Gas Headspace (5 kW)

Reactor	Xe-133 Concentration ^(a) (MBq/L)		Time After Start-up ^(b)
	Water	Gas	
RMC	1.9×10^{-5}	1.4×10^{-5}	92
KIPF	0.08	0.06	72
EP	0.68	0.34	72
U of T	1.4	2.5	72

(a)The typical error is less than 10%.

Table 4: Fitting Parameters of Fission Product Release Model^(a)

Reactor	Fitting Parameters ^(a)	
	a (fissions/s ²)	c (fission/s)
U of T	$6.3 \times 10^7 \pm 25\%$	$2.0 \times 10^{10} \pm 17\%$
EP	$4.5 \times 10^7 \pm 22\%$	$7.7 \times 10^9 \pm 23\%$
KIPF	$7.2 \times 10^8 \pm 44\%$	$3.3 \times 10^9 \pm 22\%$

(a)Errors are quoted to one standard deviation.

(b)See Equation 10.

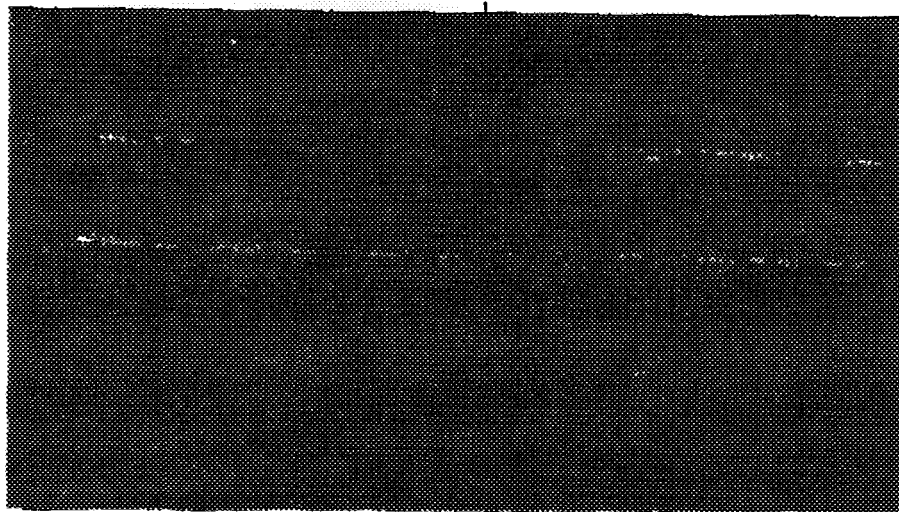
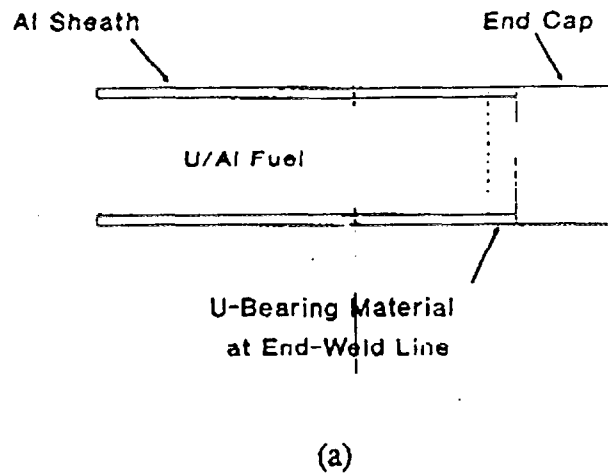


Figure 1. (a) Schematic diagram of a uranium-aluminide fuel pin showing the location of the exposed fuel.
 (b) Photograph of the uranium-aluminide fuel pin as welded (bottom) and with the final machined end caps (top).
 (Courtesy of Atomic Energy of Canada Limited)

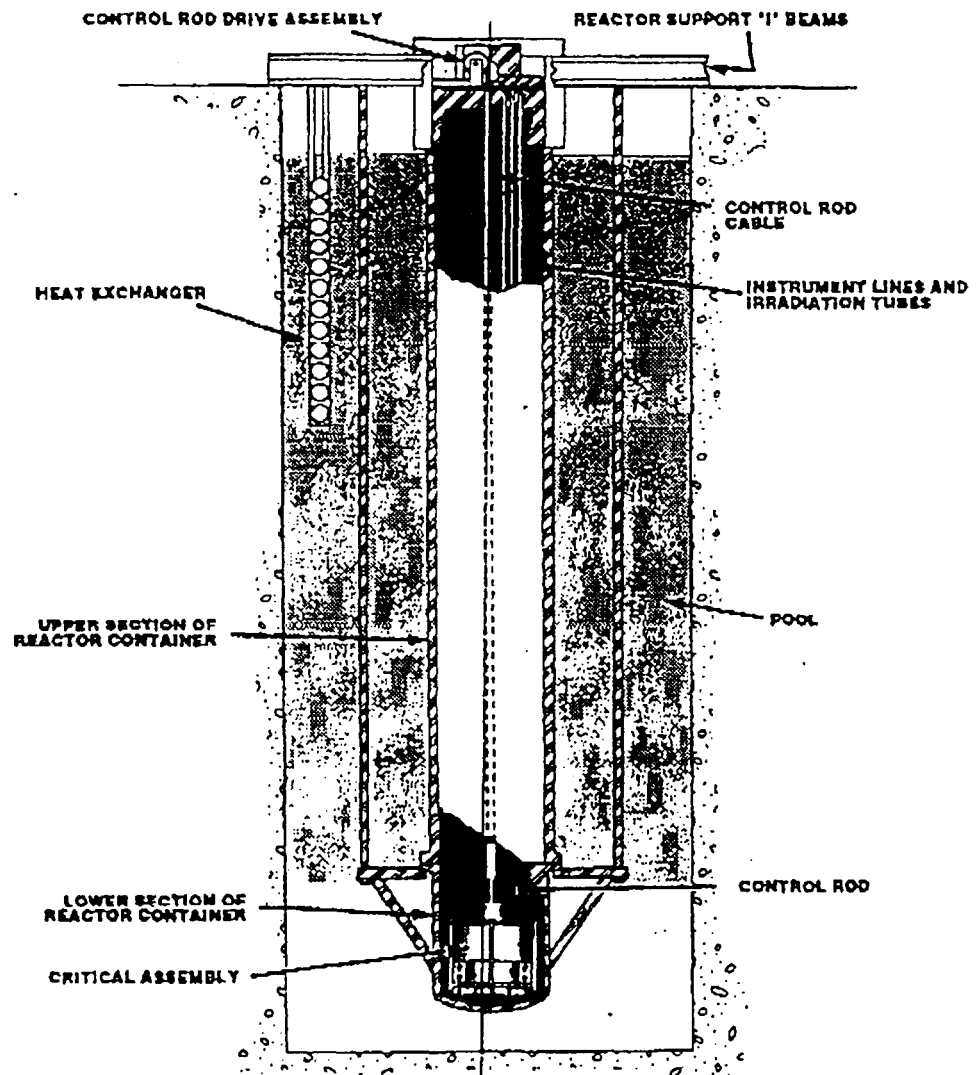


Figure 2 The SLOWPOKE-2 reactor general assembly (taken from Reference 2.)

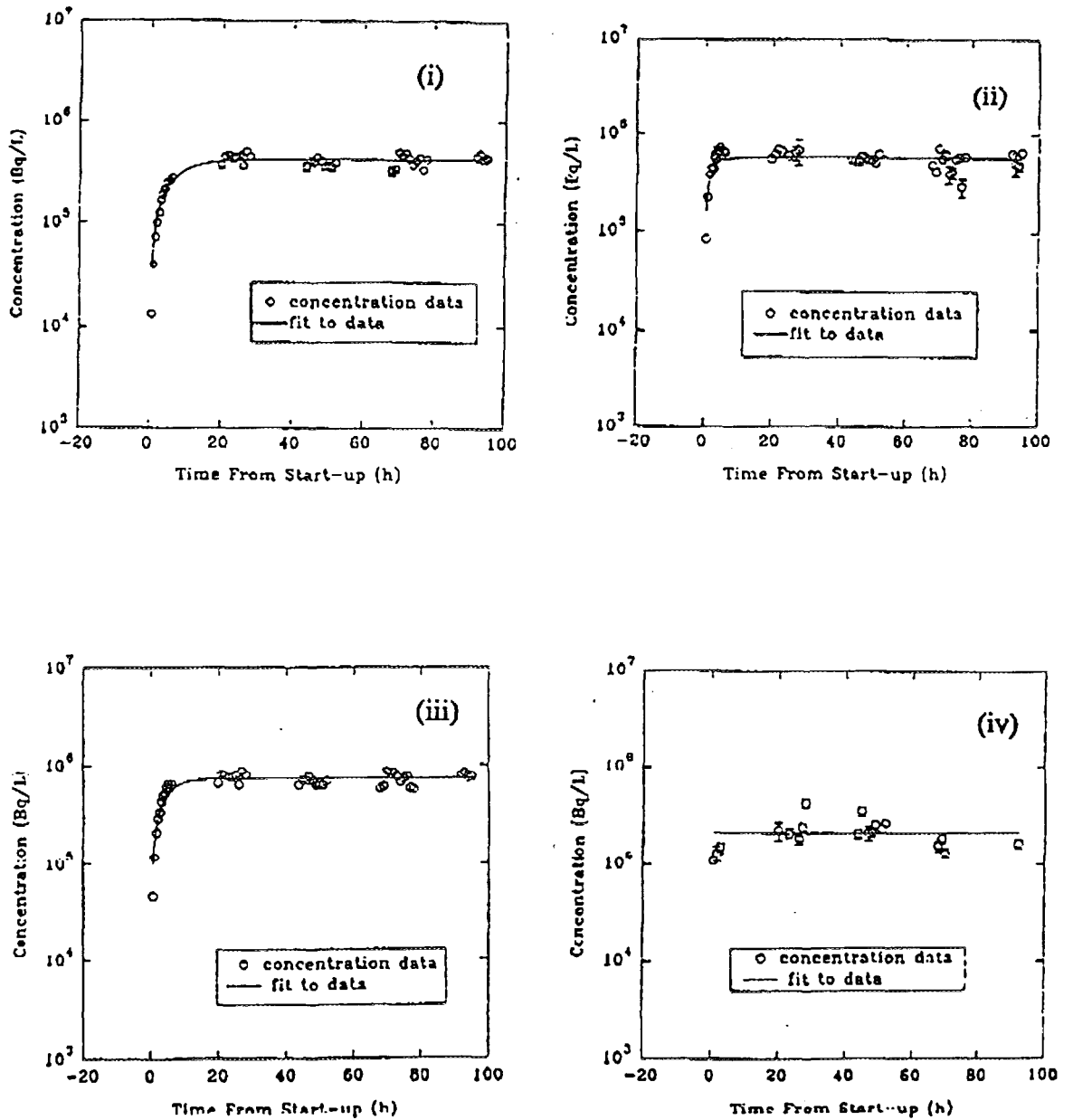


Figure 3(a): The concentration of the radioactive isotopes of krypton present in the UT reactor container water.
 (i) Kr-85m, (ii) Kr-87, (iii) Kr-88, (iv) Kr-89

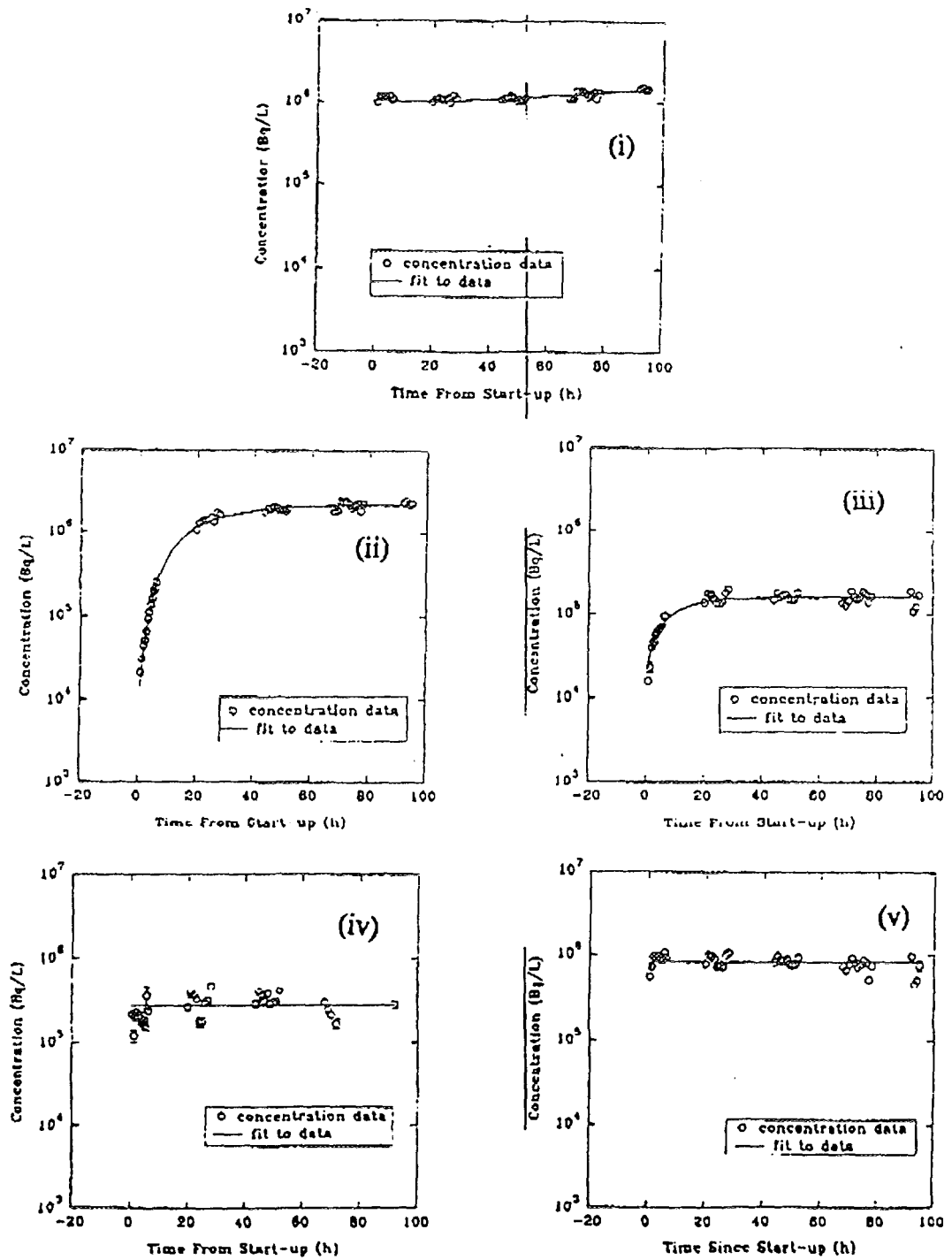


Figure 3(b): The concentration of the radioactive isotopes of xenon in the UT reactor container water. (i) Xe-133, (ii) Xe-135, (iii) Xe-135m, (iv) Xe-137, (v) Xe-138

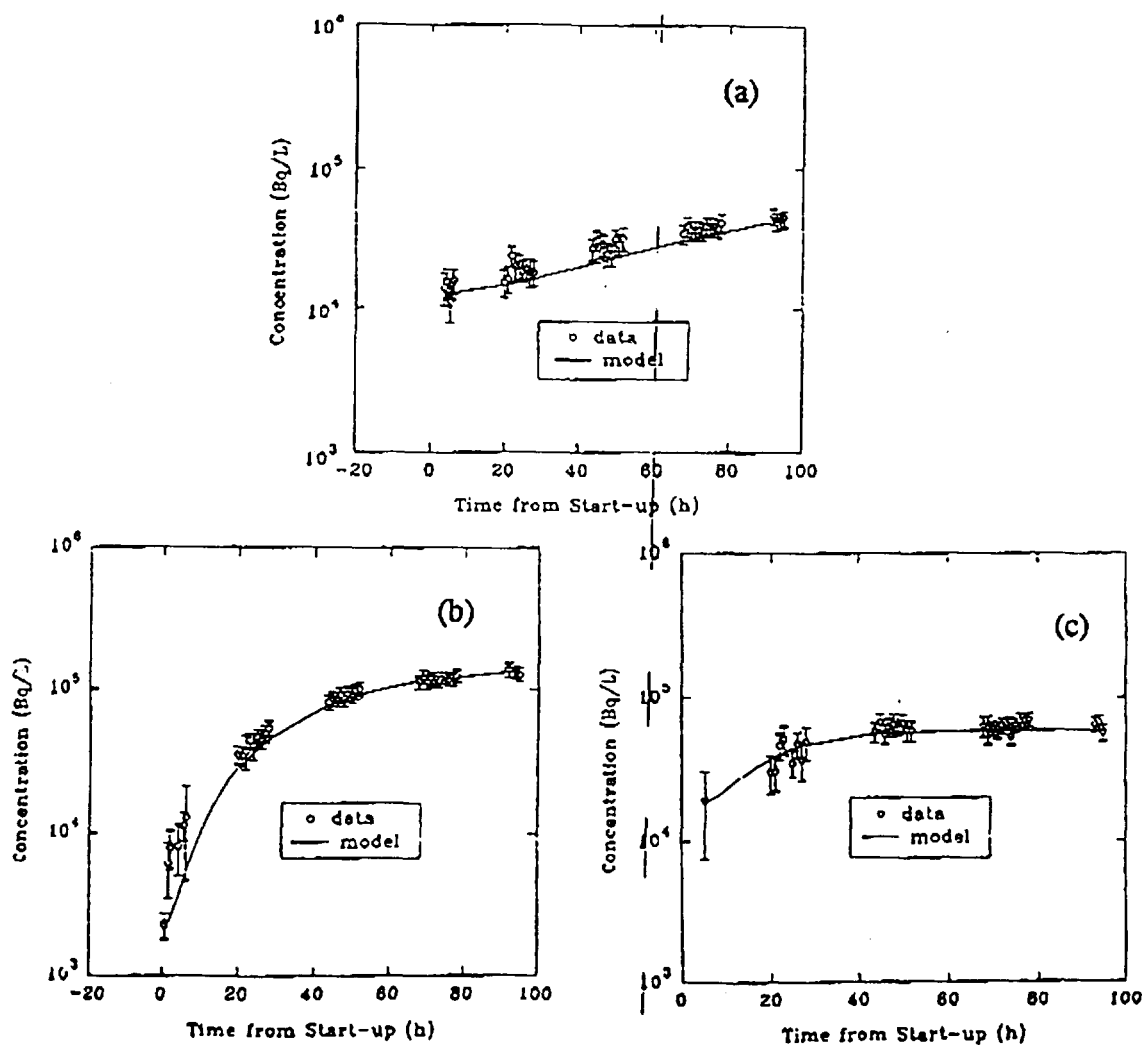


Figure 4 The activity concentration of (a) I-131, (b) I-133, and (c) I-135

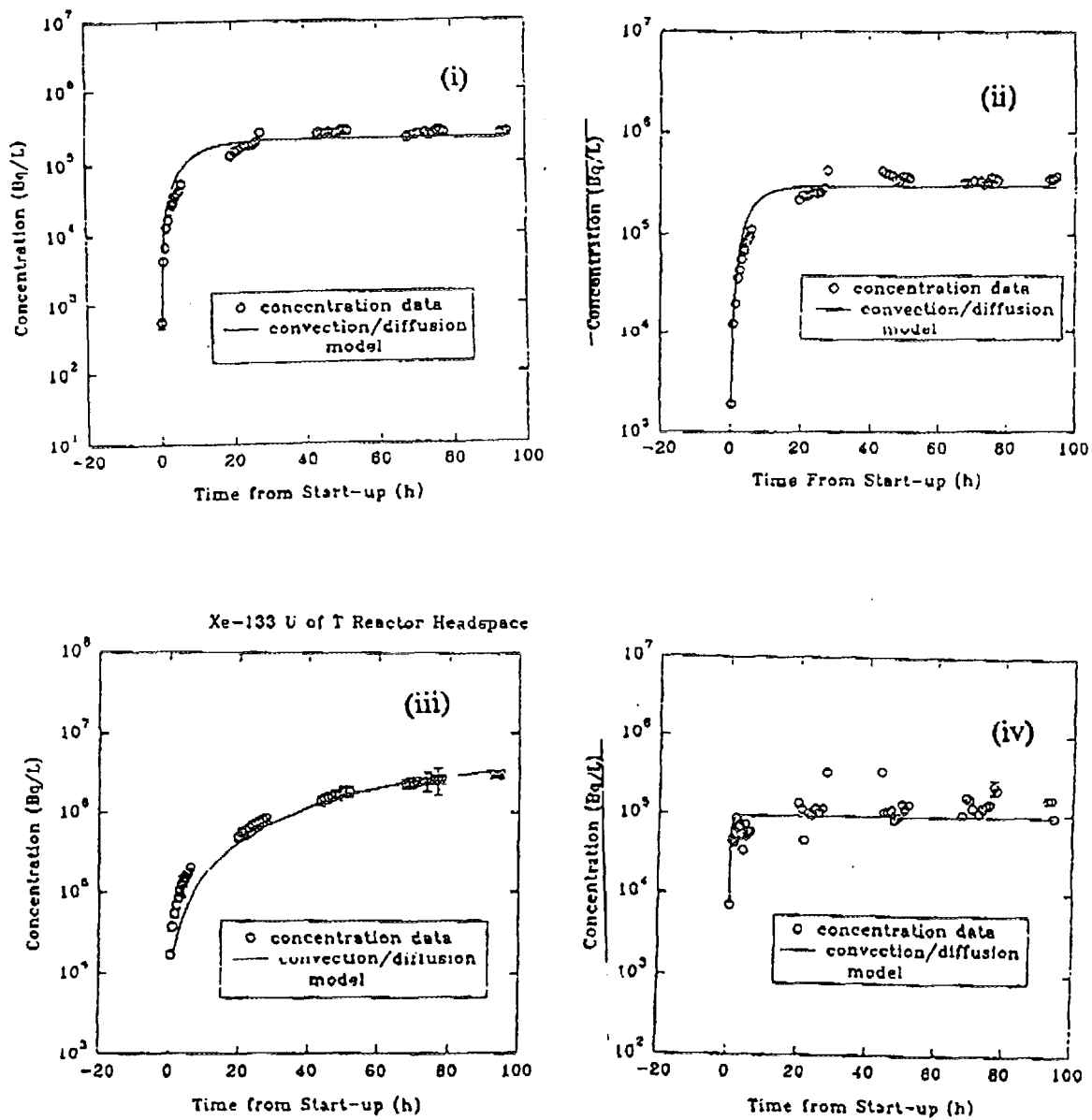


Figure 5: The activity concentration of (i) Kr-85m, (ii) Kr-88, (iii) Xe-133, and (iv) Xe-138 in the UT gas headspace.

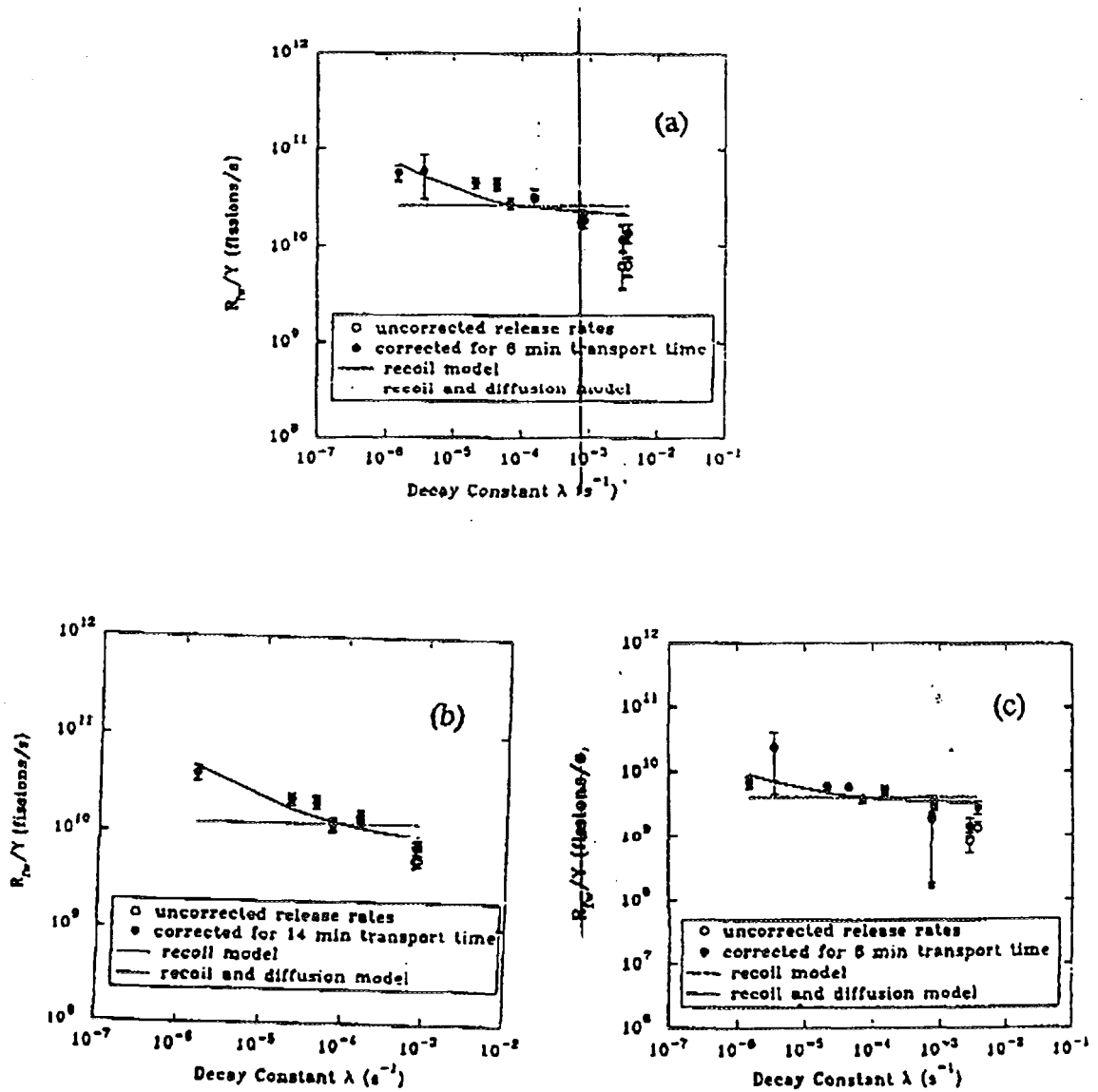


Figure 6: R_n/Y vs λ for the three HEU reactors.
 (a) UT, (b) EP, and (c) KIPF

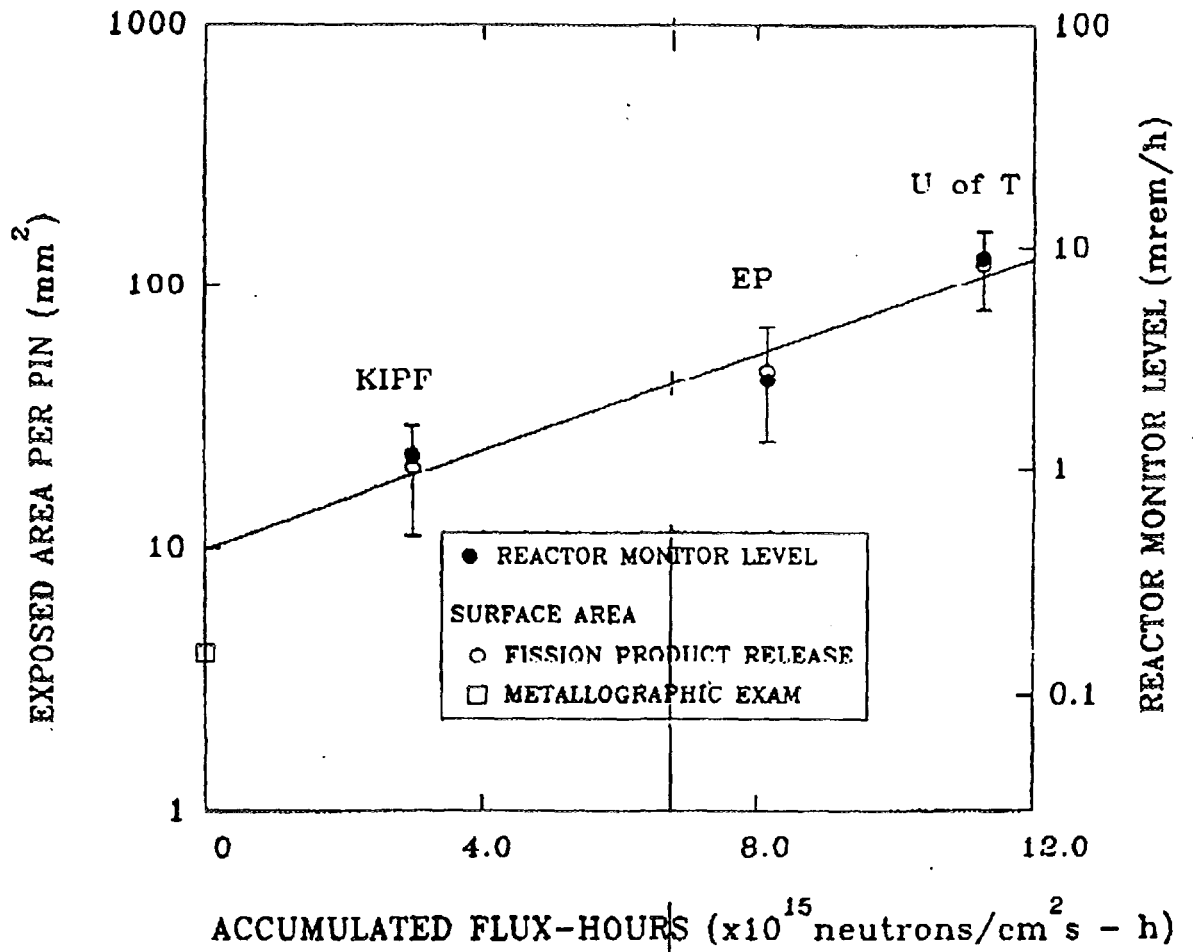
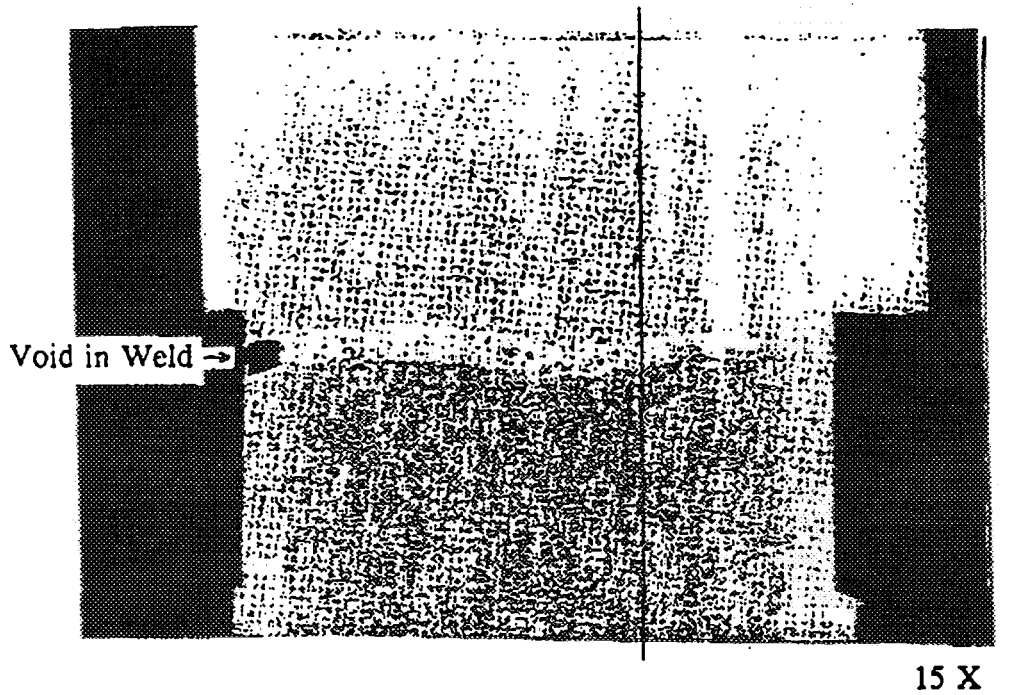


Figure 7: Increasing exposed fuel and alarm levels with burnup for the UT, EP and KIPF reactors. (The error bars indicate 95% confidence limits)



15 X

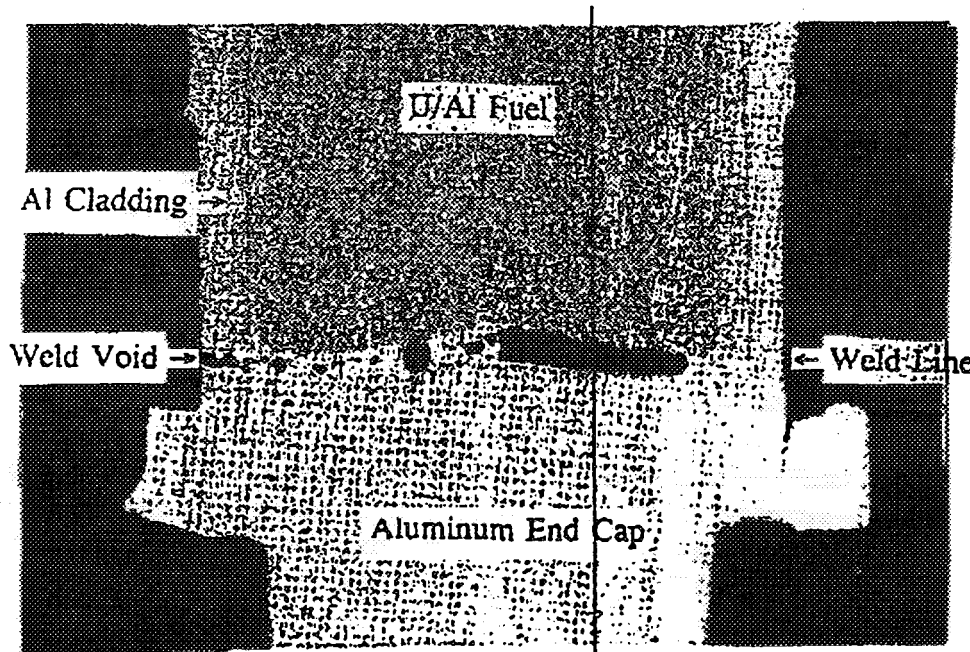


Figure 8: Metallographic examination of an archive HEU SLOWPOKE-2 fuel pin showing large voids in the end-weld line and sheath. A band of exposed fuel material can also be seen. (Courtesy of Atomic Energy of Canada Limited.)



THE RETENTION OF IODINE BY STAINLESS STEEL

Christopher A. Deir

Department of Chemical Engineering and Applied Chemistry
University of Toronto
Toronto, Ont.
M5S 1A4

Faculty Advisor: Prof. G.J. Evans

Following an accident at a multi-unit CANDU reactor it may be necessary to vent air from containment directly to the environment, to ensure that the pressure within containment remains sub-atmospheric. One of the most hazardous fission products that may be present in this air stream is ^{131}I , possibly in the form of I_2 . At CANDU stations in Ontario there is in place a system designed to measure the levels of any I_2 in the vented air. Recent studies have indicated that I_2 may retain to stainless steel in significant amounts, and since the any sampling system may include up to 20 metres of stainless steel tubing significant errors may arise due to line losses.

An experimental apparatus has been designed and constructed to allow the measurement of the various parameters that are thought to have the greatest effect on the deposition of molecular iodine to stainless steel. These parameters are divided into two major groups, gas phase properties and surface properties. The gas phase properties include air temperature and humidity, gas phase velocity and iodine gas phase concentration. The surface parameters include temperature of the steel, type of steel (ie 316 or 304), and the physical condition of the steel (ie cleaned, dirty, new, old etc.). The apparatus not only allows the determination of these parameters but also allows the control of all the parameters to a large degree. That is the humidity can be set to within 5% of the required value and the gas phase concentrations of iodine can be controlled to within an order of magnitude.

Since it is known that the deposition velocity is controlled by both the gas phase mass transfer and the surface chemical reaction, it becomes necessary to be able to measure one aspect independent of the other. Therefore the use of tubes that have been coated with Amercoat 90 nuclear grade paint. This arrangement is known to have a high affinity for retaining iodine, therefore the rate of chemical reaction at the surface will be high in comparison with the rate of mass transfer through the gas phase. Therefore the measured deposition velocities should be limited by the gas phase with surface interactions playing a minor role. Tests using this arrangement have resulted in deposition velocities ranging from 2.5 cm/s for low gas flow rates to 600 cm/s for higher gas flow rates. These values are in general agreement with standard engineering correlations, in that as velocity increases so should the deposition velocity. More work is needed to determine the exact nature of the relationships.

Tests with stainless steel tubing, deposition velocities as high as 0.87 cm/s have been recorded at 50°C and 50% RH, along with maximum loading of the stainless steel of 1.5×10^{-10} mol/cm². The value of the deposition velocity, however, is generally around 0.1 cm/s with maximum loadings in the 10^{-11} mol./cm² range. The importance of the deposition velocity is that the concentration of iodine within a tube will have an exponential decrease with distance travelled multiplied by the deposition velocity. Therefore the larger the deposition velocity the greater the loss to the tube surface. Experimental results indicate that almost all of the initial iodine may be absorbed by a length of tube that is typical of sampling lines for deposition velocities of 0.87 cm/s.

RADIATION DAMAGE ON HIGH POLYMER EPOXIES

H. M. Pak

Department of Chemicals and Materials Engineering
The Royal Military College of Canada
Kingston, Ontario K7K 5L0

INTRODUCTION

The uses of high polymer epoxies today are many and varied. Their application as an adhesive is particularly attractive due to their characteristic resistance to weathering and chemicals, low shrinkage upon cure, flexibility, good electrical properties, ease of use, high tensile strength, low weight, and excellent adhesive properties. As a structural adhesive in applications such as in the aerospace industry, building construction, and the automotive industry, use of epoxy glues have become widespread.

Numerous studies of the effects of ionizing radiation on epoxies have been conducted, but their main focus has been on the mechanical properties after irradiation. Research on epoxy adhesives and the effects of radiation on their adhesive properties is one area that has not been explored. The use of epoxy adhesives as an alternative to other fastening techniques has grown to such an extent that knowledge of the effects of radiation is necessary for their safe and effective application in high radiation environments.

This project investigated the effects of radiation on the adhesive properties of epoxy glues. The results could be applied as design criteria for the use of high polymer epoxies in high radiation environments as well as providing an objective method of evaluating the relative radiation resistance of various epoxy adhesives.

EXPERIMENTAL

The ASTM D897 standard testing procedure for evaluating the adhesive strength of glues was chosen as the method by which the epoxy adhesive strength would be tested. The irradiations were carried out in the SLOWPOKE-2 nuclear reactor at the Royal Military College of Canada in Kingston.

Once a suitable epoxy adhesive was obtained, it was necessary to become familiar with the manufacturer's preparation instruction, as outlined in the ASTM test procedure. As with most epoxies, the test adhesive came in two parts and required mixing of proportional parts when used. To ensure that accurate amounts of resin and hardener were mixed, a dual-syringe applicator was designed to dispense accurately appropriate quantities of both parts, as required by the manufacturer's use procedure.

The preparation of the sample aluminum glue surfaces was an important procedure to standardize. It was found that a simple and accepted method of surface preparation for the adhesion of aluminum surfaces was simply to grind the surfaces down on grinding surfaces, with flowing water continually cleansing the aluminum particles from the grinding surface.¹

The next step was to obtain a holder for the twelve samples that would be irradiated together during each irradiation. A simple, yet effective, sample holder was designed. With this holder, it was possible to position all twelve samples at an equal distance from the SLOWPOKE-2 reactor core. The holder had a curvature designed to compensate for the curvature of the reactor vessel. Sealed plastic bags were used to encapsulate the samples and to prevent the possibility of water interacting with the sample epoxies during irradiation.

A hand-operated elevator, that would be used to lower the sample holder to mid-reactor height level, was then installed. The elevator, when lowered, stopped at a set level and the arm with the holder was then swung towards the reactor casing, so

that the curvature of the holder would conform to the exterior curvature of the reactor casing.

Samples in batches of twelve were glued together for testing at a particular radiation dose.

The entire testing procedure is outlined in Table 1.

Table 1. Test procedure outline.

1. aluminum samples were ground to 400 grit
2. samples were glued together and encapsulated in plastic
3. samples secured on the holder and then mounted onto the elevator arm
4. elevator arm and sample holder lowered into position
5. irradiation carried out with the reactor at half power (10kW)
6. elevator arm and holder raised halfway up and allowed to decay to acceptable levels
7. holder fully retracted and samples placed in a lead cask for further decaying
8. after sufficient decay, samples tested on the tensile testing machine
9. excess epoxy cut off and stored for later analysis
10. process repeated for a different length of irradiation time

DISCUSSION

The results (Table 2) clearly show that an increase in adhesive strength was observed for the epoxy glue when exposed to the higher doses of radiation. Upon closer inspection of the results, it would appear that at higher levels of radiation dose the accuracy of the measurements also increased. This is not the case. When the higher dose samples were tested on the tensile tester, most of the samples' ultimate yield strength exceeded the load cell limit of 9.5 kN. When the limit was reached an automatic shut-off condition was activated. This is easily seen from the numerous sample ultimate strengths at 9.5 kN. The samples that did not break were later tested on a load cell with

a 50 kN limit and they all displayed ultimate tensile strengths below 6.1 kN. Interestingly, none of the samples that had previously reached 9.5 kN exceeded that strength or even approached it. It would appear that the bond between the adhered surface and the adhesive had been weakened from stress fatigue during the earlier test, or that the epoxy had reacted with the environment since the last test. As the storage environment was relatively non-hostile, dry, and shielded from radiation, it would appear that the sample storage did not present conditions for possible epoxy reaction with the environment or contamination. The stress fatigue of the bonds after the first test would seem the most likely reason for the inability to reproduce the results of the previous adhesive strength testing.

Calculation of Gamma-Ray and Thermal Neutron Doses

The large error bars associated with the calculated radiation dosages (Figures 1 and 2) would indicate the fact that the dosages were not well defined. Fast neutron doses were not determined because of the non-availability of fast neutron flux measurements at the irradiation site. Fast neutron fluxes decrease rapidly past the reflector of the nuclear reactor and since the irradiation site was outside the reactor vessel, their effect was assumed to be minimal. The calculations involving the gamma-ray dosages were derived from many assumptions, since the gamma-ray flux at the irradiation site was not measured for this experiment. The gamma-ray flux was determined from bubble dosimeter measurements recorded in another investigation performed by an outside agency (DREQ)². Assumptions were made that the bubble detector sensitive absorbing material was comparable to living tissue, that human tissue had a density close to water, and that the epoxy molecule was a standard epichlorohydrin-Bisphenol A based type. Firstly, the assumption that the bubble detector material was comparable to living tissue is valid since the dosimeter is used to measure the radiation doses that the human user might have been exposed to. The second assumption is valid since an exceptionally high proportion of

One observable change in the epoxies after irradiation was in their colour, which gradually changed from yellow to a deep orange with increasing amounts of radiation. The presence of additives would seem to have accounted for the marked colour change at these relatively low radiation dosages. Colour changes of polymers usually occur after much higher doses of radiation, around 50 kGy.⁴

Possible Surface Interactions, Inconsistencies, or Impurities

As described in adhesion science theory⁵, the surface condition of the adherends has the most dramatic effect on the bonding. It was found that grinding the surfaces with 400 grit sand paper was an acceptable method of exposing fresh material, and is considered a relatively reliable method of removing surface contaminants. Thus, the possibility of epoxy contamination on the surface of the aluminum sample gluing surfaces was small. The possibility of epoxy reaction with the atmosphere was small, due to the isolated thin layer of actual adhesive epoxy between the adherend surfaces, with an encompassing circumferential layer of excess epoxy that effectively sealed the inner thin layer from the air. Reaction of the inner thin layer of epoxy with any atmospheric moisture is unlikely, since the sealing excess epoxy was effectively providing a physical barrier. In addition to moisture, microscopic dust particles in the air may have embedded themselves on the rough surface of the adherend. The SEM microphotographs were taken to observe the relatively rough surface of the aluminum. Whether or not the transition layer of the surface of the adherend contained elements that may have reacted with the epoxy during irradiation was impossible to determine due to the high radioactivity of the aluminum sample glue surfaces. The possibility of the aluminum surfaces oxidizing with the atmosphere was minimal as the gluing of the samples immediately followed the grinding of the surfaces.

Gluing process

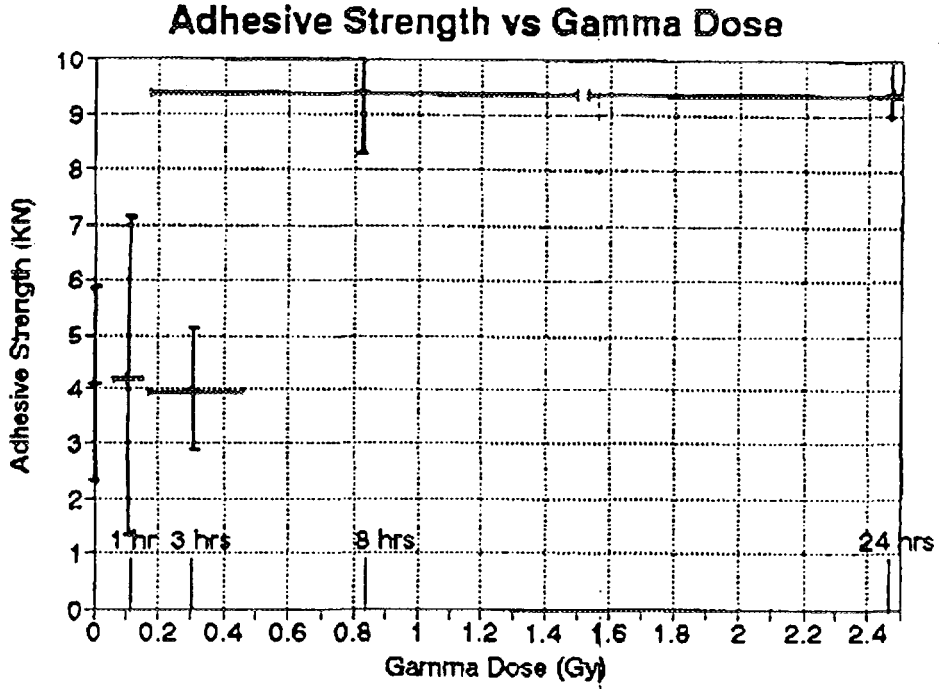
The most probable source of error or inconsistency would be attributed to the gluing process itself. The method used was not entirely satisfactory but was necessary due to time constraints. As can be seen from the adhesive strength testing of the non-irradiated sample, the variance of the measurements was significant. Adding credibility to the observed results would be the fact that twelve samples were used for each radiation dose. Nonetheless, a different method of gluing must be found to obtain better precision and more acceptable results.

SUMMARY

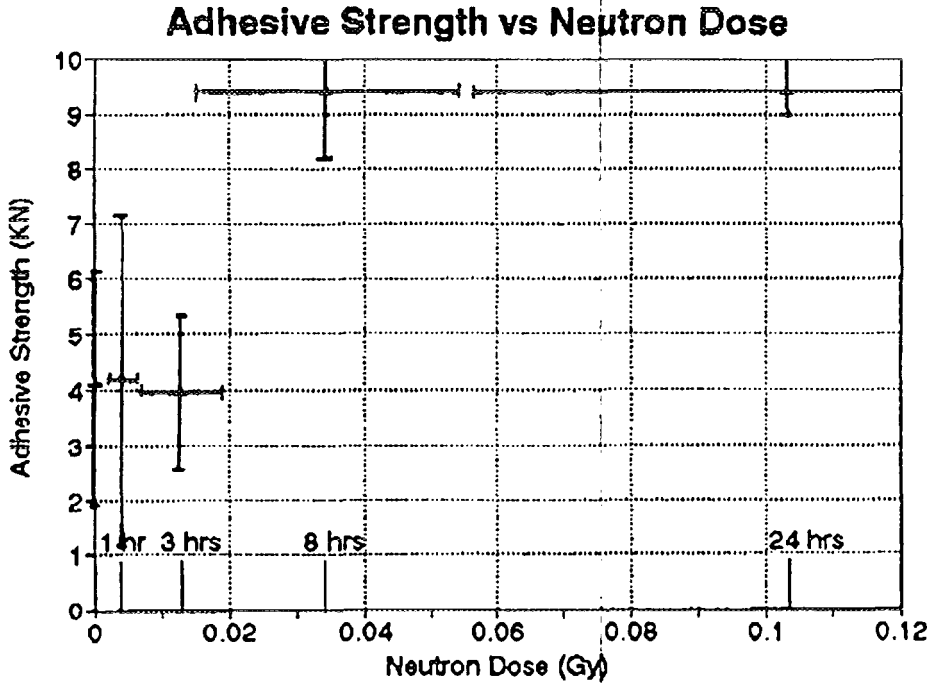
In spite of the possible sources of error and the imprecision of the measurements attributable to the gluing procedure, the great difference in adhesive strength observed cannot be easily dismissed as experimental error. Some type of radiation effect is strongly indicated with the observed adhesive strength. Radiation-induced crosslinking is the most probable explanation, although some type of interface phenomena may also be involved. Further study is required to determine conclusively the cause of the observed increase in adhesive strength with increasing levels of ionizing irradiation.

REFERENCES

1. Rabinowicz E., Friction and Wear of Materials, John Wiley and Sons Inc., New York, 1965.
2. Hoffart B.E., DREO Trip Report, RMC, 1986.
3. Encyclopedia of Polymer Science and Engineering, John Wiley and Sons, New York, 1988.
4. Ibid.
5. Bikerman J.J., The Science of Adhesive Joints, Academic Press, New York, 1961.



Graph 1. Graph of adhesive strength versus gamma dose.



Graph 2. Graph of adhesive strength versus neutron dose.

Table 2. Results of adhesive strengths of Irradiation Times

Sample no	Strength (KN)						
	Irradiation Time						
	0 hrs	1 hrs	3 hrs	8 hrs	8 hrs(*)	24 hrs	24 hrs(*)
1	3.988	4.044	2.459	9.511	2.725	9.517	4.715
2	3.689	4.148	5.001	9.509		8.942	
3	4.974	3.773	4.762	9.517		8.876	6.18
4	4.062	4.11	3.545	9.501		9.508	4.453
5	3.53	4.47	6.728	9.501		9.463	4.36
6	3.851	4.137	3.27	9.517		6.503	4.595
7	3.545	3.635	5.091	9.511	4.731	9.514	5.785
8	4.43	2.058	4.499	9.514		9.506	4.754
9	3.813	5.63	3.156	9.519	3.643	9.514	5.552
10	2.004	4.762	1.944	9.517	3.765	9.501	5.484
11	3.707	5.096	3.499	9.506	3.54	9.514	4.46
12		9	3.489	8.07	4.808	9.511	
avg	3.78	4.58	3.95	9.39	4.64	9.41	5.03
Variance (+)	1.78	2.5	1.49	1.32		0.534	

* denotes samples broken one week later with a higher load cell limit



POTENTIAL DROP CRACK MEASUREMENT SYSTEMS FOR CANDU COMPONENTS

Reena Sahney
Carleton University
Department of Mechanical and Aerospace Engineering
1125 Colonel By Drive
Ottawa, ON K1S 5B6
Faculty Advisor: Dr. P. Frise

Abstract

A project to develop an automated crack measurement system for CANDU pressure tube burst testing is currently underway. The system will utilize either Direct Current Potential Drop (DCPD) or Alternating Current Potential Drop (ACPD) techniques for crack measurement. The preliminary stage of the project involves testing and comparison of both ACPD and DCPD methods on a Zr - 2.5% Nb alloy plate with saw cuts (used to simulate cracks).

Preliminary results show that both ACPD and DCPD techniques are capable of detecting cracks; further testing is in progress to determine the ability of each of the two systems to make accurate crack depth measurements.

This paper will describe the two potential drop techniques and will present test results from the experimental program.

Introduction

Pressure tubes containing fuel and primary coolant in CANDU nuclear reactors have experienced Delayed Hydride Cracking (DHC) which has resulted in several pressure tube failures [1] and [2]. In an effort to gain a better understanding of the cracking mechanism involved, and assure the integrity of in-service pressure tubes, Atomic Energy of Canada Limited (AECL) has implemented a pressure tube burst testing program at the Chalk River Laboratories.

The testing program at Chalk River is part of an extensive program to study DHC. The program involves the growth of DHC induced flaws from a small starter notch machined into previously irradiated pressure tubes. The testing is carried out, at temperatures up to 300 °C (the majority of the test is carried out at 250°C) and a pressure of 10 MPa, until the pressure tube fails [3]. Data from the experimental program should lead to methods of prolonging pressure tube life, further improving reactor safety and economics.

To accommodate crack growth data acquisition during burst testing of irradiated pressure tubes, an automated system for crack detection and measurement is being developed using electrical potential drop technology. While potential drop techniques are well established for materials such as offshore structural steels, literature indicates that it has yet to be applied to zirconium alloy components in nuclear reactors. In light of this, a test program to evaluate two potential drop systems for zirconium alloy (Zr - 2.5% Nb) pressure tube material is underway and will be the focus of this paper. The two systems being tested for suitability are an alternating current (AC) and a direct current (DC) system.

Potential Drop Theory

Potential drop technology can be used to measure flaws in any material that is electrically conductive. The general basis for this technique is to connect the specimen to a circuit such that a current is flowing through the specimen. The potential field in the sample is then measured in two separate regions. That

is, a voltage reading, V_r , is taken over an unflawed area (preferably adjacent to the crack) while a second voltage reading, V_c , is taken across the crack. If the field distribution is known (either through theoretical calculations or by experimental calibration), then the two voltage measurements can be related to crack depth.

Alternating Current Potential Drop Theory

One of the most important characteristics of the ACPD method is that the current in the specimen is carried in a "thin skin" over the surface of the specimen. The skin thickness for a given situation is quantified by the following equation:

$$\delta = (\mu_r \mu_0 \pi \sigma f)^{-1/2} \quad (1)$$

where δ = skin depth (m)
 μ_r = relative permeability of conductor
 μ_0 = permeability of free space
 $4\pi(10)^{-7}$ H/m
 σ = conductivity of specimen (S/m)
 f = frequency of alternating current (Hz) [4]

The theory can be extended to give a simple one-dimensional relationship between (the measured voltages) V_r , V_c and crack depth:

$$a = \Delta_r / 2 [V_c / V_r - \Delta_r / \Delta_c] \quad (2)$$

where a = crack depth
 Δ_r = spacing between reference probe contacts
 Δ_c = spacing between probe contacts straddling crack
 V_c = voltage across crack face
 V_r = voltage across reference surface

This "Thin Skin" model is illustrated schematically in Figure 1 [4]. This equation is valid as long as the crack depth is quite large in comparison to this skin depth. In practice, the value of δ/d and δ/Δ should be less than 0.1. In some situations however, the crack depth is actually quite small in comparison to the thickness of the current carrying skin. In this case, where the ratio of δ/d is greater than 2, the above equation is modified to yield the "Thick Skin" model:

$$a = \Delta_r / 2 [V_c / V_r - \Delta_r / \Delta_c] (V_r / V_c)^{1/2} \quad (3)$$

where a = crack depth
 Δ_r = spacing between reference probe contacts
 Δ_c = spacing between probe contacts straddling crack
 V_c = voltage across crack face
 V_r = voltage across reference surface

It is important to note that equations (2) and (3) have been developed for cracks with an aspect ratio of at least 10 (ie. long and thin). A different crack shape may necessitate further modification of equations (2) and (3) in order to obtain accurate values for experimental crack depth [5].

Direct Current Potential Drop Theory

The DCPD technique also relies on relating voltage difference to crack depth. However, DCPD systems operate differently because the direct current used is conducted over the entire cross section of the component (as compared to a thin skin for the AC situation). The DCPD theory is also based on the premise

that current flow will be redirected around any flaw in the specimen, resulting in a measurable voltage change. As in the ACPD method, two readings are taken: a reading across the crack face, V_c , and a second reading adjacent to the crack, V_r . The difference in voltage can then be calibrated to crack depth through either analytical or experimental calibration relationships. Analytical calibrations, although well established for some configurations, are complex and must be modified for any change in probe or lead wire positioning. In fact, simple experimental calibrations have been found to give satisfactory results [6].

Specimen Geometry

In order to determine which of the two potential drop methods is more suitable for use with Zr - 2.5% Nb alloy, initial testing was carried out on a flat plate. The plate, obtained from AECL, was taken from the pressure tube fabrication process just before the tubes are rolled; as a result, the plate has similar material (and electrical) properties to actual pressure tubes.

The plate has a thickness of 4.2 mm and is 650 mm X 300 mm in size. In order to simulate cracks in the plate, two saw cuts were made in the centre of the plate. Crack #1 was machined to have a maximum depth of 2.38 mm, while Crack #2 was machined to have through the plate thickness. See Figure 2 for details of the plate and simulated cracks.

Experimental Equipment

Testing involved using a probe consisting of spring loaded contacts fixed in a plexiglass template with epoxy. The contacts were then soldered to shielded, twisted cable which was then connected to the data acquisition system. The plexiglass template was then mounted on a stepper motor driven lead screw which was used for positioning of the probe along the surface of the plate. A schematic of a typical probe and experimental equipment appears in Figure 3

The DCPD testing used an MDT Model M100 PC controlled multi-channel data acquisition system produced by the MDT Company of Waterloo, Ontario and modified at Carleton University. The probe consisted of four contacts where the outer two were used to input the 2.5 Amp direct current and the inner two were used to sample the potential drop [7] and [8]. In order to obtain measurable voltages, a spacing of approximately 2 mm was used between probe contacts.

The ACPD testing was carried out using a Unit Inspection Ltd. U-7 Crack Microgauge. In this case, the potential field was injected at the ends of the plate using two leads bolted to the specimen. Two different types of probes were used for this method. The first set of tests used a three contact probe where one channel was used to measure the voltage drop across the crack while the other channel was used to measure a reference voltage. A Keithely 706 switching unit provided multi-channel data acquisition capability. The second set of tests was carried out using a single channel and a two contact probe in an effort to reduce noise and signal degradation through minimizing cable length and stray field interference [9].

High temperature testing was carried out at 242 °C. In order to do this, hot plates were placed under the specimen on either side of the flawed region. A stepper motor driven probe positioning frame was placed across the flawed region while the remainder of the plate was covered with three layers of insulation. An Omega 2168A digital thermometer was attached to one end of the plate to allow temperature monitoring. The plate was allowed to come to thermal equilibrium for one hour before testing was carried out.

Experimental Program

The experimental program involved testing both the ACPD and DCPD systems. The testing was primarily carried out on the deeper crack (Crack #2). A method incapable of detecting a through thickness crack would not be useful for the detection of a shallower crack.

Initial DCPD testing was done with spot welded zirconium wire probes spaced 1 cm apart. None of the tests carried out with this fixed probe configuration yielded satisfactory results so a second, moveable, probe was built using a contact spacing of 2 mm. This probe was equipped with four contacts and was used to make several passes across Crack #2. Two methods of positioning the moveable probe were used: hand positioning and positioning with the aid of a frame holding a stepper motor driven lead screw. Figure 3 shows a schematic of the moveable probe and a schematic of the experimental equipment.

Initial testing done with the second probe gave satisfactory results. Several tests were then carried out across the entire width of the plate, in order to ensure repeatability of the test results. The DCPD testing was then further subjected to the same test at high temperature to determine the effect, if any, of this variable. Trials were carried out at 242 °C.

The first ACPD testing also involved the use of spot welded zirconium wire probes spaced 1 cm apart. The initial probe configuration did not give satisfactory results so a three contact probe was built using a 2 mm contact spacing. It was connected through existing cables to a switching unit and a micro computer for data acquisition. Several passes were carried out on Crack #2 - positioning the probe by hand. These results were not satisfactory as can be seen in Figure 4.

In an effort to reduce noise pickup, existing connections and the switching unit were by-passed; this allowed the probe to be connected directly to the U-7 Crack Microgauge through a low noise connector. The results of this configuration are illustrated in Figure 5. High temperature testing was not carried out since configurations subsequent to the first hand held probe test were unable to detect the presence of a crack.

Discussion of Results and Conclusions

Several conclusions can be made based on this preliminary testing. The DCPD technique looks promising. It appears to be capable of both detecting the presence of a crack, and determining the size of the crack with the use of a calibration curve. Figure 6 shows a plot of normalized voltage and actual crack depth vs position on the plate. High temperature does not appear to affect the accuracy of the method as can be seen from Figure 7 which presents the results of DCPD testing at 242 °C. The repeatability of the results supports these conclusions.

Note that the DCPD data presented in Figures 6 and 7 is not truly the depth of the cracks but rather the normalized potential drop. This normalization is done to provide convenient scaling so that the data can be presented on the same set of axes as the actual crack depth. True crack depths will be obtained from the DCPD data once a calibration curve has been determined.

The ACPD testing had very limited success. It was found that ACPD is capable of detecting a through the plate thickness crack using a specific probe configuration but is unable to provide accurate depth data as can be seen in Figure 4.

This could partly be a result of the limitations of the equipment available for testing. The U-7 Crack Microgauge available for use operates at a field

output frequency that is fixed at approximately 6 kHz [10]. In zirconium alloy, this leads to calculated skin thickness (Equation (1)) of 5.13 mm which is greater than the 4.2 mm thickness of the plate. This introduces several problems since neither of the theoretical models (Equations (2) and (3)), discussed earlier, are valid for experimental crack depth calculations.

Also, while the skin thickness results in a situation similar to DCPD configurations, the ACPD is further susceptible to interference from stray electrical and magnetic fields. This in fact proved to be a problem during testing. Furthermore, stability and accuracy of the U-7 Crack Microgauge could be improved using newer electronics technology.

It is felt that in order to draw a reasonable conclusion regarding the use of ACPD on Zr - 2.5% Nb further testing needs to be done using different frequencies and newer equipment.

Future Work

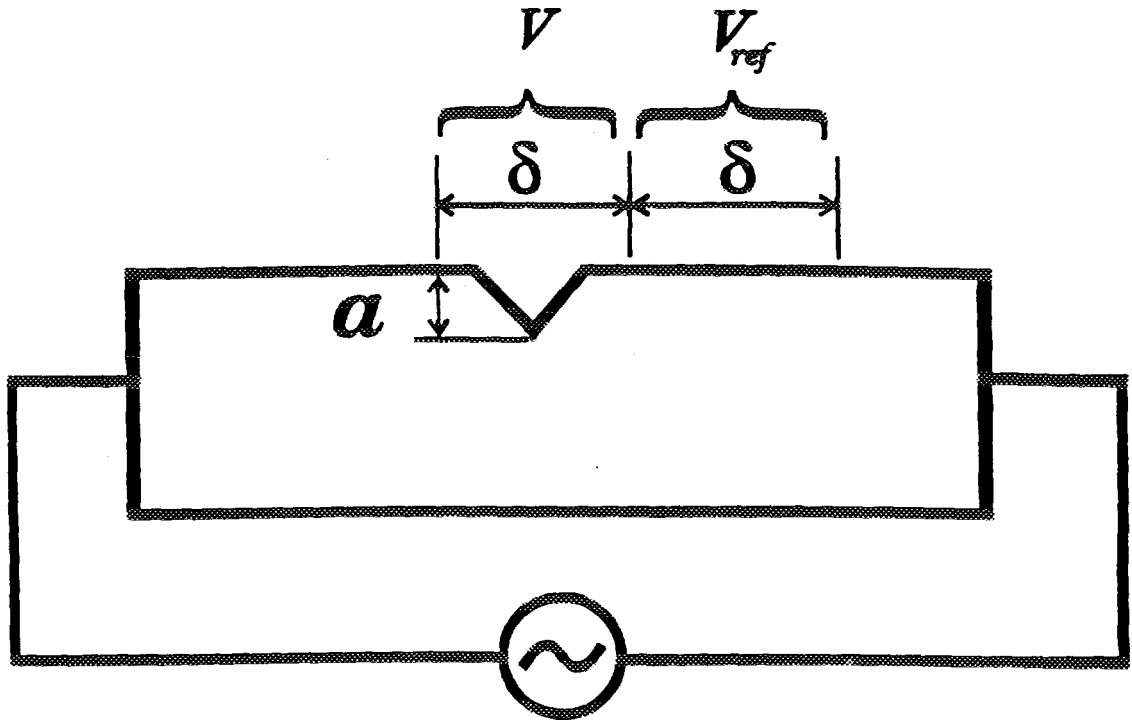
Further study will involve testing using the DCPD method in order to develop and test accurate calibration curves. If possible, further ACPD testing will also be carried out using newer multi-frequency equipment as well as testing a non-contacting method called Alternating Current Field Measurement (ACFM) [6]. This testing will be done before making a recommendation to AECL for a method of crack measurement and before designing an automated system that will be used in the Chalk River test cell on pressure tube specimens.

Acknowledgements

The author would like express her appreciation to Mr. D.K. Rodgers and Mr. R.R. Hosbons of Atomic Energy of Canada Ltd., Chalk River for their guidance and support throughout this project.

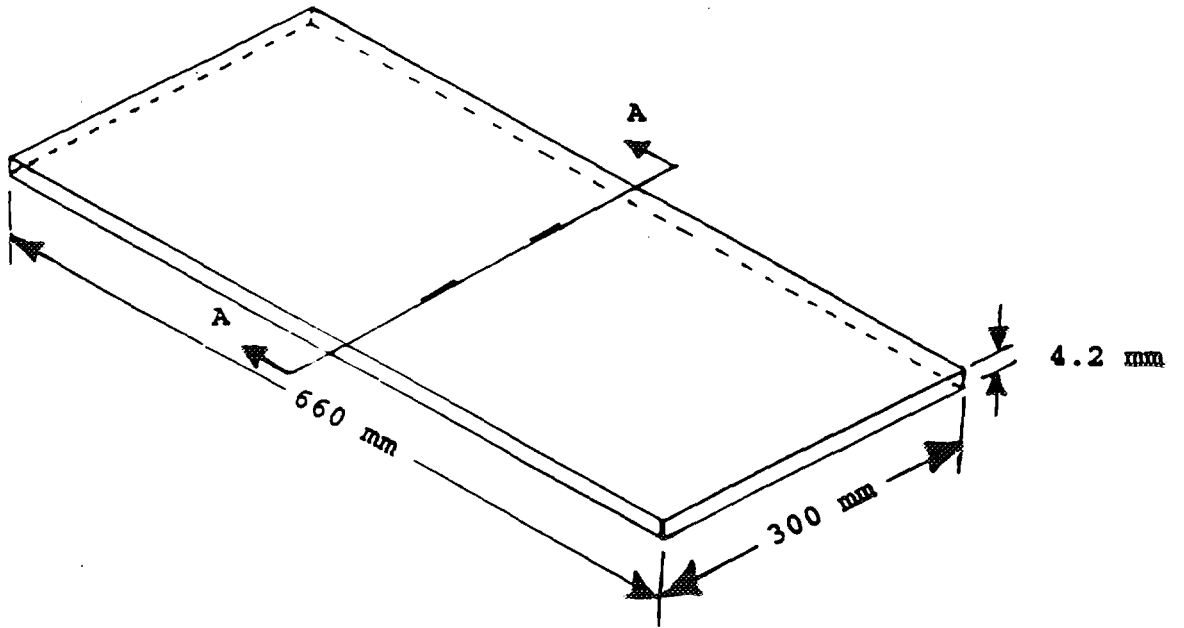
References

1. Dunn, J. T., Jackmann, A. H., "Delayed Hydrogen Cracking of Zirconium Alloy Pressure Tubes," AECL 5691, Atomic Energy of Canada Limited, October 1976.
2. Rodgers, D. K., "DHC - Initiation in Zr - 2.5% Nb Alloys", Seminar given at the University of Ottawa on March 27, 1992.
3. Personal Communication with D.K. Rodgers, Atomic Energy of Canada Limited, Chalk River, Ontario, May 1992.
4. Lugg, M. C., "Data Interpretation in ACPD Crack Inspection," *NDT International*: Volume 22, Number 3, June 1989, pp. 149-154.
5. Personal Communication with M.C. Lugg, Technical Software Consultants Limited, Milton Keynes, U.K., January 7, 1993.
6. Donald, J. K., Ruschau, J., "Direct Current Potential Difference Fatigue Crack Measurement Techniques," *Fatigue Crack Measurement: Techniques and Applications*, K. J. Marsh, R. A. Smith, R. O. Smith, eds., Engineering Materials Advisory Service Limited, London, 1991, pp. 11-38.
7. "MDT Model M100 Data Acquisition System Operating Manual", MDT Engineering Limited, 1990.
8. Costanza, V., Mohaupt, U. H., "A Local Field Potential Drop Crack Measurement System for Sizing and Characterizing Cracks," *Abstracts and Summaries of Canadian Fracture Conference 21*, J. R. Mathews ed., Defence Research Establishment Atlantic, Halifax, Nova Scotia, April 1990, pp 350-367.
9. Frise, P. R., "Fatigue Crack Growth and Coalescence in a Notch Region," Ph.D. Thesis, Carleton University 1990, pp. 42-55.
10. Dover, W. D., Charlesworth, F. D. W., Taylor, K. A., Collins, R. and Michael, D. H., "The Use of AC Field Measurements to Determine the Shape and Size of a Crack in Metal", *Eddy Current Characterization of Materials and Structures*, ASTM STP 722, 1981, pp. 401-427.



$$a = \frac{\delta}{2} \left(\frac{V}{V_{ref}} - 1 \right)$$

Figure 1 Schematic of the ACPD method of crack measurement showing the 1-D equation for relating potential drops and crack depth.



Sec. A-A

Figure 2 Test specimen geometry including a section view showing the simulated cracks.

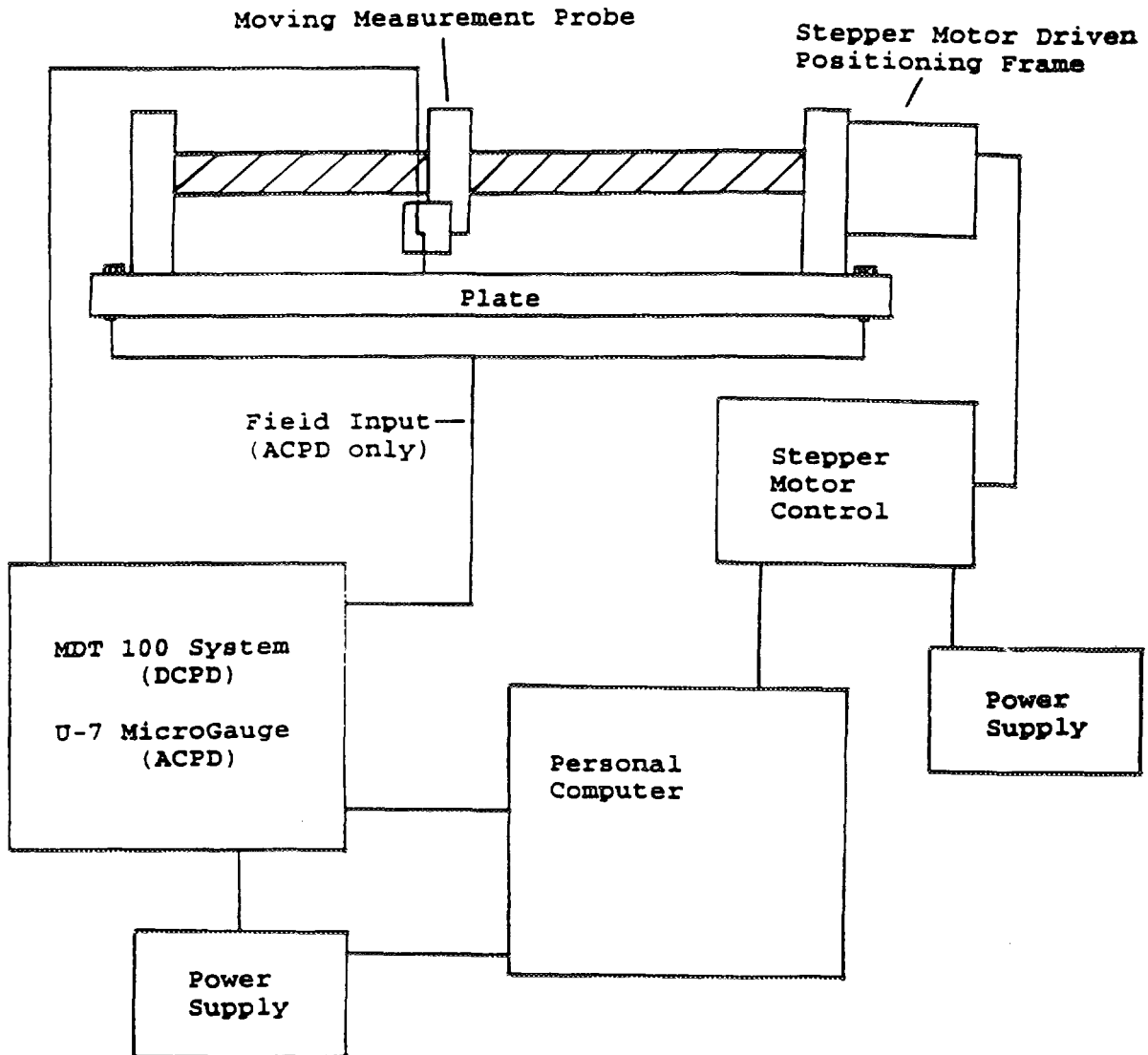


Figure 3 Typical equipment configuration for ACPD and DCPD crack measurement.

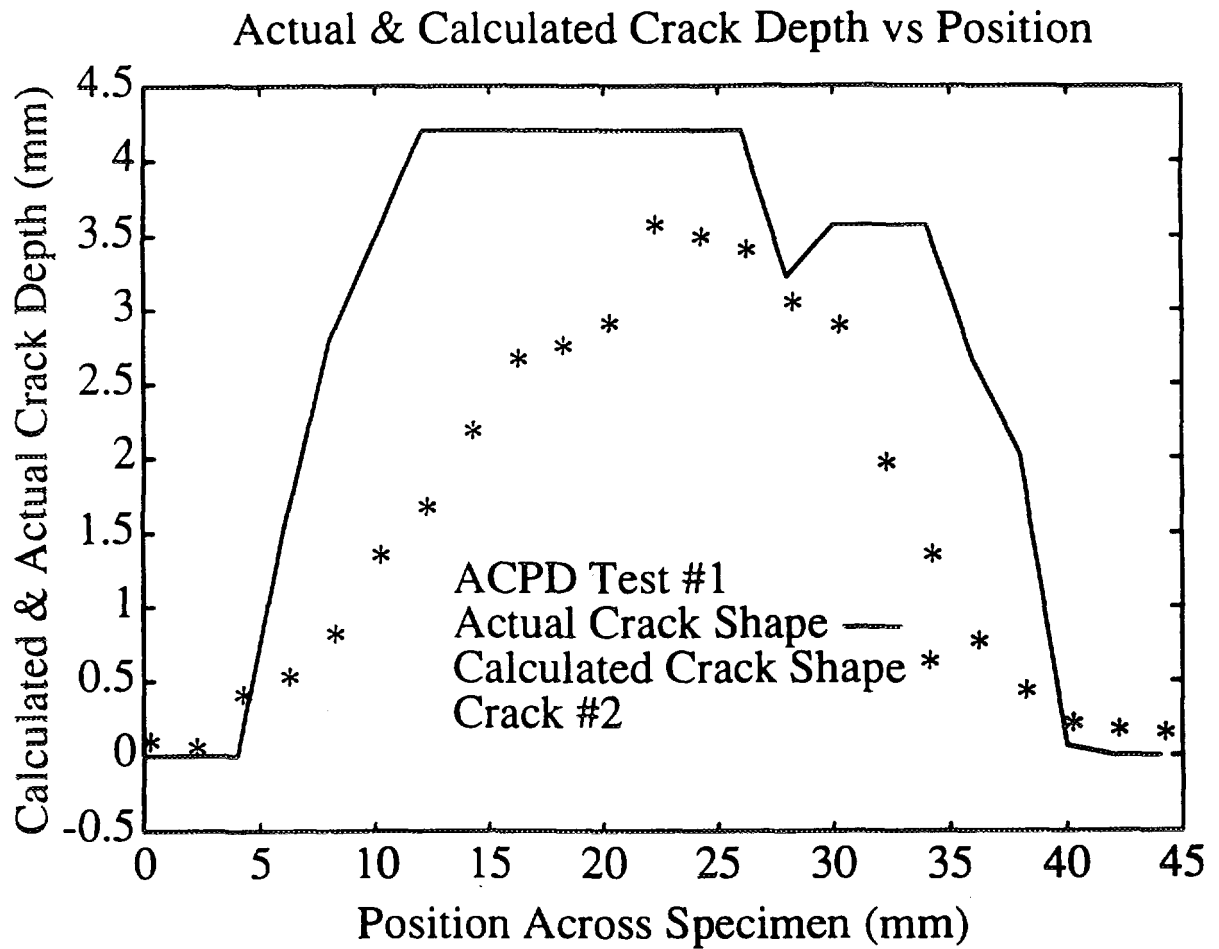


Figure 4 Experimental and actual crack depth from ACPD measurements - test #1. Note the poor agreement between the actual and calculated depths demonstrating the unsatisfactory performance of the ACPD equipment with the pressure tube material.

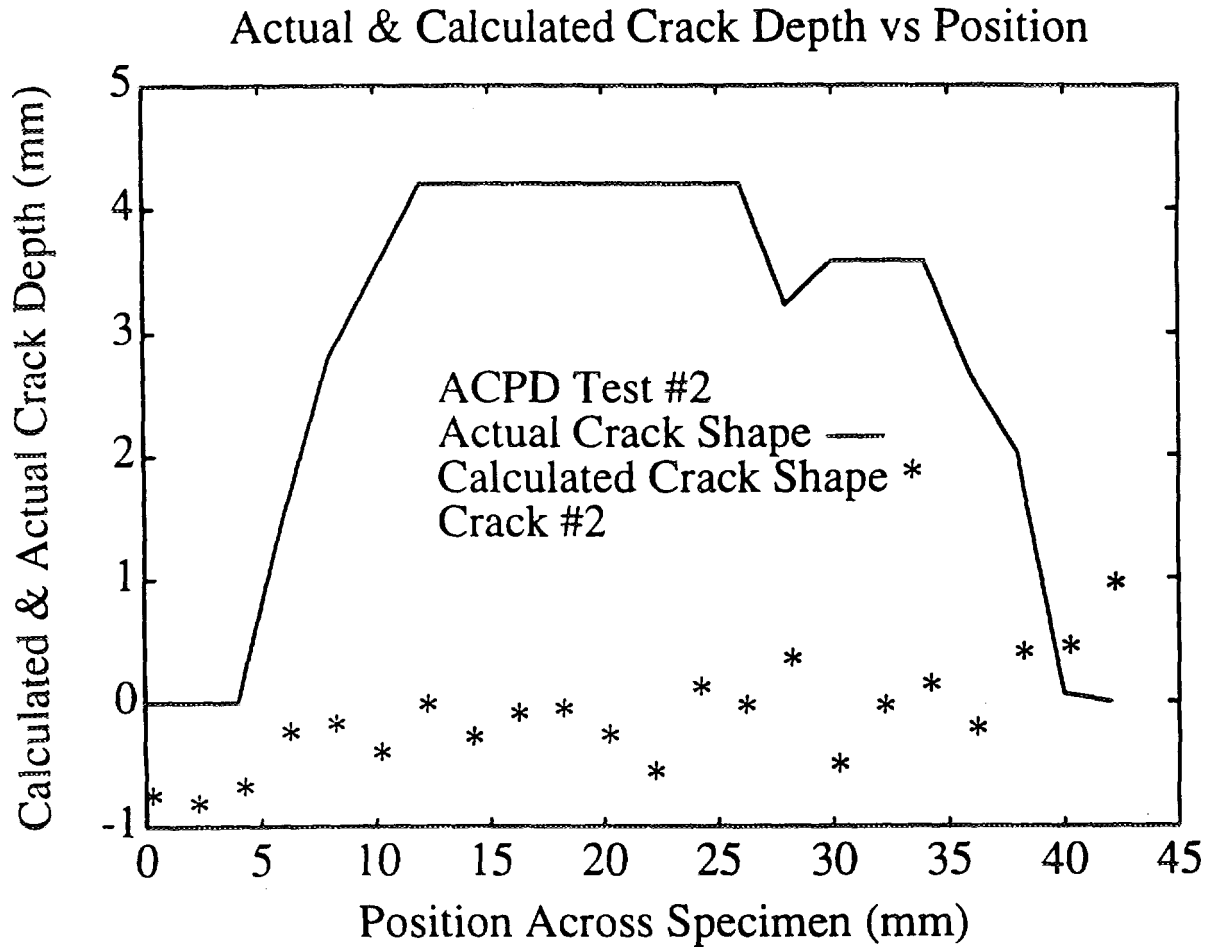


Figure 5 Experimental and actual crack depth from ACPD measurements test #2.

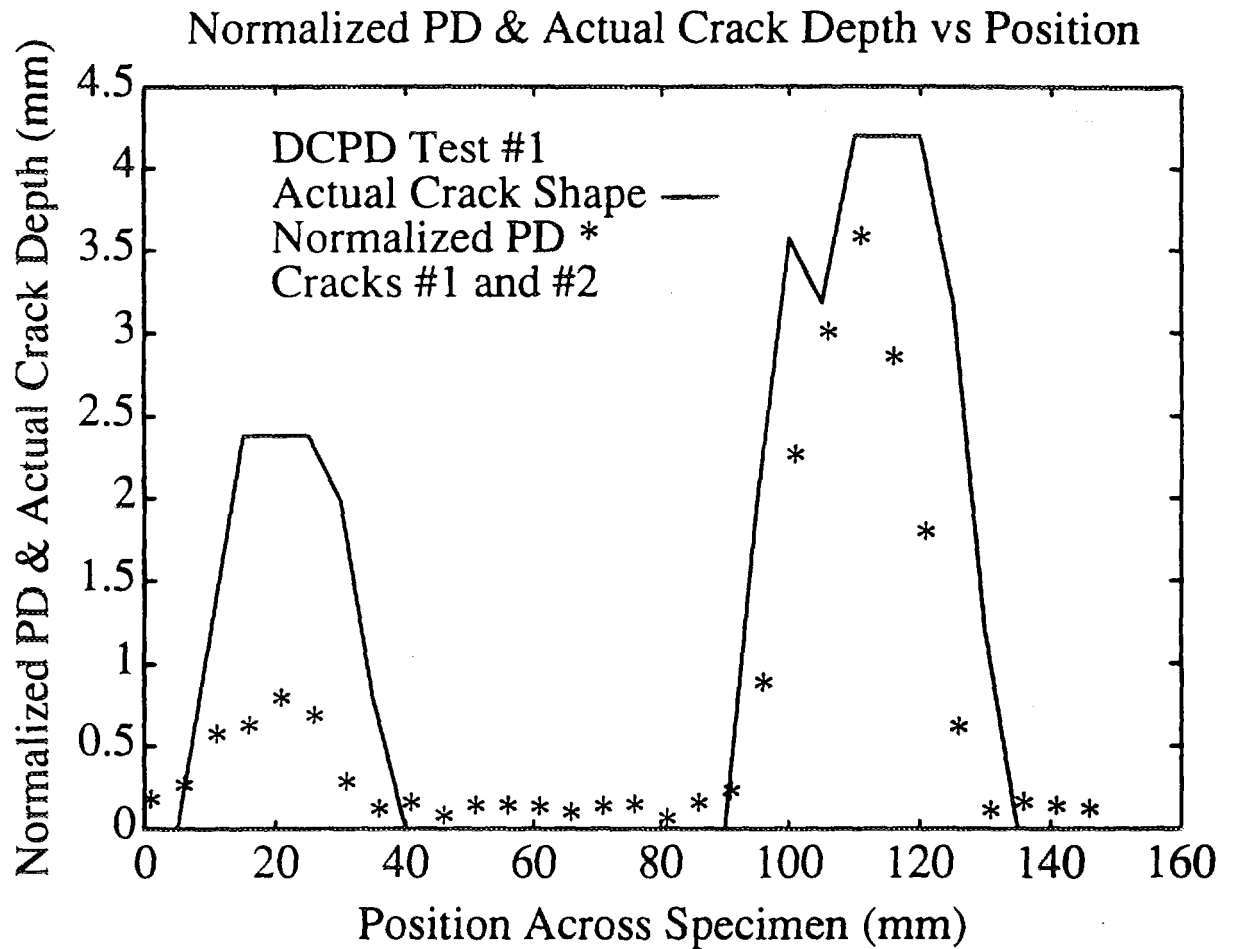


Figure 6

Experimental and actual crack depth from DCPD measurements - room temperature test #1. Note the good agreement between the actual crack depths and the normalized potential drop data including the good indication of the surface breaking points of the cracks. It should be noted that the normalized PD data must be calibrated with a measured sawcut to provide true crack depths.

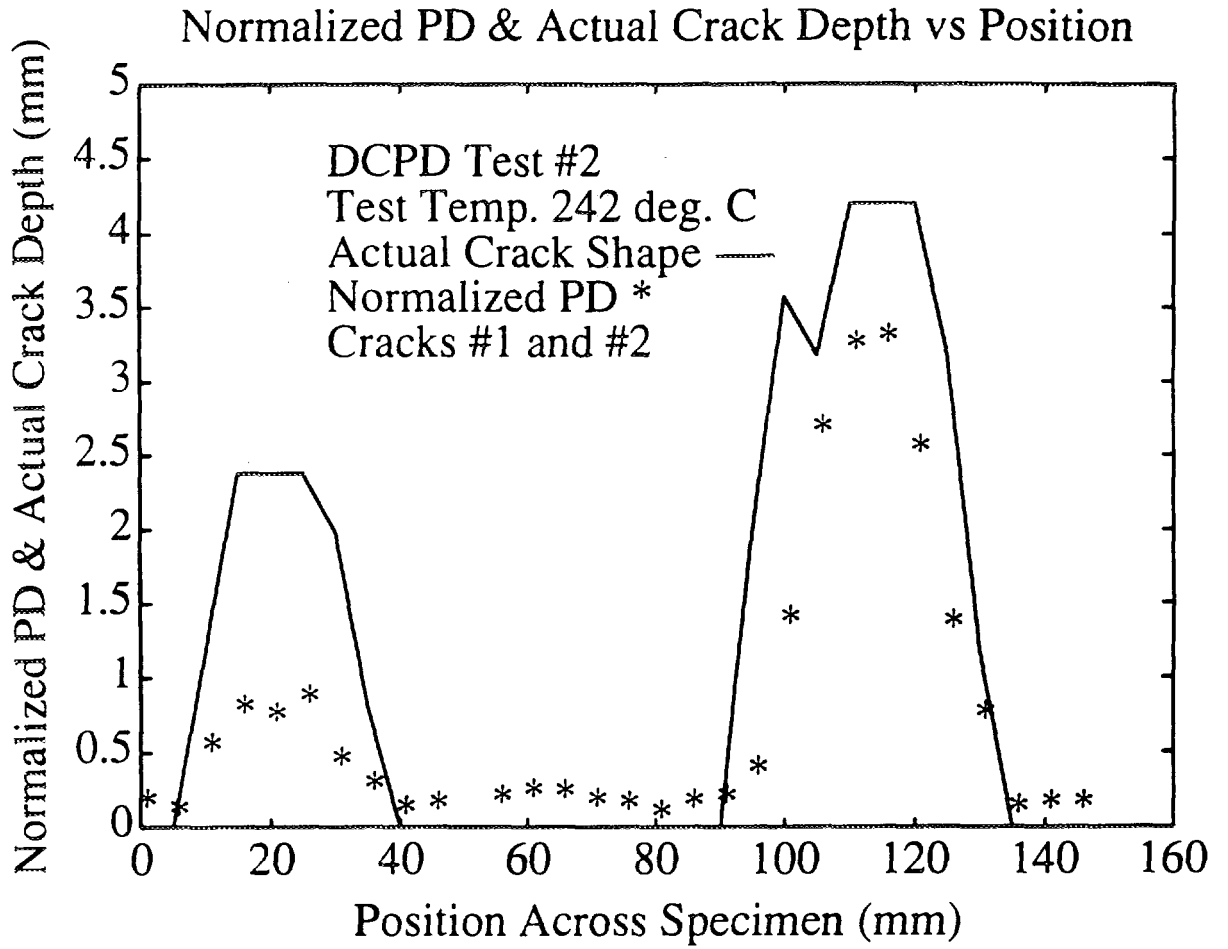


Figure 7 Experimental and actual crack depth from DCPD measurements - elevated temperature test at 242°C. Even at the elevated test temperature the DCPD equipment is capable of measuring the simulated cracks. Calibrated rather than normalized PD data would provide a true crack depths.

(Samedi 3 avril 8:30 → 10:10)
(Saturday April 3rd 8:30 → 10:10)

SESSION 3A

GESTION DES DÉCHETS & NEUTRONIQUE / WASTE MANAGEMENT & NEUTRONICS

Président / Chairman: Dr. M. Beaudet, Hydro Québec

Salle / Room: C-632

- G.F. Naterer University of Waterloo
Species Redistribution During Solidification of Nuclear Fuel Waste Metal Castings
- B. Arsenault I.G.E., École Polytechnique
Calculation of the Negative Reactivity Inserted by Shutdown System Number Two (SDS2) of
a CANDU Reactor
- J. Whitlock McMaster University
Dependence of Calculated Void Reactivity on Film Boiling Representation in a CANDU Lattice

SPECIES REDISTRIBUTION DURING SOLIDIFICATION OF NUCLEAR FUEL WASTE METAL CASTINGS

G.F. Naterer¹ and G.E. Schneider²

University of Waterloo
Waterloo, Ontario, Canada



CA9700544

Nomenclature

c	specific heat [kJ/kgK]
C	solute mean composition
D	mass diffusivity [m ² /s]
e	mixture internal energy [kJ/kg]
f	mass fraction
Fo	Fourier modulus [$\frac{at}{L^2}$]
h	mixture enthalpy [kJ/kg]
J	species diffusive flow [kg]
k	thermal conductivity [W/mK]
L	latent heat of fusion [kJ/kg]
S	control surface, or source term
Ste	Stefan number [$\frac{c_s \Delta T_r}{L}$]
t	time [s]
T	temperature [K]
x	cartesian coordinate
X	reference length [m]

Greek

α	thermal diffusivity [m ² /s]
ρ	mixture density [kg/m ³]

Subscripts

E	eutectic
i	initial
k	phase k
L, S	liquid, solid
liq, sol	liquidus, solidus
M	melt
r	reference value, or relative
w	wall

Superscripts

o	previous time level
.	dimensionless
-	spatial average

Abstract

An enthalpy-based finite element model and a binary system species redistribution model are developed and applied to problems associated with solidification of nuclear fuel

waste metal castings. Minimal casting defects such as inhomogeneous solute segregation and cracks are required to prevent container corrosion and radionuclide release. The control-volume-based model accounts for equilibrium solidification for low cooling rates and negligible solid state diffusion for high cooling rates as well as intermediate conditions. Test problems involving nuclear fuel waste castings are investigated and correct limiting cases of species redistribution are observed.

Introduction

The disposal of fuel recycle waste from nuclear power systems requires an effective isolation of the fuel waste from the biosphere by natural and engineering barriers. In the container method, fuel bundles are cast within low-melting-point metallic alloy containers [1] (Figs.1-2). The containers are then placed in rock vaults below the surface of the earth at a depth of approximately 1000m. The casting must be corrosion resistant and have minimal cracks to provide an effective barrier to radionuclide release. Otherwise, groundwater can collect and promote corrosion and interconnected container cracks can provide direct paths for radionuclide release. Therefore, binary alloy properties such as chemical inhomogeneities, which directly affect the container corrosion performance, are important factors for effective nuclear fuel disposal.

The mechanical and corrosion properties of alloy castings depend on the degree of species segregation in the casting. For example, lead-antimony alloys with less than 0.5 wt % antimony are susceptible to preferential interdendritic corrosion; for higher antimony concentrations, the corrosion distribution becomes uniform [1]. For binary alloys, the species transport during solid-liquid phase change is

¹Research Assistant, University of Waterloo.
Copyright ©1993 by G.F. Naterer.

²Professor of Mechanical Engineering.

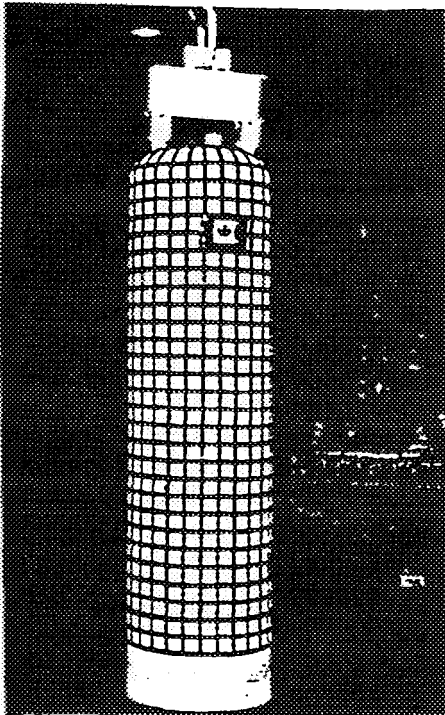


Figure 1: Prototype nuclear waste container

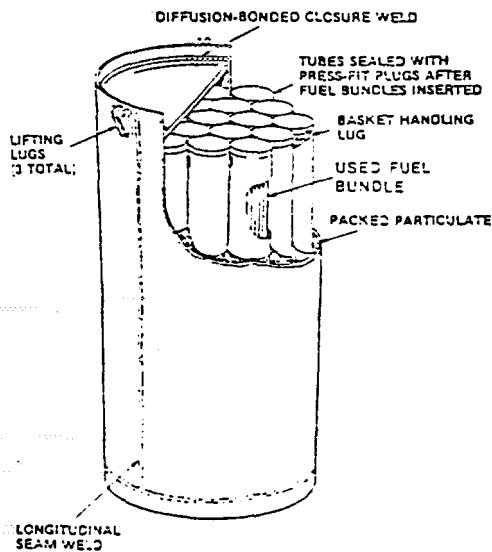


Figure 2: Fuel bundle container design

coupled to the energy transport at the phase interface. During the initial stages of binary alloy solidification, the solid concentration is less than the original mean solute composition. The balance of the solute from that original concentration remains in the liquid. This species transfer due to the phase transformation is often referred to as solute 'rejection' at the phase interface. Differences in solubilities of constituents within each phase lead to the solute rejection at the solid-liquid interface.

The nature of the species redistribution during solidification affects the final casting composition. Assuming solidification is slow enough to allow extensive solid species diffusion, the solid and liquid will be homogeneous with compositions in accordance with the phase equilibrium diagram. This solidification is possible if $X^2 \ll D, t$, where X represents a reference length in the solid portion of the physical domain [2].

However, if the rate of cooling is too rapid to allow mass diffusion in the solid phase during solidification, then the solute composition in the solid will be different than the corresponding solidus value. At any stage during solidification, local equilibrium at the phase interface exists, but since there is negligible mass diffusion, the separate layers of solid retain their original compositions. As a result, the mean composition of the solid remains less than the solid composition at the phase interface. Assumptions regarding the extent of species diffusion in the solid phase may have significant influence on the solidification characteristics, such as the final casting species segregation and the transient variations of the melt region thickness [3].

In practice, binary solid-liquid phase change will usually possess features of both of the above cases. Thermodynamic equilibrium is often not achieved globally throughout the system, but solute transport in the solid phase occurs through substitutional or interstitial

diffusion. The non-equilibrium computational model of Clyne [4] accounts for solid species diffusion but not conservation of solute, and its applicability is limited to regions near the Scheil and equilibrium lever rule limits. As a result, latent heat absorption through an incremental decrease in the liquid fraction, and the melt region thickness, are not predicted correctly in regions outside of the Scheil equation limit during solidification.

In this paper, a model which simulates a range of species redistribution conditions during solidification of typical nuclear fuel waste metal castings will be presented. The results from several problems are investigated to evaluate the applicability of the model. It is shown that the species redistribution model allows an accurate description of the solidification process for a range of cooling rates and therefore provides an effective tool for the analysis of casting properties of nuclear fuel waste containers.

Mathematical Model

The continuum equations governing conservation of species and energy during solid-liquid phase transition have been developed for binary systems and diffusion-dominated transport [5]. For binary systems, species conservation equations only need to be considered for one constituent because the sum of constituent mass fractions must add to unity. Neglecting the Soret and Dufour effects [6], and assuming that the phase densities are equal, the equations governing conservation of solute and energy may be expressed as

$$\frac{\partial(\rho C)}{\partial t} = \nabla \cdot (\rho(g, D, \nabla C, + g_l D_l \nabla C_l)) \quad (1)$$

$$\frac{\partial(\rho h)}{\partial t} = \nabla \cdot (k \nabla T) \quad (2)$$

where the phase enthalpy is defined as

$$h_k(C, T) = \int_{T_r}^T c_{r,k}(\zeta) d\zeta + h_{r,k}(C, T) \quad (3)$$

In Eq.(3), $c_{r,k}(T)$ represents the effective specific heat of phase k .

The mixture enthalpy, h , is a non-linear function of solute composition and temperature in the multiphase region. A piecewise linear enthalpy equation of state can be approximated by one equation, where the subscripts $k = 1, 2, 3$ refer to the solid, melt, and liquid phases, respectively, as

$$e^* = e_{r,k}^*(C, T^*) + c_{r,k}^*(C, T^*)[T^* - T_{r,k}^*(C)] \quad (4)$$

and where the subscript r denotes a reference value. These values have been consistently set to

$$\begin{aligned} k = 1: \quad & e_{r,1}^* = 0 \\ & T_{r,1}^* = 0 \text{ (eutectic)} \\ & c_{r,1}^* = \frac{\bar{c}}{c_l} \end{aligned} \quad (5)$$

$$\begin{aligned} k = 2: \quad & e_{r,2}^* = \frac{\bar{c}}{c_l} T_{sol}^* \\ & T_{r,2}^* = T_{sol}^* \\ & c_{r,2}^* = \frac{\bar{c}}{c_l} + \frac{1}{Ste(T_{liq}^* - T_{sol}^*)} \end{aligned} \quad (6)$$

$$\begin{aligned} k = 3: \quad & e_{r,3}^* = \frac{\bar{c}}{c_l} (T_{liq}^* - T_{sol}^*) + \frac{\bar{c}}{c_l} T_{sol}^* + \frac{1}{Ste} \\ & T_{r,3}^* = T_{liq}^* \\ & c_{r,3}^* = 1 \end{aligned} \quad (7)$$

where $\bar{c} = \frac{1}{2}(c_s + c_l)$, and it has been assumed that the differentials of energy and enthalpy are equal.

The above governing differential equations can now be non-dimensionalized by employing the following definitions,

$$D^* = \frac{D}{D_l} \quad (8)$$

$$z^* = \frac{z}{X_r} \quad (9)$$

$$\rho^* = \frac{\rho}{\rho_l} \quad (10)$$

$$T^* = \frac{T - T_w}{T_i - T_w} \quad (11)$$

$$e^* = \frac{e - e_r}{c_l(T_i - T_w)} \quad (12)$$

and the definition of the Fourier modulus, given as

$$Fo \equiv \frac{\alpha t}{X_r^2} \quad (13)$$

where α is the thermal diffusivity. These definitions lead to the following non-dimensional equations for the conservation of species and energy:

$$\frac{\alpha_l}{D_l} \frac{\partial C}{\partial Fo} = \nabla^* \cdot (g_s D_s^* \nabla^* C_s + g_l D_l^* \nabla^* C_l) \quad (14)$$

$$\rho^* \frac{\partial h^*}{\partial Fo} = \nabla^* \cdot k^* \nabla^* T^* \quad (15)$$

Closure of the system of conservation equations requires a supplementary relationship for the liquid fraction in the melt region. Alternative models of the functional form of the liquid fraction will be presented in the following section.

Non-Discrete Phase Transition Models

If the rate of advance of the phase interface is slow compared with the solute diffusion rate in the solid, then the solid and liquid will have uniform compositions in accordance with the phase equilibrium diagram (Fig.3). Assuming local equilibrium, and neglecting solidus and liquidus line curvature, the liquid fraction may be expressed as

$$f_l = \frac{C - C_{s,ol}}{C_{l,liq} - C_{s,ol}} \quad (16)$$

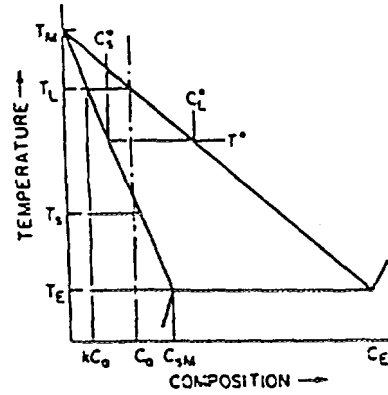


Figure 3: Binary phase equilibrium diagram

This solidification process is possible if $X^2 \ll D_s t$, where X represents a reference length in the solid portion of the physical domain [2]. The numerical models of Naterer and Schneider [7] and Bennon and Incropera [8] employ the equilibrium lever rule [2] to determine the local liquid fraction in the multiphase region. The use of the equilibrium phase diagram in a discrete model [7, 8] would imply an analogous assumption, $\Delta z^2 \ll D_s \Delta t$, where $\Delta t = t^{n+1} - t^n$ and Δz is a characteristic mesh length scale.

In many industrial casting processes, the solidification cooling rates are too high to allow extensive mass diffusion in the solid phase and therefore the solid composition is not uniformly equal to the corresponding solidus value. The computational model of McCay and Hopkins [3] employs the Scheil equation [9], or non-equilibrium lever rule [2], to specify the mean solid composition. Assuming negligible solid species diffusion and complete liquid diffusion, a generalized form of the Scheil

equation [9] may be expressed as

$$f_l = f_{l,r} \left[\frac{\bar{C}_L}{\bar{C}_{L,r}} \right]^{1/(k-1)} \quad (17)$$

Assuming $C_L \approx \bar{C}_L$, and employing the binary phase diagram, Eq.(17) may be written as

$$f_l = f_{l,r} \left[\frac{C(T - T_M)(T_{L,r} - T_M)}{C_r(T_r - T_M)(T_L - T_M)} \right]^{1/(k-1)} \quad (18)$$

The effects of solid state diffusion for a one-dimensional solute redistribution model for regimes between the Scheil and equilibrium cases have been presented by Clyne and Kurz [10]. This analysis allows a more accurate description of the freezing range, species transport and multiphase region characteristics during solidification processes. In order to accommodate multidimensional diffusive flows and remove assumptions for the dendritic microstructure geometry, the following alternative species redistribution model will be considered.

During a time increment Δt the liquid volume portion of the control volume in Fig.4 will decrease due to an elemental solid fraction increase df_s . The integral conservation of solute for the liquid volume, V_L , can be expressed as

$$\int_{V_L} C_L^o dV_L + C_L df_s \Delta V = \int_{V_L} C_L dV_L \quad (19)$$

$$+ C_S df_s \Delta V + \int_S \bar{J} \cdot \bar{dS} \Delta t \quad (20)$$

Assuming diffusion-dominated transport, and dividing Eq.(20) by ΔV , we obtain

$$C_L(1 - k)df_s = [1 - (1 - pk)]d\bar{C}_L \quad (21)$$

where $p = \frac{D\sigma}{RL_0}$ is a solid diffusion parameter. The constant σ denotes the geometric surface to volume ratio (ie. $\sigma = 6$ for a cubic control volume), L_0 is a volume characteristic length, and R represents the solidification velocity.

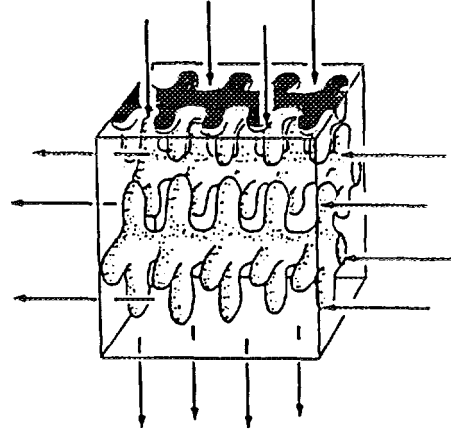


Figure 4: Control volume with phase transition

We observe that for rapid solidification, $p \rightarrow 0$ and Eq.(21) approaches the Scheil model [9]; also, for equilibrium conditions, $p \rightarrow \infty$ and C_S approaches its corresponding solidus value in Eq.(21).

Integrating Eq.(21) and applying the boundary condition $\bar{C}_L(f_s = f_s^o) = \bar{C}_L^o$ we obtain the following species redistribution model,

$$\bar{C}_L = \bar{C}_L^o \left[\frac{\frac{1}{1-pk} - f_s}{\frac{1}{1-pk} - f_s^o} \right]^{\frac{k-1}{1-pk}} \quad (22)$$

Several solid fraction distributions for different solid diffusion parameters are illustrated in Fig.5. The proposed model approaches the equilibrium and Scheil limiting cases for high and low diffusion parameters, respectively. In order to conserve solute ($C = 0.01$) during the non-equilibrium solidification process, the solid composition must decrease with f_L (or C_L must increase with f_s) as shown in Fig.5. In other words, as the solidification proceeds,

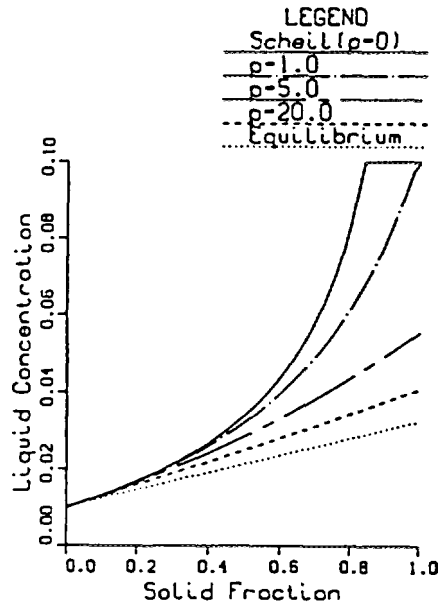


Figure 5: Species redistribution models

the mean solid composition is less than the equilibrium composition because the separate solid layers retain their original compositions. For equilibrium conditions, the liquid retains its equilibrium composition along the liquidus line throughout the solidification process. The results in Fig.5 illustrate the species redistribution for intermediate conditions between the above two limiting cases.

Numerical Solution Methodology

The two-dimensional equations governing the conservation of species and energy, Eqs.(1)-(2), were solved with a control-volume-based finite element model [7]. Since each of the governing equations is valid throughout the problem domain, interface tracking and coordinate transformations were not required.

The phase change non-linearity appears in the discrete model as a non-linear equation

state and the solution dependence of the Ste number appears through this equation of state. The implicit interaction between the phase transition and the thermal and solute concentration fields is specified through an orderly progression of phase interface movement determined by the physics of the energy and species transport. A direct solution method is used to solve the resulting algebraic equation system.

The numerical model provides a phase iteration procedure which couples the temperature and solute concentration fields in the melt region and may execute the phase transition on structured or unstructured grids. The model also permits the prediction of single and binary constituent phase change processes and the application to high and low Ste number problems.

Applications to Solidification Processes

Calculations were performed for the solidification of Pb-Sb cylindrical shell containers. Low-melting-point metals such as lead and its alloys are often used for nuclear fuel waste matrix castings because of their corrosion performance, availability and mechanical properties. Test problems involving container hardening and pure lead melting are presented for preliminary validation of the model. A description of equilibrium data for lead-antimony systems is presented in Table 1.

The first example problem involves species diffusion from the Dirichlet-specified left boundary. The source of the diffusing solute is typically a gas phase whose partial pressure is held constant in metal surface hardening applications. The results of Fig.6 indicate that the early stages of the transient mass diffusion are essentially described by the closed-form analytic error function solution [11].

Description	Symbol	Dimension	Pb-Sb System
Equilibrium partition ratio	k	-	0.35
Solidification contraction	δ	-	0.03
Maximum solubility of primary α phase	$C_{\alpha}^0(\max)$	wt%	3.45
Eutectic solute concentration	C_E	wt%	11.1
Eutectic temperature	T_E	$^{\circ}\text{C}$	252

Table 1: Problem data

An example of a pure material melting problem with $Ste = 1$ and Dirichlet boundary conditions, is illustrated in Fig.7. Comparison of the results with the analytic solution [11] indicates an accurate transient evolution of the phase front and diffusion within the single phase regions. At large values of the Fourier modulus, the solution approaches its pure diffusion character as most of the domain melts.

The effects of species redistribution during solid-liquid phase change on the Pb-Sb composition and corrosion performance will now be considered. In the following problems, statically cast cylindrical containers are cooled from the outer boundaries and the energy transport, species transport and phase front propagation are observed during the solidification process.

Initial distributions of antimony composition and temperature were $C(x^*, 0) = 0.0345$ and $T^*(x^*, 0) = 1.0$, respectively. Neumann zero transport boundary conditions were specified in all cases, except for the outer boundary for the energy conservation equation, where

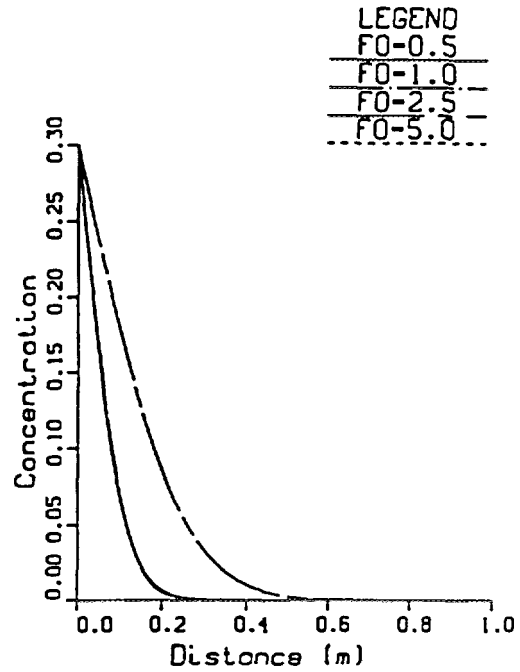


Figure 6: Single phase species diffusion

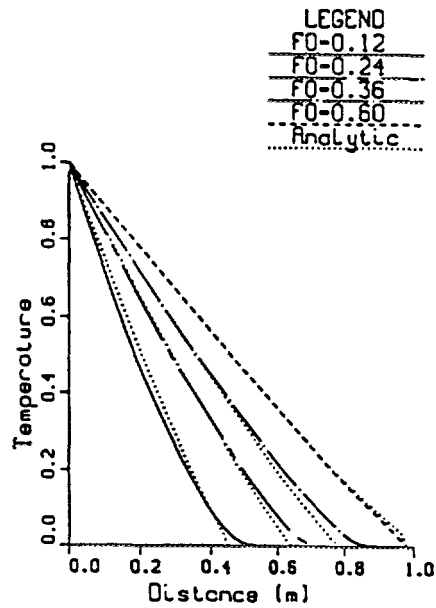


Figure 7: Pure material phase change

$T^*(1, Fo) = 0$ was specified.

In Fig.8, the sharp changes in curvature of the temperature profiles provide an indication of the phase front movement. As solidification proceeds, species redistribution at the phase interface leads to antimony enrichment ahead of the interface (Fig.9). The nature and transient evolution of the phase interface is illustrated in Fig.10. In Figs.11-12, movement of the liquidus and solidus fronts are illustrated by discontinuities in the solid and liquid concentration profiles, respectively.

The mean solid composition near the outer casting layers is an important factor for corrosion assessment. For the previous phase change simulation, equilibrium conditions were assumed and the outer mean solid composition was 0.14 wt% antimony. This indicates a susceptibility to preferential intergranular corrosion [1]. This may lead to crevice corrosion or stress corrosion cracking over hundreds of years. Since corrosion of the container must penetrate the metal matrices before the aqueous fluid reaches the fuel elements, the species segregation of the inner container layer will also affect the total time of penetration.

In the final two figures, the sensitivity of the species redistribution model on the Pb-Sb solidification is examined. The multiphase region characteristics with non-equilibrium conditions at the interface [9] are illustrated in Fig.12. For this solidification problem, the mean solid composition of the outer container layer was 0.11 wt% antimony. This suggests that zero species diffusion at the phase interface leads to a lower mean solid composition because the separate solid layers have not had sufficient time to diffuse up to their equilibrium solidus value. However, application of Eq.(22) for species redistribution at the phase interface takes into account limited solid state diffusion (Fig.13). In this case, the solid composition of the outer layer is 0.12 wt% anti-

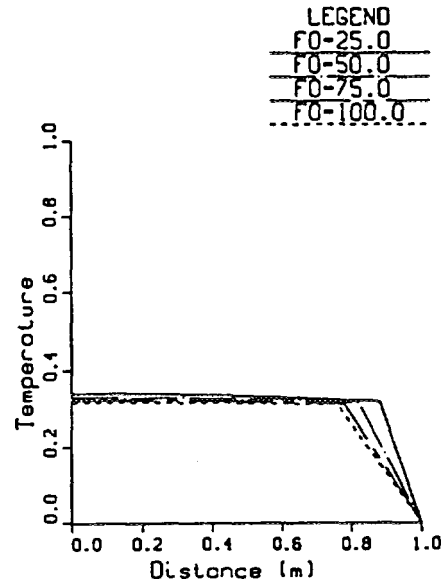


Figure 8: Pb-Sb solidification (Ste=0.001)

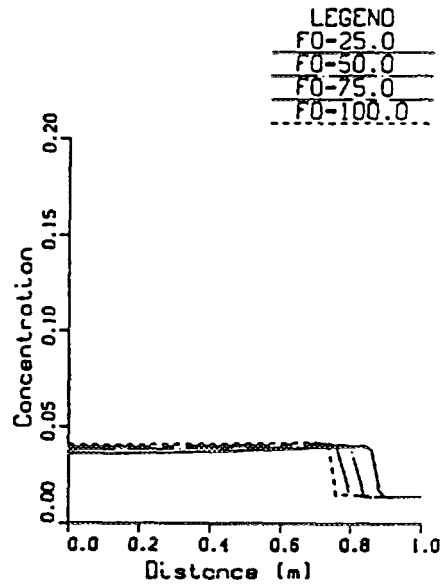


Figure 9: Pb-Sb solidification (Ste=0.001)

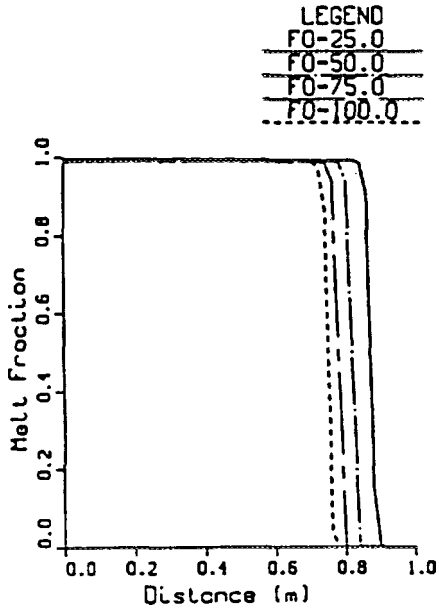


Figure 10: Pb-Sb solidification (Ste=0.001)

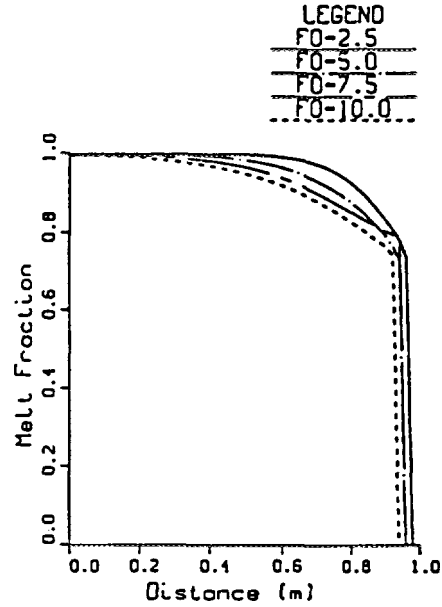


Figure 12: Melt fraction field (Scheil model)

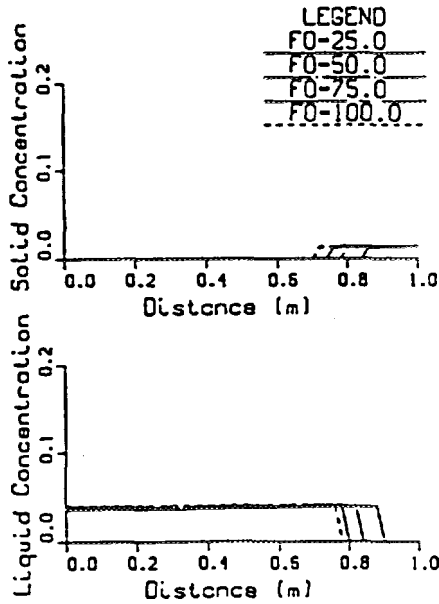


Figure 11: Pb-Sb solidification (Ste=0.001)

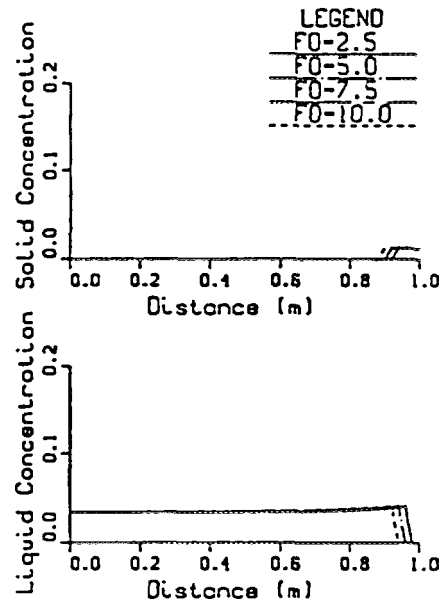


Figure 13: NS model

mony for $p = 9.0$. For early stages of the outer layer solidification, this value agrees well with available one-dimensional analytic results [2].

Conclusions

A transient control-volume-based finite element method has been developed and applied to the simulation of statically cast nuclear fuel waste Pb-Sb containers. Preliminary investigation of the model indicates an accurate agreement with available analytic solutions of solidification and mass diffusion problems. The species redistribution model accounts for limited solid state diffusion at the phase interface and describes conditions between the Scheil and equilibrium limiting cases. It is concluded that the effects of molecular diffusion on the solute concentration and liquid fraction fields are significant in terms of the corrosion performance of the casting.

Acknowledgements

The authors thank the Natural Sciences and Engineering Research Council of Canada for the financial support of this work.

References

1. Mathew, P.M., "Casting Properties of Metal Matrices for Nuclear Fuel Waste Disposal", Technical Record TR-371, AECL Research Company, 1986.
2. Flemings, M.C., Solidification Processing, McGraw-Hill Inc., 1974.
3. McCay, T., McCay, M., Hopkins, J.A., "Thermal and Solutal Conditions at the Tips of a Directional Dendritic Growth Front", AIAA Paper 91-1333, 1991.
4. Clyne, T.W., "Numerical Modelling of Directional Solidification of Metallic Alloys", *Metal Science*, vol.16, pp.441-450, 1982.
5. Schneider, G.E., "A Computational Model for the Analysis of Diffusive Binary Alloy Solid/Liquid Phase Change Energy Transport", AIAA Paper 91-1331, Report, University of Waterloo, Waterloo, Ontario, 1991.
6. Alexiades, V., Wilson, D., Solomon, A., "Macroscopic Global Modeling of Binary Alloy Solidification Processes", *Quarterly Journal of Applied Mathematics*, vol.43, no.2, pp.143-158, 1985.
7. Naterer, G.F., Schneider, G.E., "Enthalpy-Based Finite Element Model of Binary Alloy Solid-Liquid Phase Change", AIAA Paper 93-0277, AIAA 31st Aerospace Sciences Conference, 1993.
8. Bennon, W., Incropera, F., "Numerical Analysis of Binary Solid-Liquid Phase Change Using a Continuum Model", *Numerical Heat Transfer*, vol.13, pp.277-296, 1988.
9. Scheil, E., *Z. Metallk.*, vol.34, pp.70, 1942.
10. Clyne, T.W., Kurz, W., "Solute Redistribution During Solidification with Solid State Diffusion", *Metallurgical Transactions A*, vol.12A, pp.965-971, 1981.
11. Carslaw, H., Jaeger, J., Conduction of Heat in Solids, Oxford University Press, Oxford, 1959.



Calculation of the Negative Reactivity Inserted by the Shutdown System Number Two (SDS2) of a CANDU Reactor

B. Arsenault

Faculty Advisors : Robert Roy and Jean Koclas

Groupe d'Analyse Nucléaire, Institut de Génie Énergétique

École Polytechnique de Montréal, Montréal, Québec, Canada H3C 3A7

1. Introduction

The secondary shutdown system (SDS2) of a CANDU reactor consists of liquid poison injection through nozzles disposed horizontally across the core. The nominal poison concentration ($GD(NO_3)_2$) is 8000 ppm.

With the tools available to the nuclear industry for calculating the reactivity inserted by the SDS2, some approximations are needed and a simplified model of poison propagation has to be used in order to calculate the differential cross sections. The objective of this paper is to evaluate the errors introduced by the approximations in the supercell calculations and core calculations.

2. Analysis Method

Figure 1 illustrates procedure for this analysis. One of the most important steps in this analysis is to accurately represent the shape of the poison propagation in order to be able to calculate the condensed and homogenized cross sections of the supercells needed for the diffusion calculations used to model the entire reactor core.

3. Approximations

The nuclear industry uses MULTICELL¹ to calculate the differential cross sections for different shapes of poison propagation. MULTICELL solves the diffusion equation in a supercell, but the diffusion approximation is not applicable in strong absorbers due to the strong variation of the neutrons speed with the angular distribution. Boundary conditions applicable to strong absorbers are supplied by the use of the KUSHNERIUK² equations that give current to flux ratios (CFR).

The following approximations are used in MULTICELL :

- CFR values are taken from KUSHNERIUK equations.
- Constant fast flux approximation.
- Each supercell material is represented in a Cartesian geometry.

3.1 KUSHNERIUK Equations

The KUSHNERIUK equations give the extrapolation length of the thermal neutron group for a cylindrical absorber of effective infinite length, invariant under a translation and rotation about its axis and surrounded by a large volume of a predominantly scattering medium. These equations are applicable to non-regenerative absorbers which implies that neutrons which are produced do not belong to the velocity group in which they are absorbed. The KUSHNERIUK equations are:

$$\lambda = \Sigma_{tr} \left[\frac{4}{3\beta} - g(a\Sigma_{tr}) \right] \quad (1)$$

$$\beta = \frac{(1-c)P_1\left(\frac{a}{l}\right)}{1-cP_c(\nu)} \quad (2)$$

$$g(a\Sigma_{tr}) = a\Sigma_{tr} \left[\frac{0.623}{a\Sigma_{tr} + 0.50025002} + \frac{0.360013}{(a\Sigma_{tr} + 0.9005002)^{15}} \right] \quad (3)$$

$$P_1(a/l) = \frac{4a}{l} \int_1^\infty \frac{dy}{y^2} K_1\left(\frac{ay}{l}\right) I_1\left(\frac{ay}{l}\right) \quad (4)$$

$$P_{es}(\nu) = \frac{a\nu}{l} \int_1^\infty \frac{dy}{y(\nu^2 - y^2)} K_1\left(\frac{ay}{l}\right) \left[\nu I_0\left(\frac{ay}{l}\right) - \frac{y I_0\left(\frac{a\nu}{l}\right) I_1\left(\frac{ay}{l}\right)}{I_1\left(\frac{a\nu}{l}\right)} \right] \quad (5)$$

$$P_c(\nu) = 1 - P_{es}(\nu) \quad (6)$$

$$c = \frac{\Sigma_{1 \rightarrow 2}}{\Sigma_t} \quad (7)$$

$$\nu = \sqrt{3(1-c)} \quad (8)$$

λ	Extrapolation length in the cylinder(cm).
Σ_{tr}	Transport cross section of the scattering medium(cm^{-1}).
β	Blackness of the cylinder.
g	Characteristic function of the cylinder.
a	Cylinder radius(cm).

l	Diffusion length in the cylinder(cm).
$\Sigma_{1 \rightarrow 2}$	Cylinder moderation cross section(cm^{-1}) .
Σ_t	Cylinder total moderation cross section(cm^{-1}).
Σ_{tr}	Scattering medium transport cross section(cm^{-1}).
$p_1(a/l)$	Inward collision probability for a source distributed as $2 \cos(\theta)$ at the cylinder surface.
$P_{cs}(\nu)$	Collision escape probability for an isotropic source distributed according to the solution of the diffusion differential equation in the cylinder medium, i.e. the source distribution is proportional to $I_0(r\nu/l)$.
K_1, I_0, I_1	Bessel functions

By substituting the linear extrapolation length equation

$$\phi(a) + \lambda \vec{\nabla} \phi \cdot \eta |_{a=0} = 0 \quad (9)$$

into Equation (1) we get the CFR2 value for the thermal group as seen by the cylinder:

$$CFR2 = -\frac{J_{net}(a)}{\phi(a)} = -\frac{1}{\frac{4}{\beta} - 3g(a\Sigma_{tr})} \quad (10)$$

Equation (1) is valid only for a non-regenerative cylinder. The fraction of the neutrons that are produced by thermalization and are absorbed has to be given. This probability is³ :

$$P_{abs} = \frac{(1-c)P_c\nu}{1-cP_c(\nu)} \quad (11)$$

3.2 Fast Group Boundary Condition

An equation for the boundary condition of the fast group has to be developed remembering that the fast flux is imposed constant in MULTICELL. The conservation equation in a steady state can be integrated in the fuel⁴ to get the following relation :

$$\begin{aligned} \int_{fuel} \vec{\nabla} \cdot \vec{J}(\tau, E) dv &= \int_{fuel} -\Sigma(\tau, E)\phi(\tau, E) dv \\ &+ \int_{fuel} \left[\int_0^\infty dE' \Sigma_s(\tau, E' \rightarrow E)\phi(\tau, E') \right] dv \\ &+ \int_{fuel} \left[\chi_p(E) \int_0^\infty dE' \nu_p(E')\Sigma_f(\tau, E')\phi(\tau, E') \right] dv \\ &+ \int_{fuel} S_d(\tau, E) dv + \int_{fuel} s(\tau, E) dv \end{aligned} \quad (12)$$

The fast flux approximation means that the fast neutrons produced in a supercell originate from the neighbouring supercells. The last three terms of Equation (12) are then equal to zero. Also, upscattering is supposed to be negligible. Equation (12) can be simplified in the following way.

$$\left[\frac{J_{out} - J_{in}}{\phi_s} \right] = CFR1 = [\Sigma_{a1} + \Sigma_{1 \rightarrow 2}] \frac{a}{2} \quad (13)$$

4. Supercell Calculation With DRAGON

The MULTICELL code calculates the homogenized cross sections of a complete supercell from the two condensed group cross sections for each material and the CFR values of the black bodies. In order to assess the validity of the results obtained by MULTICELL, another code which can simulate the three approximations has to be used. The chosen code is DRAGON⁵. This code uses collision probabilities and can perform calculations on lattice cells and supercells. The characteristics of this code are :

- 69 group microscopic cross sections library
- Self-shielding calculations
- Multi-group neutron transport calculation
- Editing and calculation of nuclear properties
- Calculation of isotopic evolution equations

The 3D modelling of a reactivity mechanism in DRAGON involves a rectangular domain which will be divided into L homogeneous zones of volume V_i , with its external boundary divided into Λ external surfaces S_α (Greek symbols are used to identify surface-related quantities). These zones are combination of cylindrical and rectangular regions, preserving the global cylindrical geometry for the fuel cells and the adjusters.

First-flight collision probabilities (CP) are then computed independently using the total transport-corrected cross section in each energy group. The one-group first-flight CP matrix Q can be written in a symmetrized form:

$$Q = \frac{\Lambda}{L} \begin{pmatrix} T_{\alpha\beta} & E_{\alpha j} \\ E_{i\beta} & C_{ij} \end{pmatrix} = \begin{bmatrix} T & E^t \\ E & C \end{bmatrix}$$

with the following definitions using the reduced collision, escape and transmission probabilities⁶:

$$C_{ij} = V_i p_{ij} = V_j p_{ji} = \frac{1}{4\pi} \int_{4\pi} d^2\Omega \int_{\perp_{\vec{\Omega}}} d^2r' \int dt \int dt' \chi_{V_i}(t) \chi_{V_j}(t') \exp(-\tau(t', t)) \quad (14)$$

$$E_{i\beta} = V_i P_{i\beta} = \frac{S_\beta}{4} P_{\beta i} = \frac{1}{4\pi} \int_{4\pi} d^2\Omega \int_{\perp_{\vec{\Omega}}} d^2r' \int dt \chi_{V_i}(t) \chi_{S_\beta}(t'_-) \exp(-\tau(t'_-, t)) \quad (15)$$

$$T_{\alpha\beta} = \frac{S_\beta}{4} P_{\beta\alpha} = \frac{S_\alpha}{4} P_{\alpha\beta} = \frac{1}{4\pi} \int_{4\pi} d^2\Omega \int_{\perp_{\vec{\Omega}}} d^2r' \chi_{S_\alpha}(t_+) \chi_{S_\beta}(t'_-) \exp(-\tau(t'_-, t_+)) \quad (16)$$

where a tracking line is defined by its tracking orientation given by the angle $\vec{\Omega}$ and a starting point taken in a plane $\perp_{\vec{\Omega}}$, which is perpendicular to the tracking orientation. The optical path τ depends on the local coordinates t' and t of the tracking line; $[t'_-, t_+]$ where t'_- and t_+ corresponds to the starting and ending external surface. In these last formulas, the characteristic function $\chi_D(t)$ is defined by:

$$\chi_D(t) = \begin{cases} 1 & \text{if the local track point } t \text{ is in region (or surface) } D \\ 0 & \text{otherwise.} \end{cases}$$

Currently, DRAGON uses the EQ_N equal-weight quadrature set. This angular quadrature set has two main features: it does not introduce any undesired bias in the supercell and it simplifies the CP evaluation since there will be no angular weighting.

The user of DRAGON specifies two tracking parameters:

- The degree N for the EQ_N quadrature;
- The density of tracks for perpendicular plane scanning.

In 3-D models, this density is in tracks/cm² and it is used in the process of generating tracks in the perpendicular plane $\perp_{\vec{\Omega}}$. After discretization of the angular variable and of the perpendicular planes to each angle using these user-input parameters, the collision, escape and transmission probabilities are computed. These probabilities are properly normalized in order to ensure the conservation of neutrons within the supercell domain⁷. The current components are then coupled and a new CP matrix is formed. Finally, these last group matrices are used in the multigroup flux transport solver of DRAGON⁸. Two main options are available for calculation in the fully reflected supercell:

- K_{eff} computation with or without imposed B^2 value;
- Critical B^2 computation assuming $K_{eff} = 1$ using an homogeneous B_0 or B_1 model for leakage coefficients.

The 3-D geometries that can be actually processed in the *EXCELL* module include cylinders that can be located in any directions, but no clusters are available for the moment in these cylinders.

5. MULTICELL/EXCELL Comparison

The representation of a CANDU fuel bundle is given to DRAGON to get the properties of each cell material. The cross sections obtained from the lattice calculation are introduced into supercell calculations, condensed in two groups and homogenized for each material. The EXCELL module is then used to check the approximations of the diffusion code MULTICELL.

The first effect to be checked is the use of a Cartesian geometry in a supercell instead of a cylindrical geometry. When the grey and black bodies are represented in a Cartesian geometry, it is important that the Cartesian representation has the same surface area as in the cylindrical representation. By doing this, we assume that the CFR values found in a cylindrical geometry are still valid in the Cartesian geometry for MULTICELL. When the volume of a material is changed, the cross sections have to be adjusted to maintain constant reaction rates. The results of the comparison from a Cartesian with a cylindrical geometry are not reproduced in this paper but showed a difference of less than .01 %.

The next effects to be checked are the fast flux approximation and the KUSHNERIUK equations. The main idea is to get the CFR and P_{abs} values from the cross sections calculated with EXCELL when a flat fast flux is simulated and when a two-group calculation is imposed. MULTICELL uses each set of values to calculate the homogenized cross sections and the results are compared with the output generated by EXCELL with a two-group calculation and a fast flux approximation. Table 1 gives the results of the comparisons and it shows that the best results are obtained when the KUSHNERIUK equations for the grey and black bodies are calculated with the cross sections taken from a simulation of the flat fast flux in the collision probabilities code.

6. Simulation of Poison Propagation

Now that the best way to calculate the input values for MULTICELL is known, the supercell poison configurations have to be determined. Representation of poison propagation is very complex. The code CURTAIN from Ontario-Hydro is used to simulate the poison propagation. This code simulates the poison propagation by four paralepipeds (poison curtains) along each nozzle. The size of each poison curtain is adjusted in time to make sure the total amount of injected poison is conserved. In this study two data sets similar to CURTAIN outputs are used to simulate the poison injection. Each injection time is chosen in order to get a weak reactivity insertion for the first time and a second injection time corresponding to a strong reactivity insertion. Two problems have to be solved when

using such data to simulate the poison injection :

- Some nozzles inject the poison with a 45 degree angle whereas simulations are only for horizontal and vertical injections.
- Simulation of poison propagation along the nozzle does not take into account the absence of injection holes under the calandria tubes.

The first problem is solved by representing a 45-degree configuration from a right angle configuration changed into a step configuration. The surface of the right angle poison curtain has to be the same as the curtain in the step configuration because poison absorption phenomena are acting at the surface of the poison curtain. Then, a change in the poison curtain surface would have an effect on the supercell absorption rate.

The second problem is solved by representing only the poison curtains between the calandria tubes. An increase in the poison concentration is then needed to conserve the amount of poison injected in the moderator.

In this study, the poison propagation is modeled by eleven supercell configurations. The comparative results obtained on the supercell configurations with MULTICELL and EXCELL are shown in Table 2.

7. Reactor Calculations

The objective of reactor calculation is to get the flux and power of the fuel bundles. The reactor is subdivided axially in 12 planes. Each plane is represented by supercell assemblies representing the fuel bundles. The reactivity insertion of SDS2 is calculated with the reactor code by adding the differential cross sections due to the poison injection, to the unperturbed supercell cross sections. The reactor code used for this study is OPTEX⁹ and the differential cross sections come from MULTICELL and EXCELL. Figures 2 and 3 show respectively the power distributions calculated from cross sections obtained with MULTICELL and EXCELL for a plane including two injection lines with a 45-degree configuration and one injection line with a right angle configuration. Figure 4 shows the difference in percentage of the power distributions obtained from MULTICELL compared to EXCELL.

8. Conclusion

The supercell and reactor calculations obtained from MULTICELL show some differences with EXCELL. The first reason is that the CFR values given in MULTICELL for the fuel and the gadolinium solution are found for an equivalent cylinder of infinite extent. It means that the CFR values for the gadolinium absorber included between the calandria tubes cannot be taken from the KUSHNERIUK equations. The second reason is the fast flux approximation. In EXCELL, the ratio of the maximum to the minimum value of the fast flux is approximately equal to 2.

Extension of this work is now to calculate the reactivity inserted by SDS2 with a better representation of poison injection and a space-time dependence of the flux distribution.

REFERENCES

- 1 A.R.Dastur, J.V.Marczak, F.Piva, J.V.Donnely, "Multicell User's Manual", AECL Report TDAI-208/1, Ontario (1979).
- 2 S.A. Kushneriuk, "Neutron Capture by Long Cylindrical Bodies Surrounded by Predominantly Scattering Media", AECL Report CRT-712, Ontario (1957).
- 3 A.R.Dastur and D.B.Buss, "MULTICELL a 3-D Program Description", AECL Report TDAI-104, Ontario (1983).
- 4 D.Rozon, "Introduction à la cinétique des réacteurs nucléaires", École Polytechnique de Montréal, Québec (1992).
- 5 G.Marleau, A.Hébert, R.Roy, "Guide de l'utilisateur du code DRAGON", Report IGE-71R, École Polytechnique de Montréal, Québec (1991).
- 6 R. Roy, A. Hébert and G. Marleau, "A Transport Method for Treating Three-Dimensional Lattices of Heterogeneous Cells", *Nucl. Sci. Eng.*, **101**, 217-225 (1989).
- 7 R. Roy and G. Marleau, "Normalization Techniques for Collision Probability Matrices," Proceedings of the *International Conference on the Physics of Reactors PHYSOR-90*, pp. IX:40-IX:49, Marseilles, France, April 23 - 27 (1990).
- 8 G. Marleau, R. Roy and A. Hébert, "New Computational Methods Used in the Lattice Code DRAGON", *Proc. Top. Mtg. on Advances in Reactor Physics*, Charleston, SC, March 8-11, 1992.
- 9 M.Beaudet, D.Rozon, J.Tajmouati, "Guide de l'utilisateur du code OPTEx-4", Report IGE-104, École polytechnique de Montréal, Québec (1990).

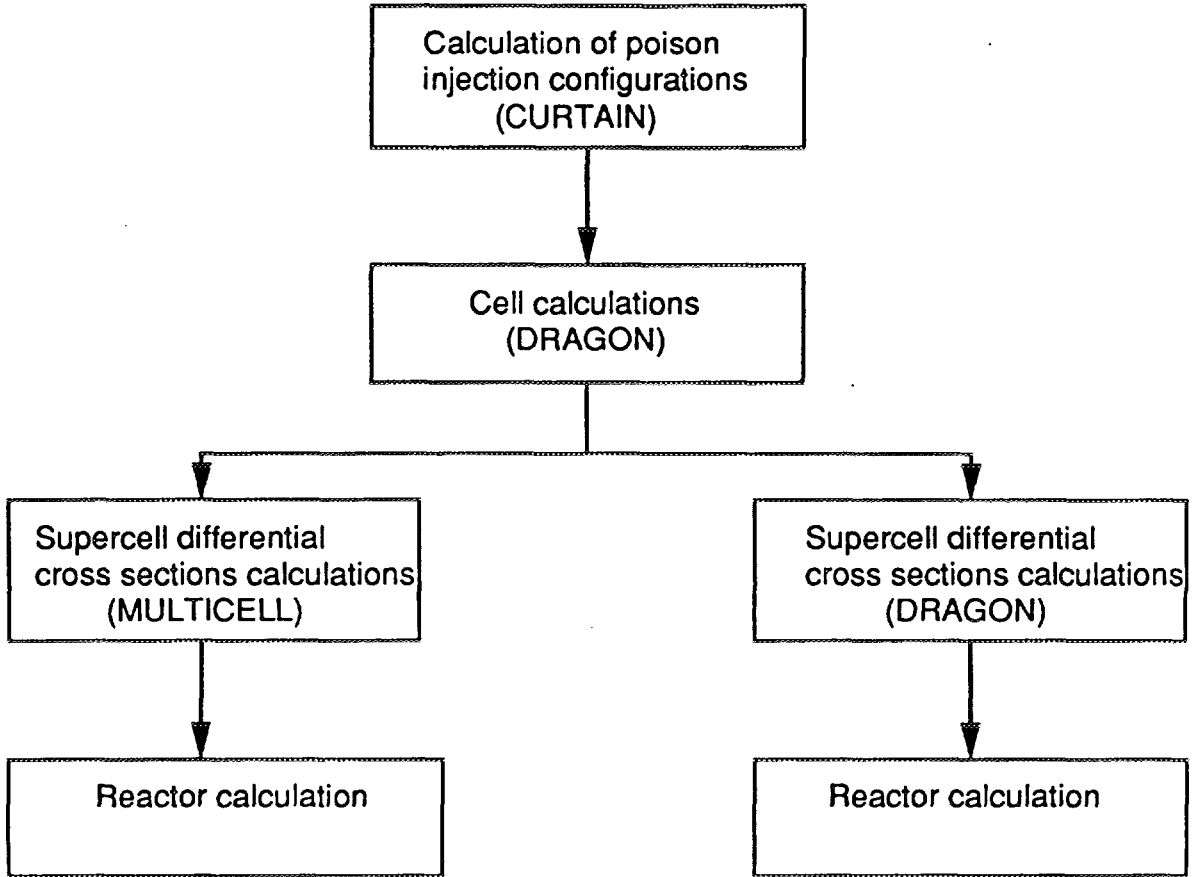
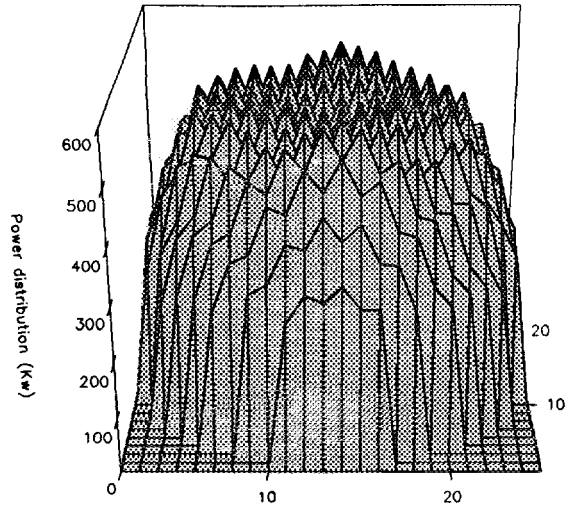
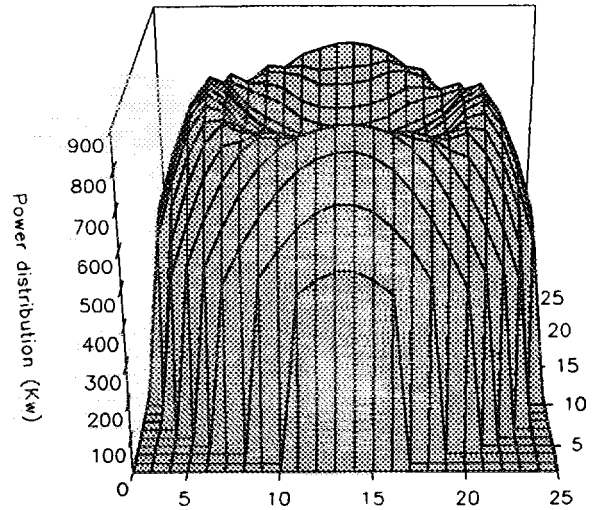


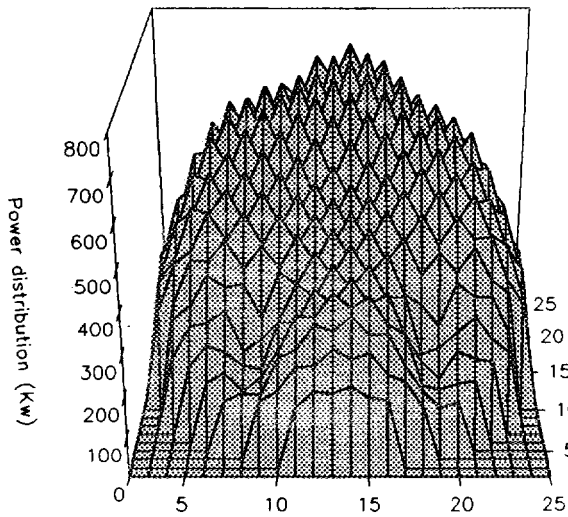
Figure 1: Calculation Chart



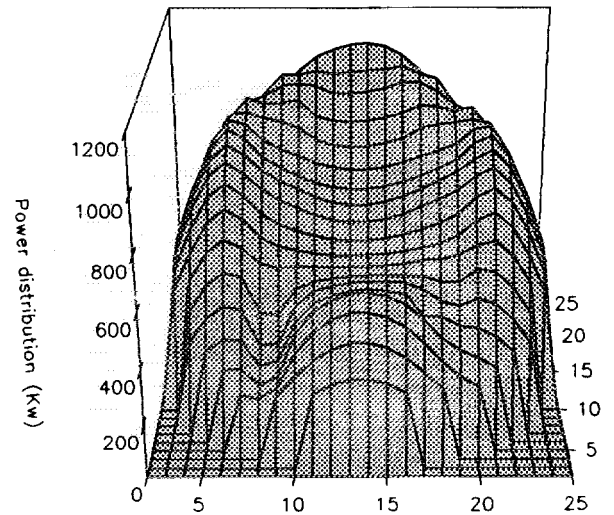
t=t0 for two injection lines at 45 degrees



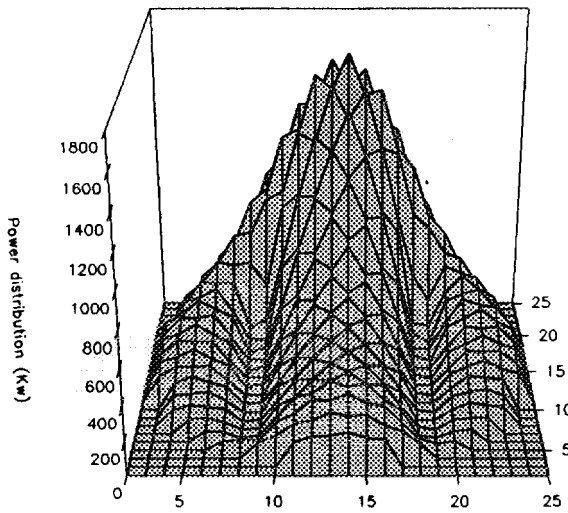
t=t0 for one injection line at right angles



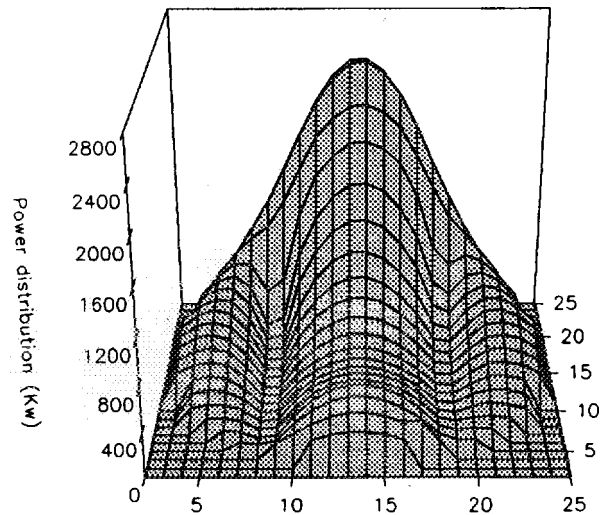
t=t1 for two injection lines at 45 degrees



t=t1 for one injection line at right angles



t=t2 for two injection lines at 45 degrees



t=t2 for one injection line at right angles

Figure 2: Reactor Power Distribution from MULTICELL Cross Sections

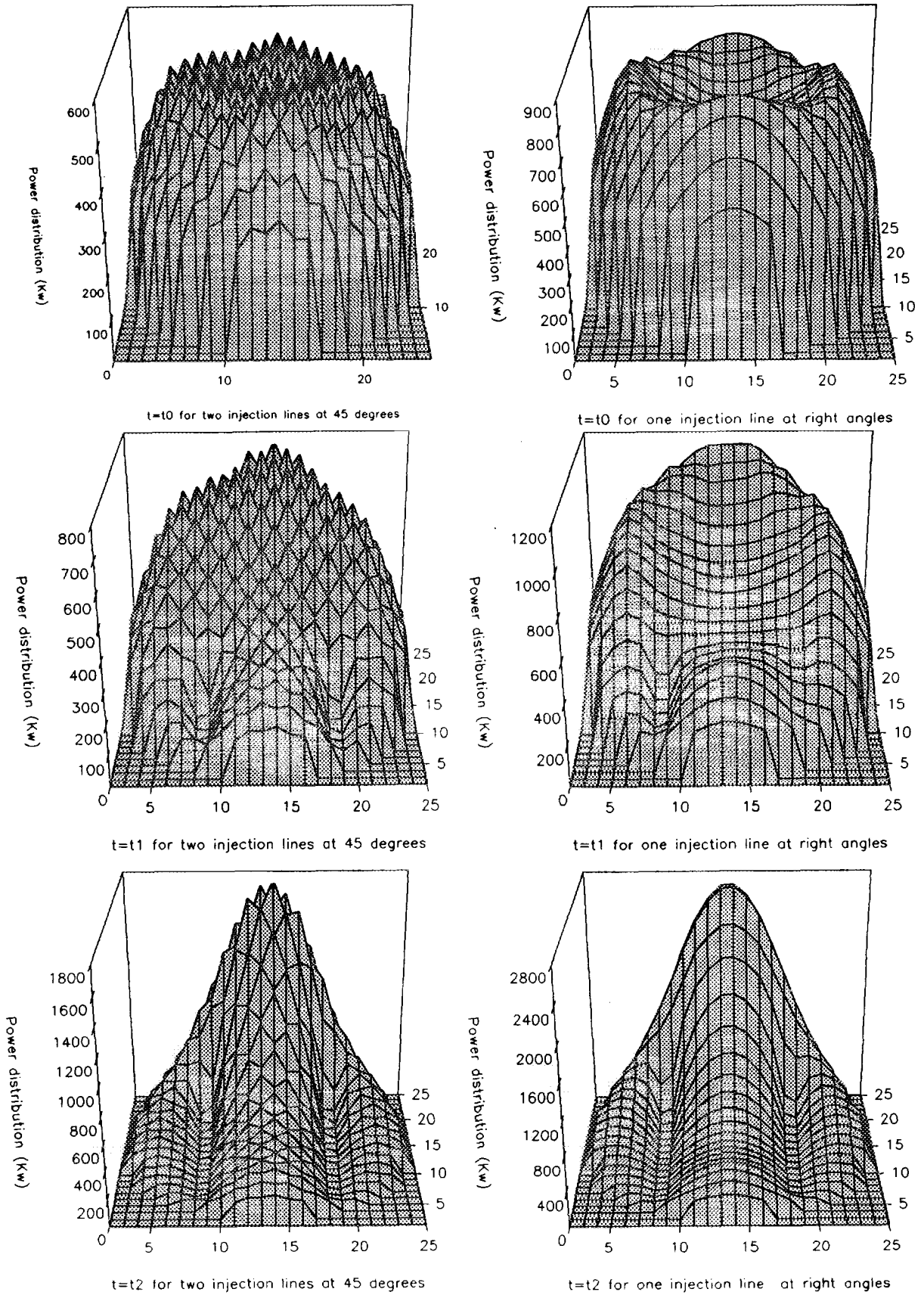


Figure 3: Reactor Power Distribution from EXCELL Cross Sections

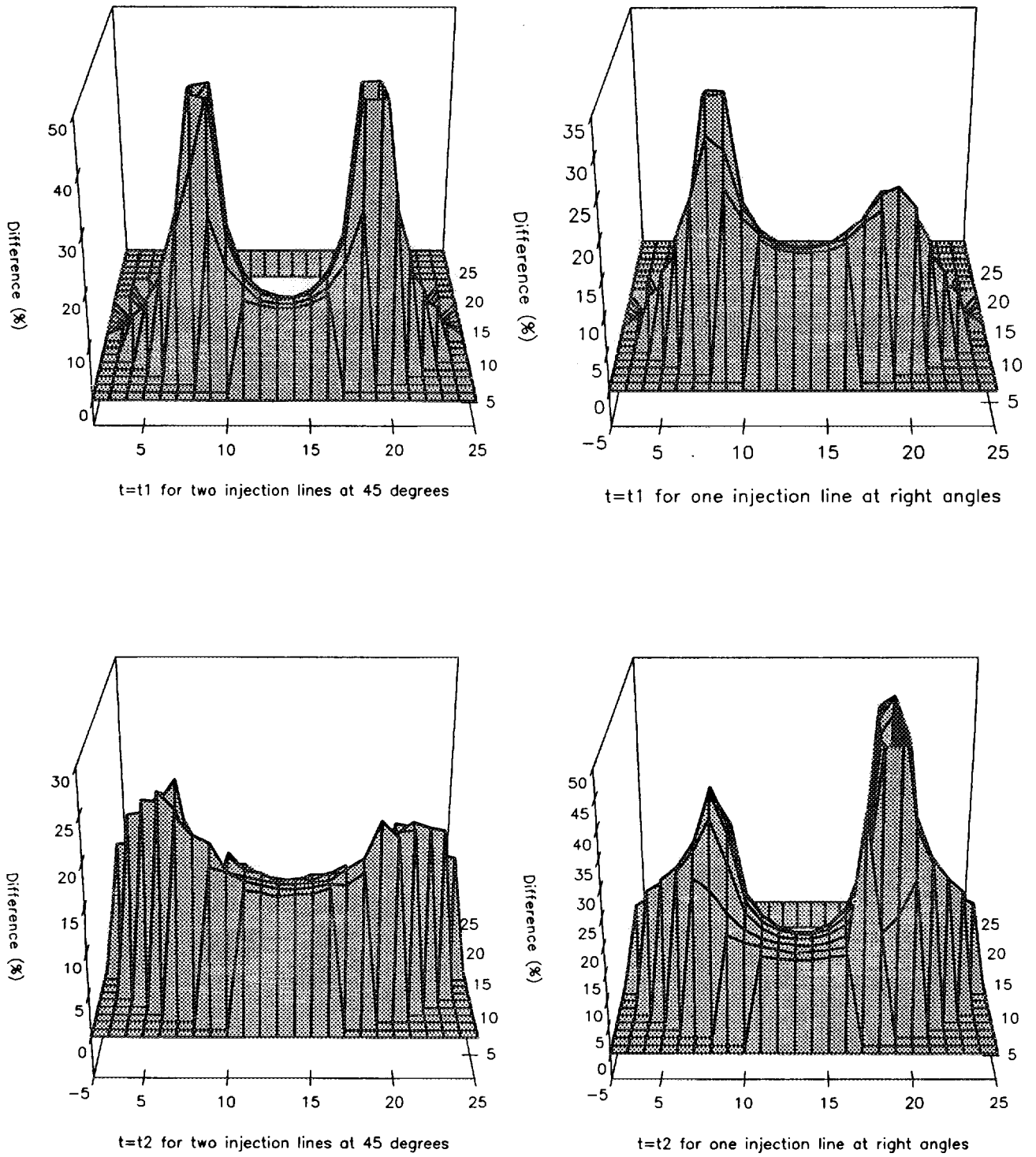


Figure 4: Difference in Power Distribution from MULTICELL Compared to EXCELL

Parameters	Fast flux simulated	Fast flux not simulated
Fast transport cross section	-0.0186 %	-2.19 %
Thermal transport cross section	-0.0136 %	-0.32 %
Fast absorption cross section	-0.0422 %	-43.57 %
Thermal absorption cross section	-6.37 %	-16.13 %
Moderation cross section	0.0136 %	10.77 %
Thermal yield cross section	-6.57 %	-16.81 %
K infinity	-0.21 %	-0.63 %

Table 1: Comparisons of a typical supercell of MULTICELL with EXCELL.

Configurations name	K infinity (MULTICELL)	K infinity (EXCELL)	$\Delta\%$
Right angle type A	0.978943	1.015349	-3.58
Right angle type B	0.658577	0.739330	-10.92
Right angle type C	0.857210	0.839001	2.17
Right angle type D	0.443198	0.521545	-15.02
Extension A	1.04389	1.074991	-2.89
Extension B	0.984098	1.026448	-4.12
Step type A	0.993685	0.634533	56.60
Step type B	0.64198	0.717632	-10.54
Step type C	0.886571	0.618547	43.33
Step type D	0.328869	0.453193	-27.43
Nozzle	0.943080	0.929147	0.53

Table 2: Comparisons of representative supercells of MULTICELL with EXCELL.

Dependence of Calculated Void Reactivity on Film Boiling Representation in a CANDU Lattice

Jeremy Whitlock

Department of Engineering Physics
McMaster University, Hamilton, Ontario
Advisors: Prof. Bill Garland (same address)
Dr. Mike Milgram (AECL-Chalk River)



CA9700546

Abstract

The distribution dependence of void reactivity in a CANDU (CANada Deuterium Uranium) lattice is studied, specifically in the regime of film boiling. A heterogeneous model of this phenomenon predicts a 4% increase in void reactivity over a homogeneous model for fresh fuel, and 11% at discharge. An explanation for this difference is offered, with regard to differing changes in neutron mean free path upon voiding.

Introduction

Partial voiding of a fuel channel can lead to complicated neutronic analysis due to highly non-uniform spatial distributions. Total void reactivity is usually calculated by modelling a lattice cell with and without coolant and defining either an absolute quantity (Equation 1), based on deviation in multiplication factor (k), or a relative quantity (Equation 2), based on deviation in reactivity (ρ).

$$\Delta k \equiv [k_{\infty}(\text{voided}) - k_{\infty}(\text{cooled})] \times 1000 \quad mk \quad (1)$$

$$\Delta \rho \equiv \rho(\text{voided}) - \rho(\text{cooled}) = \left[\frac{\Delta k}{k_{\infty}(\text{voided}) k_{\infty}(\text{cooled})} \right] \times 1000 \quad mk \quad (2)$$

Such calculations of void reactivity in a CANDU lattice agree favourably with both experiments¹ in a small test reactor, and Monte-Carlo neutron transport simulation². In practice there is only slight deviation in the predictions of Equations 1 and 2, the latter having more direct relevance to kinetics calculations. For simplicity, however, Equation 1 for reactivity differences will be used in this paper.

Partial voids can be modelled in a similar manner after determining an effective coolant density based on void fraction. This study was initiated by curiosity over the legitimacy of such a homogeneous treatment of partial voiding, given that voiding processes generally lead to highly heterogeneous partial void distributions. In boiling phenomena, for example, there are several different spatial distributions between initial and full boiling³. Although one could argue in favour of homogenous modelling in the regime of turbulence, it is not clear that this approach is valid in more spatially distinct regimes such as film boiling.

Film boiling begins when heat is no longer transported efficiently from the fuel sheath by nucleate boiling. Bubbles coalesce and a period of fuel sheath "dry-out" begins, during which coolant no longer

wets the sheath surface. In a critical CANDU fuel lattice this condition is significant since it removes scattering material from a location (between fuel elements) of relatively high neutron importance. It should be noted that this boiling regime represents a radical departure from operating conditions, and therefore the core is not expected to remain critical. However, a study of this nature does augment current knowledge of void reactivity in the CANDU lattice. It should also be noted that concurrent physical phenomena such as thermal expansion and fuel temperature rise have not been included in this analysis, in order to isolate the film boiling effect.

The effect on reactivity of coolant voiding in this lattice has been well-documented^{4,5}. Upon coolant voiding, loss of moderation near the fuel causes a shift of the neutron energy spectrum. Less down-scattering from the fast region (> 1 MeV) increases both fast fission and leakage, while decreasing resonance absorption. Less up-scattering in the thermal region (< 0.625 eV) increases the yield in U^{235} by softening the spectrum, while decreasing the yield in Pu^{239} by shifting thermal flux away from the 0.3 eV resonance. Additionally, thermal neutron flux increases near the centre pins and decreases in the outer region and moderator. The net reactivity effect (see Eqn. 1) is on the order of +20 mk for complete voiding from operating conditions, decreasing with burnup but always positive.

Details of Study

A description of the CANDU reactor system can be found elsewhere⁶. The lattice cell used in this study, shown in Figure 1, is typical of contemporary CANDU designs. A cylindrical array of 37 natural Uranium fuel pins (each O.D. 1.3 cm) at 882°C sits in a Zircalloy pressure tube (O.D. 10.3 cm) filled with D_2O coolant at 290°C. This is surrounded by a Zircalloy calandria tube and D_2O moderator at 71°C, with an overall square pitch of 28.6 cm.

The lattice code WIMS-AECL⁷ and Winfrith 69-group library were used in this study of the partial voiding phenomenon. Two approaches were employed: a "homogeneous model" averaged partial void over area, and a "heterogeneous model" used actual void distribution. Film boiling was represented as a voided annulus around each fuel pin, with thicknesses up to the "geometric limit" of 0.9 mm, where neighbouring annuli intersect (void fraction 0.43) and further partial void expansion can no longer be simply modelled in the heterogeneous case.

The effect was studied first at zero burnup, followed by an analysis over fuel burnup. Since CANDU cores are continuously refuelled, conclusions about total core reactivity have most relevance when considering mid-burnup results, which best approximate equilibrium core behaviour⁵.

Results and Discussion

Figure 2 shows the two reactivity effects, defined here using Equation 1. The results show a small but distinct difference in the predictions of the two models, with a maximum deviation (heterogeneous — homogeneous) of +0.37 mk, or approximately 4% of the predicted effect.

To investigate concerns that this small difference might be an artifact of the numerical treatment in WIMS-AECL, a second geometry with a single, central pin was studied (coolant and fuel temperatures: 600K and 300K, respectively). This amplified the effect by increasing the coolant-to-fuel ratio, which in turn permitted verification of the results using MCNP 4⁸, a Monte-Carlo neutron transport code (it was

impossible to detect the effect in the 37-element fuel array using MCNP 4 due to the large statistical error in k_{∞} for practical run times). The results in Figure 3 show a maximum deviation of about +10 mk around 50% voiding, with good agreement between WIMS-AECL and MCNP 4. This exercise helps to confirm the existence of a physical effect, as well as instill confidence in the methodology.

Figure 4 illustrates the fast flux spectral change in the inner fuel pin of the 37-element fuel array, with 0.9 mm annular void formation. Average fast flux (> 0.821 MeV) increased by 5.5 % for the heterogeneous case, and 4.5 % for the homogeneous case. A comparison of flux change throughout the fuel in three different spectral ranges is given in Table 1. Note that the heterogenous model predicts a greater change in most fuel rings and spectral ranges; the exception is the non-fast flux (< 0.821 MeV) in the outer (fourth) fuel ring. The last column in Table 1 summarizes the spectral effect alone, obtained by taking a weighted sum of all fuel rings.

The origin of the effect is geometrical. A collection of discrete voids in the heterogeneous case allows a greater increase in neutron mean free path length within the fuel array, despite conservation of average coolant density. This is attributable to the proximity of fuel elements with the array, causing the slightest film voiding to lead to both a larger increase in streaming between elements, and a larger reduction in coolant moderation. The effect on the flux, evident in Table 1, can be summarized using three groups:

(1) *Thermal Flux* arises from the moderator. Upon voiding, an increase in mean free path length leads to a spatial flux shift towards the centre of the fuel array. The heterogeneous model, therefore, predicts an increase in this shift relative to the homogeneous model, although cancellation between the outer and inner regions causes the net effect on thermal flux throughout the fuel to be very small in both cases (about 0.2 – 0.3 %). Additionally, upon voiding, the spectral shift towards a lower average neutron temperature is observed to be greater in the heterogeneous case, although this information is not presented in Table 1.

(2) *Fast Flux* arises from the fuel. Upon voiding, this component is increased by loss of coolant moderation and decreased by greater leakage to the bulk moderator. The loss of moderation is the dominant effect, and the heterogeneous model predicts a greater increase in fast flux across the fuel array.

(3) *Resonance Flux* arises partly from coolant moderation within the fuel array. Upon voiding, reduction of this moderation leads to a corresponding reduction in resonance flux across the fuel array, with a smaller effect in the outer rings. Accordingly, the heterogeneous model predicts a greater reduction in resonance flux across the array, with a smaller effect in the outer rings.

Such differences in flux response will be manifested in nuclide reaction rates. Table 2 lists the partial reactivity (isotopic yield / total cell absorption) for U^{235} and U^{238} in the cooled and 0.9 mm annular void (0.43 void fraction) cases. Since fresh fuel was modelled, these partial reactivities are the only components of fissile reactivity in the fuel. A total increase of 0.52 mk for U^{238} is observed between the heterogeneous and homogeneous results, while a slight decrease (-0.17 mk) is observed for U^{235} , indicating that the effect is not significantly related to thermal flux (for this geometry and for fresh fuel). Rather, the difference between the two models appears mostly related to differences in predicted U^{238} reactivity across the fuel, while a greater difference in U^{235} reactivity in the inner three rings of fuel is almost cancelled by a decrease in the outer ring.

The results for single-pin geometry, on the other hand, show entirely opposite behaviour. A comparison of the cooled and 1.85 cm annular void (void fraction 0.24) cases in Table 3 shows the important component here to be the doubling of U^{235} reactivity, since the U^{238} contribution is small. This is to be expected, since the absence of surrounding fuel pins decreases the effects of fast fission and resonance absorption.

Figure 5 shows the effect on reactivity of burnup in the 37-element, 0.9 mm film void case, as predicted by the two models. The time-dependent discrepancy is shown in Figure 6 in terms of both absolute reactivity and a percentage of the total effect. At discharge burnup (7500 MWd/Mg-initial U) the difference is 0.70 mk, or about 11 %. At mid-burnup the difference is 0.56 mk, or about 8 %.

Table 4 is another listing of partial reactivities (isotopic yield / total cell absorption), this time at discharge burnup, and includes both Pu^{239} and Pu^{241} . Since U^{238} is fairly insensitive to burnup its contribution to both total reactivity and the film void model discrepancy does not change significantly. U^{235} contributes less to both total reactivity and the discrepancy, due to depletion. Pu^{239} is affected by the same opposing shifts in thermal flux across the fuel array as is U^{235} , although its net contribution is less negative in the heterogeneous case than in the homogeneous case, adding +0.13 mk to the observed discrepancy. The effect of burnup, therefore, is to increase the difference in predictions of the homogeneous and heterogeneous models due to the depletion of U^{235} , which has a reducing effect on the discrepancy, and the creation of Pu^{239} , which has an enlarging effect.

Conclusion

A reactivity difference is found when film boiling is modelled heterogeneously and homogeneously. An increase in fast flux, due to a greater increase in mean free path length, is the explanation. The effect increases with burnup due to depletion of U^{235} and creation of Pu^{239} . In contemporary designs the effect is minor (about 4 % and 11 % at zero and full burnup, respectively), but a small effect could still be significant in postulated low void reactivity CANDU fuel bundles⁹.

Acknowledgement

The author wishes to thank Mike Milgram, AECL – Chalk River Laboratories, for his invaluable assistance and guidance throughout this study.

References

1. R.E. Kay, *Lattice Measurements With 37-Element Bruce Reactor Fuel in Heavy Water Moderator: Detailed Lattice Cell Parameters*, AECL-5307, Chalk River Laboratories, AECL, June 1976
2. D.S. Craig, *A Comparison of Lattice Parameters for CANDU-type Lattices Obtained Using MCNP, WIMS, and WIMS With Resonance Reaction Rates From MCNP*, AECL-9778, Chalk River Laboratories, AECL, March 1989

3. J.G. Collier, Convective Boiling and Condensation, 2nd ed., McGraw-Hill Inc., 1981, Sec. 7.5.3
4. A.R. Dastur, D.B. Buss, *The Influence of Lattice Structure and Composition on the Coolant Void Reactivity in CANDU*, Proc. 11th Annual Conference of the Canadian Nuclear Society, Toronto, Ontario, June 1990.
5. J. Griffiths, *Lattice Characteristics that Influence the Change in Reactivity with Coolant Voiding in CANDU Lattices*, Proc. 13th Annual Simulation Symposium, Canadian Nuclear Society, Chalk River Laboratories, April 1987.
6. J. Griffiths, *Reactor Physics and Economic Aspects of the CANDU Reactor System*, AECL-7615, Chalk River Laboratories, AECL, February 1983.
7. J.V. Donnelly, *WIMS-CRNL. A User's Manual for the Chalk River Version of WIMS*, AECL-8955, Chalk River Laboratories, AECL, January 1986.
8. *MCNP 4, Monte Carlo Neutron and Photon Transport Code System*, CCC-200A/B, RSIC Computer Code Collection, Radiation Shielding Information Centre, Oak Ridge National Laboratory, June 1991.
9. A.R. Dastur, P.S.W. Chan, D. Bowslaugh, *The Use of Depleted Uranium for the Reduction of Void Reactivity in CANDU Reactors*, Proc. 13th Annual Conference of the Canadian Nuclear Society, St. John, New Brunswick, June 1992.

Figure 1. Geometry of 37-element CANDU lattice cell.

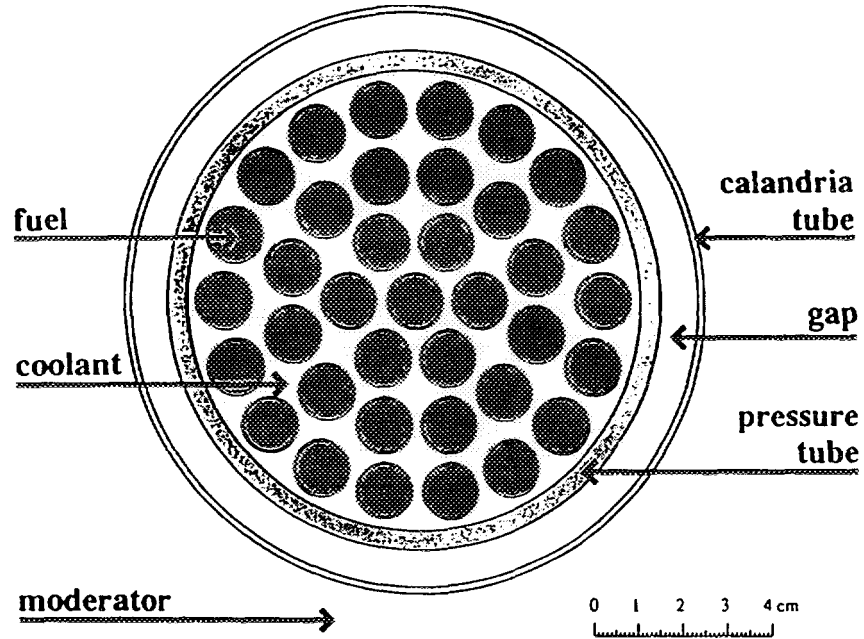


Figure 2. Void reactivity due to film boiling in 37-element cell, as a function of void fraction: Comparison of predictions using heterogeneous and homogeneous models.

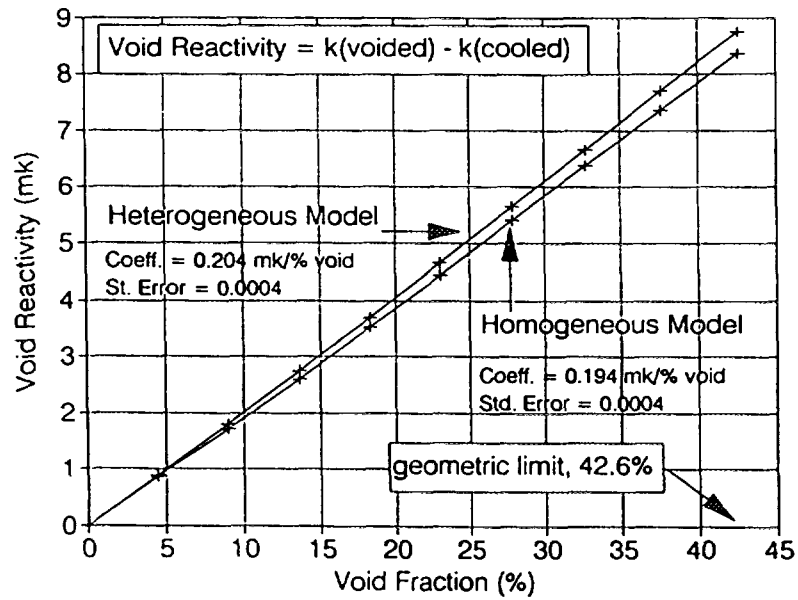


Figure 3. Void reactivity due to annular voids in single pin cell, as a function of void fraction: Comparison of WIMS-AECL and MCNP 4 predictions.

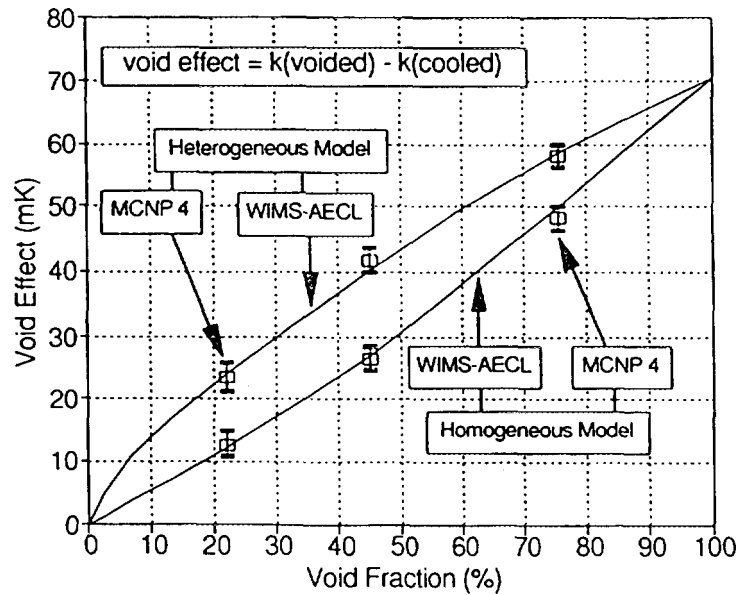


Figure 4. Fast neutron spectrum in inner fuel pin of 37-element cell, before and after 0.9 mm annular void formation (43% void fraction): Comparison of predictions using heterogeneous and homogeneous models.

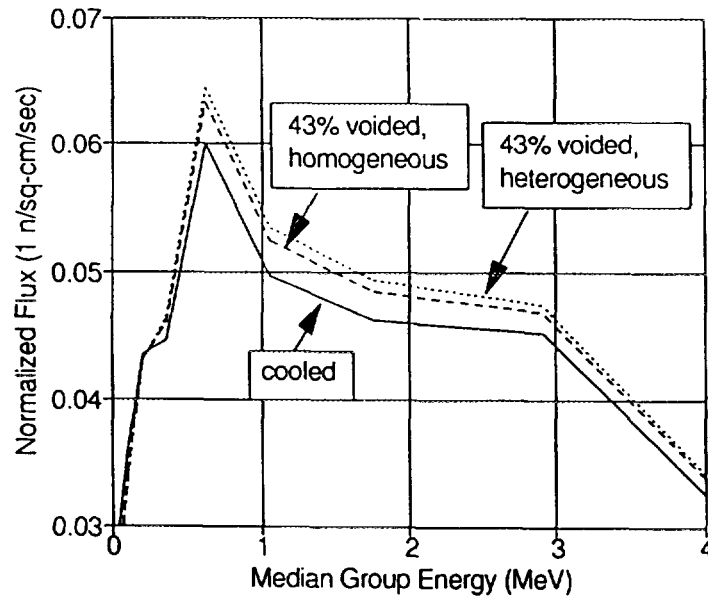


Table 1. Change (%) in average fuel flux spectral distribution with 0.9 mm annular void formation (43% void fraction) in 37-element cell.

Spectrum Range	Model Used	Fuel Ring 1	Fuel Ring 2	Fuel Ring 3	Fuel Ring 4	Total Fuel
		(%)	(%)	(%)	(%)	(%)
Fast (> .821 MeV)	heterogeneous	6.70	6.26	5.59	5.17	5.52
	homogeneous	4.81	4.85	4.58	4.32	4.50
	het. / hom.	1.39	1.05	1.22	1.20	1.23
Resonance (.625 eV - .821 MeV)	heterogeneous	-2.66	-2.28	-1.47	-0.15	-0.99
	homogeneous	-2.21	-1.96	-1.38	-0.29	-0.97
	het. / hom.	1.21	1.50	1.06	0.53	1.03
Thermal (< .625 eV)	heterogeneous	1.50	1.05	0.16	-0.88	-0.17
	homogeneous	1.17	0.70	-0.03	-0.93	-0.32
	het. / hom.	1.29	1.50	4.66	0.95	0.52

Table 2. Change in reactivity ($\Delta^{Yield}/_{Total\ Absorption}$) of U^{235} and U^{238} with 0.9 mm annular void formation (43% void fraction) in 37-element cell.

	Model Used	Fuel Ring 1 (mk)	Fuel Ring 2 (mk)	Fuel Ring 3 (mk)	Fuel Ring 4 (mk)	Total (mk)
U^{238}	heterogeneous	0.11	0.52	0.99	1.17	2.85
	homogeneous	0.08	0.45	0.82	0.98	2.33
	het. - hom.	0.03	0.13	0.17	0.19	0.52
	% difference	39.2 %	28.6 %	21.2 %	19.1 %	22.3 %
U^{235}	heterogeneous	0.65	3.28	3.78	-1.68	6.03
	homogeneous	0.59	2.83	3.50	-0.72	6.20
	het. - hom.	0.07	0.45	0.27	-0.96	-0.17
	% difference	11.2 %	16.0 %	7.8 %	132.9 %	-2.7 %

Table 3. Change in reactivity ($\Delta \text{Yield} / \text{Total Absorption}$) of U^{235} and U^{238} with 1.85 cm annular void formation (24% void fraction) in single element cell.

	Model Used	Reactivity (mk)
U^{238}	heterogeneous	-0.16
	homogeneous	-0.03
	het. - hom.	-0.13
	% difference	433.3 %
U^{235}	heterogeneous	19.37
	homogeneous	9.76
	het. - hom.	9.61
	% difference	98.5 %

Figure 5. Effect of burnup on void reactivity with 0.9 mm annular void formation (43% void fraction): Comparison of predictions using heterogeneous and homogeneous models.

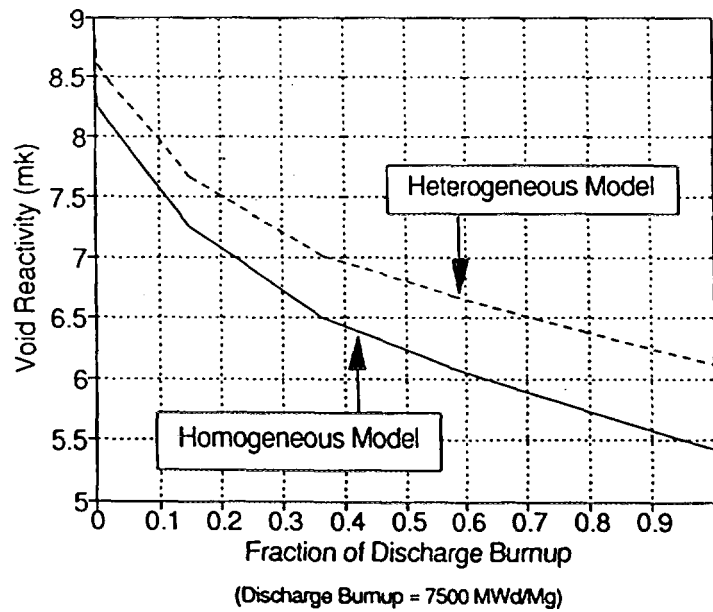


Figure 6. Effect of burnup on discrepancy between predictions of heterogeneous and homogeneous models for void reactivity with 0.9 mm annular void formation (43% void fraction).

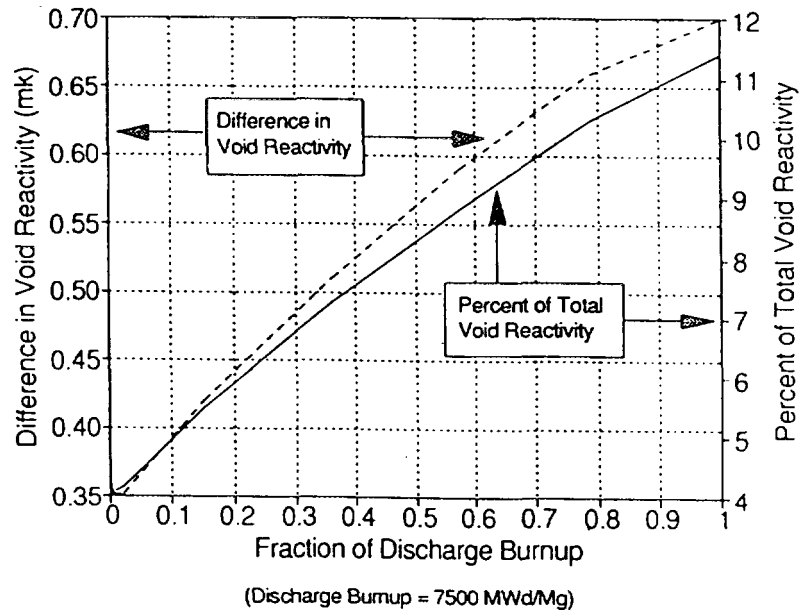


Table 4. Change in reactivity ($\Delta^{Yield}/_{Total\ Absorption}$) of U^{235} , U^{238} , Pu^{239} and Pu^{241} with 0.9 mm annular void formation (43% void fraction) in 37-element cell at discharge burnup (7500 MWd/Mg-U).

	Model Used	Fuel Ring 1 (mk)	Fuel Ring 2 (mk)	Fuel Ring 3 (mk)	Fuel Ring 4 (mk)	Total (mk)
U^{238}	heterogeneous	0.11	0.61	1.03	1.22	2.98
	homogeneous	0.08	0.48	0.85	1.02	2.43
	het. - hom.	0.03	0.13	0.18	0.20	0.55
	% difference	38.1 %	27.9 %	21.3 %	19.9 %	22.6 %
U^{235}	heterogeneous	0.30	1.49	1.75	0.25	3.79
	homogeneous	0.28	1.35	1.67	0.46	3.75
	het. - hom.	0.03	0.14	0.08	-0.21	0.04
	% difference	9.4 %	10.7 %	4.7 %	-45.8 %	1.0 %
Pu^{239}	heterogeneous	0.23	1.01	0.63	-2.50	-0.64
	homogeneous	0.21	0.87	0.50	-2.35	-0.77
	het. - hom.	0.02	0.13	0.13	-0.15	0.13
	% difference	7.7 %	15.4 %	26.0 %	-6.3 %	17.0 %
Pu^{241}	heterogeneous	0.03	0.14	0.17	-0.15	0.19
	homogeneous	0.02	0.12	0.16	-0.12	0.19
	het. - hom.	0.00	0.02	0.02	-0.03	0.00
	% difference	9.9 %	13.5 %	10.2 %	-29.5 %	0.3 %

(Samedi 3 avril 8:30 → 10:10)
(Saturday April 3rd 8:30 → 10:10)

SESSION 3B
DÉTECTION & ACTIVATION NEUTRONIQUE-1 DETECTION AND ACTIVATION-1
Président / Chairman: Dr. G. Evans, University of Toronto
Salle / Room: C-630

- M. Samri Université Laval
Système multidétecteur pour l'identification et la mesure des énergies des ions lourds aux énergies intermédiaires
- P. Roy Université de Montréal
Étude de la réponse d'un détecteur Si irradié par des neutrons de 1 Mev
- M.E. Abdelbaky University of New Brunswick
Design of Intermediate Energy Filters for Neutron Beams
- M. Gourde Université Laval
Développement et performances de détecteurs de particules chargées appliqués à l'étude des réactions avec ions lourds



Système multidétecteur pour l'identification et la mesure des énergies des ions lourds aux énergies intermédiaires

**M Samri, L. Beaulieu, B. Djerroud,
D. Doré, P. Gendron, M. Gourde,
E. Jalbert, R. Laforest, Y. Larochelle,
J. Pouliot, R. Roy, C. St-Pierre,**

**Département de Physique, Université Laval
Ste-Foy, Québec, G1K 7P4**

**G. Ball, A. Galindo-Uribarri, E. Hagberg, D. Horn
Laboratoires de Chalk River, Recherche EACL,
Chalk River, Ontario, K0J 1J0**

Directeur de recherches: Prof. C. St-Pierre

1. Introduction

La disponibilité récente de faisceaux d'ions lourds très énergétiques permettant l'étude des réactions nucléaires dans le domaine des énergies intermédiaires ($10 < E < 100$ A MeV), s'est accompagnée par des progrès considérables dans la réalisation de systèmes multidétecteurs. En effet, à ces énergies, les réactions nucléaires sont caractérisées par la formation de systèmes nucléaires très excités qui décroissent en émettant des particules en nombre et variété élevés sous un grand angle solide. Une analyse quantitative détaillée exige la détection et l'identification de tous les fragments émis. Ceci est réalisé en disposant autour de la cible une multitude de détecteurs devant assurer une bonne granularité et une couverture angulaire suffisante. À cause de leur coût, facilité de fabrication et de certaines propriétés qui leur sont spécifiques, les détecteurs à scintillation sont particulièrement adaptés à la réalisation de tels systèmes [1,2,3,4]. Le groupe de Physique des Ions Lourds du Laboratoire de Physique Nucléaire de l'Université Laval et une équipe de chercheurs des laboratoires de l'Energie Atomique du Canada Limitée à Chalk River ont mis au point un système multidétecteur à scintillation pour l'étude des mécanismes de réactions nucléaires aux énergies intermédiaires. Ces derniers et en particulier les processus d'émission de multifragments suscitent un intérêt évident et font actuellement l'objet d'études intensives [5,6,7,8].

2. Description

Le système multidétecteur, dénommé matrice, est composé actuellement de 80 détecteurs à scintillation groupés en 5 anneaux centrés sur le faisceau et comprenant chacun 16 détecteurs. Les trois premiers anneaux sont constitués de scintillateurs de type phoswich de forme trapézoïdale. Des détecteurs CsI(Tl) également de forme trapézoïdale forment les deux autres anneaux. La matrice a une hauteur de 67 cm et une largeur de 63 cm; elle occupe l'espace compris entre les angles polaires 6° et 46° , tout angle azimutal, assurant ainsi une couverture angulaire d'une large fraction de 4π . Quelques caractéristiques géométriques des anneaux sont données dans le tableau 1 et la figure 1 en donne une vue de face et une coupe latérale.

Tableau 1. caractéristiques géométriques de la matrice

anneau	angle solide en stéradians	distance à la cible [cm]
6° à 10°	0.0499	51
10.5° à 16°	0.1124	51
16° à 24°	0.2730	51
24° à 34°	0.5491	21
34° à 46°	0.9837	21

2. Choix des scintillateurs.

Un détecteur de type phoswich est en fait constitué de deux scintillateurs accolés; l'un, mince et de constante de temps rapide; l'autre beaucoup plus épais et de constante de temps lente. Le choix des scintillateurs a été fait principalement en fonction de ce critère. Ainsi, un scintillateur plastique mince de type BC408 a été choisi en raison de sa constante de temps courte (2.1 ns). Le scintillateur épais, de type BC444, a une constante de temps beaucoup plus longue (187 ns). De cette façon, le plastique mince peut être utilisé pour mesurer la perte d'énergie ΔE d'une particule chargée alors que le plastique épais en mesure l'énergie résiduelle E. Un tel détecteur constitue un télescope ΔE -E. Chaque détecteur phoswich est relié à un seul photomultiplicateur XP2252 de Philips. Des caractéristiques plus détaillées de ces détecteurs sont données à la référence [9]. Le tableau 2 en résume quelques unes.

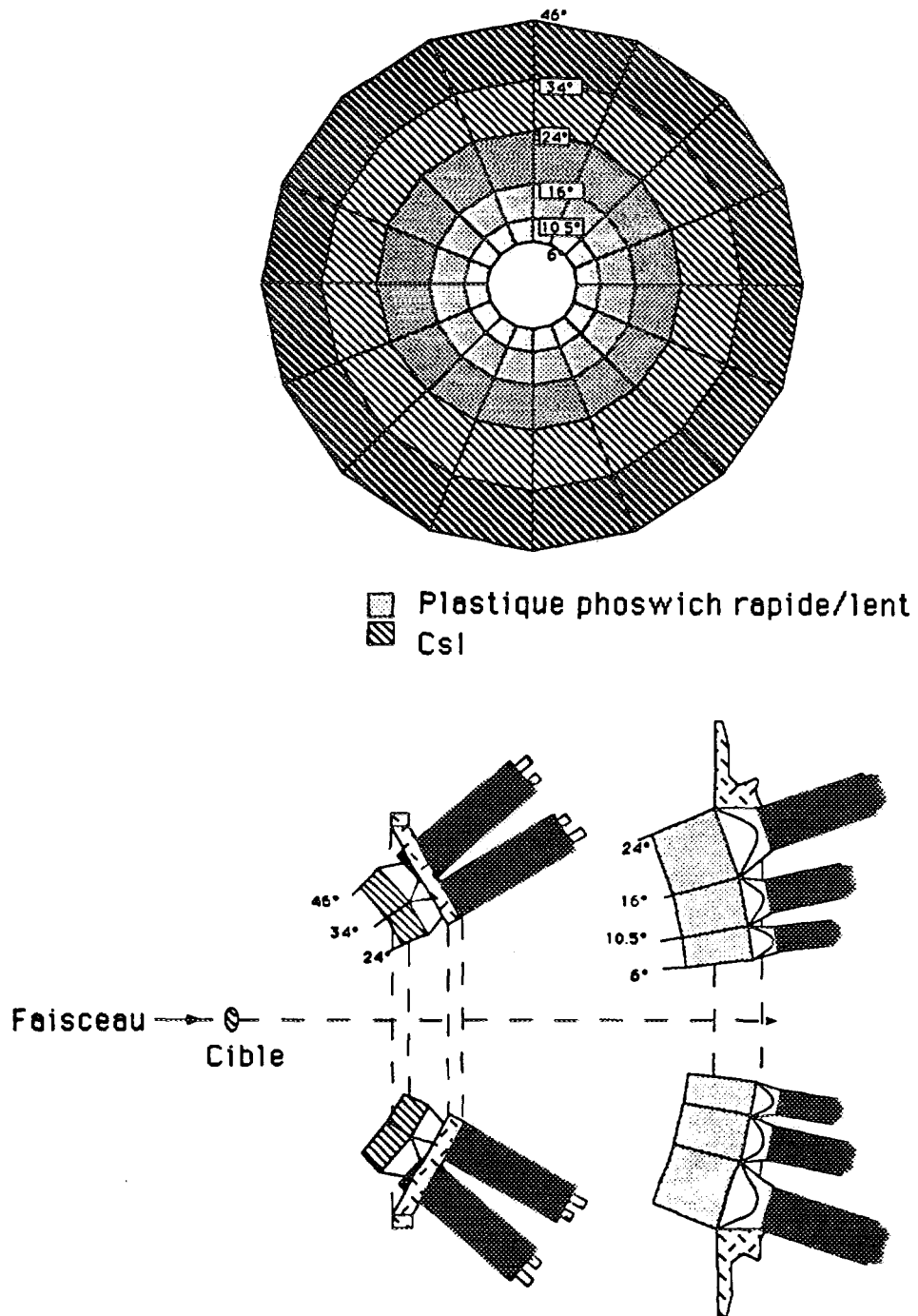


Figure 1 Géométrie de la matrice CRL-Laval. En haut, vue de la cible; en bas, coupe latérale.

Tableau 2. Caractéristiques des scintillateurs

scintil- lateur	épaisseur [mm]	constante de temps [ns]	lumière é- mise en (% anthracène)	longueur d'onde [nm]
ΔE (BC408)	0.7	2.1	64	425
E (BC444)	120	187	41	428
CsI(Tl)	350	1000 - 7000	95	580

Les détecteurs de type phoswich sont caractérisés aussi par leur seuil qui représente l'énergie minimum nécessaire à une particule pour traverser le scintillateur mince . Le tableau 3 donne les valeurs de ces seuils pour quelques particules de $Z = 1$ à $Z = 12$ calculées par le code STOPX [10].

Tableau 3 Seuil des détecteurs phoswich

parti- cule	^1H	^4He	^{12}C	^{16}O	^{20}Ne	^{24}Mg
seuil [AMeV]	7.5	7.5	14	16	18	19.5

Le CsI(Tl) est souvent préféré à d'autres scintillateurs inorganiques tels le NaI(Tl) ou le BaF₂ en raison de ses propriétés d'être faiblement hygroscopique, d'avoir un pouvoir élevé d'absorption des particules et d'émettre la lumière dans le spectre visible. En outre, il possède des constantes de temps très différentes [11]; une électronique semblable à celle utilisée pour le détecteur de type phoswich permet de distinguer entre les composantes lente et rapide du signal. Une discussion des propriétés de ce détecteur est fournie dans l'article de M. Gourde présenté à cette conférence.

3. Principe et technique de mesure.

Une particule chargée, en pénétrant dans un matériau scintillateur, perd son énergie cinétique à la suite de nombreuses collisions avec les atomes du milieu. Ces collisions ont pour effet de laisser les molécules dans des états excités dont la désexcitation produit une lumière qui sera captée par un photomultiplicateur et convertie en un signal électrique. Dans notre cas et du fait que les détecteurs utilisés ont des constantes de temps très différentes, les molécules excitées n'émettent pas la lumière dans le même intervalle de temps. Le signal électrique obtenu après

conversion de la lumière par le photomultiplicateur est la superposition de deux impulsions: une rapide et due à la constante de temps courte, l'autre lente et due à la constante de temps lente. Des modules électroniques permettent de placer des fenêtres d'intégration de courant sur l'impulsion résultante. Pour observer la composante rapide de l'impulsion, une fenêtre de durée courte est utilisée. Le courant ainsi obtenu, nommé signal ΔE , est proportionnel à l'énergie déposée par la particule dans le scintillateur mince. Une fenêtre de durée plus longue placée sur la composante lente donne le signal E . Ceci est illustré sur la figure 2.

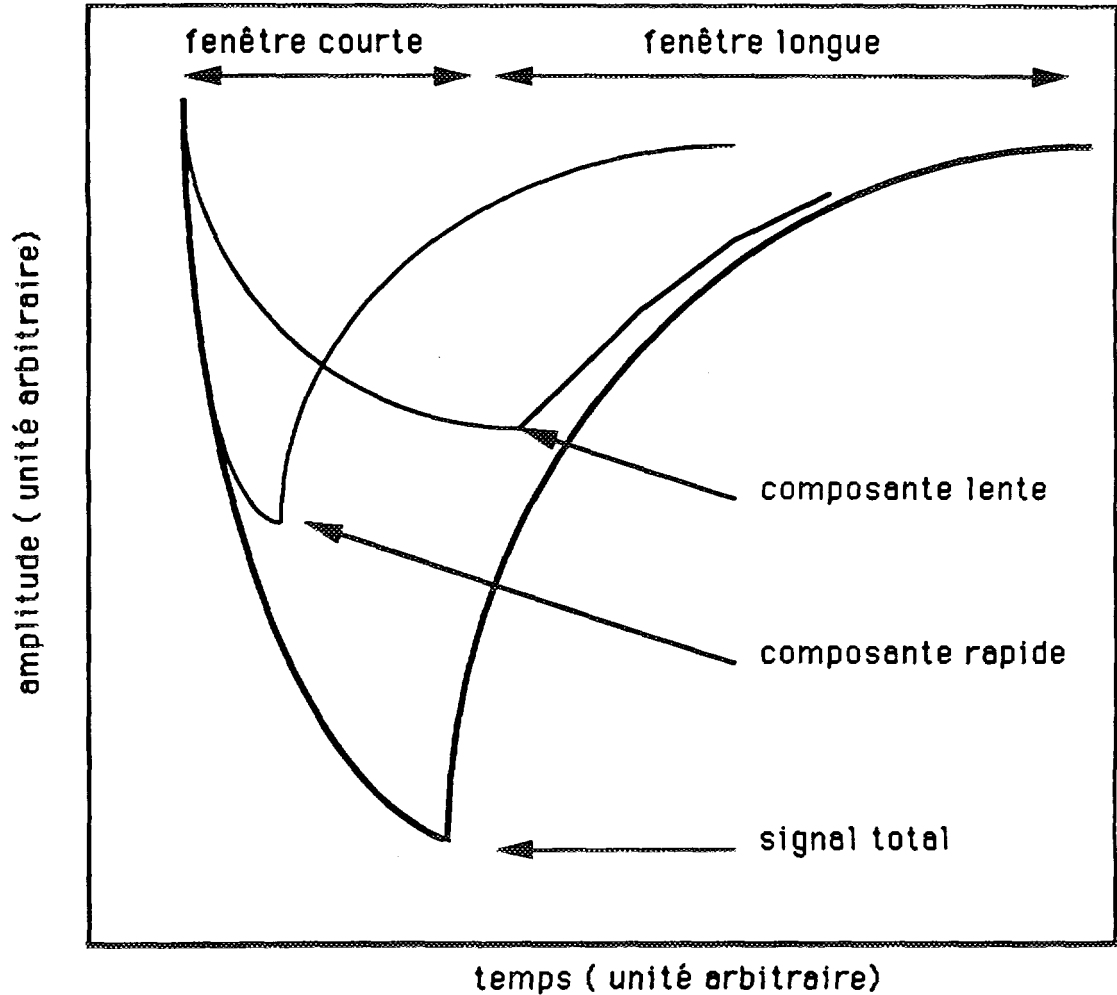


Figure 2. En trait gras, signal d'un détecteur phoswich produit par la détection d'une particule chargée. Sa décomposition en des composantes lente et rapide est représentée en traits fins. Les positions des fenêtres d'intégration sont indiquées. On observe la contribution de la fenêtre courte dans la fenêtre longue et vice versa.

Le signal de chaque photomultiplicateur à la sortie d'un amplificateur rapide est divisé en trois branches. Deux d'entre elles fournissent les signaux linéaires ΔE et E . La troisième alimente un discriminateur qui fournit trois types de signaux logiques. Le premier type de signaux sert à générer les différentes portes. Le deuxième type est utilisé pour synchroniser les fenêtres d'intégration et pour déclencher le signal départ du convertisseur temps amplitude alors que le signal arrêt est fourni par le troisième type de signaux.

4. Performances de la matrice.

4.1 Identification des particules

La matrice a été utilisée dans des expériences auprès du cyclotron à aimants supraconducteurs des laboratoires de Chalk River. Un faisceau de ^{24}Mg de 25 et 35 AMeV était dirigé sur une cible d' ^{197}Au de 2.9 mg/cm^2 d'épaisseur. Le faisceau avait une faible intensité (environ 1 nA) pour ne pas saturer les détecteurs sur les anneaux intérieurs.

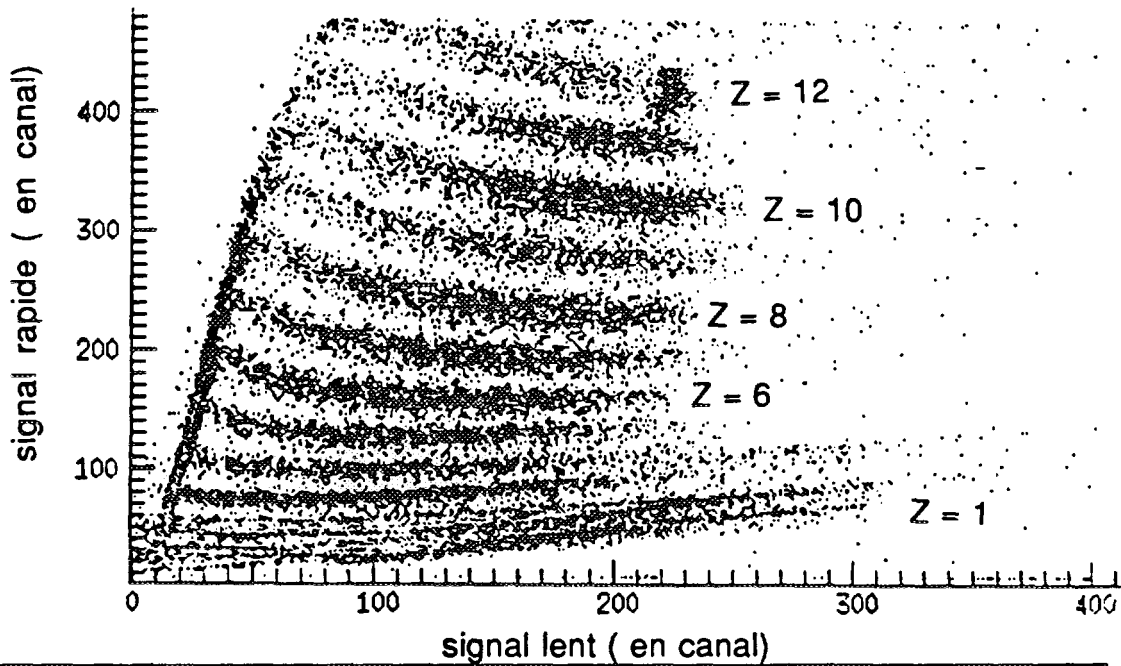


Figure 3a. Spectre bi-dimensionnel représentant le signal rapide ΔE en fonction du signal lent E pour la réaction ^{24}Mg (600 MeV) + ^{197}Au obtenu avec un détecteur phoswich du premier anneau. Toutes les bandes représentant les éléments de $Z = 1$ à 12 sont bien visibles.

Un spectre caractéristique d'un détecteur phoswich est représenté sur la figure 3a, avec en abscisse le signal lent E et en ordonnée le signal rapide ΔE . Les différentes bandes horizontales représentant les charges de $Z = 1$ à 12 sont bien visibles. La bande oblique est due aux particules dont l'énergie cinétique est insuffisante pour franchir le scintillateur mince et correspond donc aux particules complètement arrêtées dans le scintillateur mince.

La figure 3b représente un spectre d'un détecteur Csl. Les différentes lignes représentent les ions de numéro atomique $Z = 1, 2, 3, 4$ et 5. Dans ce cas, on observe une résolution isotopique pour $Z = 1$ et $Z = 2$.

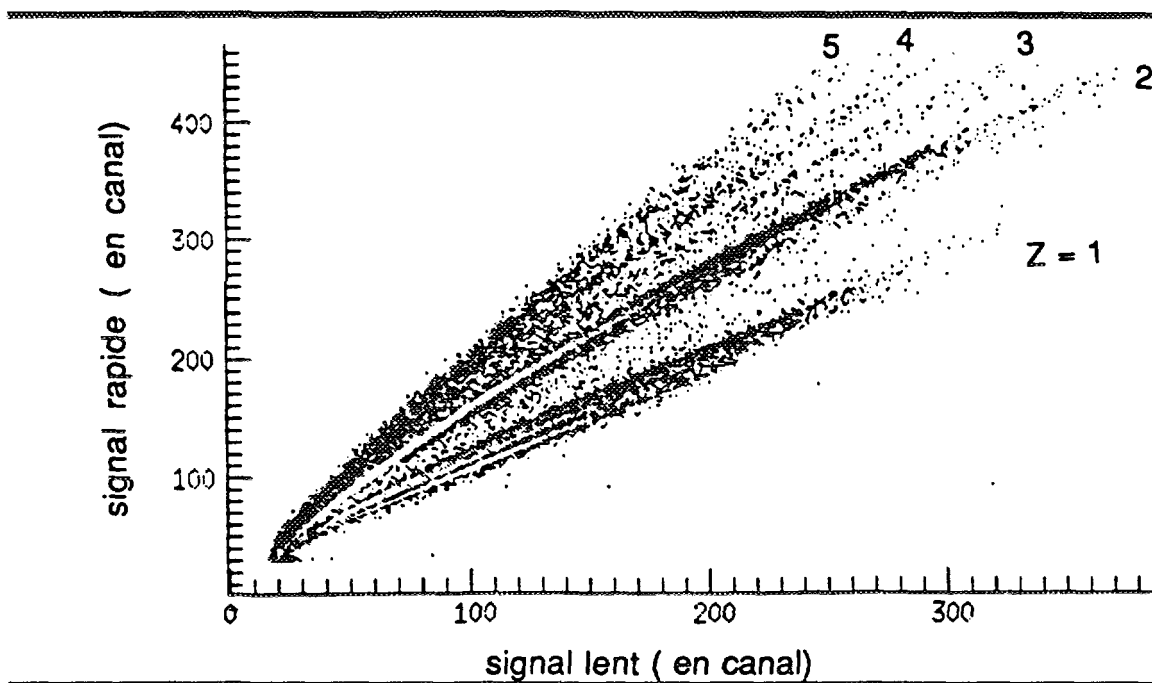


Figure 3b. Signal rapide ΔE en fonction du signal lent E d'un détecteur Csl du quatrième anneau. Pour $Z = 1$, on observe les trois bandes représentant les protons, deutons et tritons.

4.2 Etalonnage en énergie

Un des problèmes que pose l'utilisation des détecteurs à scintillation est la détermination de leur fonction réponse. Celle-ci n'est pas linéaire avec l'énergie des particules. En outre, elle dépend du type et de la masse des particules. L'étalonnage en énergie s'avère donc être une opération très délicate et qui mérite beaucoup de soin, nécessitant plusieurs points pour chaque particule. Dans notre cas, les énergies des protons diffusés élastiquement sur une cible d'or à 15 et 25 MeV sont utilisées.

D'autres points d'étalonnage sont obtenus en utilisant la technique des faisceaux secondaires qui consiste à placer des cibles de production en carbone sur le trajet du faisceau de ^{24}Mg en amont de l'aimant d'analyse. En choisissant une certaine valeur de la rigidité magnétique $B\rho$, on peut sélectionner un certain type de particules d'énergies et de masse données. En choisissant une autre valeur de $B\rho$, d'autres types de particules peuvent être sélectionnés. Les taux de comptage dans les détecteurs CsI situés sur les quatrième et cinquième anneau, donc à des angles relativement élevés, sont assez faibles car les particules sont surtout émises vers l'avant. Pour augmenter ces taux, des cibles d'or placées à des positions 9.5 cm et 84 cm en amont de la position centrale des cibles sont utilisées.

Pour la détermination de la fonction réponse, un point de départ commun à tous les calculs est la formulation de Birks [12] qui relie la lumière spécifique dL/dx en fonction de la perte d'énergie spécifique dE/dx .

$$dL/dx = S(dE/dx)/(1 + QdE/dx)$$

où S est l'efficacité de scintillation et Q est la constante de Birks dite facteur de quenching. Se basant sur cette formule, Horn et al. [13] ont proposé pour les CsI une fonction réponse dépendant de l'énergie E , du numéro atomique Z et du nombre de masse A .

$$L = a_0 + a_1\{E - a_2AZ^2\ln[(E + a_2AZ^2)/a_2AZ^2]\}$$

où a_1 et a_2 sont des facteurs qui dépendent du gain d'amplification et de l'efficacité de scintillation et a_0 est un facteur qui dépend uniquement de l'électronique. D'autres auteurs [14] ont proposé une fonction réponse pour des ions de $Z < 36$ et d'énergies jusqu'à 25 A MeV.

$$L = c_1\gamma E + c_2\beta(e^{-\alpha E} - 1)$$

où α, β et γ dépendent du numéro atomique Z et c_1 et c_2 dépendent de l'électronique utilisée et de l'efficacité de scintillation. Dans les deux cas, une dépendance en fonction de la masse a été observée, c'est à dire que pour une énergie donnée, la lumière émise par les isotopes lourds est plus petite que celle produite par les plus légers. Toutefois ces formules ne sont pas très pratiques lors de l'analyse car elles relient la lumière émise L en fonction de l'énergie E et non l'inverse.

Pour les détecteurs phoswich, la lumière émise peut être exprimée, d'après Bechetti et al. [15] par $E = F(Z)L\gamma$ où $F(Z)$ est une fonction polynômiale du numéro atomique Z . Pouliot et al. [16] ont introduit une correction en multipliant l'expression par une fonction $G(A)$ dépendant du nombre de masse A et ont proposé pour le paramètre γ l'expression suivante.

$$\gamma = 0.8 + 0.4/Z^{1.6}$$

5. Conclusion

Un ensemble multidétecteur à scintillation constitué actuellement de 80 détecteurs a été décrit et ses performances reportées. Par rapport aux autres systèmes actuellement utilisés, il présente la particularité d'être composé à la fois par des détecteurs de type phoswich et de scintillateurs Csl. De nombreux travaux consacrés récemment à l'étude des détecteurs Csl ou phoswich [17,18,19] ont montré que la réponse de ces scintillateurs à des ions lourds d'énergies intermédiaires n'est pas encore quantitativement bien élucidée. Cependant, cette difficulté peut être évitée en étalonnant les détecteurs en énergie. Dans notre cas, l'utilisation de la technique des faisceaux secondaires s'est révélée être très efficace. La couverture angulaire du système de détection a permis l'étude des mécanismes de réaction aux énergies intermédiaires pour les collisions périphériques ainsi que pour les collisions centrales dans le cas de la cinématique inverse (projectile lourd et cible légère). Pour augmenter encore plus la couverture angulaire du système de détection, d'autres anneaux dont les scintillateurs prototypes sont en développement, pourraient être ajoutés au système.

Références

- [1] D. Drain, A. Giorni, D. Hilscher, C. Ristori, J. Alarja, G. Barbier, R. Bertholet, R. Billery, B. Chambon, B. Cheynis, J. Crançon, A. Dauchy, P. Désesquelles, A. Fontenille, L. Guyon, D. Heuer, A. Lières, M. Maurel, E. Monnard, C. Morand, H. Nifenecker, C. Pastor, J. Poux, H. Rossner, J. Saint-Martin, F. Schussler, P. Stassi, M. Tournier et J.B. Viano, Nucl. Instr. and Meth. A281 (1989) 528.
- [2] G.D. Westfall, J.E. Yurkon, J. Van Der Plicht, Z.M. Koenig, B.V. Jacak, K. Fox, G.M. Crawley, M.R. Maier, B.E. Hasselquist, R.S. Tickle et D. Horn, Nucl. Instr. and Meth. A238 (1985) 347.
- [3] D.W. Stracener, D.C. Sarantites, L.G. Sobotka, J. Elson, J.T. Hood, Z. Majka, V. Abenante, A. Chbihi et D.C. Hensley, Nucl. Instr. and Meth. A294 (1990) 485.

- [4] A. Paden, H.H. Gutbrod, H. Löhner, M.R. Maier, A.M. Poskanzer, H. Riedesel, H.G. Ritter, H. Spieler, A. Warwick, F. Weik et H. Wieman, Nucl. Instr. and Meth. A203 (1982) 189.
- [5] J. Pouliot, G. Auger, P. Bricault, Y. Chan, D. Doré, S. Groult, D. Horn, S. Houde, R. Laforest, R. Roy, C. St-Pierre, Phys. Lett. B263 (1991) 18.
- [6] D. Guerreau dans Proceedings of The International School of Physics «Enrico Fermi» Course CXIII, ed. C. Detraz et P. Kienle (1991).
- [7] C. Ngô, R. Boisgard, J. Desbois, C. Cerruti, J.F. Mathiot, dans Proceedings of The International School of Physics «Enrico Fermi» Course CXIII, ed. P. Kienle, R.A. Ricci, A. Rubbiero (1989).
- [8] L.G. Moretto, Progress. Part. Nucl. Physics 21 (1989) 401
- [9] C.A. Pruneau, G.C. Ball, P. Dmytrenko, E. Hagberg, D. Horn, M.G. Steer, R.B. Walker, T. Whan, C. Rioux, R. Roy, C. St-Pierre, T.E. Drake, A. Galindo-Uribarri, Nucl. Instr. and Meth. A297 (1990) 404.
- [10] Code STOPX par T.C. Awes, basé sur U. Littmark et J.F. Ziegler, Handbook of Range Distributions for Energetic Ions in All Elements, ed. J.F. Ziegler (Pergamon,1980) Vol.6, p.4.
- [11] R.S. Storey, W. Jack, et A. Ward, Proc. Phys. Soc. 75 (1958) 72.
- [12] J.B. Birks, The Theory and Practice of Scintillation Counting (Pergamon,1964) 465.
- [13] D. Horn, G.C. Ball, A. Gallindo-Uribarri, E. Hagberg, R.B. Walker, R. Laforest, J. Pouliot, Nucl. Instr. and Meth. A320 (1992)273.
- [14] N. Colonna, G.J. Wozniak, A. Veek, W. Skulski, G.W. Goth, L. Manduci, P.M. Milazo et P.F. Mastinu, Nucl. Instr. and Meth. A321 (1992) 529.
- [15] F.D. Bechetti, C.E. Thorn et M.J. Levine. Nucl. Instr. and Meth. 138 (1976) 93.
- [16] J. Pouliot, Y. Chan, A. Dacal, A. Harmon, R. Knop, M.E. Ortiz, E. Plagnol, R.G. Stokstad. Nucl. Instr. and Meth. A270 (1988) 69.
- [17] E. Valtonen, J. Peltonen, J.J. Torsti, Nucl. Instr. and Meth. A28 (1990) 169.
- [18] D.W. Stracener, D.G. Saratites, L.G. Sobotka, J. Elson, J.T. Hood, Z. Majka, V. Abenante, A. Chbihi, D.C. Hensley Nucl. Instr. and Meth. A294 (1990) 485.
- [19] C.J.W. Twenhöfel, P.F. Box, P. Schotanus, T.M.V. Bootsma, G.J. Van Nieuwenhuizen, P. Decowski et R. Kamermans, Nucl. Instr. and Meth. B51 (1990) 58.



Etude de la réponse d'un détecteur Si irradié par des neutrons de 1 MeV

Patrick Roy

**Université de Montréal
Laboratoire de physique nucléaire
Case postale 6128, succursale A
Montréal, Québec
H3C 3J7**

Directeur: Claude Leroy

Introduction

Des études très poussées sont menées actuellement sur les dommages créés par les radiations dans les détecteurs au silicium, en vue de leur utilisation dans des expériences de physique des particules à haute énergie (Large Hadron Collider, CERN, Genève, Suisse) [1,2].

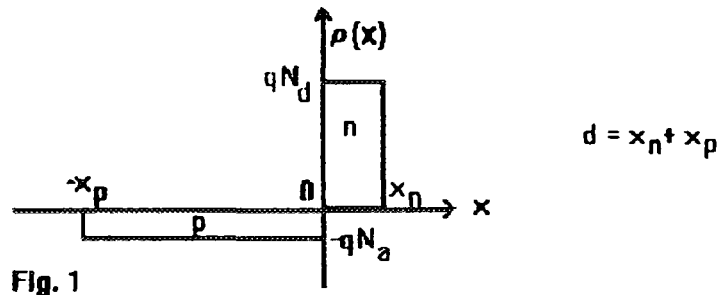
Ces détecteurs sont soumis à de fortes doses de radiations (neutrons, protons, particules ionisées) dans l'environnement expérimental et sont donc sujet à la dégradation de leurs propriétés électriques [3,4,5] qui se traduit par:

- une forte augmentation du courant inverse
- une perte d'efficacité de la collection de charge à cause du piégeage
- une possible inversion du type de la jonction.

Dans ce travail, nous étudions la réponse d'un détecteur silicium de type n (single pad), irradié par des neutrons de 1 MeV. L'irradiation a été effectuée en décembre 1991 auprès de l'accélérateur PSAIF du CERN. Le détecteur ($S = 1 \text{ cm}^2$, $w = 317 \text{ }\mu\text{m}$) a été soumis à des fluences de $.26 \times 10^{13}$ à 11.19×10^{13} neutrons / cm^2 . Par la suite, le détecteur a été placé devant une source d' ^{241}Am , pour étudier sa réponse au passage de particules alpha (5.49 MeV). Il était relié à un amplificateur et à un oscilloscope pour visualiser l'impulsion recueillie aux bornes du détecteur.

Modèle théorique:

On considère une distribution de charge uniforme des électrons dans la région n, et des trous dans la région p de la jonction (Fig. 1).



À partir de l'équation de Poisson et en considérant N_d , N_a constants, on peut écrire:

$$\frac{d^2V}{dx^2} = \frac{-\rho(x)}{\epsilon} = \begin{cases} +\frac{qN_d}{\epsilon} & 0 < x < x_n & (1a) \\ -\frac{qN_a}{\epsilon} & -x_p < x < 0 & (1b) \end{cases}$$

Une première intégration nous donne le champ électrique causé par la séparation de charges. Avec les conditions aux limites $E(x_n) = 0$ et $E(x_p) = 0$, on trouve:

$$E(x) = -\frac{dV}{dx} = \begin{cases} -\frac{qN_d}{\epsilon}(x - x_n) & 0 < x < x_n & (2a) \\ +\frac{qN_a}{\epsilon}(x + x_p) & -x_p < x < 0 & (2b) \end{cases}$$

Si on applique une différence de potentiel $-V_b$ du côté p de la jonction et qu'on néglige le potentiel de contact ($V_0 \approx 0.5$ Volt), avec $V(-x_p) = -V_b$ et $V(x_n) = 0$, on a:

$$V(x) = \begin{cases} -\frac{qN_d}{2\epsilon}(x - x_n)^2 & 0 < x < x_n & (3a) \\ +\frac{qN_a}{2\epsilon}(x + x_p)^2 - V_b & -x_p < x < 0 & (3b) \end{cases}$$

En $x = 0$, on a :

$$-\frac{qN_d}{2\epsilon}x_n^2 = \frac{qN_a}{2\epsilon}x_p^2 - V_b \quad (4)$$

Le voltage minimum à appliquer pour que le détecteur soit complètement déplété ($d=w$ sur Fig. 2) est :

$$V_{b_{min}} = V_d = \frac{q}{2\epsilon}(N_d x_1^2 + N_a x_2^2) \quad (5)$$

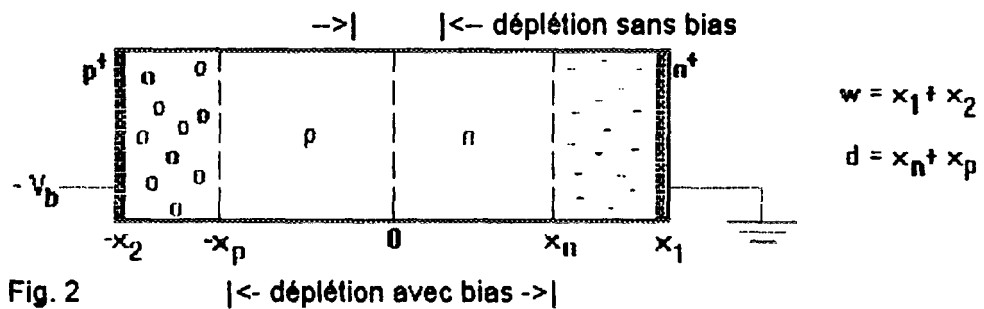


Fig. 2

Le détecteur étant totalement déplété, on aura donc :

$$w = x_1 + x_2 = \sqrt{\frac{2eV_d}{q} \frac{N_a + N_d}{N_a N_d}} \quad (6)$$

Dans notre cas, le détecteur est de type n. C'est-à-dire que $N_d \gg N_a$. En utilisant l'équation de neutralité ($N_d x_1 = N_a x_2$), on a $x_2 \gg x_1$.

$$\text{d'où } w \approx x_2 \approx \sqrt{\frac{2eV_d}{qN_a}} \quad (7)$$

$$\text{et } \frac{dV}{dx} = -\frac{qN_a}{\epsilon}(x-w) \quad 0 < x < w \quad (8)$$

La tension de déplétion s'écrit alors :

$$V_d = \frac{w^2 q N_a}{2\epsilon} \quad (9)$$

Les charges s'accablent de chaque côté de la jonction, donc la région de déplétion se comporte comme un condensateur chargé. La capacité par unité d'aire est :

$$C = \frac{\epsilon}{d} = \sqrt{\frac{q\epsilon N_a}{2V_b}} \quad \begin{array}{l} 0 \leq d \leq w \\ 0 \leq V_b \leq V_d \end{array} \quad (10)$$

où d est la longueur déplétée.

Puisque la tension appliquée est supérieure à V_d , la jonction est sur-déplétée. Il y a donc une composante supplémentaire qui s'ajoute au champ:

$$E(x) = -\frac{dV}{dx} - \frac{V - V_d}{w} = \frac{2V_d}{w^2}(x - w) - \frac{V - V_d}{w} \quad (11a)$$

Qu'on peut mettre sous une forme plus pratique, soit:

$$E(x) = b(x - a) \quad (11b)$$

$$\text{Où } b = \frac{2V_d}{w^2} \quad \text{et} \quad a = \frac{w}{2} + \frac{V}{bw} \quad (11c)$$

Pour obtenir la réponse en courant du détecteur, il faut donc avoir une équation du courant en fonction du temps. On part du fait qu'un électron, ou un trou, induit une charge ΔQ sur l'électrode:

$$\Delta Q = q \frac{\Delta x}{w} \quad (12)$$

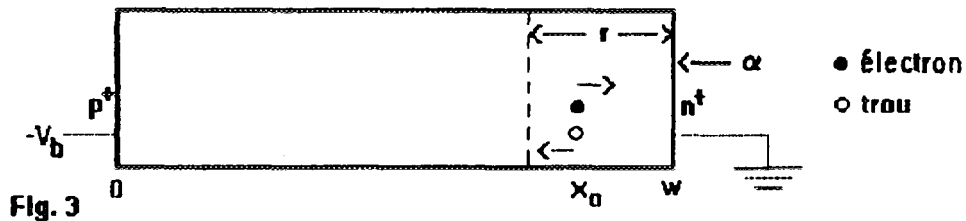
Le courant s'obtient alors par:

$$I(x) = \frac{\Delta Q}{\Delta t} = \frac{q \Delta x}{w \Delta t} = \frac{q}{w} \mu E(x) \quad (13)$$

Où on a utilisé la vitesse de dérive donnée par:

$$\frac{dx}{dt} = \mu E(x) \quad (14)$$

En intégrant l'équation (14) on obtient $x(t)$. On suppose pour ce faire que la création de la paire électron-trou s'est produite en x_0 (Fig. 3), que la particule alpha était incidente en $x = w$ (back) soit le côté n de la jonction et que la tension de bias négative est appliquée en $x = 0$.



$$x_h(t) = a + (x_0 - a) \exp(\mu_h bt) \quad (15.a)$$

Où $\mu_{e,h}$ constantes

$$x_e(t) = a + (x_0 - a) \exp(-\mu_e bt) \quad (15.b)$$

On définit deux temps de collection, soit celui où les électrons sont collectés en $x = w$ et celui où les trous sont collectés en $x = 0$.

$$T_{ch} = \frac{1}{b\mu_h} \ln\left(\frac{a}{a - x_0}\right) \quad \text{et} \quad T_{ce} = \frac{1}{b\mu_e} \ln\left(\frac{a - x_0}{a - w}\right) \quad (16)$$

On réintroduit les valeurs de $x(t)$ dans $I(x)$, ce qui nous donne le courant produit par la paire électron-trou créée en x_0 .

$$I_h(t) = \frac{q}{w} \mu_h b(x_0 - a) \exp(\mu_h b t) \quad 0 \leq t \leq T_{ch} \quad (17a)$$

$$I_e(t) = \frac{q}{w} \mu_e b(x_0 - a) \exp(-\mu_e b t) \quad 0 \leq t \leq T_{ce} \quad (17b)$$

Afin d'obtenir le signal tel qu'il est fourni par l'oscilloscope, il faut tenir compte de la réponse du système. L'amplificateur a une résistance d'entrée (R_a) de 50 ohms et un gain (G_a) de 1000. On considère qu'il forme un simple circuit RC, où C est la capacité du détecteur, dont la réponse est représentée par une gaussienne ayant comme temps caractéristique $\sigma = R_a C$. Le signal réel est simplement la convolution du courant et de la réponse du système. Il faut sommer sur tous les points de créations de paires électrons-trous.

$$V(t) = \sum_{x_0} \frac{\int_{-\infty}^{\infty} I(t_0) \cdot \text{réponse}(t, t_0) dt_0}{\int_{-\infty}^{\infty} \text{réponse}(t, t_0) dt_0} G_a R_a \quad (18)$$

La particule alpha a une énergie de 5.5 MeV. Elle perd environ 0.5 MeV dans la distance (5 mm) séparant la source du détecteur. La création d'une paire électron-trou nécessite 3.62 eV. On a donc environ 1.4 million de paires (n) créées sur le parcours de la particule alpha ($r \approx 25 \mu\text{m}$). Plutôt que de considérer la création et le déplacement de ces charges séparément, on considère qu'elles se déplacent par groupe, qu'on définit par la quantité n/L :

$$L = \frac{r}{\Delta x_0} \quad \text{où } \Delta x_0 = \text{le pas utilisé pour } x_0$$

$$V(t) = \frac{n G_a R_a}{L \sqrt{2\pi} \sigma} \sum_{x_0} \int_0^{T_c} I(t_0) \cdot \exp\left[-\frac{(t_0 - t)^2}{2\sigma^2}\right] dt_0 \quad (19)$$

En faisant analytiquement l'intégration et en définissant de nouvelles variables, on obtient:

$$B_e = -b \mu_e \quad B_h = b \mu_h \quad (20a)$$

$$T_{e,h} = \sigma^2 B_{e,h} + t \quad (20b)$$

$$F = -\frac{G_a R_a q n b}{2Lw} \quad (20c)$$

$$F_{e,h} = F \mu_{e,h} \exp[B_{e,h} t + \frac{1}{2}(\sigma B_{e,h})^2] \quad (20d)$$

Ce qui nous permet d'écrire:

$$V_e(t) = F_e(a - x_0) \left(\operatorname{erf}\left(\frac{T_{ce} - T_e}{\sigma\sqrt{2}}\right) + \operatorname{erf}\left(\frac{T_e}{\sigma\sqrt{2}}\right) \right) \quad (21a)$$

$$V_h(t) = F_h(a - x_0) \left(\operatorname{erf}\left(\frac{T_{ch} - T_h}{\sigma\sqrt{2}}\right) + \operatorname{erf}\left(\frac{T_h}{\sigma\sqrt{2}}\right) \right) \quad (21b)$$

Le détecteur a été irradié par des neutrons de 1 MeV à différentes fluences. L'interaction des neutrons avec les atomes de silicium produit des défauts dans le réseau cristallin (centres de dommage). Ceci introduit des niveaux d'énergie profonds dans la bande interdite, qui peuvent piéger les électrons ou les trous. On tient compte de cet effet en introduisant un temps caractéristique de piégeage (τ). Ce qui nous donne donc comme relation pour le nombre de charges $n(t)$ [6]:

$$n(t) = n_0 \exp\left(\frac{-t}{\tau}\right) \quad (22)$$

L'introduction de l'exponentielle cause simplement un décalage des variables B:

$$B_h = b \mu_h - 1 / \tau_{th} \quad \text{et} \quad B_e = b \mu_e - 1 / \tau_{te} \quad (23)$$

On a considéré que les mobilités ($\mu_{e,h}$) étaient constantes. Cependant la vitesse de dérive des électrons et des trous atteint la saturation lorsque le champ électrique devient trop intense [8,9,10]. On montre sur la figure 5 le comportement des mobilités en fonction du champ. Dans notre cas, on s'attend à ce que le champ électrique se situe entre 3×10^3 et 7×10^3 volts / cm. D'après la figure on peut considérer que μ_h est constante. Le comportement de la mobilité des électrons étant sensiblement le même, on utilise la formulation donnée dans la référence [8], qui donnent des équations simples pour la convolution.

$$\mu_e(x) = \mu_{e0} \sqrt{\frac{-E_e}{E(x)}} \quad (24)$$

On utilise la même méthode qu'auparavant pour obtenir le courant créé par les électrons ce qui nous donne:

$$I_e(t) = -\frac{q\mu_{e0}}{w} \left(\sqrt{(a-x_0)E_e} b - \frac{\mu_{e0}E_e b t}{2} \right) \quad (25)$$

$$T_{ce} = \frac{2}{\mu_{e0} \sqrt{E_e}} \left(\sqrt{\frac{a-x_0}{b}} - \sqrt{\frac{a-w}{b}} \right) \quad (26)$$

Comme précédemment on introduit le piégeage et on refait la convolution. On obtient:

$$V_e(t) = F \mu_{e0} (D_1 + D_2) \quad (27)$$

Avec:

$$D_1 = \left(\operatorname{erf}\left(\frac{T_{ca} - t}{\sigma\sqrt{2}}\right) + \operatorname{erf}\left(\frac{t}{\sigma\sqrt{2}}\right) \right) \left(\sqrt{\frac{(a - x_0)E_a}{b}} - \frac{\mu_{a0}E_a t}{2} \right) \quad (28a)$$

$$D_2 = \frac{\mu_{a0}E_a\sigma}{\sqrt{2\pi}} \left(\exp\left(\frac{-(T_{ca} - t)^2}{2\sigma^2}\right) - \exp\left(\frac{-t^2}{2\sigma^2}\right) \right) \quad (28b)$$

On considérait initialement que la particule alpha déposait son énergie uniformément, mais ce n'est pas le cas. En utilisant les données fournies par la référence [7] et à l'aide d'une interpolation par spline cubique naturelle, on donne un poids différent aux groupes en fonction de x_0 .

$$\text{groupe} = \frac{n \cdot \text{densité}(x_0)}{\sum_{x_0} \text{densité}(x_0)} \quad (29)$$

Résultats et discussion:

Nous montrons dans la figure 4, la réponse du détecteur au passage de particules alpha (5.5 MeV). Le fit est obtenu par minimisation du χ^2 .

La fig. 6 montre l'évolution de la concentration effective (N_{eff}) en fonction de la fluence (Φ). N_{eff} change de signe à partir de $\Phi \approx 3 \times 10^{13}$ n / cm² et croît ensuite de façon linéaire. La jonction qui était à l'origine de type n, a changé en une jonction apparente de type p. Ce résultat a été observé par plusieurs auteurs [11,12,13], pour une fluence du même ordre, en utilisant d'autres méthodes telle que la mesure de la caractéristique C-V. L'évolution de la concentration effective, et par conséquent la tension de déplétion (V_d) est décrite par une expression de la forme

$$N_{eff} = N_0 e^{-c\Phi} - \beta\Phi$$

où le terme en exponentielle décrit la décroissance de la concentration des ions donneurs et le terme linéaire montre la création d'ions accepteurs.

D'après la figure 7, on constate que lorsque la fluence est nulle il y a peu de piègeage (τ_h est assez grand devant $T_{ch} \approx 15$ ns) alors qu'il augmente (τ_h diminue) de façon linéaire en fonction de la fluence.

REFERENCES:

- 1) T. Akesson, Proc. workshop on physics at future accelerators - La Thuile (1987), CERN 87-07 vol. 1, p. 174
- 2) E. Fretwurst et al, Radiation hardness of silicon detectors for future colliders, Sixth European symposium on semiconductor detectors, Milano, February 24-26, (1992)
- 3) E. Borchini et al, Nucl. Instr. and Methods A301, 215-218, (1991)
- 4) Z. Li and H.W. Kraner, IEEE Trans. Nucl. Sci. Vol. 38 No 2, (1992)
- 5) D. Pitzl et al, Nucl. Instr. and Methods A311, 98-104, (1992)
- 6) Z. Li and H.W. Kraner, Modelling and simulation of charge collection properties for neutron irradiated silicon detectors, présenté à Como 22-26 juin 1992.
- 7) C. F. Williamson, J-P Boujot, J. Picard, Tables of range and stopping power of chemical elements for charged particles of energy 0,05 to 500 MeV, 321, (1992)
- 8) A. Alberigi Quaranta et al, Nucl. Instrum. Methods 35, 93, (1965).
- 9) P. A. Blakey et al, IEEE Trans. Electron. Devices ED26, 1718, (1979)
- 10) S. R. Shukla and M. N. Sen, Solid-St. Electron. 35, 593-597, (1992)
- 11) F. Lemeilleur et al, IEEE Nucl. Sci. Symposium - Santa Fe Vol. 1, 308, (1991)
- 12) P. Giubellino et al, Nucl. Instr. and Methods A315, 156-160, (1992)
- 13) M. Edwards et al, Nucl. Instr. and Methods A310, 283-286, (1991)

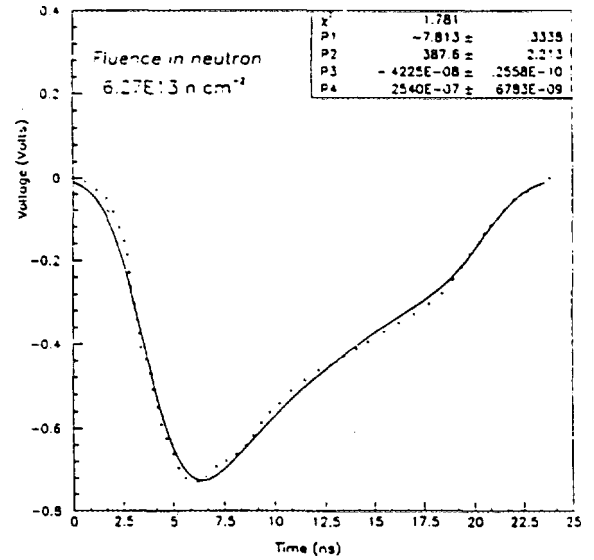
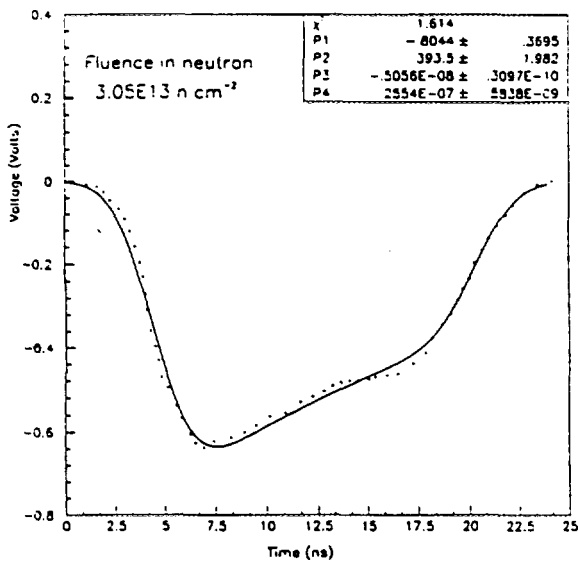
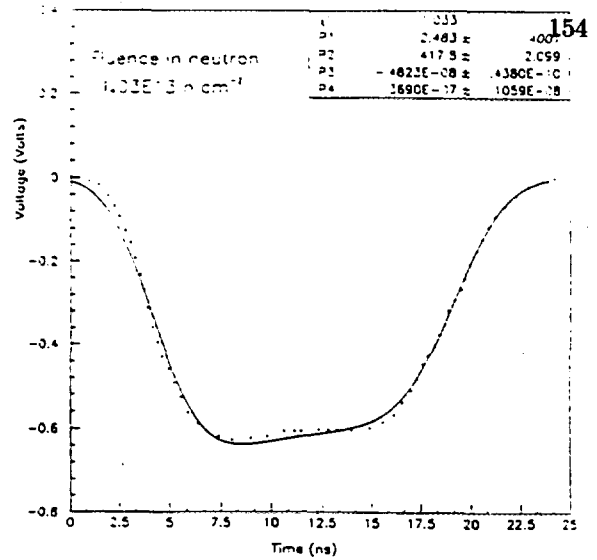
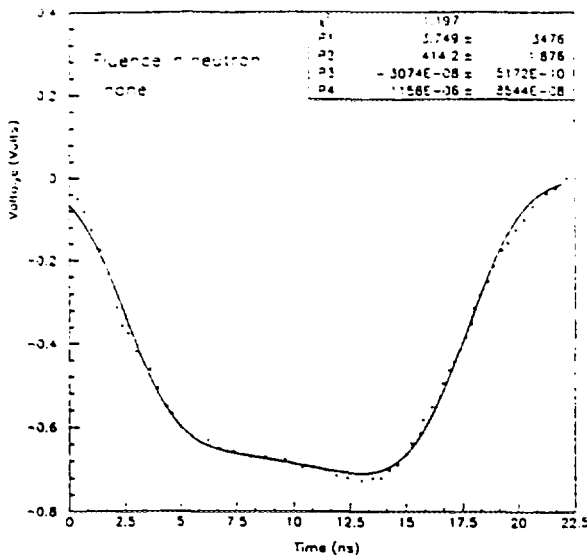
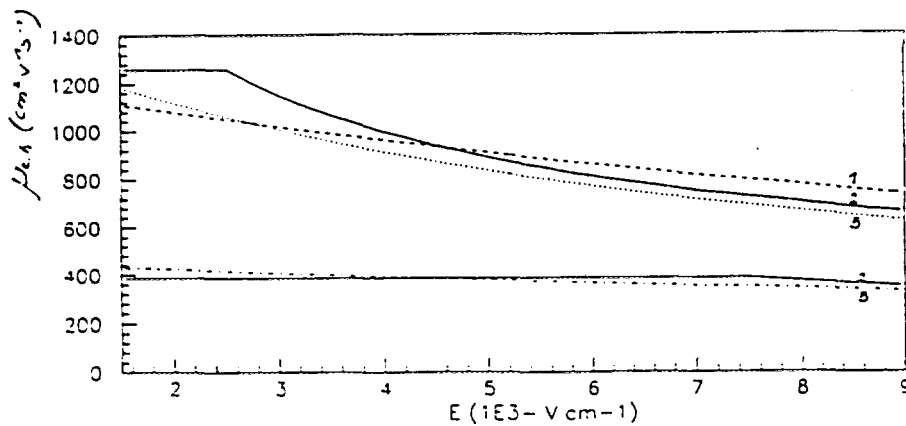


Fig. 4

P1: $N_{eff} = (N_d - N_a)$ (cm⁻³) P2: μ_h (cm² V⁻¹ s⁻¹)
 P3: Time shift (s) P4: τ_h Trapping time (s)



Figs: variations de μ_h en fonction de E à T = 300° K
 1: ref(9), 2: ref(9), 3: ref(10)

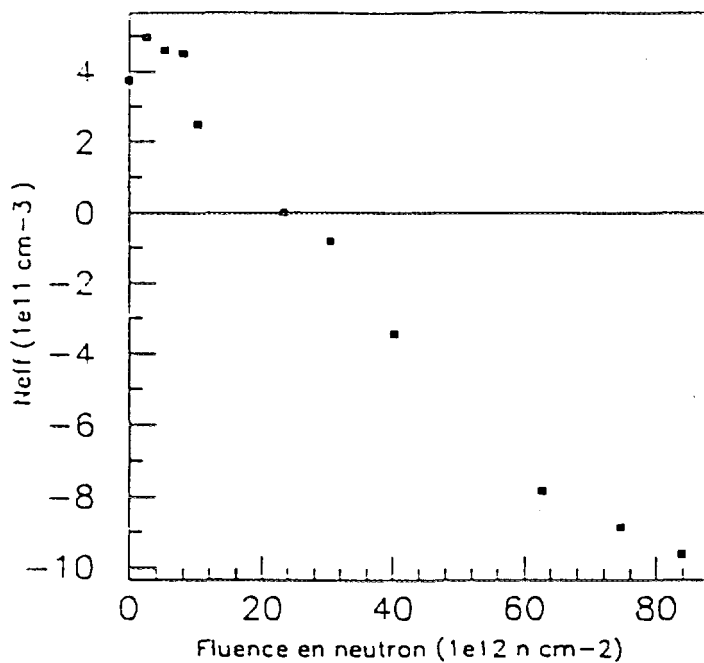


Fig. 6 Evolution de la concentration effective en fonction de la fluence. Le détecteur est de type N à l'origine

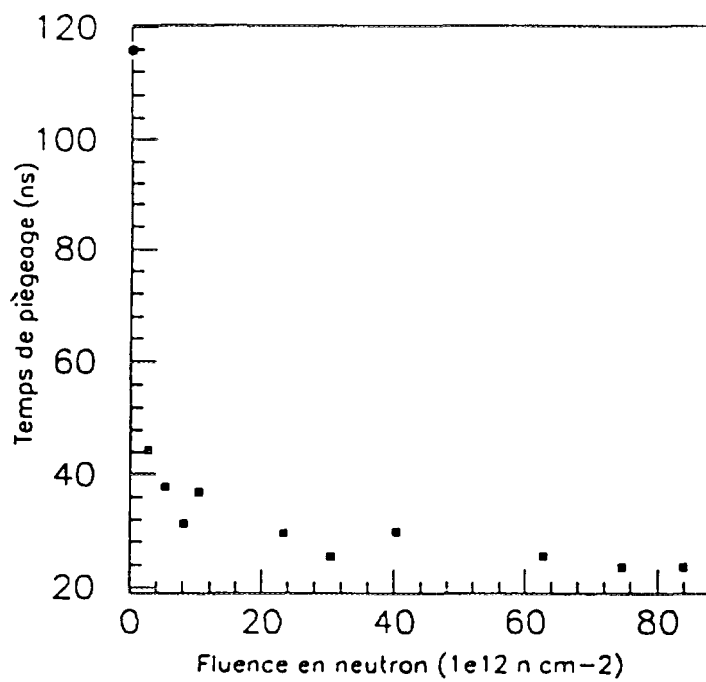


Fig. 7 Diminution du temps de piègeage en fonction de la fluence.



CA9700549

Speaker: Mamdooh Abdelbaky

Title: Design of Intermediate Energy Filters for Neutron Beams

University: University of New Brunswick

ABSTRACT

A computational technique is developed for the design of intermediate energy filters for neutron beams. This technique utilizes the phenomena of neutron windows associated with the resonance cross sections of certain elements. Neutron resonance scatterers are also used in combination with the primary filters. These scatterers soften the incident beam spectrum before its transmission through the filters. The filtered beam qualities are predicted via a special purpose Monte Carlo model. The analogue Monte Carlo technique was utilized here in order to allow accurate representation of the cross sections at the window energies of the filter materials. These fine cross section characteristics can be lost in any other multigroup transport calculations. The beam intensities and beam areas are calculated using a simple analytical model. Both the monte carlo and the analytical model can be used as a design package to develop a variety of intermediate energy neutron beams using different combination of materials and a high intensity neutron source such as a high flux research reactor. This design package is intended to be an alternative to the complicated and expensive experimental techniques which are commonly employed to specify the filter parameters. The above design package was utilized to propose two filter systems for intermediate energy neutrons using data of an existing research reactor. The calculated beam characteristics are compared with those obtained using experimental measurements in a similar research reactor facility. This comparison shows that the calculations and measurements are in good agreement.



Développement et performances de détecteurs de particules chargées appliqués à l'étude des réactions avec ions lourds

Mireille GOURDE, Luc BEAULIEU, Diane DORÉ, Richard LAFOREST, Jean POULIOT, René ROY, Claude ST-PIERRE

Université Laval

Département de physique
Pavillon Vachon
G1K 7P4

directeur : René Roy

Cette présentation décrira le développement ainsi que les premières performances d'un nouveau détecteur de particules chargées. Ceux-ci furent développés pour compléter un système de détection installé aux Laboratoires de Chalk River et utilisé dans le cadre d'études sur les réactions avec ions lourds. La présentation de M. Samri traite de la nécessité d'un tel système et de ses principales caractéristiques.

Quant à nous, nous préciserons, dans un premier temps, les informations que nous désirons obtenir des détecteurs ainsi que les paramètres spécifiques à leur cas dont il faudra tenir compte. Une description détaillée du détecteur et de ses composantes suivra avec quelques remarques au sujet de l'assemblage. Pour terminer, les résultats positifs obtenus lors de tests et des premières expériences réalisés à Chalk River seront présentés.

SPÉCIFICATIONS

Les données à obtenir des détecteurs sont la charge de la particule, sa masse pour les cas de $Z=1$ et 2 , et l'énergie de la particule. Ils devront couvrir la région située entre 24° et 34° et entre 34° et 46° par rapport au faisceau afin de compléter la matrice de détecteurs déjà existante. À ces angles le taux de comptage est moins élevé qu'à des angles inférieurs, il ne sera donc pas nécessaire d'avoir une constante de temps du signal très courte. Puisque les expériences au cours desquelles le système de détection sera mis à contribution utiliseront des faisceaux d'énergies intermédiaires, les détecteurs devront avoir la capacité d'arrêter des fragments possédant jusqu'à 100 MeV/A sur une distance raisonnable.

PROFIL DU DÉTECTEUR

La méthode privilégiée pour détecter des particules chargées avec un multidétecteur possédant les caractéristiques requises est la scintillation. Le scintillateur principal sera un cristal de CsI(Tl) et un scintillateur plastique mince le complétera (figure 1). Un guide de

lumière facilitera le passage de l'impulsion lumineuse entre le scintillateur et le photomultiplicateur. Ce dernier transforme l'impulsion lumineuse en impulsion électrique qui sera par la suite traitée électroniquement. Les détecteurs seront montés en une matrice consistant en deux anneaux concentriques centrés sur le faisceau et la cible formant ainsi une calotte sphérique de 24° à 46° . Pour pouvoir faire des mesures en coïncidence, il faut que le nombre de détecteurs soit de l'ordre du carré de la multiplicité à étudier. Dans ce cas-ci, on désire observer jusqu'à 8-10 événements en coïncidence: chaque anneau du multidétecteur sera donc constitué de 16 détecteurs pour un total de 80 unités.

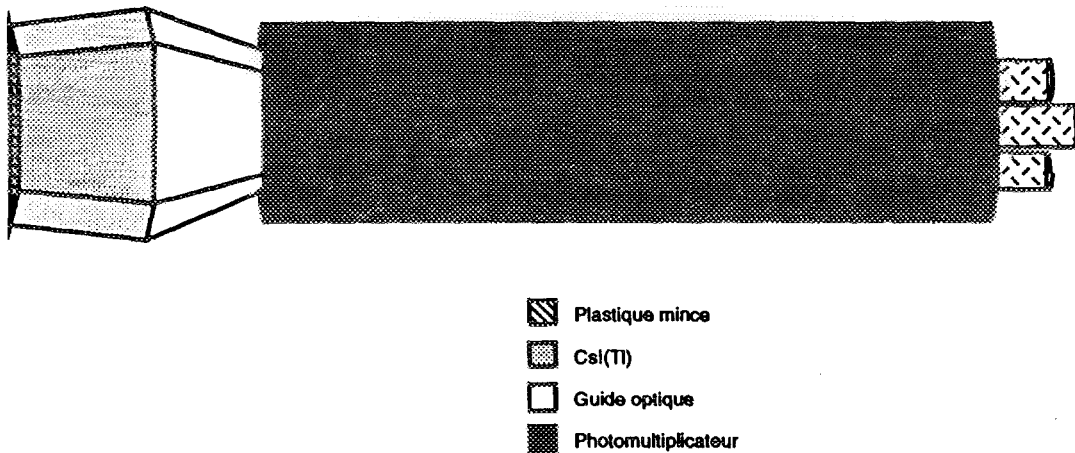


Figure 1. Profil d'un détecteur plastique-CsI(Tl)

LE SCINTILLATEUR PRINCIPAL

Dans le choix des composantes le scintillateur est évidemment le plus critique. Les qualités d'un bon scintillateur sont (1, 2):

- une émission de lumière proportionnelle à l'énergie de la particule captée pour la plage qui nous intéresse,
- une durée d'impulsion aussi courte que possible pour un temps de réponse rapide,
- la transparence à sa propre fluorescence,
- un bon rendement de production de photons,
- ne pas s'altérer avec le temps et d'un montage facile et robuste.

D'autres caractéristiques sont à rechercher pour l'application actuelle:

- la possibilité d'arrêter des particules ou ions à des énergies qui vont jusqu'à 100MeV/A,
- la capacité de discriminer les particules par leur charge Z jusqu'à 4, et par leur masse pour $Z \leq 2$.

Historique du CsI(Tl)

Un scintillateur qui rencontre ces critères est le CsI(Tl). C'est un scintillateur inorganique monocristallin. Les cristaux d'halogénures alcalins ont commencé à intéresser les chercheurs en physique nucléaire pendant les années '50(3,4,5,6,7,8). On a alors étudié les caractéristiques de scintillation de ces cristaux telles la longueur d'onde d'émission suivant la température et la concentration d'un dopant à l'intérieur du cristal (9). On a par la suite découvert dans le cas du CsI(Tl), une variation du temps de décroissance de l'impulsion lumineuse selon le type de particule absorbée (3,8,10). Des études un peu plus poussées ont démontré que l'impulsion observée était en fait le résultat de deux scintillations: l'une rapide et l'autre plus lente dont le temps de décroissance varie selon la nature de la particule détectée. L'impulsion peut s'écrire sous la forme:

$$L = A_l \exp (-t/\tau_l) + A_r \exp (-t/\tau_r)$$

où A_l et A_r sont les amplitudes des composantes lente et rapide respectivement et τ_l et τ_r les constantes de temps de ces composantes de scintillation.

On proposa alors une technique pour discriminer les particules selon la forme de l'impulsion. Quand on parle de particules, à cette époque on étudiait surtout les protons et les rayons α , β , et γ . Le cristal de CsI(Tl) fut par la suite délaissé entre 1960 et 1984 au profit des scintillateurs plastiques. Au début des années '80, les expériences exploitant des régions de plus en plus élevées en énergie et utilisant des faisceaux plus élevés en charge, l'intérêt pour les cristaux se raviva, entre autre parce que leur pouvoir d'arrêt est plus important. Grâce aux progrès faits depuis en électronique et dans les systèmes d'acquisition, on a pu développer une autre technique de discrimination par la forme de l'impulsion s'appliquant au cristal de CsI(Tl).

Caractéristiques du CsI(Tl)

Le CsI(Tl) est un matériau inorganique qui émet une impulsion lumineuse qui scintille à une longueur d'onde autour d'un maximum à 580 nm. Ceci correspond à une lumière dont la couleur tend vers le vert. L'indice de réfraction est passablement élevé soit de 1,788. Il faudra en tenir compte lors du couplage optique avec le photomultiplicateur. Le cristal a une densité de 4,51 g/cm³, ce qui permettra d'arrêter des particules possédant des énergies jusqu'à 100AMeV sur une distance raisonnable. C'est un scintillateur efficace puisqu'il fournit un rendement à 95% de celui de l'anthracène. Mécaniquement c'est un matériau résistant, facile à usiner et beaucoup moins hygroscopique que le NaI(Tl), un cristal équivalent qui a souvent été employé dans le passé. Possédant un point de fusion assez élevé, 620°C, il résiste bien à la chaleur.

L'amplitude de l'impulsion en fonction du temps peut se décrire de la manière suivante:

$$L = A_l \exp (-t/\tau_l) + A_r \exp (-t/\tau_r)$$

- où
- le rapport A_l/A_l+A_r augmente quand la densité d'ionisation diminue,
 - la constante de temps de la composante rapide, τ_r , augmente avec la diminution de la densité d'ionisation,
 - la constante de temps de la composante lente ne varie pas avec la nature de la particule (11).

Le temps de décroissance de l'impulsion totale est d'environ 1100 ns, mais comme dit précédemment cette impulsion peut se décomposer et on retrouve alors un temps de décroissance rapide entre 400 ns et 700 ns et un temps de décroissance lent de 1000 ns (12).

LE PLASTIQUE MINCE

Le cristal de CsI(Tl) seul ne peut remplir toutes les fonctions qu'on attend du détecteur. Son pouvoir de discrimination tend à saturer pour des Z (charges) supérieures à 3 (11), c'est-à-dire qu'au-delà du lithium il devient difficile de reconnaître l'ion détecté. Il s'agit alors de passer en mode "phoswich". Le plastique mince est placé sur la face avant du cristal de CsI(Tl) de sorte qu'une particule doit le traverser pour parvenir au cristal. Une partie de l'énergie est alors absorbée par le plastique et on la surnommara ΔE . Le reste de l'énergie sera complètement absorbé par le cristal et sera désigné E. En mettant en graphique les deux quantités d'énergie on parvient à discriminer les particules (fig. 2).

Caractéristiques du plastique mince

Le plastique mince utilisé ici est le NE-102A. Il a une épaisseur de 80 μm . Ce plastique émet sur une distribution centrée sur 423 nm. La densité du plastique est de 1.032 g/cm^3 , ce qui explique un pouvoir d'arrêt beaucoup moins important que le CsI(Tl) donc une perte d'énergie partielle, même à Z élevé, ΔE pour une particule. Son efficacité est de 65% de celle de l'anthracène, moins efficace que le cristal, mais, comme on le verra dans la section sur le photomultiplicateur, bénéficiera d'une amplification plus importante par le photomultiplicateur. Le signal du plastique est beaucoup plus rapide: sa constante de temps est de 2,4 ns, comparativement à 1 μs pour le CsI(Tl).

LE GUIDE DE LUMIÈRE

Il y a deux raisons qui nous ont amenés à l'utilisation d'un guide de lumière entre le cristal de CsI(Tl) et le photomultiplicateur. La plus évidente est la différence entre la surface de la face de sortie du cristal et celle de la fenêtre du photomultiplicateur. La face du cristal est de forme trapézoïdale ayant pour dimensions:

	<u>petit anneau</u>	<u>grand anneau</u>
base	5,254 cm	6,798 cm
sommet	3,822 cm	5,284 cm
hauteur	4,117 cm	4,966 cm

La fenêtre du photomultiplicateur quant à elle est circulaire et possède un diamètre de 3,8 cm.

Il y a aussi la différence importante entre l'indice de réfraction du cristal et du verre de la fenêtre. On sait que les pertes de lumière en réflexion augmentent avec la différence d'indice de réfraction lorsqu'on passe d'un milieu à indice élevé vers un milieu à indice plus faible. Les graphiques de la figure 3 montrent la variation de ces pertes pour le passage CsI(Tl)($n=1.788$)→guide→fenêtre du photomultiplicateur($n=1.55$) pour différents indices de réfraction pour le guide.

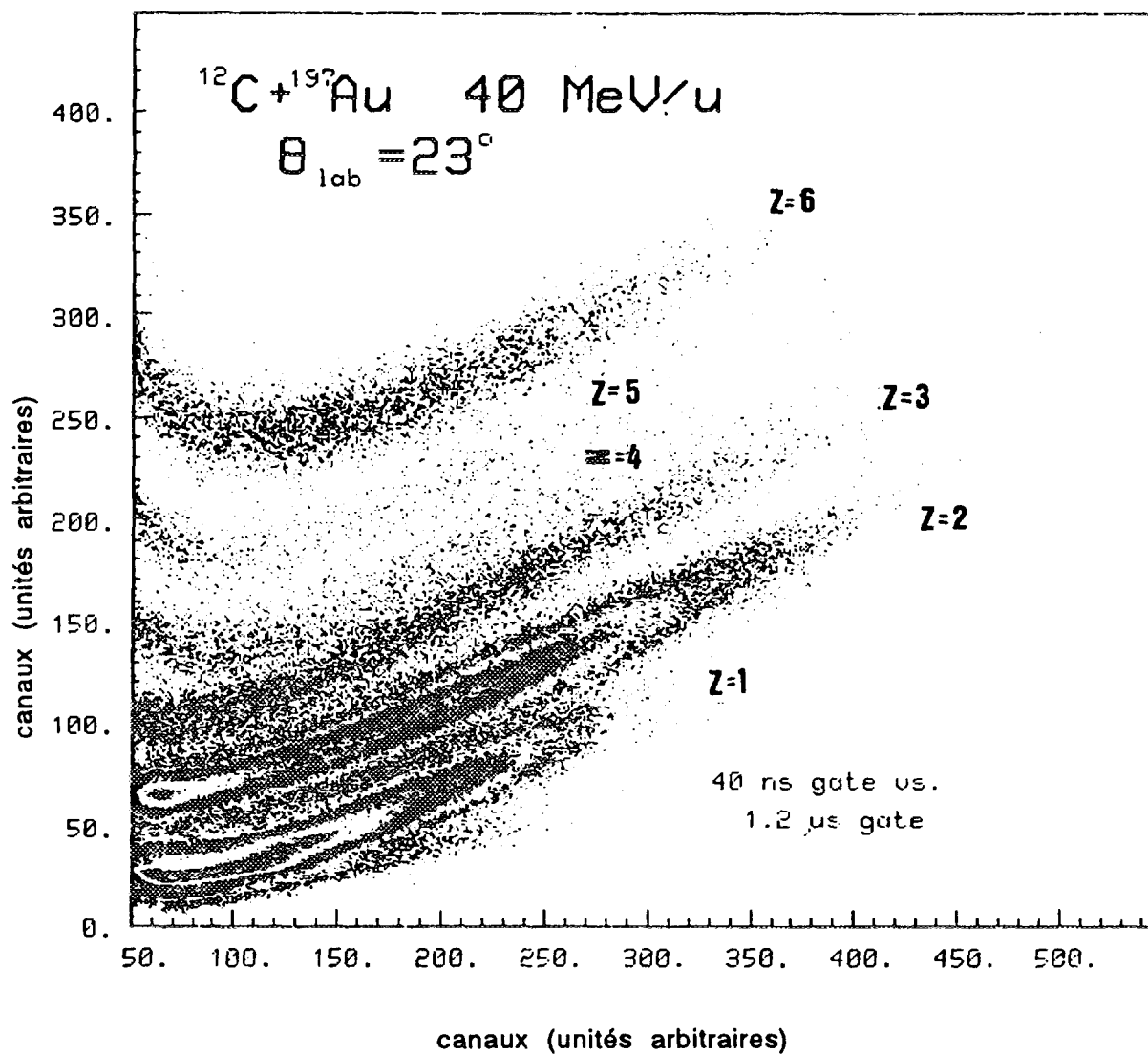


Figure 2. Spectre obtenu avec le signal du scintillateur plastique versus la composante lente du cristal de CsI(Tl). Les fragments sont ici discriminés en charge.

Le minimum de pertes se situe autour d'un indice de 1.65. Le verre nous offrait une gamme très étendue d'indice de réfraction où on pouvait facilement choisir celui qui nous convenait. Mais le verre est un matériau lourd et difficilement usinable, ce qui fait augmenter les coûts dramatiquement. Les plastiques, quant à eux, sont beaucoup plus légers. Ce qui n'est pas négligeable compte tenu que le cristal de CsI(Tl) est déjà un matériau lourd. Le plastique est aussi facilement usinable et son coût est très abordable si on compare au verre. Cependant il n'offre pas la diversité en indice de réfraction du verre et pour une bonne partie des plastiques qui offrent une bonne qualité optique nécessaire ici, l'indice de réfraction est plus faible que celui de la fenêtre du photomultiplicateur. La famille de plastiques qui offre l'indice de réfraction le plus élevé est celle des polycarbonates. Nous avons utilisé le Lexguard® qui possède un indice de 1,586 donc près de celui qui nous offre le minimum de pertes. Le guide a la forme d'une pyramide trapézoïdale tronquée dont le sommet s'inscrit à l'intérieur du diamètre de la fenêtre du photomultiplicateur. Nous avons calculé pour le guide une longueur de 2,54 cm. Le guide permet aussi d'isoler thermiquement le cristal du photomultiplicateur, la longueur d'onde et la constante de temps de l'impulsion étant influencées par la température du cristal.

LE PHOTOMULTIPLICATEUR

Le photomultiplicateur possède aussi une part importante dans la qualité des performances du détecteur. Il doit être bien adapté aux caractéristiques des impulsions lumineuses du cristal et du plastique scintillant. Le modèle H 3178 de Hamamatsu a été désigné comme étant le plus compatible. Sa plage de sensibilité en longueur d'onde doit couvrir celle où se fait l'émission par scintillation. Ici, comme nous l'avons mentionné plus tôt, la longueur d'onde d'émission du CsI(Tl) est autour de 560 nm et celui du plastique autour de 423 nm. Il est plus sensible au signal du plastique qu'à celui du CsI(Tl). C'est un photomultiplicateur à dynodes linéaires. Il fonctionne sous haute tension négative. L'amplification est de $1,5 \times 10^5$ à une tension de -1250 V. Le temps entre l'arrivée de l'impulsion lumineuse sur la photocathode et la sortie du signal électrique varie entre 47 ns et 40 ns pour la région de haute tension que nous utiliserons, soit entre -1000V et -1200V. Son temps de réponse doit être du même ordre ou même plus rapide que celui du scintillateur. Le temps de montée diminue avec l'augmentation de la tension appliquée au photomultiplicateur. Entre -1000V et -1200V, le temps de montée varie entre 5 ns à 4,2 ns.

ASSEMBLAGE DU DÉTECTEUR

La façon dont on assemble les composantes du détecteur est aussi importante que le choix de celles-ci. Différents aspects sont à considérer, tant pour obtenir un détecteur efficace que pour avoir un système solide et pratique.

POLISSAGE

L'expérience nous a démontré qu'on obtenait de meilleurs résultats quand les faces du cristal et du guide étaient polies. Après usinage, les parois des cristaux de CsI(Tl) présentaient une surface striée, marquée par la scie. Un polissage par sablage successifs a été effectué sur chaque face de tous les cristaux. Malheureusement le matériau ne permet pas d'obtenir un fini vraiment beau et brillant, mais le maximum a été fait. En ce qui concerne le guide, la même méthode a été appliquée mais avec de plus beaux résultats.

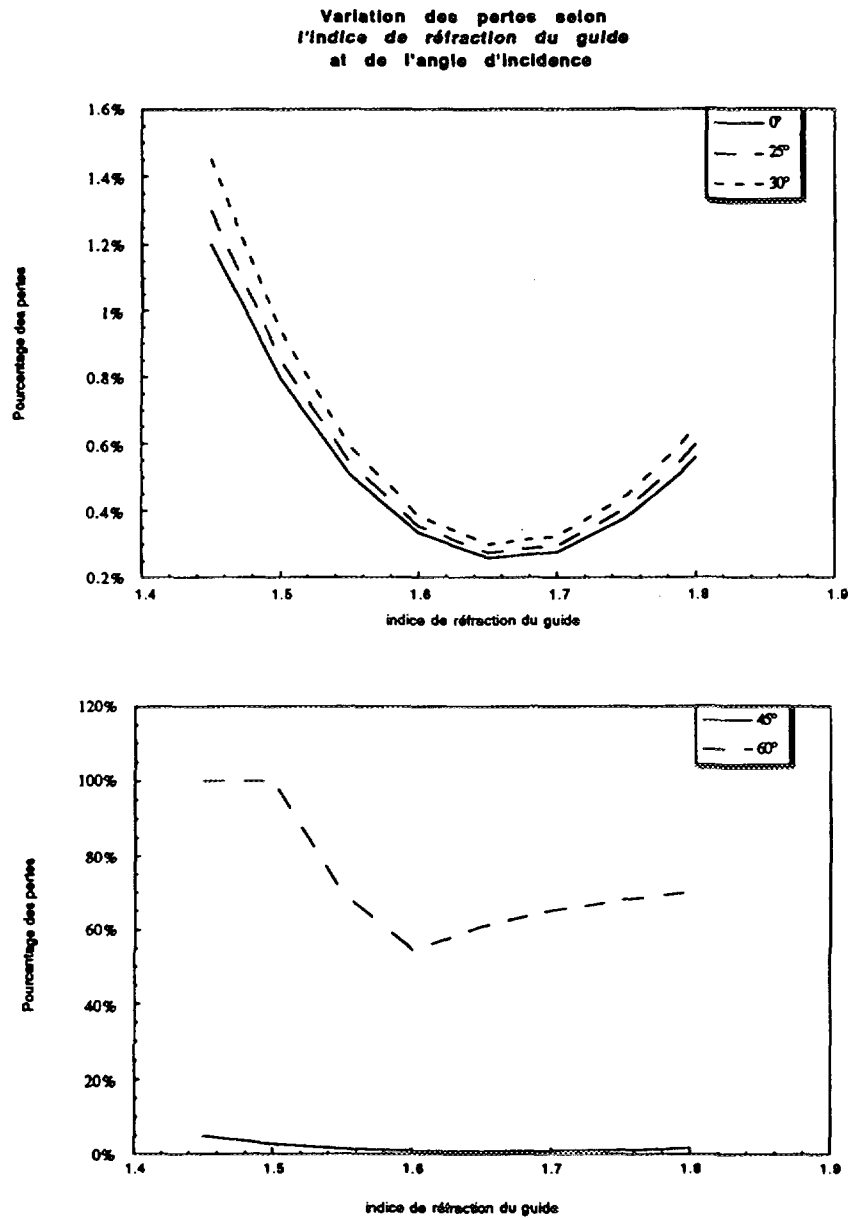


Figure 3. Graphiques démontrant la variation des pertes selon l'indice de réfraction du guide. a) pour incidence normale et pour 25° et 30° d'angle d'incidence. b) pour 45° et 60° d'angle d'incidence.

COLLAGE DES DIFFÉRENTES COMPOSANTES

Le choix du matériau du guide a été optimisé afin de parvenir à la meilleure transmission possible. Il ne fallait pas amenuiser cette optimisation par un mauvais choix de colle ou d'adhésif. Évidemment cette colle devait former un joint parfait sans bulle et sans défaut, présenter une grande transparence aux longueurs d'ondes des émissions fluorescentes ainsi qu'une bonne compatibilité avec les indices de réfraction du cristal et du guide. On a essayé d'appliquer la même technique que pour les pièces du guide, mais le polycarbonate n'adhère pas du tout au cristal de Csl(Tl). Les adhésifs optiques n'offrent généralement que des indices de réfraction trop faibles. Un adhésif optique à durcissement par rayons ultra-violet conçu spécialement pour les polycarbonates a été sélectionné. Il s'agit du Norland optical adhesive NOA 68.

Deux autres joints importants étaient à faire: entre le scintillateur plastique et le Csl ainsi qu'entre le guide et la fenêtre du photomultiplicateur. Dans ces derniers cas l'indice de réfraction ne causait pas vraiment de problème. Mais encore-là la transparence et l'absence de défaut sont très importantes. Entre le plastique et le cristal de Csl, la colle est une couche morte dans laquelle une particule y laisse quand même une partie de son énergie. Pour ne pas fausser ou du moins compliquer l'étalonnage en énergie, il est souhaitable d'avoir une couche de colle la plus mince possible. L'adhésif UV ne pouvait être utilisé dans ce cas-ci, puisque l'exposition du scintillateur plastique aux rayons UV risquait de gravement l'endommager. Le plus simple alors était d'utiliser un mélange d'époxy optique.

EMBALLAGE

Les détecteurs sont montés en anneaux juxtaposés les uns aux autres. Il faut donc les isoler afin d'éviter de l'interférence provenant de la lumière ambiante ou de la fluorescence des détecteurs voisins. Du même élan, nous pouvons profiter du matériau isolant pour augmenter la réflectivité des parois. Nous avons opté pour une feuille d'aluminium de 75 μm d'épaisseur. La feuille est assez rigide pour permettre de la plier pour qu'elle épouse bien la forme du scintillateur et du guide.

Le réflecteur-isolateur à mettre sur la face avant ne devait pas perturber les particules entrant dans le détecteur. Ceci signifie que le matériau devait être très mince afin que la perte d'énergie soit la plus faible possible, même pratiquement inexistante. Le compromis idéal s'est retrouvé en une feuille de polymère aluminisé, Mylar[®], très mince soit 2 μm .

Le tout, sauf la face avant, est recouvert de papier autocollant aluminisé pour bien fixer la feuille d'aluminium et bien isoler le photomultiplicateur de la lumière ambiante.

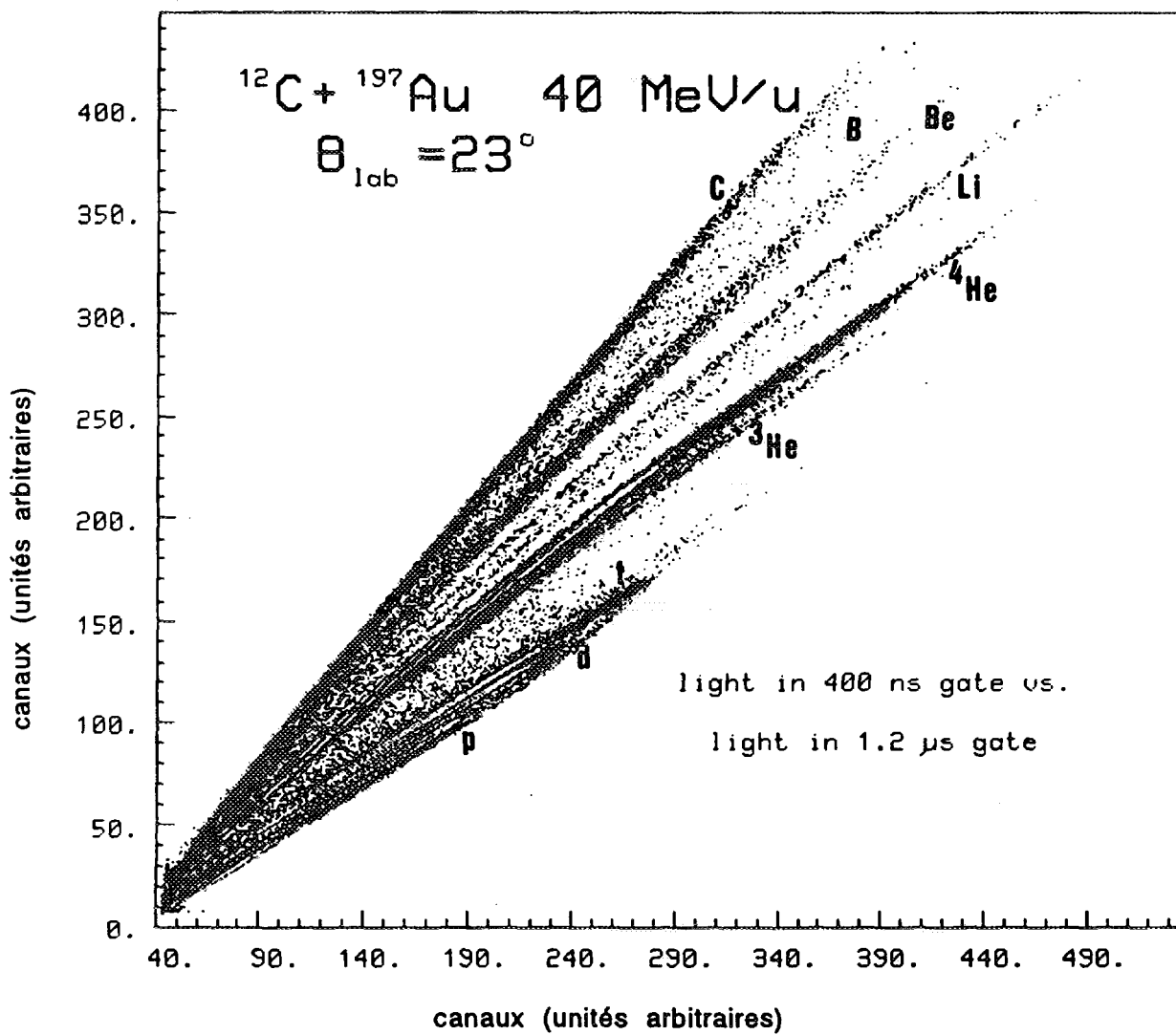


Figure 4. Spectre obtenu avec le signal du cristal de Csl(Tl). La composante rapide de l'impulsion est en ordonnée et la composante lente en abscisse

RÉSULTATS

Nous avons obtenu des résultats au niveau de notre attente et de nos besoins durant les tests effectués aux Laboratoires de Chalk River. Les spectres montrent une bonne discrimination en masse pour $Z=1$ et $Z=2$ (fig.4). La matrice complète de 80 détecteurs a été utilisée lors d'expériences tenues en juillet-août 1992 et en novembre 1992. Les deux anneaux ici discutés ont bien fonctionné et les données recueillies sont actuellement sous analyse. Ce qui reste à bien maîtriser pour l'instant est l'étalonnage en énergie. Une connaissance plus approfondie du mécanisme de scintillation aiderait probablement à une meilleure analyse.

Références:

- [1] BLANC D., Les rayonnements ionisants, Masson, 1990
- [2] LEO W.R., Techniques for nuclear and particle physics experiment, Springer-Verlag, 1987
- [3] BASHKIN S., CARLSON R.R., et al., Response of CsI(Tl) to energetic particles, Physical Review, vol. 109, no.2, 1958, p.434-436
- [4] FULMER C.B., Scintillation response of CsI(Tl) crystals to fission fragments and energy vs range in various materials for light and heavy fission fragments, Physical Review, vol. 108, no. 5, 1957, p.1113-1116
- [5] MEYER A., MURRAY R.B., Scintillation response of activated ionic crystals to charged particles, IRE Transactions on Nuclear Science, vol. 2-3, 1960, p.22-25
- [6] MEYER A., MURRAY R.B., Scintillation response of activated inorganic crystals to various charged particles, Physical Review, vol. 122, no.3, 1961, p.815-826
- [7] QUINTON A.R., ANDERSON C.E., KNOX W.J., Fluorescent response of cesium iodide crystals to heavy ions, Physical Review, vol. 115, no. 4, 1959, p.886
- [8] STOREY R.S., JACK W., WARD A., The fluorescent decay of CsI(Tl) for particles of different ionization density, Proceedings of the Physical Society, vol. 72, part 1, no.463, 1958, p.1-8
- [9] ROBERTSON J.C., LYNCH J.G., JACK W., The luminescence of CsBr(Tl) as a function of temperature, Proceedings of the Physical Society, vol. 78, 1961, p.1188-1194
- [10] ROBERTSON J.C., WARD A., Particle selection in crystals of CsI(Tl), Proceedings of the Physical Society, vol. 73, 1959, p.523-525
- [11] BENRACHI S. et al., Investigation of the performance of CsI(Tl) for charged particle identification by pulse shape analysis, Nuclear Instruments and Methods in Physics Research, A281, 1989, p.137-142
- [12] ALARJA J., et al., Charged particles identification with a CsI(Tl) scintillator, Nuclear Instruments and Methods in Physics Research, A242, 1986, p.352-354

(Samedi 3 avril 10:40 → 12:00)
(Saturday April 3rd 10:40 → 12:00)

SESSION 4A
MATÉRIAUX NUCLÉAIRES-2 NUCLEAR MATERIALS-2
Président / Chairman: M.A. Petrelli, Hydro Québec
Salle / Room: C-632

- S. Gong University of Toronto
Mass Spectrometric Studies of Cluster Formation of Radon Progeny
- N.V. Arendtsz University of New Brunswick
Material Density Differentiation: A Nonintrusive Method Using High Energy Gamma Rays
- T. Dhoum† University of Toronto
Radiolytic Abatement of NO_x from Flue Gas
- M. M. Oskui University of Toronto
Measurement of Interfacial Transfer of Iodine Species

† Denotes Undergraduate student
Indique un(e) étudiant(e) au Baccalauréat



MASS SPECTROMETRIC STUDIES OF THE CLUSTER FORMATION OF RADON PROGENY

S.L. Gong

Department of Chemical Engineering and Applied Chemistry
University of Toronto, 200 College St., Toronto, Ont. M5S 1A4

Faculty Advisor: R.E. Jervis

ABSTRACT

A new experimental system is developed to study the cluster formation of radon progeny with neutral molecules in the environment, which includes a modified mass spectrometer and a surface barrier detector. With the system, the cluster research is carried out at molecular level at which the mass of individual cluster formed is measured. A theory is also proposed to treat the cluster formation as a discrete process based on the ion-dipole and dipole-dipole interactions. Comparison between the theory and experiment is given.

1 INTRODUCTION

The health problems associated with the exposure to radon and its decay products are attributed to their radioactive properties. Being an unstable radioactive gas, the radon isotope of most concern, ^{222}Rn , decays with a half-life of 3.82 days to form ^{218}Po with an alpha particle released of 5.48 MeV energy. ^{218}Po is also unstable and undergoes alpha decay with a half-life of 3.05 minutes to form ^{214}Pb . After a succession of decays, the ^{238}U series stabilizes as ^{206}Pb . The decay products are also called radon progeny or daughters. Figure 1 shows the decay scheme of ^{222}Rn . Most energy release in the radon decay chain is in the form of alpha (α) particles. While these particles produce little or no health effect externally because of their low penetrating power, significant health effects may result from inhalation and ingestion of alpha emitting radionuclides with inhalation being the principal pathway. Because of its longer half-life than the breathing time and its gaseous nature, the inhaled radon can be exhaled without any significant absorption and decay during its passage through human respiratory system and present little health effect. The radiation dose to respiratory tissue and any resulting biological effects come from the inhalation of existing radon progeny in the air rather than from inhaled radon and its subsequent decay products. Once inhaled, however, the relatively short-lived radon progeny (e.g. ^{218}Po , ^{214}Pb and ^{214}Bi) will deposit along the respiratory tract and decay at the original place of deposition. Consequently, their energy and that of their subsequent short-lived daughters is transmitted to surrounding tissue and produces deleterious effects. High incidence of lung cancer in uranium mines and some residential areas of high indoor radon concentrations are attributed to the exposure of radon progeny.

At birth, radon progeny (^{218}Po , ^{214}Pb and ^{214}Bi) consists of 90 percent of positively charged ions, unattached to any aerosols. Once exposed to the atmosphere, these ions may participate in one of the following processes: (1) neutralization by one of the three mechanisms (Chu and Hopke 1988); (2) attachment to aerosols, (3) association with other molecules (including chemical reaction and clustering) and (4) deposition on surfaces (Figure 1). The individual progeny ion does not necessarily follow the order of the processes stated above. Depending on the conditions where it is born, it may undergo all the processes or just one of them. Before the progeny finally settles down on any surface, it will end up with a state that is different from the new-born ions. The form of this pre-deposited progeny is governed by the processes encountered by the progeny during its life-time. Both neutral and charged ions, clusters and aerosols with attached progeny are expected to exist in the environment.

Clustering and chemical reactions of radon progeny with some neutral molecules are of primary importance in understanding the physical and chemical natures of the progeny. They are the early life-time reactions for the progeny. The concept of the clustering reaction of radon progeny with water molecules was first introduced by Raabe (Raabe 1969) to explain a low value of the diffusion coefficient of radon progeny in the presence of water molecules. Six water molecules were suggested to form a cluster with ionized radon progeny. The cluster thus formed has a lower diffusion coefficient because of its larger size. Since then, this concept has been often used to interpret some of the experimental results, for example, the effect of the relative humidity on the diffusion coefficient. The importance of the cluster formation is far more beyond the effect on the particle size. Clustering affects growth, influences mobility, and hence plays a role in the overall attachment process to pre-existing aerosol particles or possibly in other transformation (nucleation) mechanism to the particulate state. The clustering also changes the physical and chemical form of the progeny and influences further interactions for the transport and removal processes. The chemical form of the progeny may influence biological uptake. Whether the progeny is bound to molecules with extended polar group, or alternatively with nonpolar heads extending outward, could dramatically affect its attachment to lung tissues and ultimate incorporation within cells.

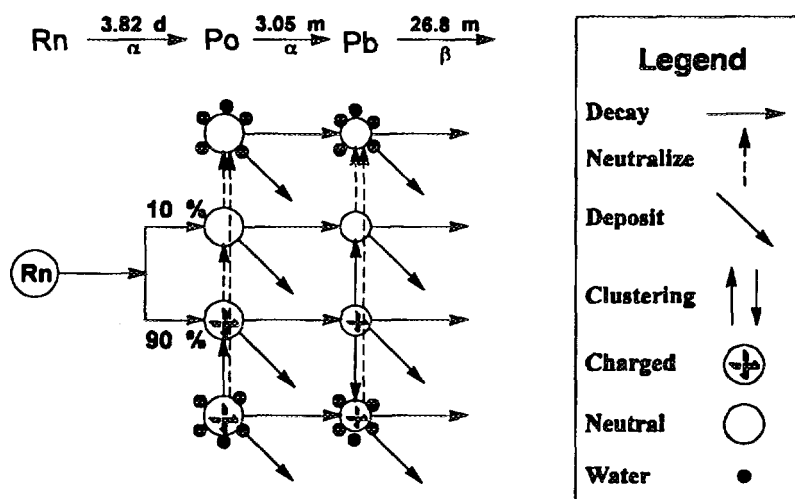


Figure 1 The interactions between radon progeny and its environment

Although the phenomenon of the cluster formation between metal ions and neutral ligands has been a research subject for more than a century, the present knowledge of the cluster formation of the radon progeny with neutral molecules is only based on the speculation from some indirect experimental observation, especially about polonium. Using the experimental results of the cluster formation of stable isotopes of Pb and Bi ion with water molecules, Castleman (1991) examined the chemistry of radon progeny, alleging that the cluster formation with water molecules is the early stage chemistry of the progeny. Since the experiment was carried out in a condition where only stable isotope ion of Pb or Bi was used and no radiation ionization was present, the results may differ under real conditions where radon gas and its progeny co-exists. This paper presents an experiment system which allows the direct observation of the cluster formation of radon decay products with neutral molecules, and a theory for the ion-molecule cluster formation.

2 INSTRUMENTATION

The clustering reaction of an ion with neutral molecules falls in the category of general chemical ion-molecule reaction. The difference between them lies in the bonding force to hold the ion and molecules together. Despite of the difference, the experimental techniques (Franklin 1972, Franklin 1979) used to study the ion-molecule reactions can still be applied to investigate the ion-molecule clustering with some modifications. Of these methods, mass spectrometric analysis of the product is the most sophisticated one. The advantage of the mass spectrometry is that the mass to charge ratio of the product can be determined accurately. If the charge on the product (usually +1) is known, the mass of the product is readily attained. The fragment information due to the ionization can then be used to establish the structure or composition of the product.

In the system of radon progeny and its clusters (Figure 1), both charged (positive) and neutral species are present. The charged ones can be detected by a mass spectrometer even without any ionization. However, the system of radon progeny are different from other ordinary ion system. One of the most distinguishing feature of the system is that the ions are radioactive. The ion concentration which is a function of both experimental conditions and equipment configurations is far below the detecting limit of a conventional MS detector. The experimental system designed for studying the radon progeny ion clusters has been incorporated these factors.

The system developed in this project is basically a nuclear mass spectrometry (NMS). Figure 2 shows the schematic structure of the experimental system which can be conceptually divided into two regions: the reaction cell and mass analyzer. The reaction cell is a cylindrical tube where the ions will be generated and react with neutral molecules to form a mixture of ions and ion clusters in a controlled environment. The product ions and clusters are sampled into the second part through an interface between the high pressure region of the reactor and the high vacuum region of the mass spectrometer, sorted by a quadrupole mass filter and detected by a surface barrier detector. Detection and measurement of the positive ions sorted by the mass filter can be accomplished by electrical and photographic means. Ion currents in conventional mass spectrometer are in the range of 10^{-8} (6.25×10^{10} ions s^{-1}) to 10^{-16} (6.25×10^2 ions s^{-1}) ampere. If the sampling rate is 1 cc s^{-1} , according our mathematical model of the behaviour of the radon progeny in a cylindrical tube (Gong 1992), the maximum ion current which can be obtained from the source ($100 \mu\text{Ci}$ of RaCl_2) at no neutralization is 90 ions s^{-1} . This is apparently below the lowest limit for conventional detector. A more sensitive detector is required for this MS system.

The nature of the cluster ions of the radon progeny makes it possible to use detectors for radioactive particles. $^{218}\text{Po}^+$ is unstable and will undergo alpha decay with energy release of 6.00 MeV. Clusters and compounds formed with $^{218}\text{Po}^+$ will have the same feature and, therefore, can be detected the same as for $^{218}\text{Po}^+$. The radiation detector is a transducer that converts energy of the incident radiation into another form of energy, usually of the electric type. The detection is based on the interaction of the radiation with the detector by excitation or ionization of its molecules and atoms. The charged particle such as alpha ionizes or excites the detector medium directly. The most common type of solid medium detector is the surface-barrier detector. The solid medium for this kind of detector is semiconductor which can result in a much larger number of carrier for a given incident radiation event than is possible with any other detector type. Thus the best energy resolution can be achieved by this detector. The basic information carriers are *electron-hole pairs* created along the path taken by the charged particle (primary radiation or secondary particle) through the detector. The electron hole pair is somewhat analogous to the ion pair created in the gas-filled detector. Their motion in an applied electric field generates the basic electrical signal from the detector. Regardless of the detailed mechanisms involved, the quantity of practical interest for detector

applications is the average energy expended by the primary charged particle to produce one electron-hole pair. This quantity, often loosely called the "ionization energy", is about 3 eV for silicon or germanium. If the detector efficiency of collecting radiated alpha particles from the polonium clusters that hit the detector surface is 50%, the *electron-hole pairs* created by one cluster ion from the detector is about 1×10^6

$\left(\frac{1}{2} \left[6 \times 10^6 \text{ eV} / 3 \text{ eV} \right]\right)$. This number of *electron-hole pairs* will generate a significant amount of electric current if a voltage is applied between two electrodes of the detector (Knoll 1979). The sensitivity of this kind of detector for α particles could reach as low as a single particle.

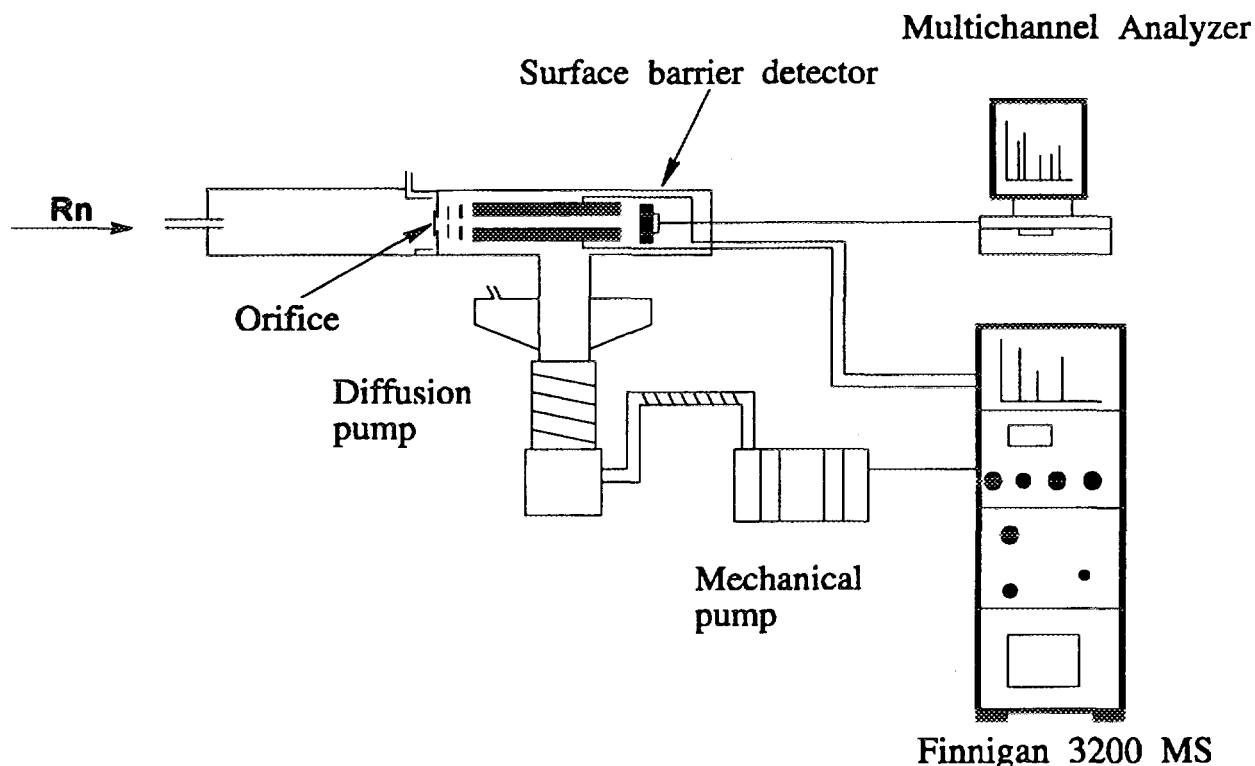


Figure 2 Schematic Diagram of the Experimental System

3 THE THEORY AND RESULTS

The theory for the cluster formation of radon progeny with neutral polar molecules such as H_2O and H_2SO_4 was studied by Raes (1985) and Hawrynski (1984). The approaches used by them are based on the thermodynamic principle of a droplet formation model. The free energy of the formation is minimized to obtain the critical size of the cluster as a function of other variables such as relative humidity and temperature. The liquid droplet model has been used to describe both heteromolecular homogeneous and heterogeneous nucleation processes (Wiendl 1974, Yue 1979a, Yue 1979b, Castleman et al. 1978). Heteromolecular heterogeneous nucleation is a process by which more than two species (e.g. H_2O and H_2SO_4) nucleate on a pre-existing particle or ion which acts as a condensation center. The effect of the ion is to provide an attracting force between the ion center and the bulk nucleating phase and reduce the Gibbs free energy of formation. Castleman et al. (1978) assessed the validity of the classical

charged liquid drop model used to describe the ion clustering. They found that this kind treatment of ion clustering is only qualitative for most of the molecules except for water vapour. The failure is partially due to some macroscopic properties such as surface tension and dielectric constant utilized in the model to describe the microscopic and discrete clustering process. All the available models (Yue 1979b, Raes 1985, Hawrynski 1984, Wiendl 1974) consider the presence of an ion in the bulk-nucleating molecules as a macroscopic process. The electrostatic term due to the ion is taken as (Yue 1979b, Raes 1985):

$$\frac{Q^2}{2} \left(1 - \frac{1}{\epsilon}\right) \left(\frac{1}{r} - \frac{1}{r_0}\right)$$

which is the difference between the electrostatic energy of a single-charged ion of radius r_0 in a vacuum and in a sphere of dielectric constant ϵ and accounts for the polarization of the liquid molecules around the ion.

There are several deficiencies of the treatment. Because the clustering molecules are regarded as a "continuous" dielectric right up to the periphery of the ion where the field of the ion is greatest and distance factors are most important, the real finite shape and size of the clustering molecules has to be considered. The discrete electrical nature of the clustering molecules viz. their dipole moment and the location of the dipole in the molecules is not considered. The assumption that ϵ is a constant value near ions can not be held because the fields of the ion are high enough to cause appreciable saturation orientation of the dipoles and result a lower ϵ near the ion.

In view of the shortcomings of the existing models, a theory was developed by Gong et al (Gong 1992b). The theory treats the cluster formation as a discrete process and includes the ion-dipole and dipole-dipole interactions as the basis for dealing with the electrostatic force between the central ion and the clustering molecules.

For ion-water system, the free energy of a cluster formation with n H₂O molecules around a polonium ion ($z=1$) can be expressed as

$$\frac{\Delta G_c^n}{kT} = -n \ln \frac{P}{P^\infty} + \frac{4\pi r^{+2} \sigma}{kT} - \frac{\Theta n e \mu}{r^2 kT} \left(1 - \frac{3 \ell^2}{8 r^2}\right) + \frac{\Theta C_2^n \mu^2}{r_d^3 kT}$$

where C_2^n is the dipole-dipole interaction number taken as the combination number of two from n molecules and the constant Θ depends on the units in which the charges and distances are expressed.

The entropy and enthalpy of the cluster formation can be readily obtained from the established thermodynamic relations. Except in certain cases of intramolecular rotation about single bonds, the dipole moment is temperature independent. Therefore,

$$-\Delta S = -nk \ln \frac{P}{P^\infty} - nkT \frac{\partial}{\partial T} \left(\ln \frac{P}{P^\infty} \right) + 4\pi r^{+2} \frac{\partial \sigma}{\partial T}$$

and

$$\Delta H = nkT^2 \frac{\partial}{\partial T} \left(\ln \frac{P}{P^\infty} \right) + 4\pi r^{+2} \left(\sigma - T \frac{\partial \sigma}{\partial T} \right) - \frac{\Theta e n \mu}{r^2} \left(1 - \frac{3 \ell^2}{8 r^2}\right) + \frac{\Theta C_2^n \mu^2}{r_d^3}$$

The probability distribution of the clusters can be expressed by the Gibb's energy as:

$$I_n \propto \exp(-\Delta G_{\min} / kT)$$

where the absolute minimum of $\Delta G/kT$ corresponds to the most probable cluster concentration in that condition.

Figure 3 shows the Po^+ cluster distribution at $RH=1\%$. The experiment results are compared with the theory prediction which agrees fairly well. The fraction of the cluster for both experimental results and theoretical predictions was normalized against the most abundant peak. At low water vapour pressure ($RH=1\%$), Po^+ cluster with 4 H_2O is dominated. For $Pb-H_2O$ system, the comparison is given in Figure 4. Identical peaks from the theory and experiment were obtained for the most abundant cluster at relative humidity range from 4% to 84%. The theory was compared with the results by other theory (Yue 1979b). According to the experimental results of Tang et al (Tang 1973), Yue's theory overestimated the number of water molecules clustered with lead ion due to the dielectric constant ϵ used in the model failing to account the polarization of the dipole molecules by the central ion

The theory was also used to predict the thermodynamic properties of the cluster formation. In Figure 5, the enthalpy of the cluster formation of Pb^+ and Bi^+ with water molecules was calculated from the theory. Comparison of the prediction with the experimental data from Tang and Castleman (Tang 1973) was given.

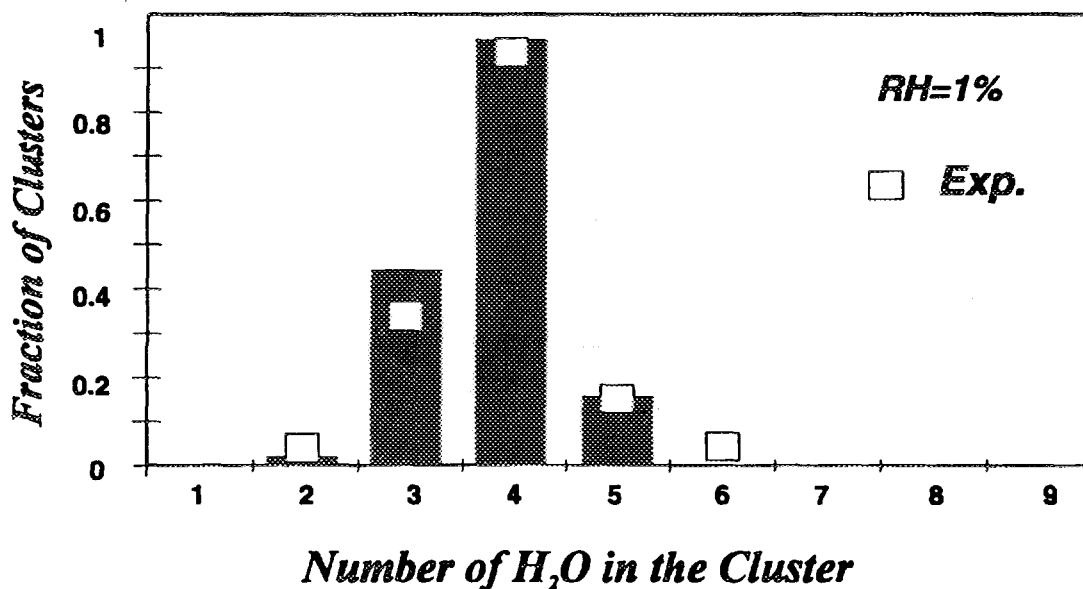


Figure 3 The Cluster Distribution as a function of RH for Polonium Ion from Radon Gas

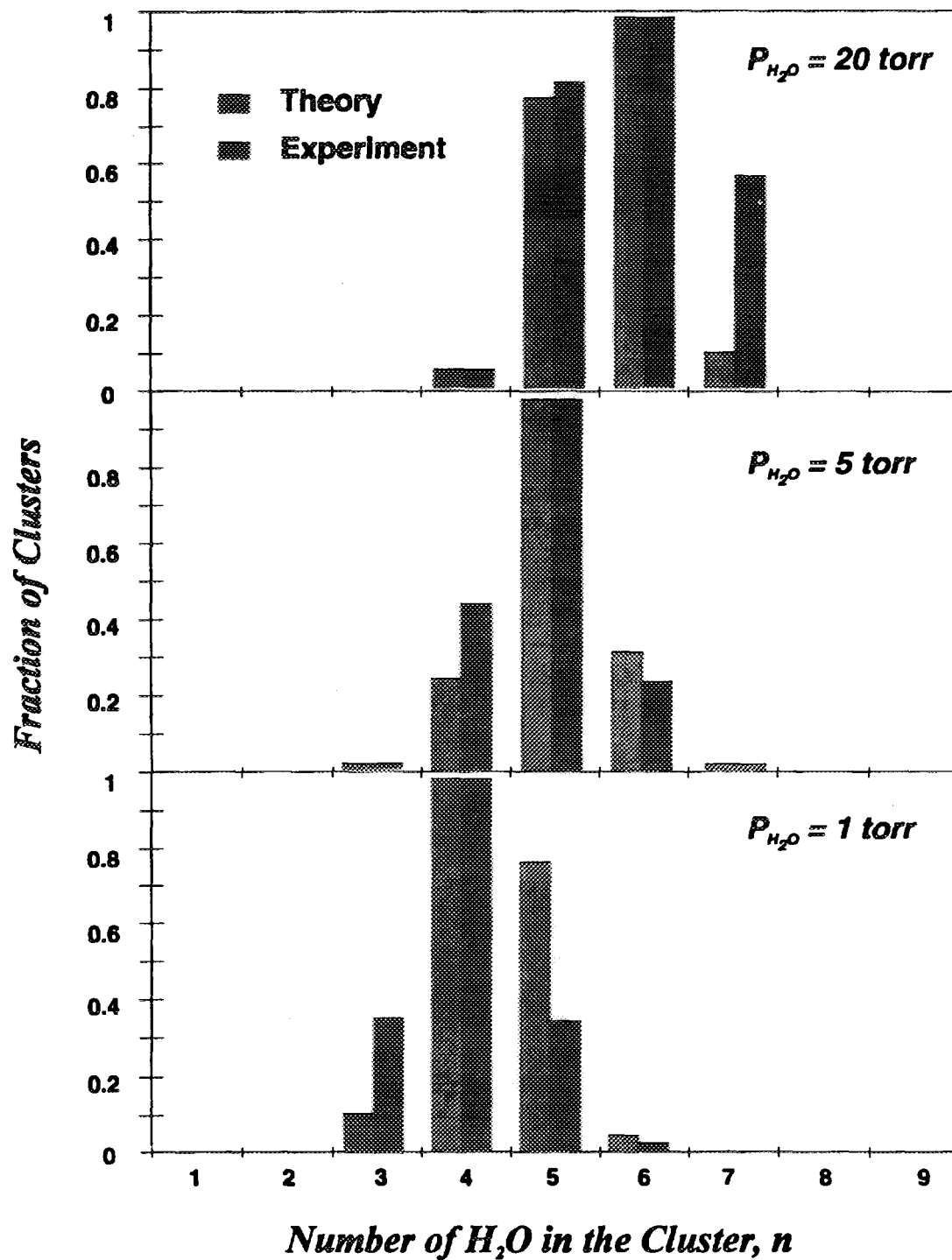


Figure 4 The Comparison of the Cluster Formation of Pb^+ with Water Molecules between Theoretical Prediction and Experimental Observation (Tang 1972)

Comparison of the Cluster Distribution by Two Theories at 300 °K

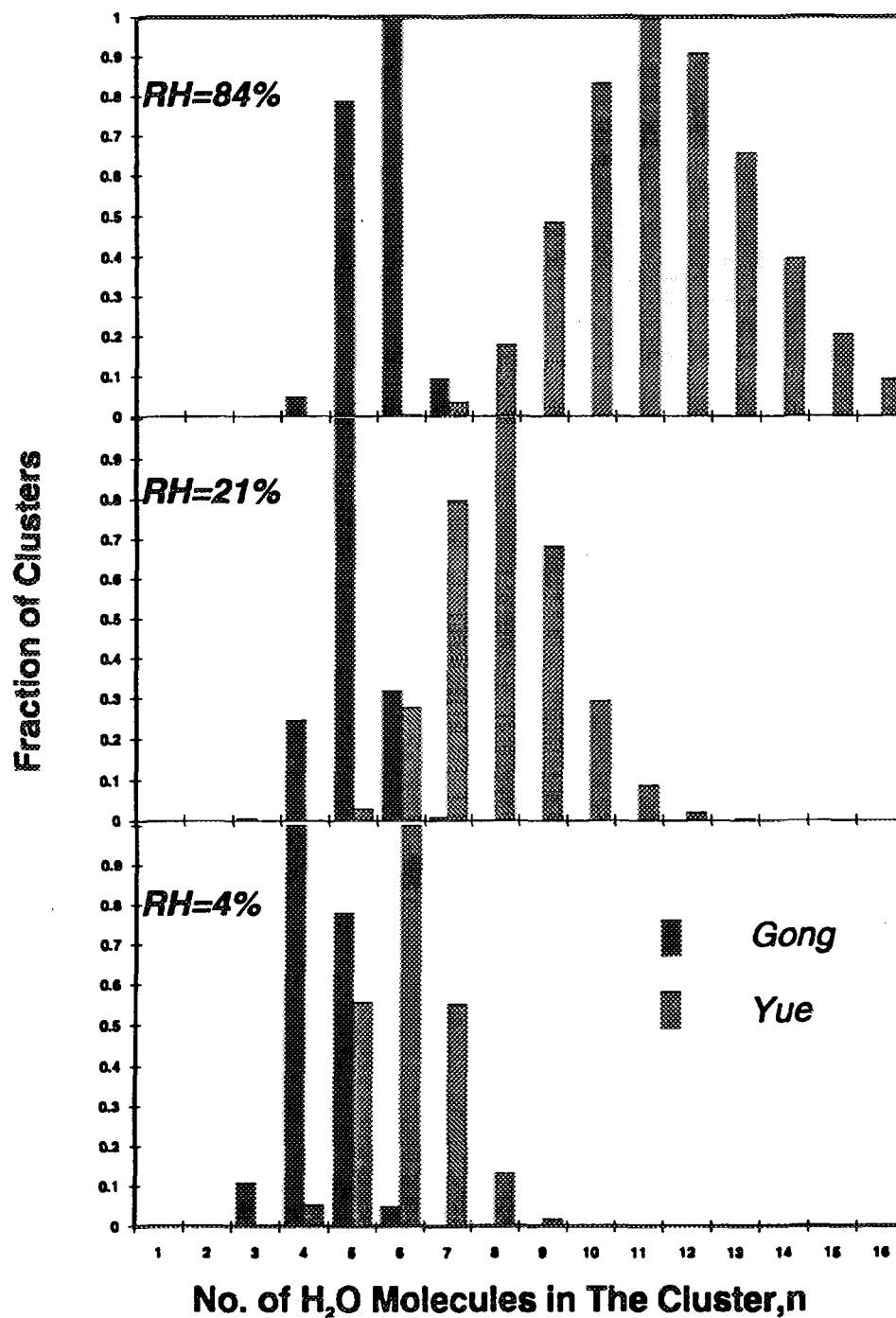


Figure 4 The Comparison of Theoretical Predictions by Different Theories

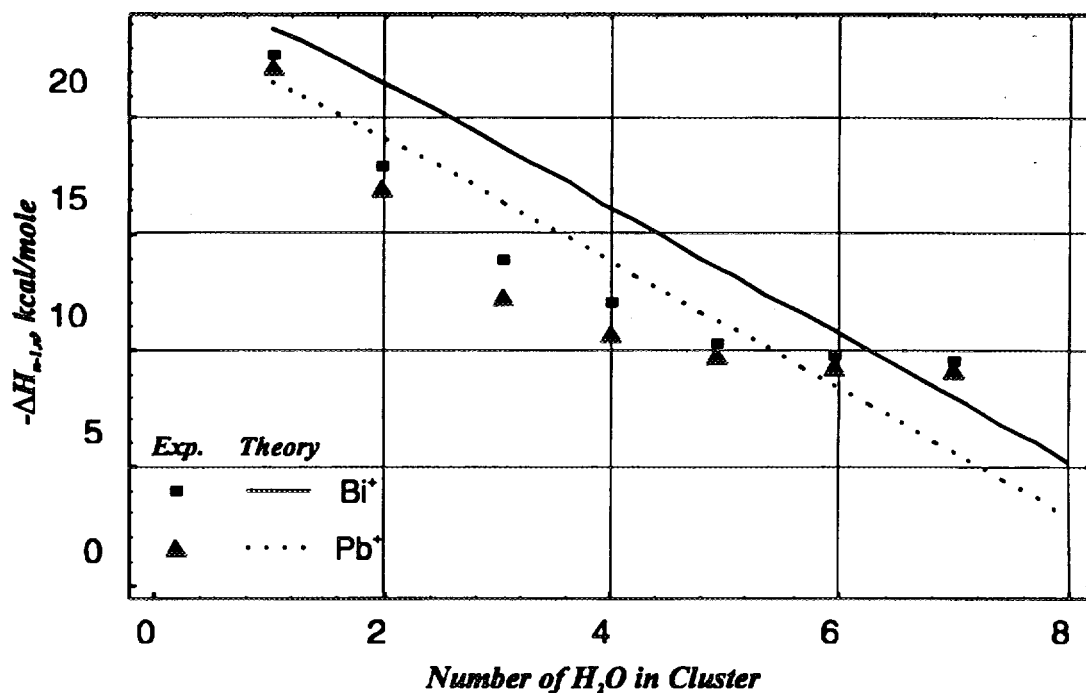


Figure 6 The Enthalpy of the Cluster Formation

4 REFERENCES

Bagnall K. W., 1957, *Chemistry of the Rare Radionuclides*, Butterworths, London.

Chu K. and Hopke P.K., 1988, "Neutralization Kinetics for Polonium-218," *Environ. Sci. Technol.*, **22**(6), 711

Raabe O.G., 1969, "Concerning the Interactions that Occur between Radon decay Products and Aerosols". *Health Phys.*, **17**, 177.

Castleman Jr. A. W., 1991, "Consideration of the Chemistry of Radon Progeny", *Environ. Sci. Technol.*, **25**, 730-735.

Franklin J.L (Ed.), 1972, *Ion-Molecule Reactions*, Vol. I & II, (Plenum Press, New York)

Franklin J.L (Ed.), 1979, *Ion-Molecule Reactions*, Parts I & II, (Dowden, Hutchinson & Ross Inc., Stroudsburg, PA.).

Gong S.L., Phillips C.R. and Jarvis R.E., 1992, "Mathematical Modeling of the Behaviour of Radon Progeny in a Cylindrical Tube", in *Indoor Air Quality*, Proceedings of the 2nd International Conference on Indoor Air Quality, April 28-30, Athens, Greece.

Gong S.L., Phillips C.R. and Jarvis R.E., 1992, "A Theory of the Po⁺-H₂O Ion-Molecule Cluster Formation", presented at the 42nd Chemical Engineering Conference, Oct., Toronto

Hawrynski M. J., 1984 "The Theory of Clusters", presented at the International Conference on the Occupational Radiation Safety in Mining, Toronto, Proceedings edited by Harold Stocker.

Knoll G.F., *Radiation Detection and Measurement*, John Wiley & Sons, New York, 1979

Raes F., 1985, "Description of the properties of unattached ^{218}Po and ^{216}Pb particles by means of the classical theory of cluster formation", *Health Physics*, **49(6)**, 1177-1187.

Tang I. N. and Castleman A. W., 1974, "Mass spectrometric study of gas-phase clustering reactions: hydration of the monovalent bismuth ion," *J. Chem. Phys.* **60(10)**, 3981-3986.

Tang I. N. and Castleman A. W., 1972, "Mass spectrometric study of gas-phase hydration of the monovalent lead ion," *J. Chem. Phys.* **57(9)**, 3638.

Wiendl E., 1974, "Structure of Liquid H_2SO_4 - H_2O Clusters Around Ions: Thermodynamic Theory", In: H. Dolezalek & R. Reiter (Eds.), *Electrical Processes in Atmosphere*, Proceedings of the Fifth International Conference on Atmospheric Electricity, Garmisch-Partenkirchen, West Germany, Sept. 2-7, 76-81.

Yue G.K., 1979a, "A quick method for estimating the equilibrium size and composition of aqueous sulfuric acid droplets", *J. Aerosol Sci.*, **10**, 75-86.

Yue G.K., 1979b, "On the characteristics of sulfate aerosol formed in the presence of ion sources", *J. Aerosol Sci.*, **10**, 387-393.

**18th Annual Student Conference, Canadian Nuclear Society****ABSTRACT****Material Density Differentiation: A Nonintrusive method using
High Energy Gamma Rays**

Nina V. Arendtsz and Esam M. A. Hussein

Mechanical Engineering, University of New Brunswick

P.O. Box 4400, Fredericton, N.B., E3B 2Y1

High energy gamma- rays with properties of deep penetration are highly suited for the interrogation of even dense materials. Transmission radiography methods that are based on differentiating the changes in the attenuation coefficients suffer from a severe loss of material contrast at these high energies owing to the predominance of Compton scattering and the ensuing reduction on the strong atomic number dependence that occurs at lower energies. As such, Compton scattered radiation itself can be harnessed to yield information on the electron densities of materials. In this work, a mono-energetic source of Cs-137 (662 keV) is employed to bulk irradiate a selected slice of the target to be inspected, and the radiation scattered by the target is collected by one or more Germanium detectors. The wide collimators of the detectors allows simultaneous measurement of radiation scattered from the entire target. This alleviates the need for scanning as would be the case when the detector is finely collimated. Spatially, the point of scatter is resolved from the energy spectrum of the detector, based on the unique energy-angle relationship for Compton scattering. Density reconstructions are performed using the detector energy spectra.



Radiolytic Abatement of NO_x from Flue Gas
by Tinku Dhoum

Coal burning power plants produce excessive amounts of nitrogen oxides (NO_x) and sulphur dioxides which are largely responsible for acid rain. Various conventional methods to reduce the concentration of NO_x and sulphur dioxide are currently employed but at a large cost to the utility company. A different approach to the problem of reducing flue gas emissions is by irradiation and subsequent reaction with ammonia of NO_x and sulphur dioxides. This method has been investigated for over 20 years in an attempt to reduce acid rain by research teams in Japan, Germany and the United States. In all cases the type of radiation used was electrons in the form of electron beams. Another type of radiation not yet investigated is the use gamma radiation emitted from a cobalt-60 source. Gamma radiation is to be used in an attempt to reduce the cost of treatment of flue gas and to more effectively eliminate NO_x from flue gas.

The irradiation of NO_x often leads to the absorption of the radiation by the NO_x to form an excited or more energized state of NO_x , called NO_x^* . NO_x^* is capable of reacting with other chemicals where NO_x was not. In a flue gas stream which is to be irradiated, there are other chemicals which can also be excited through radiation absorption such as nitrogen and oxygen. The actual sequence of reactions possible is very complicated and not yet understood.

Various models have been developed by all three teams in an attempt to explain the behaviour of the complex set of reactions which take place. Two models have been selected to predict the results of irradiating flue gas: Persons et al.'s model presented in *Radiation Physical Chemistry* (Vol. 31, 1988) and Sagert's model modified for NO_x presented at the *2nd CSNI Workshop on Iodine Chemistry and Reactor Safety* (1988).

Simulations have been conducted on the effect of various parameters on the concentration of NO_x . Based on previous research conducted with electron beam irradiation of flue gas by other research groups, humidity, dose, residence time, and initial concentrations of NO_x and NH_3 are key variables. Using both models, it was found that the dose imparted to the flue gas stream reduces NO_x concentrations more substantially than the addition of NH_3 , although Sagert's model predicts a significantly greater effect in reducing NO (99.3% with NH_3 and 97.3% without) than Person et al.'s (remains virtually unchanged). However, the predicted dose required for maximum reduction of NO_x varied substantially between the two models. Sagert's model

predicted a reduction in the concentration of NO by approximately 97% at a dose rate of 10 kGy/hr for 55 seconds while Persons et al.'s predicted a reduction by 99.998% at a dose rate of 0.5 kGy/hr for 150 seconds. In both models, dose rate does effects the reduction of NO_x contrary to research performed using electron beams.

Gamma irradiation of NO is to be conducted in a 1.5 L aluminum container in batch experiments to validate the results of the models. Gamma radiation is to be provided by a Gamma Cell with a cobalt-60 source capable of providing a dose approximately 15 kGy/hr. Based on previous plant trials on the irradiation of NO, approximately 84% removal is possible using electron beams.



Measurement of The Interfacial Transfer of Iodine Species

M.Mesbah-Oskui
Department of Chemical Engineering and Applied Chemistry
University of Toronto
Toronto, Ontario
Canada, M5S 1A4

Faculty Supervisor: Prof. G.J. Evans

The impact of radioiodine on the environment due to a nuclear reactor accident can be minimized by reducing the concentration of iodine in any air released from the reactor containment structure. The airborne concentration would be governed to a large extent by the production of volatile chemical forms of iodine, such as I_2 and CH_3I , through radiolytic redox reactions in any aqueous pools within containment. In this liquid-gas system, aqueous radiation chemistry would be strongly affected by dissolved gases, such as H_2 , O_2 , or CO_2 , the concentration of which could be determined by the rate of interfacial mass transfer. In order to better understand the potential role of the mass transfer rate, an investigation of its effect on the radiolytic production of volatile iodine species has recently been initiated.

An experimental set up has been designed to allow liquid/gas systems to be stirred during radiation, while continuous measurement of dissolved oxygen, pH and liquid/gas concentrations are being evaluated. This apparatus is quite suitable for evaluating transients species induced through the addition of organic compounds, such as methyl ethyl ketone (MEK), and Paraldehyde. As an initial step the rate of mass transfer was evaluated as a function of the mixing rate through measurement of their transfer of dissolved O_2 on CH_3I labelled with I^{131} . The

variables in these experiments were interfacial area, changed by using perforated plates ranging from 2.5 cm² to 105 cm², and stirring rate from 30 rpm to 500 rpm.

Samples of liquid phase were collected from a circulated liquid loop, known volume of the gas phase were collected using charcoal absorbent cartridges. The results were assayed and total mass transfer coefficients using the coupled differential equations were determined. These mass transfer coefficients values, associated with interfacial area values, (Ka values) and some other findings will be explained in this presentation.

(Samedi 3 avril 10:40 → 12:00)
(Saturday April 3rd 10:40 → 12:00)

SESSION 4B

DÉTECTION & ACTIVATION NEUTRONIQUE-2 DETECTION AND ACTIVATION-2

Président / Chairman: Dr. M. Gagnon, Fondateur du C.I.C.

Salle / Room: C-630

- D. Freed Massachusetts Institut of Technology
Time-Resolved Luminescence Spectroscopy of Trace Uranyl in Wet Sand
- P. Bekeris† University of Toronto
Iodine Behaviour in the Slowpoke Reactor
- M.S. Fila University of Toronto
Neutron Activation Measurements of Submicron Aerosol Deposition onto a Cylinder Energized with an Alternating Electric Field
- V. Awafo Institut Armand Frappier
Effect of Gamma Irradiation on the Structure of Corn Stalks and Their Subsequent Bioconversion into Protein-Rich Mycelial Biomass of Pleurotus Sajor-CAJU

† Denotes Undergraduate student
Indique un(e) étudiant(e) au Baccalauréat



TIME-RESOLVED LUMINESCENCE SPECTROSCOPY OF TRACE URANYL IN WET SAND

David Freed
Massachusetts Institute of Technology
138 Albany St. NW-13#204
Cambridge, MA 02139
Faculty Advisor: S. Simonson

Summary

The objective of this project is to develop a technique by which to observe and characterize the behavior of uranium in unsaturated groundwater flow systems, particularly with regard to unstable "fingered" flow which could dramatically reduce groundwater travel times. This paper focuses on the background and experimental considerations of the first stage of this project.

In this experiment, a high power UV laser is used to excite aqueous uranyl in a wet sand mixture. The characteristic green phosphorescence emitted in the decay transition is detected by a photomultiplier tube; the amplified signal is sent to an oscilloscope in communication with Macintosh data acquisition software. The phosphorescence signal can be used to determine the uranyl concentration in solution. Time resolution of the signal allows background fluorescences (from sand, trace organics, structural materials, etc.), most of which are short-lived (nsec) relative to uranyl phosphorescence decay time (usec), to be accounted for in the signal analysis. A green colored glass filter in front of the photomultiplier tube face provides frequency selectivity.

Similar techniques have been sensitive enough to detect uranyl at the parts per billion and parts per trillion levels in carefully controlled solution conditions, using considerably lower excitation energy than that available in this project. Initial experiments have demonstrated the feasibility of detecting trace amounts of uranyl in a sample of opaque ground material. Eventually a scheme will be developed for imaging the behavior of uranium in unsaturated flow systems. This would be accomplished by monitoring spatial and temporal concentration profiles, using the same technique but with a position sensitive detection system, possibly employing fiber optic light transmission to achieve spatial localization.

Background

In order to assess the health risk that would result from geologic burial of spent fuel, it is important to be able to predict the travel times for hazardous, long-lived radionuclides from a repository to the accessible environment. The mostly likely release scenario is thought to be groundwater infiltration resulting in dissolution of the waste form and migration of radionuclides with the water. It is expected that many of the dangerous, long-lived isotopes, particularly uranium and the transuranics, will migrate slowly due to sorption by zeolitic clays and other sorptive materials in the rock surrounding the repository. Connecting fractures of various sizes may be the dominant flow path through the unsaturated layer from the repository to the aquifer, and these fractures are also thought to contain sorptive substances that will retard the movement of relatively dilute contaminants in the groundwater.

Predictions of radionuclide migration time often take the form of calculating the groundwater velocity and some form of retardation factor for a particular element in a particular ground material. Typically this factor is calculated from a partition coefficient which is found experimentally by looking at the equilibrium distribution between dissolved and sorbed amounts of the element in batch or column systems with various water to solid ratios. The validity of this method is difficult to test, and more realistic data has not been obtained, due in part to the extremely long times and large distances in question.

Furthermore, recent work at Sandia National Laboratory has demonstrated that downward flow under certain unsaturated conditions in a fracture, simulated by crushed rock between glass plates, can deviate strongly from uniform flow [1]. When the ratio of total flux to saturated conductivity is less than one, flow instability results in the growth of "fingers" or preferred hydraulic pathways. This fingered flow results in increased water velocities at the fingertips, and drains the bulk of the flow from the overlying layer. The question arises as to whether, under such conditions, a contaminant would tend to move with the fingers or stay behind with the bulk water front, since the former could significantly reduce radionuclide travel time from a repository to an aquifer located somewhere beneath.

The experimental technique (described below) for detecting minute uranium quantities in a wet sand mixture could be adapted to examine the behavior of aqueous uranyl in a simulated groundwater flow system. It seems particularly worthwhile to investigate uranyl movement in fingered

flow; data in the form of uranyl concentration profiles at several locations could be taken in conjunction with observations of the flow field, allowing characterization of "fingered migration" under various conditions of flow rate, pH, ground material, ionic strength, and so on.

While there are many non-uranium radionuclides of concern regarding long-term geologic burial, the motivations for using uranium in this experiment are the following:

- (1) uranium decay chains include daughters important for health risk assessment, particularly Ra-226 and Ra-222, which remain in secular equilibrium with U-238
- (2) uranium movement in groundwater is thought to be representative of the actinides, possibly faster (which provides an element of conservatism)
- (3) under most conditions uranium forms uranyl (UO_2^{2+}) in aqueous solution, which can be detected by its characteristic green photophosphorescence upon excitation by ultraviolet light.

Uranyl Phosphorescence

The spectroscopic properties of uranyl are well known, and several researchers have shown the high sensitivity capable with a luminescence technique involving intense UV excitation (from a flash lamp or a laser) [2-5]. One of the most important considerations for achieving this sensitivity is separation of the phosphorescence signal from other induced fluorescences, from such sources as the sample ground material, trace organics (particularly humic acid), and structural materials like the sample container. This is accomplished in a straightforward manner by time-resolution of the signal, aided by the relatively long excited uranyl decay time for radiative transition. Fluorescence lifetimes for most materials tend to be on the order of nanoseconds, while the uranyl phosphorescence decay time is on the order of microseconds, as shown in Figure 1, a plot of luminescence intensity versus time [4]. Using time-gating and controlled solution chemistry, uranium levels on the order of parts per trillion have been monitored [5].

Figure 2 shows the typical uranyl emission spectrum [4], with peaks occurring at about 494, 516, and 540 nm. The light collected is passed through a green colored glass filter in order to block out the bulk of the stray light, any remaining (non-green) fluorescence, and most of the reflectance from the UV excitation light (which only lasts a few nanoseconds but should be isolated from detection equipment).

There are two key considerations regarding solution chemistry that can strongly affect uranyl phosphorescence intensity; one is the enhancement effect of certain acids, the other is the "quenching" effect of certain common ions. The single most potent enhancer and the one most commonly used is phosphoric acid at about 10% (volume). The phosphate ligands are believed to prevent, to a large degree, quenching of the phosphorescence, which short-circuits the excited uranyl ions by providing a nonradiative path to the ground state. Some such deactivation may occur due to interactions with surrounding water molecules, especially in the absence of phosphoric acid, but more noticeable is the effect of strong quenchers such as iron, manganese, iodine and chlorine when they are at levels above a few parts per million [4]. While acid enhancement can aid in investigation of the proposed detection technique, realistic groundwater systems of interest are not acidic and cannot benefit from this phenomenon. Nevertheless the possible effects of quenchers must always be considered.

Experimental Setup

The excitation source is a Spectra Physics GCR-3 tripled Nd:YAG laser of up to 200 mJ per 8 ns pulse. Initially the illuminated sample consisted of a saturated mixture of coarse all-purpose sand and 10 ppmw uranyl in 10% phosphoric acid, held in a methacrylate cuvet. Later a similar sample with no acid and 2 ppmw uranyl, held in a borosilicate glass test tube, was used. The change of sample holder material helped reduce background. Emission light is collected by a Hamamatsu R1924 photomultiplier tube (PMT) of 8 MHz bandwidth; the amplified signal is sent to an HP 54200A digitizing oscilloscope (20 MHz). Data acquisition and analysis is performed by Labview2 on a Macintosh, which features a graphical interface and high-level programming for instrument and information control.

The experimental configuration is shown in Figure 3. The laser beam illuminates a slice of the sample at one face; beam penetration depth is expected to be on the order of a few grain diameters (1-2 mm). Some of the uranyl phosphorescence will reach the active area for light collection by the PMT. A run consists of a single shot from the laser, which sends a synchronous trigger to the oscilloscope, which can be programmed to wait a specific delay time before data collection. All runs with uranyl are duplicated without uranyl to account for background.

There are several important experimental considerations. In addition to varying the uranyl concentration, samples can be altered with regard to particle size, porosity, and composition of the sand, water content of the mixture, type of acid, pH, and concentration of quenchers. Cooling substantially reduces quenching effects, so temperature is an important factor as well. Damage thresholds for the cuvet and sample material under intense UV laser light must be observed.

Experiments using optical fibers for light collection and transmission to the PMT are planned; one end of the single fiber would be inserted directly into the sample. By varying the position of the thin fiber (400 micron outside diameter) along the beam axis, beam penetration can be compared for various pulse energies and sample conditions. Illumination and collection via optical fibers could provide an effective way to observe uranium concentrations at localized spots within the sample.

The preliminary objective of this work was to demonstrate the feasibility of the proposed detection technique. A more sophisticated sample configuration is under development for flow imaging of uranium as discussed earlier.

References

- [1] Glass, R.J., "Laboratory Research Program to Aid in Developing and Testing the Validity of Conceptual Models for Flow and Transport Through Unsaturated Porous Media," Sandia National Laboratories, June 1990 (SAND89-2359C)
- [2] Azenha, M.E.D.G., et.al., "On the Uranyl Ion Luminescence in Aqueous Solutions," Journal of Luminescence, 1991, 48&49 (522-526)
- [3] Darmanyan, A.P., Khudyakov, I.V., "Study of Luminescent Forms of the Uranyl Ion," Photochemistry and Photobiology, 1990, Vol.52, No.2 (293-298)
- [4] Park, Y.Y., et.al., "Deactivation Mechanism of Excited Uranium(VI) Complexes in Aqueous Solutions," Journal of the Chemical Society - Faraday Transactions, 1990, 86(1) (55-56)
- [5] Kaminski, R., Purcell, F.J., Russavage, E., "Uranyl Phosphorescence at the Parts-per-Trillion Level," Analytical Chemistry, 1981, 53 (1093-1096)

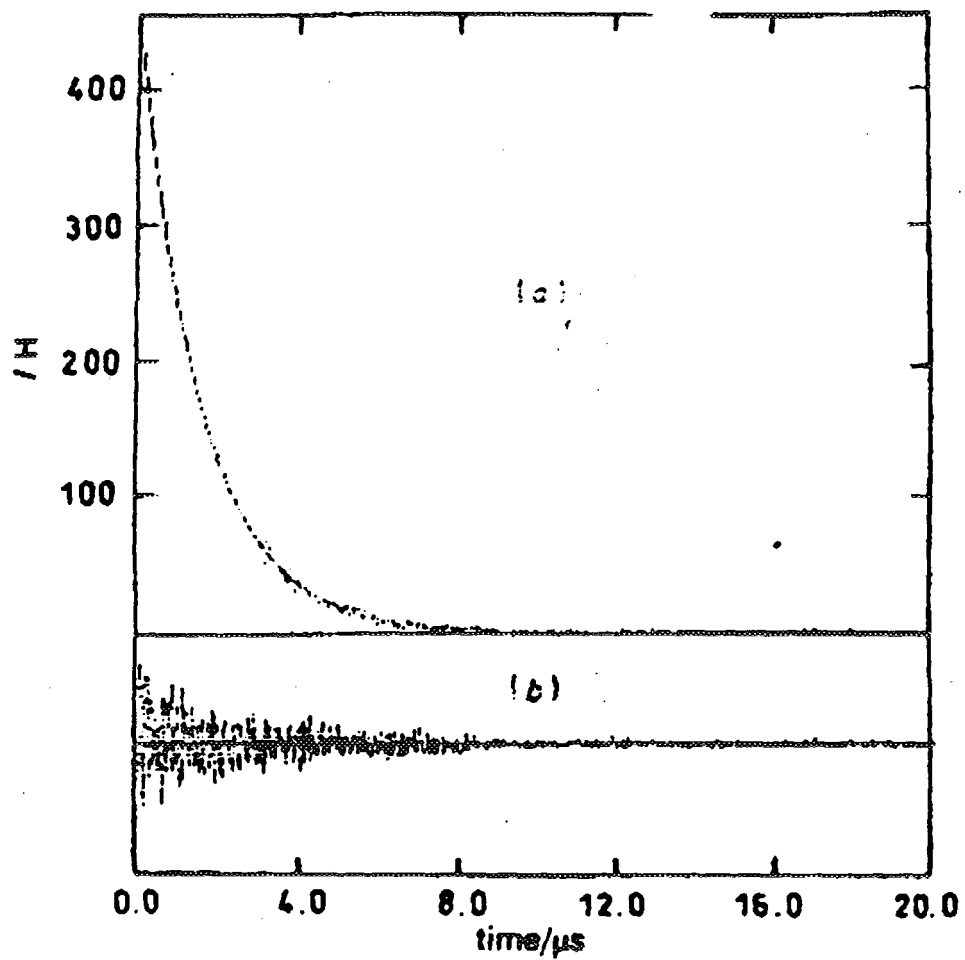


Figure 1: Luminescence Decay of Uranyl

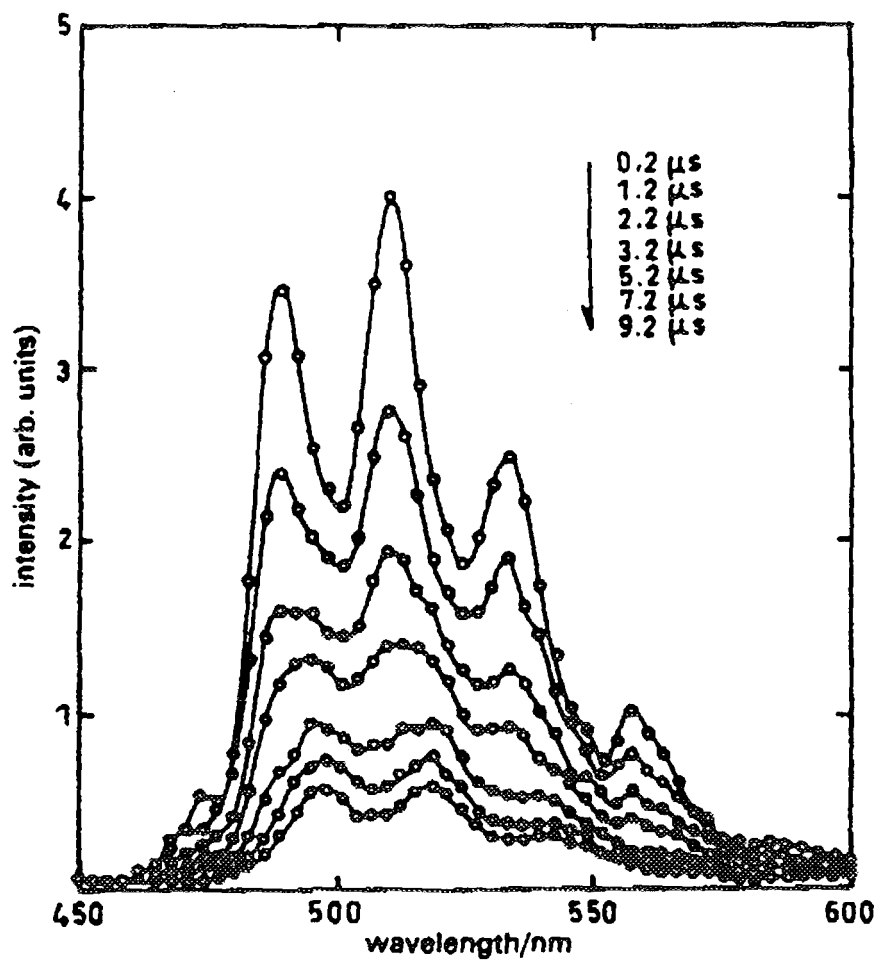


Figure 2: Time-Resolved Emission Spectra of Uranyl Ion.

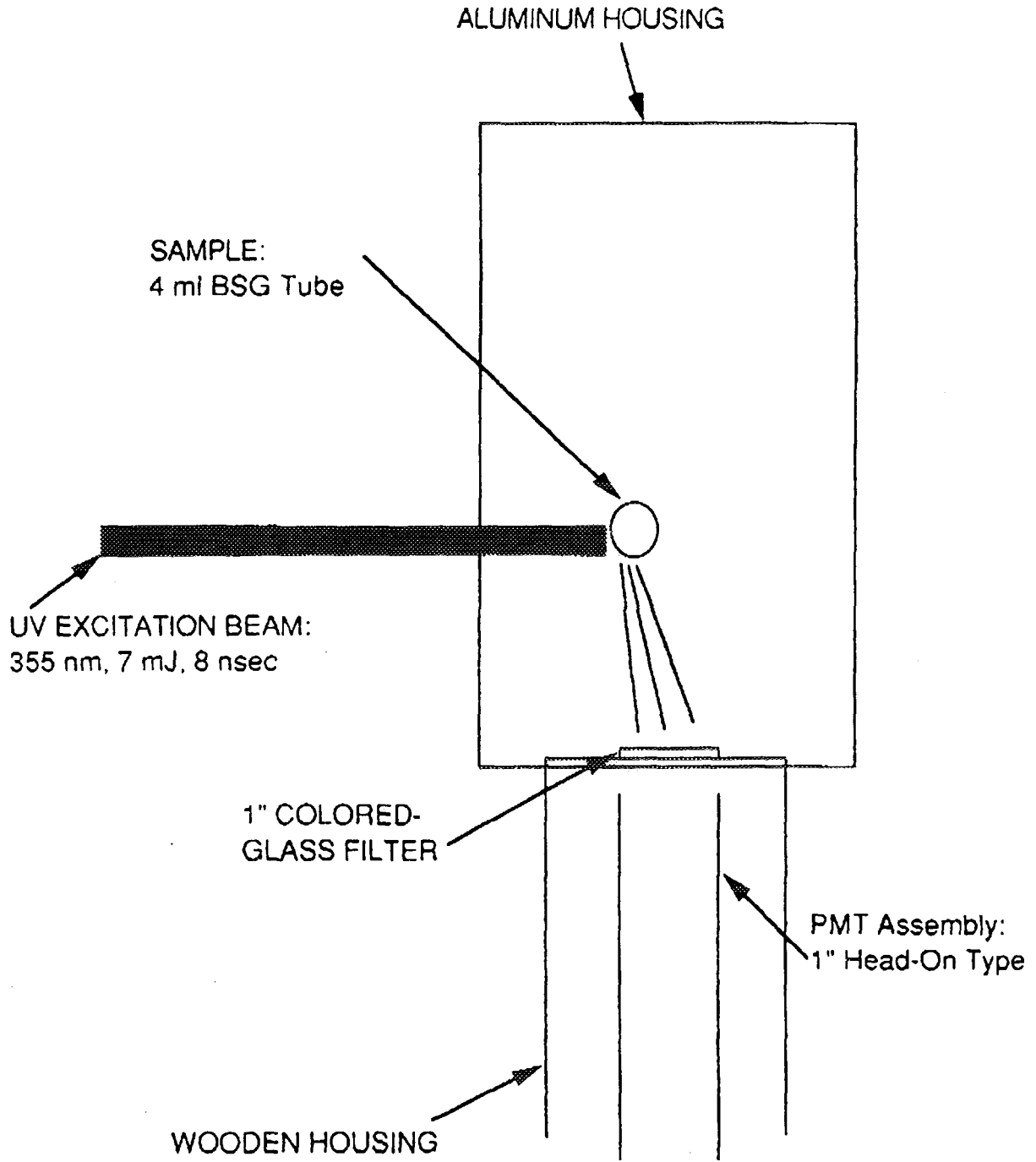


Figure 3: Sample Configuration



Iodine Behaviour in the SLOWPOKE Nuclear Reactor

P.A. Bekeris, G.J. Evans

Department of Chemical Engineering, University of Toronto, Toronto, Ontario, M5S 1A4
* Faculty advisor

ABSTRACT - The purpose of this project is to measure and attempt to explain the presence and volatility of iodine isotopes present as fission products in the SLOWPOKE-2 reactor. Liquid sampling and extraction procedures developed indicated that approximately 40% of the reactor iodine is in the form of iodate (IO_3^-), and 60% is in the form of iodide (I^-). No appreciable amount in non-polar forms such as molecular iodine (I_2) or organic iodides (RI) were detected. This goes contrary to past expectations that all of the iodine in the liquid phase would be in the form of I^- . In addition partition coefficients for I-131 were determined as $2\text{-}6 \times 10^6$ at a neutral pH. Kr-88 is suspected as a possible interfering isotope in the measurement of I-131 in the liquid and gas phases.

INTRODUCTION

One of the objectives of this undergraduate thesis project is to measure and attempt to explain the volatility and speciation of iodine isotopes present as fission products in the SLOWPOKE-2 reactor at the University of Toronto. As yet, no work specifically focused on the study of iodine in the reactor has been encountered.

Experiments involving the SLOWPOKE provide a unique opportunity to evaluate iodine volatility under more realistic reactor conditions and thereby provide insight into the volatility following accidents in full size nuclear generating stations (such as CANDU stations). An understanding of iodine volatility is important because it is potentially hazardous if released to the environment and under specific conditions it is possible that this would be one of the primary fission products released.

LITERATURE SURVEY

IODINE CHEMISTRY

Iodine is an element with only one stable isotope (^{127}I) and possibly greater than 30 isotopic forms. Many of the heavier iodine isotopes are possible slow neutron fission products of uranium-235 nuclei with half-lives ranging from 0.2 seconds to 15.7 million years (Walker, et al).

Radioiodine is produced within uranium

dioxide (UO_2) and other fuel pellets and escapes into the free (gap) spaces within the fuel rods where it reacts with another fission product cesium to form cesium iodide (CsI) (Malinauskas). It is believed that under normal operating conditions, the bulk of the iodine in the reactor is in this form (I^-).

Iodine has principal valence numbers of -1, 0, +1, +3, +5, and +7 and compounds are known in each of these oxidation states (Kirk, et al). Since so many different possible iodine compounds can form, it is difficult to predict what compounds will emerge under reactor conditions. Some of the most common chemical forms of iodine mentioned in related literature are: I^- , I_2 , HOI , IO_3^- , and RI .

RADIATION CHEMISTRY OF SOLUTIONS

Radiation chemistry is a fundamentally important phenomenon when considering the myriad of reaction mechanisms in a reactor core. Ionizing radiation has a very significant effect on the chemical state of matter. This type of radiation has two main effects on matter - an ionic effect and a free radical effect (Spinks and Woods). This is to say that radiation effects are principally ionic and/or free radical reactions, induced by the absorption of ionizing radiation, which in turn cause alterations in the chemical states of matter.

Water generally constitutes the greater portion of an aqueous system and secures a correspondingly large fraction of the absorbed

radiation energy. Therefore, chemical changes occur to the solutes when these react with the products of water radiolysis. In addition to this, radiolysis reactions can occur directly to the solute molecules (Spinks, Woods) and any combination of the two.

IODINE VOLATILITY

A useful parameter in quantitatively expressing the extent to which a substance such as iodine partitions into the aqueous and vapour phases is the instantaneous partition coefficient (IPC) (Lutz, Kelly).

$$IPC = \frac{Aq. Phase Iodine Conc.}{Vap. Phase Iodine Conc.}$$

Occasionally, this is also referred to as H.

Compounds with higher volatilities have lower values of IPC and conversely, those with low volatilities have high IPC values. Increased IPC values are favourable since the goal is to minimize the amounts of iodine in the gas phase.

In non-irradiated systems containing I_2 , pH is a significant parameter in determining the relative fraction of the various species. Depending on concentration, in acidic systems (pH-5), the I_2 species is favoured while in basic systems (pH-9) the I_2 is slowly converted to non-volatile I^- and IO_3^- . Since a reactor core under accident conditions can surely be assumed to be highly radioactive, it is more prudent to consider these effects under radioactive conditions. Irradiated systems containing I_2 or I^- are also pH dependent. Lutz and Kelly have reported that under conditions of irradiation of 0.003 to 0.06 Mrad/hr and pH of 5, the predominant species formed is I_2 . If the pH is increased to 9, then the main iodine species becomes I^- with a very large IPC value ($>10^5$) indicating low volatility. Studies of the effect of pH on IPC values of radioiodine in solution (as CsI) indicate that IPC increases proportionally with higher pH values which demonstrate that basic systems favour less volatility (Ma, Lem).

A recent similar study by Harnden et al indicated that iodine isotopes were present in the reactor water but not in the reactor head space. The

reactor used by Harnden was that of the University of Toronto. The report did not attempt to explain the apparent absence of iodine in the head space where it may have been expected to be present. Some speculation (independent of the above author) leads to the suggestion of very high IPC values for iodine in Harden's experiments.

NOBLE GAS BEHAVIOUR

Krypton is a gas having no chemical compounds under natural conditions. There exist 28 isotopes of which 6 are stable (Walker, et al). The majority of these have relatively short half-lives which do not accumulate in the environment, for the most part, and therefore have little basis for study or concern from an environmental standpoint (Styra, Butkus). An exception, though for a different reason, is Kr-88 with a half life of 2.8 hours and a gamma decay energy very close to that of I-131. It is suspected that this krypton isotope may present a hurdle in the immediate measurement of I-131 in a reactor sample.

The decay scheme for Kr-88 is as follows:



Krypton may be adsorbed on some solid surfaces and it adsorbs on porous surfaces of the charcoal type. This adsorption becomes greatly enhanced at low temperatures ranging from -20 to -60°C for example.

PROCEDURE

Liquid and gas samples from the reactor were taken and counted for gamma decay on a multi-channel analyzer (MCA). The liquid samples were solvent extracted in a manor such that any chemical speciation differences would have been observable. In order to prove the credibility of this analysis a series of test extractions with I-131 tracer (NaI) were carried out to demonstrate that the extraction procedure was efficient. Following this, the same procedure was used on actual reactor water samples. Gas samples were taken by pumping air through specially made solid adsorbent sample tubes. Samples were generally taken at the end of the week after the reactor

had been running for some time and fission products had accumulated.

The work conducted thus far may be subdivided into three separate sections.

- 1) Test extractions with I-131 tracer
- 2) Similar extractions with actual reactor water samples
- 3) Gas sampling using solid adsorbent filter tubes

The critical piece of equipment used in this project was the Canberra multi-channel germanium detector. This was connected to an IBM compatible personal computer with an Aptec spectrum program installed which nearly instantaneously provided a full spectrum of the sample. Isotope identification was conducted with the use of gamma energy tables and repetitive counts for half-life determination.

TEST EXTRACTIONS

The procedure used here was very similar to that illustrated in Figure 1 below. The objective here was to create conditions that would selectively separate ionic, neutral, and tightly bound iodine molecules (IO_3^-). Some I-131 tracer, in the form of NaI, was mixed with some deionized water. Chloroform with some I_2 were added and mixed to allow atom exchange to take place. The chloroform phase with the now labelled I_2 was removed and some additional washes with clean chloroform followed. The labelled iodine phase was further combined with sodium thiosulphate to reduce all I_2 to I^- . All separated phases were counted and the activities were expressed as percentages of the total starting activities in the original aqueous samples.

SLOWPOKE WATER EXTRACTIONS

The same process as described above was used for the water samples taken from the SLOWPOKE reactor. This process is depicted in Figure 1 below.

GAS SAMPLING

Gas sampling was accomplished with the use of solid adsorbents. A diagram of this process is presented in figure 2 below. Gas

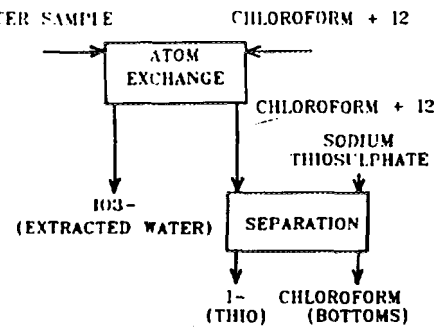


FIGURE 1: LIQUID EXTRACTION PROCEDURE

was passed through the head space sampling line, through the filter tube, then a coarse filter (to prevent solids from entering the pump), and finally through the pump before being sent back to the reactor. The adsorbents cadmium iodide (CdI_2), iodophenol, and TEDA (activated charcoal) were used in this order within the filter tube. Immediately following a calibrated pumping period of approximately 3.5 hours, the tubes were vented with an air stream for 1/2 hour to remove as much of the noble gases as possible and prevent their progeny from adding to the background counts of the sample. The tubes were then sectioned and counted for 6-12 hour periods on the MCA.

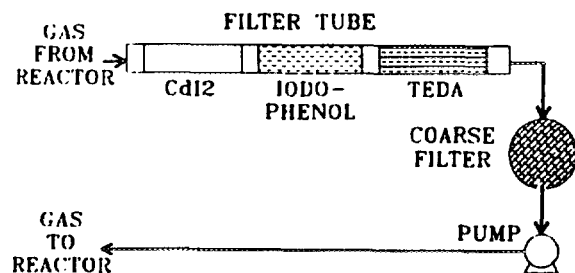


FIGURE 2: GAS SAMPLING PROCEDURE

RESULTS AND DISCUSSION

TEST EXTRACTIONS

Table 1 presents the results of the test extractions. The last four experiments yielded a 93% recovery rate with virtually little residual activity left in the extracted water phase. This was regarded as sufficient proof that the extraction process was working. Since all of the tracer was in the form of I⁻ it was readily able to atom exchange with the I₂. Had the tracer not been in the form of I⁻, but rather as IO₃⁻, then the iodine atoms would have been more tightly bound and atom exchange would not have been as complete. As a result, appreciable residual activity would have been left in the extracted water phase.

TABLE 1: IODINE-131 TEST EXTRACTION RESULTS

	EXPT.1	EXPT.2	EXPT.3
EXTRACTED WATER	30%	24%	<1%
1st CLEAN CHLOROFORM WASH	NA	3%	3%
2nd CLEAN CHLOROFORM WASH	NA	NA	1%
1st SODIUM THIO ADDITION	50%	62%	83%
2nd SODIUM THIO ADDITION	NA	4%	10%
3rd SODIUM THIO ADDITION	NA	4%	1%
USED CHLOROFORM (BOTTOMS)	10%	1%	<1%
LOSSES	10%	2%	1%
TOTAL	100%	100%	100%

	EXPT.4	EXPT.5	EXPT.6
EXTRACTED WATER	1%	1%	<1%
1st CLEAN CHLOROFORM WASH	18%	NA †	NA †
2nd CLEAN CHLOROFORM WASH	2%	NA †	NA †
1st SODIUM THIO ADDITION	72%	92% ‡	92% ‡
2nd SODIUM THIO ADDITION	4%	NA	NA
3rd SODIUM THIO ADDITION	<1%	NA	NA
USED CHLOROFORM (BOTTOMS)	<1%	<1%	<1%
LOSSES	5%	7%	7%
TOTAL	100%	100%	100%

% Percentages refer to fraction of initial I-131 activity in sample
 † Chloroform washes not counted separately, but rather added to I₂ - chloroform initial addition
 ‡ 1st, 2nd, 3rd sodium thio extractions though separate were combined

SLOWPOKE WATER EXTRACTIONS

The results of these tests are presented in Table 2 below. The primary result was that approximately 40% of the activity remained in the extracted water suggesting that 40% of the iodine in the reactor is in the form of IO₃⁻. The pH of these solutions were measured in the range of 6.8-7.1. In addition nearly all of the remaining activity was present in the sodium thiosulphate phase demonstrating that this portion was all I⁻. Very little was of the form of an organic iodide or I₂ since some activity would have been present in

the clean chloroform pre-wash phase.

TABLE 2: SLOWPOKE WATER EXTRACTION SUMMARY

	I131	I133
I	64%	58%
IO ₃ ⁻	35%	41%

GAS SAMPLING

Little in the way of gas phase speciation was revealed through these experiments. Overall I-131 partition coefficients of $2-6 \times 10^6$ were determined. This corresponded to a gas phase concentration of 0.3 pCi/L. In addition a strong suspicion exists that the interfering isotope was Kr-88 since the decay energy of this isotope is close to that of I-131 and the activity of this single peak dropped off greatly over the first 24 hours and then levelled off indicating that two modes of decay were present. In addition, Rb-88 was observed which most possibly came from Kr-88 decay.

REFERENCES

Hamden, A.M.C., Lewis, B.J., Bennett, L.G.I., "Final Report on the Experimental investigation of Fission Product Release in Slowpoke-2 Reactors", AECB, Ottawa, Feb. 1992.

Kirk, Othmer, et al., Encyclopedia of Chemical Technology, vol 13, Wiley Publ., Toronto, 1981.

Lem, W.; B.A.Sc. Thesis, University of Toronto, Dept. of Chemical Engineering. 1991.

Lutz, J.B., Kelly, J.L., "The Effects of Organic Impurities on the Partitioning of Iodine". Nuclear Technology, vol 80. 1988.

Ma, P., B.A.Sc. Thesis. University of Toronto, Dept. of Chemical Engineering. 1992.

Malinauskas, Bell; "The Chemistry of Fission Product Iodine Under Nuclear Reactor Accident Conditions". Nuclear Safety, vol 28 no 4. 1987.

Spinks, J.W., Woods, R.J., An Introduction to Radiation Chemistry, John Wiley & Sons, Toronto, 1990.

Styra, B., Butkus, B., Geophysical Problems of Krypton-85 in the Atmosphere. Mokslas Publishers, Vilnius, Lithuania, 1991.

Walker, F.W., et al, Nuclides and Isotopes, Chart of the Nuclides, 14th ed., General Electric Co., 1989.



NEUTRON ACTIVATION ANALYSIS MEASUREMENTS OF SUB MICRON AEROSOL DEPOSITION ONTO A CYLINDER ENERGIZED WITH AN ALTERNATING ELECTRIC FIELD

M.S. Fila

Graduate Student

**Department of Chemical Engineering, University of Toronto
200 College Street, Toronto, Ontario, M5S 1A4.**

Faculty Advisors:

R.L. Hummel, M. Kawaji, C.R. Phillips¹

University of Toronto

¹ University of Technology Sydney, Australia

ABSTRACT

Experimental measurements of aerosol deposition onto a cylinder energized with a 60 Hz electric field were conducted using a neutron activation analysis technique with a hafnium salt aerosol. The measured collection efficiencies were compared to theoretical expressions based on an electrostatic collection mechanism and fair agreement was found.

Introduction

The objective of this research project is to understand the deposition of a polydisperse sub micron aerosol onto a conducting cylinder energized with an alternating voltage. This paper describes some preliminary experiments and provides a tentative correlation of the results. A sub micron aerosol can be treated as inertialess particles which obey Stoke's drag law. For a polydisperse aerosol with a size range 0.01 to 1 micron diameter, the upper fraction of the size distribution dominates the mass deposition. The larger particles which have a low diffusivity can be treated as Stoke's law particles travelling with the moving fluid and subject to electrical forces. The most significant force is the coulombic force arising from the interaction of the external electric field and the field of a charged particle. In order to examine the collection behaviour, it is necessary to know the particle size and charge as well as the geometry of the electric and fluid flow fields.

The collection efficiency, η , for a cylinder is defined as $\eta = \frac{2y_0}{D_c}$ (1)

where y_0 is the ordinate of the limiting trajectory that separates the trajectories of those particles that are collected from the trajectories of particles that pass the cylinder without being collected. This expression assumes a symmetrical flow around the cylinder which will be true for the low Reynolds numbers ($Re < 1$.) in these experiments. The limiting trajectory ordinate should be evaluated at a distance far enough upstream such that the fluid flow is not disturbed from the assumed parallel uniform flow far ahead of the cylinder. This definition of collection efficiency in terms of the limiting trajectory is useful because it provides a link between the experimental definition given below and the calculated particle trajectory resulting from the numerical integration of the particle equations of motion.

The definition of limiting trajectory given above is sufficient for a d.c. (i.e. time independent) electric field, however for a.c. electric fields, the time-averaged collection efficiency, $\langle \eta \rangle$, must be used:

$$\langle \eta \rangle = \frac{1}{2\pi} \int_0^{2\pi} \frac{2y_0(\phi)}{D_c} d\phi \quad (2)$$

The phase angle, ϕ , accounts for different particle limiting trajectories due to the time varying electric field. Integrating over all values of the phase angle provides an average ac efficiency.

In terms of experimental quantities, the collection efficiency can be equivalently defined as

$$\eta_{\text{exp}} = \frac{m}{t D_c L U_o C_o} \quad (3)$$

The numerator represents the mass deposited in a time t on a length L of cylinder across which air flows with a free stream velocity U_o and mass concentration C_o of aerosol. A reliable measurement of collection efficiency requires accurate determination of both the deposited mass as well as the aerosol mass concentration in the air.

Theoretical collection expressions have been derived for flow regimes where simple analytical expressions exist for the fluid velocity field and for a non-time-varying electric field [1],[2],[3],[4]. These expressions have the approximate form:

$$\eta \approx \pi K_{ec} \quad (4)$$

and use an electrostatic parameter K_{ec} , defined in terms of the linear charge density on the cylinder Q , the particle charge and diameter, q and d_p respectively, the cylinder diameter D_c , and the fluid viscosity μ . The Cunningham correction factor and the dielectric constant of the fluid are represented by C and ϵ_f respectively.

$$K_{ec} = \frac{qQC}{3\pi^2 \epsilon_f d_p U_o D_c \mu} \quad (5)$$

The collection efficiency expression for a cylindrical conductor energized by an a.c. electric field has the form shown in equation (6) where the cylinder radius and free stream air speed are denoted by R_c and U respectively. The voltage frequency is ω rad/s.

$$\langle \eta \rangle = \frac{K_{ec} U}{\omega R_c} \quad (6)$$

An equivalent form of equation (6), in terms of particle mobility, z_o , surface electric field strength, E_a , and cylinder radius R_c , is:

$$\langle \eta \rangle = \frac{z_o E_a}{\omega R_c} \quad (7)$$

This form is useful because measurement of particle mobility distribution is simpler than measurement of particle diameter and charge separately.

Description of the Experiment

A single-nozzle Collision atomizer is supplied with a 0.2% di-ammonium hexafluorohafniate solution. The droplets first pass through an impactor, a drying tube and a neutralizing tube and then enter a differential mobility analyzer which separates particles having a specific mobility value. The separated

aerosol enters an exposure cell containing a carbon rod coaxial with a grounded wire cage. The aerosol flows across the rod which is connected to an a.c. voltage source. At the end of the exposure, the rod is removed and the hafnium content determined by neutron activation. A schematic diagram of the experiment is shown in Figure 1.

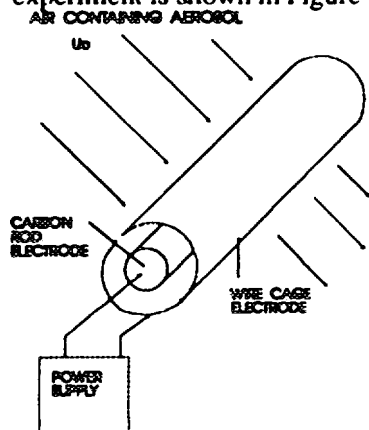


Figure 1: Schematic Diagram of the Experiment

Table 1 Aerosol Properties and Experimental Conditions

Particle mmd Diameter (micron)	0.12
Mobility ($\text{m}^2\text{V}^{-1}\text{s}^{-1}$) Positive Charge	2.6×10^{-8}
Geometric Std. Deviation	1.4
Diffusivity ($\text{m}^2 \text{s}^{-1}$)	7.7×10^{-10}
Wire Cage Diameter (m)	4.2×10^{-2}
Rod Diameter (m)	5×10^{-4}
Reynolds Number	0.7
Mass Concentration (g cm^{-3}) Density of di-ammonium hexafluorohafniate salt (g cm^{-3})	$0.8 \text{ to } 3.0 \times 10^{-11}$
Mass of deposited aerosol (nanograms)	50 to 400
Rod Charge (C m^{-1}) @V =3000 V(dc)	3.8×10^{-8}
Corona Threshold Electric Field (V m^{-1})	8.6×10^6
Surface Elec. Field (V m^{-1}) @ V=3000V(dc)	2.7×10^6

An aerosol sample is withdrawn from the exposure cell during the experiment and analyzed for particle concentration by a TSI model 3071 Electrostatic Classifier in series with a TSI model 3020 Condensation Nucleus Counter. The mass concentration is computed by multiplying the cumulative volume fraction with the density of the hafnium salt shown in Table 1.

Results

The overall agreement between theory and measured ac collection efficiency is satisfactory to within an order of magnitude. A strong correlation was observed for data grouped at Reynolds number 0.3 and 1., but poor correlation at Reynolds number 0.03 and 0.7. The standard deviation estimated by error propagation analysis was 20%, i.e. the one sigma band for an experimental collection efficiency of 0.8 would be 0.16. The largest contributions to the estimated standard deviation arise from the mass concentration on the aerosol and the mass deposit on the rod. The r.m.s. a.c. voltage was used in evaluating K_{ec} . Figure 2 shows plots of experimental ac collection efficiency compared to the theoretical value from equation (6).

Discussion of Results

Previous published experimental work by R. Lathrache [4] on aerosol penetration through charged fibrous (electret) filters concluded that the single fiber collection efficiency was proportional to the (d.c.) electrostatic parameter, K_{ec} , for small values of the fiber volume fraction. The experiments in [4] used fibers ranging in diameter from 4 to 30 microns and linear fiber charge density of approximately $10^{-10} \text{ C m}^{-1}$. The experiments reported in this paper used a cylinder of diameter approximately 500 microns with linear charge density up to $3 \times 10^{-8} \text{ C m}^{-1}$. In spite of these differences in cylinder diameter, linear charge density and voltage frequency, (d.c. vs 60 Hz) it appears that the electrostatic number can be useful in correlating charged particle deposition in both d.c. and a.c. electric fields because both situations involve electrostatic force acting on the particle.

Anticipating the application of these results to transmission lines, it should be noted that the range of a.c. voltages represented by these data correspond to a surface field strength lower than that which would be expected to produce TV and radio interference or lead to electrical (corona) discharge effects.

The mass concentration of aerosol particles used in these experiments is typical of ambient outdoor conditions [5], and in the absence of an electric field, $0.1 \mu\text{m}$ particle deposition velocities have been measured to be in the range 0.001 to 0.05 cm s^{-1} . In contrast, deposition velocities of approximately $1 - 2 \text{ cm s}^{-1}$ were observed in the experiments reported here (e.g. a typical a.c. collection efficiency of 0.1 at a Reynolds number of 1, corresponds to a deposition velocity of 2 cm s^{-1})

Conclusion

The electrostatic parameter, K_{ec} can be used to correlate the collection of charged aerosol particles by means of an electrostatic mechanism in an alternating electric field by using an expression similar to equation (6).

Possible Application of this Work

The results of these experiments could be applied to estimating transmission line pollutant deposition under fair weather conditions with low levels of pollution. Other factors that might have to be considered to obtain a better understanding of pollutant deposition would include the presence of any insulating oxide coating on the conductors, surface roughness, the fluid flow field, the non-uniform electric field around the conductor bundle, the possibility of corona discharge as well as the effect of the conductor temperature rise above ambient conditions which would be expected to cause a thermophoretic motion of particles away from the conductor surface.

References

- [1] Lathrache, R.,H.Fissan "Enhancement of Particle Deposition in Filters due to Electrostatic Effects", *Filtration & Separation*, Nov. - Dec., 1987, pp418-422.
- [2] Natanson, G.I., "The Condensation of Aerosol Particles by Electrostatic Attraction on a Cylinder Around which they are Streaming", *Proc. of the Academy of Science, U.S.S.R., Physical Chemistry Section*, v.112, pp95-99, 1957.
- [3] Nielsen, K.A., "Collection of Inertialess Particles on Circular Cylinders with Electrical Forces and Gravitation", *Journal of Colloid and Interface Science*, vol. 64, no.1, Mar. 15, 1978, pp131-142.
- [4] Lathrache, R.,H.J. Fissan,S. Neumann, "Deposition of Submicron Particles on Electrically Charged Fibers", *J. Aerosol Sci.*, vol. 17, no. 3, pp446-449, 1986.
- [5] Holsen, T.M., Noll, K. E., "Dry Deposition of Atmospheric Particles: Application of Current Models to Ambient Data", *Environ. Sci. Technol.*, v.26, n. 9,pp 1807-1815,1992.

Figure 2(a)

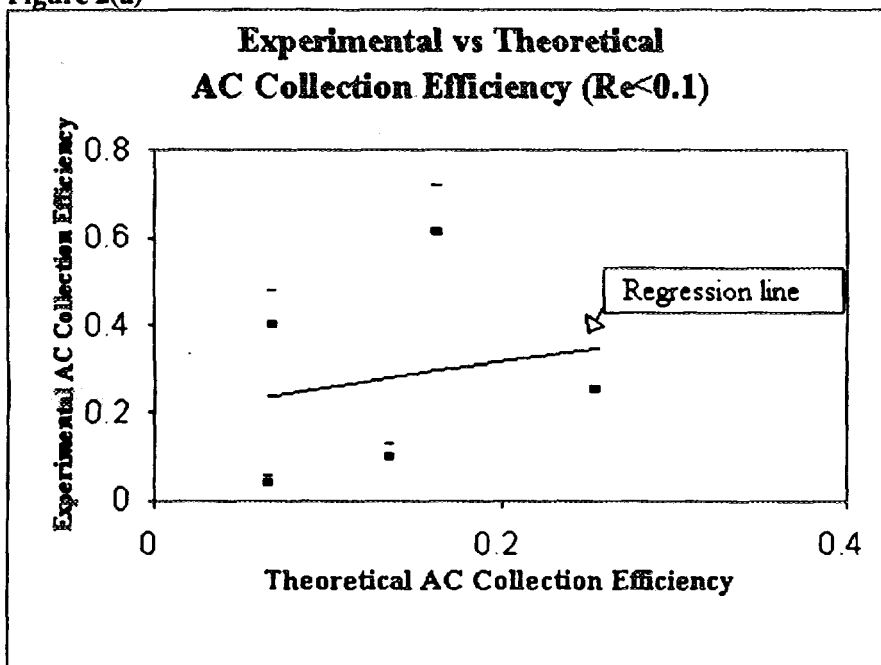


Figure 2(b)

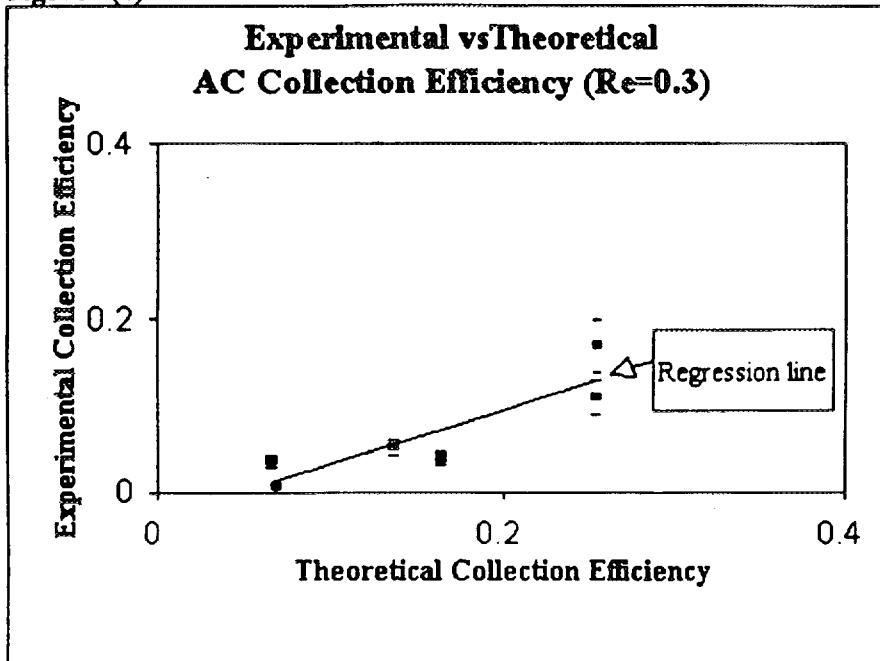
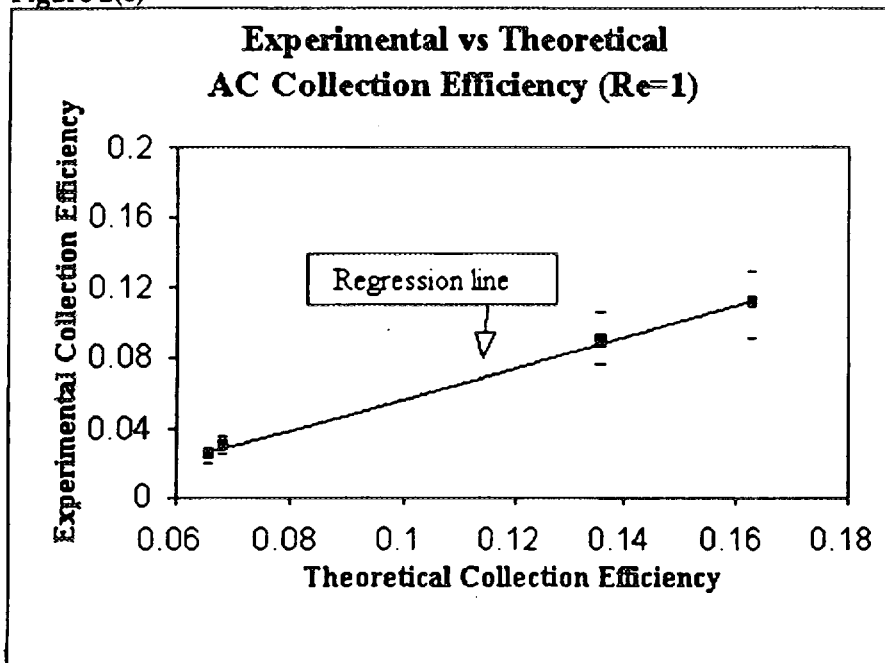


Figure 2(c)





EFFECT OF GAMMA IRRADIATION ON THE STRUCTURE OF CORN STALKS AND THEIR SUBSEQUENT BIOCONVERSION INTO PROTEIN-RICH MYCELIAL BIOMASS OF *PLEUROTUS SAJOR-CAJU*.

Victor Awafo

Université du Québec, Institut Armand-Frappier,
531, boulevard des Prairies, Laval, Québec, H7N 4Z3
Directors; D.S. Chahal and R. Charbonneau.

Abstract.

Lignocellulosic biomass like corn stalk is an abundant and renewable resource from which food, feed and chemicals may be derived. Enzymatic hydrolysis of native lignocellulosic material is prohibitively slow due to their compositional heterogeneity and structural complexity.

In this work, ground corn stalks (20 mesh) were subjected to gamma irradiation (10-170 Mrads) as pretreatments to make them more susceptible for bioconversion into protein-rich mycelial biomass of *Pleurotus sajor-caju* NRRL 18757. The irradiation was carried out in air in a ⁶⁰Co Underwater Calibrator (UC-15, Nordion International) at a dose rate of 2.5 Mrads/h as measured by Fricke dosimetry.

No apparent structural differences were observed under the light microscope. However, the protein synthesis and the proportion of mycelial biomass increased with the increase in both the dose of irradiation and time of fermentation during the bioconversion of 1% corn stalk into mycelial biomass of *Pleurotus sajor-caju*.

Gamma irradiation at the dose of 50 Mrads or lower did not produce any appreciable increase in the amount of protein synthesised. At 170 Mrads, the final product contained 28% protein representing a 2-fold increase from non-irradiated corn stalk and an efficiency of 36% conversion of total utilizable polysaccharides of corn stalks into mycelial biomass.

The lag phase during mycelial biomass production was much more prolonged at very high doses indicating possible production of some toxic substances during irradiation.

INTRODUCTION

Gamma irradiation has found useful and acceptable applications in the radiosterilization of biomedical products (I.A.E.A.,1973) and in food preservation (W.H.O.,1988). Another area in which gamma irradiation has been explored is in the pretreatment of lignocelluloses for hydrolysis and to increase their digestibility to rumen animals (Begum *et al.*, 1988; Han *et al.*, 1980; Mandels and Steinberg, 1976).

Obtained mainly from forestry and agricultural residues, lignocelluloses constitute formidable sources of renewable substrates from which food/feed, fuel and chemicals may be derived. It is estimated that the production of cereal straws alone in the world ranges from 2246 to 3644 million tons (Bano and Rajarathman, 1988; Ishaque and Chahal, 1991) and one-third of this is constituted by corn straw. Much of these straws are in the developing countries where there is less industrialisation with a concomitant increase in agricultural population.

The enzymatic hydrolysis of native lignocellulosic material is prohibitively slow due to their compositional heterogeneity and structural complexity such as cellulose crystallinity, lignin content and surface area (Fan *et al.*, 1980; Tsao *et al.*, 1978).

Physical (milling and irradiation), chemical and biological processes either singly or in combination have been reported for use in lignocelluloses pretreatments to enhance enzyme or microbiologically catalysed breakdown (Chahal, 1991; Lindisch *et al.*, 1983). Fan *et al.* (1980,1981) have suggested that enhancement in the hydrolysis rate with such pretreatments is attributable to the modification of the structural features.

This work considers the effect of irradiation dose on the structure of the corn stalk vis a vis its effect on the production of mycelial biomass of the edible mushroom, *Pleurotus sajor-caju*.

MATERIALS AND METHODS

Ground corn stalk (20 mesh) particle size was subjected to gamma irradiation of 10, 50, 100, and 170 Mrads to make them more susceptible for bioconversion into protein-rich mycelial biomass of *Pleurotus sajor-caju* NRRL 18757. The irradiation was carried out in air in a ^{60}Co Underwater Calibrator (UC-15, Nordion International). The dose rate of the gamma source was 2.5 Mrads/h as measured by Fricke dosimetry.

1% (w/v) of substrate was prepared in shake flasks of Mandels and Weber medium (1969) and inoculated at 10% (v/v) with the culture medium of *Pleurotus sajor-caju*. The cultures were incubated aerobically at 30 °C, 200 rpm and pH, 5.8.

Duplicate samples of each fermentation treatment were taken at various time intervals and analysed for crude protein and dry weight of mycelial biomass in final product. The crude protein was obtained by measuring total nitrogen in a Nitrogen Analyser (Leco Company) and multiplying by a factor of 6.25. The results also include the determination of the specific growth rate, protein productivity and conversion efficiency of substrate into protein. The structural modifications of the irradiated and non-irradiated substrate were examined under the light microscope.

RESULTS AND DISCUSSION.

EFFECT OF GAMMA IRRADIATION PRETREATMENT ON THE STRUCTURE OF CORN STALK.

The results obtained from examining the physical structural modifications of non-irradiated and irradiated corn stalk under the light microscope (results not shown) indicated that there were apparently no observable differences in the physical structures of the different pretreatments. It is expected that a physical pretreatment like gamma irradiation would decrease the crystallinity of the cellulose. Cowling (1975) and Stone *et al.* (1969) reported that the most important structural feature that influences enzymatic hydrolysis is the accessibility of cellulose surface to cellulolytic enzyme. Direct physical contact between the enzyme molecules and the substrate cellulose is a pre-requisite to hydrolysis.

The ability of *Pleurotus sajor-caju* to utilize the polysaccharide (cellulose and hemicelluloses) of both non-irradiated and irradiated corn stalk in the production of mycelial biomass would reveal the marginal differences that could not be observed under the light microscope.

EFFECT OF GAMMA IRRADIATION PRETREATMENT ON THE PRODUCTION OF MYCELIAL BIOMASS WITH PLEUROTUS SAJOR-CAJU.

Table 1 and figure 1 show the results obtained from the production of mycelial biomass of *Pleurotus sajor-caju* on 1% glucose. The results include, the protein content in the final product, the growth rate, the efficiency of conversion of substrate into protein and protein productivity.

Glucose is a monomer that is readily utilized by microorganisms as carbon and energy sources. Table 1 and figure 1 show that the proportion of mycelial biomass increases with the increase in time of fermentation. The decrease in the protein content as observed in the latter phase of the fermentation is attributable to causes such as depletion of the glucose substrate and possible proteolytic activity of *Pleurotus sajor-caju* to obtain sustainable energy in the absence of glucose. Autolysis of older mycelium is a common phenomenon in fungi (Cochrane, 1958) and this could have additionally contributed to a decline in mycelial biomass.

The results reported for the glucose substrate seek to serve as the standard base for assessing the performance of both irradiated and non-irradiated corn stalk in their bioconversion into mycelial biomass. It is expected that the more accessible the polysaccharides (cellulose and hemicelluloses) of corn stalk are to the lignocellulolytic enzyme system of *Pleurotus sajor-caju*, the closer the goal at obtaining the same or superior results compared to the glucose substrate.

Table 2 shows that the protein content and efficiency of bioconversion of corn stalk into protein increased with increase in radiation dose. The increase in protein content with increase in irradiation dose as compared to the non-irradiated corn stalk may suggest that depolymerisation of corn stalk is radiation dependent and supports the view that radiation doses greater than 50 Mrads can cause a decrease in crystallinity of lignocelluloses (Aoki *et al.*, 1977; Arthur *et al.*, 1960). At 170 Mrads, the protein content was about two-fold the protein content of the non-irradiated corn stalk but much less than that for the glucose substrate. This suggests that even at this high radiation dose there was still a limited increase in the susceptibility of corn stalk for bioconversion into protein-rich mycelial biomass of *Pleurotus sajor-caju*. The possible effects of gamma irradiation on lignocellulosic material to increase their susceptibility for enzymatic attack include, depolymerisation, solubilization and decrease in crystallinity or increased surface area. It has been reported by Han and Ciegler (1982) that gamma irradiation at or above 10 Mrads was sufficient to drastically increase the specific surface area of sugarcane bagasse for enzymatic hydrolysis. Saemen *et al.* (1982) reported that gamma irradiation dose over 50 Mrads causes a portion of lignocelluloses to become water soluble. There was however no observable solubilization of the corn stalk even at 170 Mrads.

Figures 2, 3, 4, 5, and 6 show the trend of bioconversion of non-irradiated and irradiated corn stalk into protein-rich mycelial biomass with *Pleurotus sajor-caju*. It may be noted that when corn stalk is used as substrate, there is an inverse relationship between the dry weight of the

final product and the protein content such that a decrease in final product weight gave rise to an increase in the protein content. These trends are clearly observed at the higher irradiation dose levels. This supports the theoretical base that on complete utilization of a carbon substrate by fungi, about one-half the weight of the substrate is obtained as its mycelial biomass. In 1991, Chahal and Khan reported a similar trend when they used sodium hydroxide pretreated rice straw to produce mycelial biomass of *Pleurotus sajor-caju*.

At gamma irradiation dose of 100 Mrads or above, the figures indicate that there is a much more prolonged lag phase than at the lower dose levels. Implicated in this is the possible production of toxic substances like malondiadehyde which is one of several oxidation products formed during irradiation of lignocelluloses. The production of malondialdehyde when irradiation is carried out under neutral or alkaline conditions has been reported by several workers (Bludovsky and Duchacek, 1979; Scherz, 1970).

CONCLUSION

The effective use of gamma irradiation as a single pretreatment to make corn stalk more susceptible for bioconversion into protein-rich mycelial biomass requires very high radiation doses. The possibility of combination pretreatments of gamma irradiation and chemicals could reduce the radiation dose and increase protein content in the final product since physical pretreatments can decrease cellulose crystallinity and increase surface area while chemicals cause delignification. The results of the combination pretreatments are reported elsewhere.

TABLE 1: THE PRODUCTION OF MYCELIAL BIOMASS WITH PLEUROTUS SAJOR-CAJU ON 1% GLUCOSE.

TIME OF FERMENTATION (h)	DRY WT. OF FINAL PRODUCT* (MYCELIAL BIOMASS) (g/L)	PROTEIN CONTENT OF FINAL PRODUCT (%)	PROTEIN (C) (g/L)	GROWTH RATE dC/Cdt (1/h)	EFFICIENCY $E = C-Co/So$ (%)	PRODUCTIVITY $P = C-Co/t-to$ (g/L.h)
0	1,250	25,062	0,313			
18	2,560	26,494	0,678			
24	3,480	31,994	1,113			
40	4,870	37,656	1,834			
52	5,010	39,162	1,962			
64	5,430	37,431	2,033			
70	5,390	41,956	2,261	0,045	77,926	0,028
76	4,880	38,119	1,860			
88	4,370	34,462	1,506			
112	3,330	26,987	0,899			
136	2,260	31,912	0,721			

*FINAL PRODUCT: The final product contains the newly synthesized mycelial biomass and the unutilized substrate.
The proportion of mycelial biomass increases with the increase in the time of fermentation during the bioconversion of substrate into mycelial biomass with the growth of *Pleurotus sajor-caju*.

TABLE 2: THE EFFECT OF GAMMA IRRADIATION ON THE PRODUCTION OF MYCELIAL BIOMASS WITH PLEUROTUS SAJOR-CAJU

TYPE OF SUBSTRATE AND *FERMENTATION TIME(h)	FINAL PRODUCT (MYCELIAL BIOMASS)	PROTEIN CONTENT OF FINAL PRODUCT (%)	PROTEIN (C) (g/L)	EFFICIENCY E = C-Co/So (%)	PRODUCTIVITY P = C-Co/t-to (g/L.h)	GROWTH RATE dC/Cdt (1/h)
UNTREATED CORN STALK (36h)	6,550	14,456	0,947	25,105	0,010	0,009
GLUCOSE (70h)	5,390	41,956	2,261	77,926	0,028	0,045
10 Mrads CORN STALK (36h)	6,640	11,612	0,771	24,164	0,010	0,012
50 Mrads CORN STALK (60h)	5,510	15,569	0,858	13,789	0,003	0,003
100 Mrads CORN STALK (93h)	5,550	22,334	1,240	39,848	0,006	0,011
170 Mrads CORN STALK (120h)	3,210	28,037	0,900	36,027	0,005	0,019

*FERMENTATION TIME(h) : The fermentation time is the time that resulted in the optimum protein synthesis

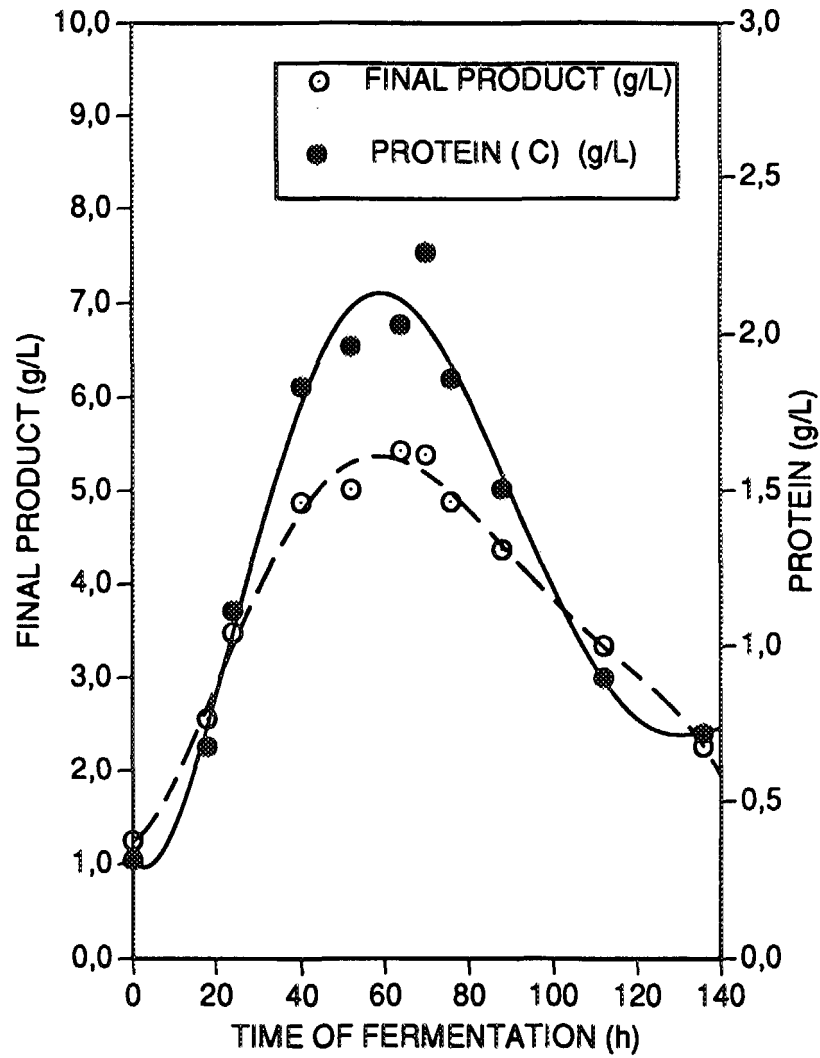


FIG.1 PRODUCTION OF MYCELIAL BIOMASS WITH *PLEUROTUS SAJOR-CAJU* ON 1% GLUCOSE

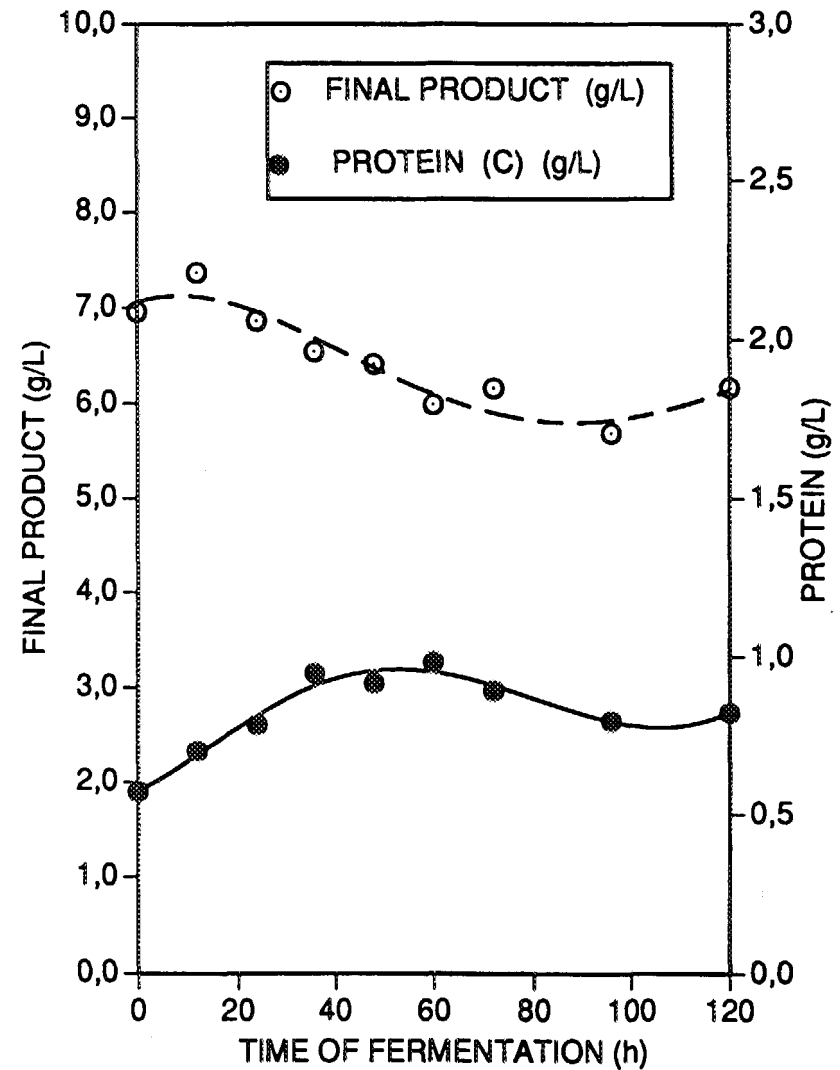


FIG.2 PRODUCTION OF MYCELIAL BIOMASS WITH *PLEUROTUS SAJOR-CAJU* ON 1% CORN STALKS WITHOUT PRETREATMENT.

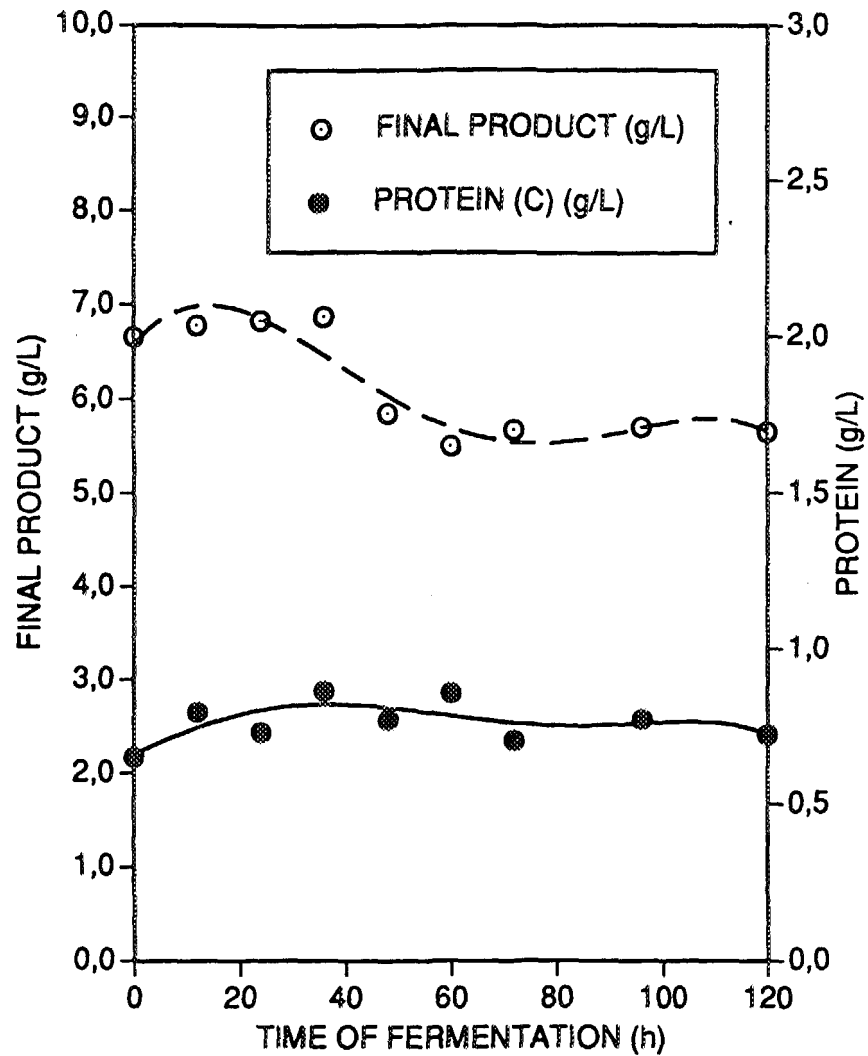


FIG.3 PRODUCTION OF MYCELIAL BIOMASS WITH PLEUROTUS SAJOR-CAJU ON 1% CORN STALK IRRADIATED AT 10 Mrads.

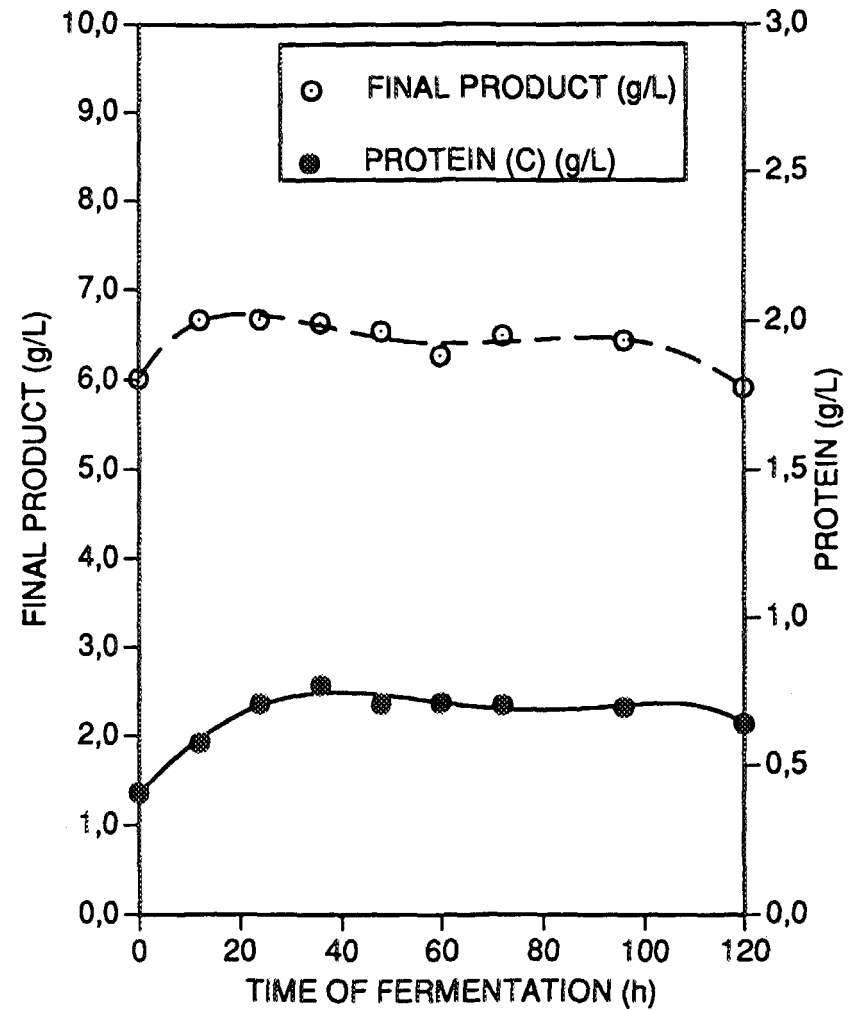


FIG.4 PRODUCTION OF MYCELIAL BIOMASS WITH PLEUROTUS SAJOR-CAJU ON 1% CORN STALK IRRADIATED AT 50 Mrads.

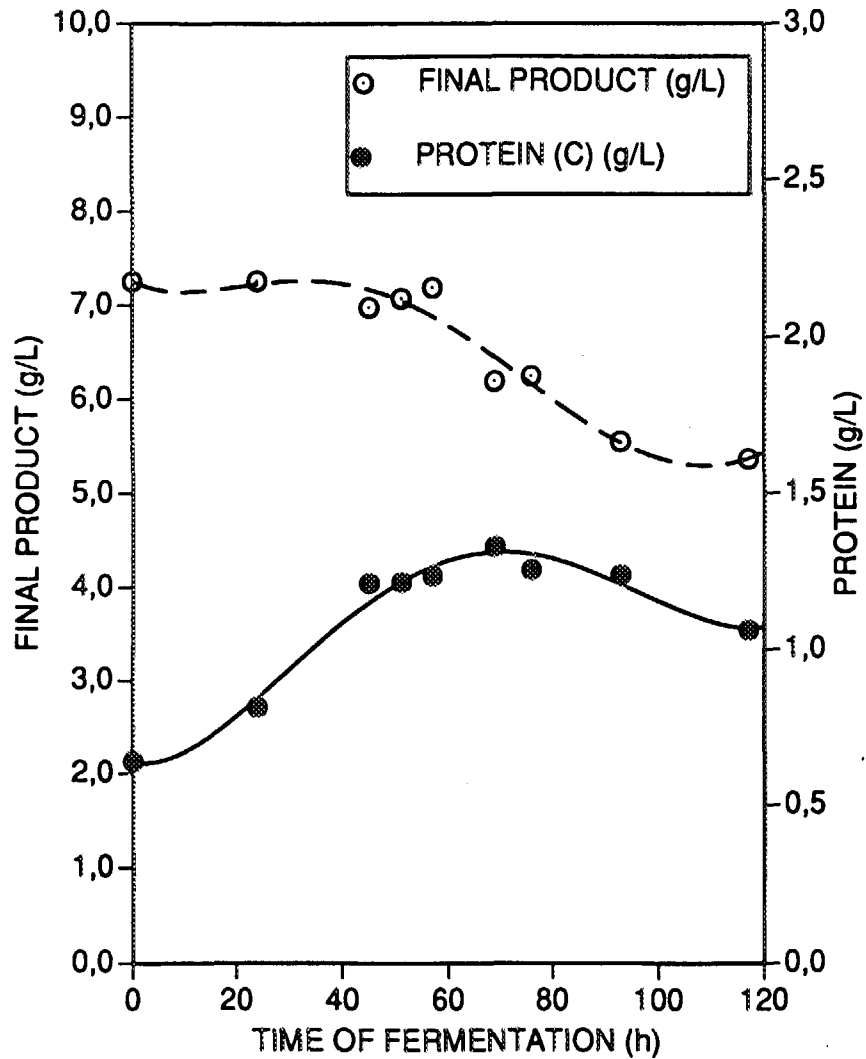


FIG.5 PRODUCTION OF MYCELIAL BIOMASS WITH PLEUROTUS SAJOR-CAJU ON 1% CORN STALK IRRADIATED AT 100 Mrads.

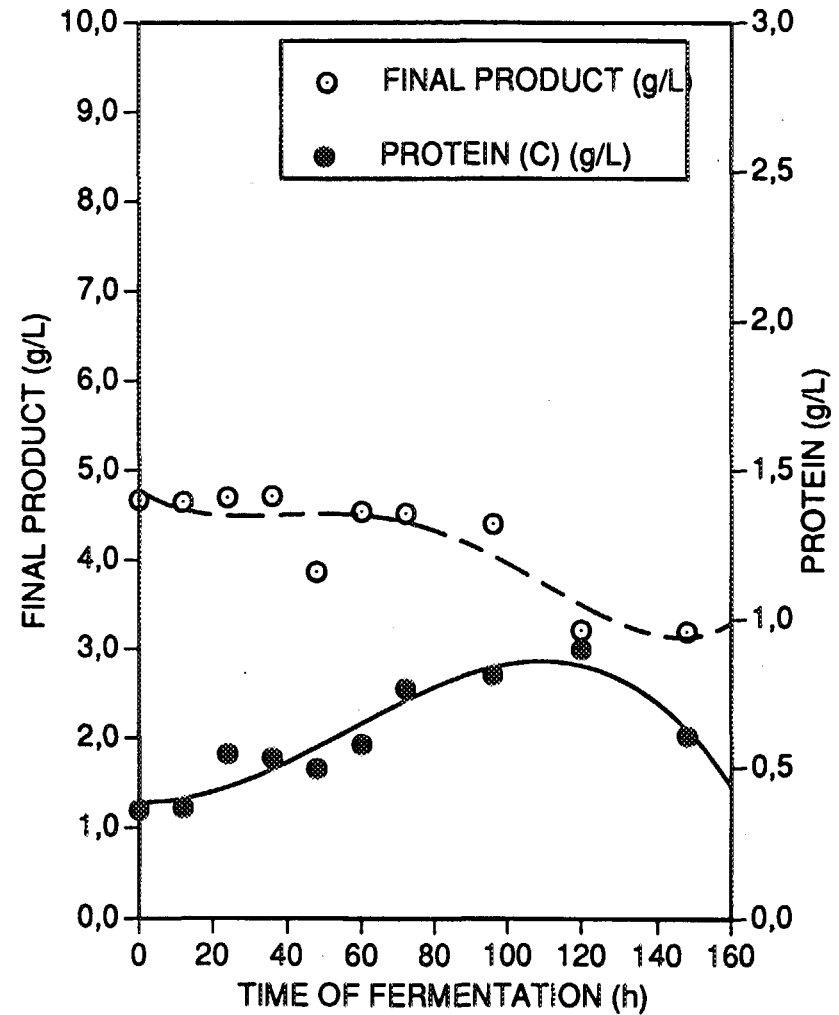


FIG.6 PRODUCTION OF MYCELIAL BIOMASS WITH PLEUROTUS SAJOR-CAJU ON 1% CORN STALK IRRADIATED AT 170 Mrads.

(Samedi 3 avril 13:30 → 15:30)
(Saturday April 3rd 13:30 → 15:30)

SESSION 5
RÉACTEUR À SUSPENSION DE PARTICULES / PELLET SUSPENSION REACTOR
Président / Chairman: Dr. A. Harms, McMaster University
Salle / Room: C-631 (AMPHITHÉÂTRE BELL)

- C.W. Baetsen McMaster University
Fuel Pellet Considerations for the PSR (Pellet Suspension Reactor)
- J. Whitlock McMaster University
Core Physics Analysis of a Pellet Suspension Reactor (PSR)
- D. Kingdon McMaster University
Pellet Suspension and Fluidization Considerations in a Pellet Suspension Reactor (PSR)
- G. Rose† McMaster University
Pellet Dynamics in a Fluidized Bed Reactor Core
- W. Fundamenski McMaster University
Pellet Entrapment in LOCA Scenerio for the PSR Reactor
- S. Day McMaster University
Fission Product Management and Fuel Reprocessing in a Pellet Suspension Reactor

† Denotes Undergraduate student
Indique un(e) étudiant(e) au Baccalauréat



FUEL PELLET CONSIDERATIONS FOR THE PSR (PELLET SUSPENSION REACTOR)

Charles W. Baetsen, B.Eng

Department of Engineering Physics
McMaster University
Hamilton, ON

Advisor: Dr. A. A. Harms

ABSTRACT

The PSR (Pellet Suspension Reactor) is a conceptual proposal which incorporates desirable aspects deemed paramount for future reactors. It is an inherently and passively safe reactor with capabilities for online refuelling and online fission product removal. The design utilizes a microsphere fuel pellet arrangement which is suspended in a fluidized bed of helium. This arrangement allows for a passive method of removing fuel elements from the core in the event of a LOCA, thus preventing a meltdown and localized supercritical fuel collection. The main focus of this paper is to address fuel pellet considerations and proposed selections. Major elements under consideration are: composition, dimensions, power generation, durability (both corrosion resistance, and mechanical hardness), reprocessing ability and thermodynamic properties. Thermodynamic properties considered refer to both normal coolant action, and LOCA properties, with emphasis on coolant action. Selection of final fuel element design is based on these properties in light of constraints to mentioned within. Both homogeneous and heterogeneous pellets will be examined.



Core Physics Analysis of a Pellet Suspension Reactor (PSR)

Jeremy Whitlock

Department of Engineering Physics
McMaster University, Hamilton, Ontario
Advisor: Prof. Archie Harms (same address)

Abstract

A fission reactor with an active volume containing spherical micro-pellets of fuel (0.5 mm diameter) suspended in columns of pressurized Helium gas, separated by low-pressure D₂O moderator, has an attractive potential for passive safety in the event of a LOCA, and also for on-line fuel management. This study examines the core physics issues relevant to such a concept. Lattice parameters are established through a criticality search, assuming both UO₂ and UC as fissile material. Reactivity feedback mechanisms such as fuel temperature, coolant temperature, and localized pellet density changes are considered. Finally, an assessment of core criticality and a preliminary burnup analysis are undertaken.

The lattice code WIMS-D4¹, with a 69-group nuclide library, is used in the criticality search, the estimation of reactivity feedback effects, and the preliminary burnup analysis. It is also used to generate few-group diffusion coefficients for the core code CITATION², used to calculate the global flux. Both codes are run in a 486/33 PC environment.

To aid the analysis, a model is employed whereby fuel pellets are homogenized with Helium coolant, keeping nuclide numbers constant. Such an approach ignores spatial effects such as resonance self-shielding in fuel surfaces, and accordingly a comparison is made of heterogeneous and homogeneous criticality values, using the Monte-Carlo code MCNP-4³. The correction is found to be minor (1 or 2 mk), due to the small volume of fuel pellets (and corresponding high surface-to-volume ratio).

¹ Askew, J.R., Fayers, F.J. and Kemshell, P.B., *A General Description of the Lattice Code WIMS*, Journal of British Nuclear Energy Society, 4(4), 564, 1966.

² Fowler, T.B., Vondy, D.R. and Cunningham, G.W., *Nuclear Reactor Core Analysis Code: CITATION*, Technical Report ORNL-TM-2496 (Rev. 2), Oak Ridge National Laboratory, Oak Ridge, Tennessee, 1971.

³ *MCNP 4, Monte Carlo Neutron and Photon Transport Code System*, CCC-200A/B, RSIC Computer Code Collection, Radiation and Shielding Information Centre, Oak Ridge National Laboratory, Oak Ridge, Tennessee, June 1991.



PELLET SUSPENSION AND FLUIDIZATION CONSIDERATIONS IN A PELLET SUSPENDED REACTOR (PSR)

Dave Kingdon
Department of Engineering Physics
McMaster University
Hamilton, Ontario
L8S 4L7

ABSTRACT

One aspect of a fission power reactor design which is inherently safe against loss of coolant accidents and provides the potential for on line fission product management is considered. Specifically, the suspension of micro-pellets in an upward flowing stream of helium gas is analyzed to determine appropriate geometries and system physical properties for such a reactor to be feasible from a fluidization perspective.

The pellets to be suspended must remain within a given vertical regime in each of several vertical fuel channels in the reactor. Thus, expansions of the tubes (yielding corresponding reductions in the superficial gas velocities) at the base and top of the designated core restrict the particles to the desired region. Within this core region, the superficial helium gas velocity must be equal to the terminal velocity of the micro-pellets - a function of helium temperature, pressure, and density, particle material density, pellet diameter, and sphericity (nearness of the particles to spherical in shape).

From a manufacturing perspective, a sphericity of 0.95 is very easily attained for UC pellets, however UO_2 pellets are also compatible with a PSR design. Gas temperature has little direct effect on the fluidization of the system, but the helium pressure does play a significant role. In order to minimize the required gas velocity (which helps maintain an even particle distribution) without forcing the pellet size too small to be manageable, an operating pressure of 50 atmospheres (similar to many high temperature gas reactors) is selected, and a temperature limit of 800 °C similarly determined.

Following the selection of these quantities, the dependence of particle distribution uniformity on gas velocity and particle size is investigated utilizing analogous fluidization technology and correlations from the fluidization literature. In order that the pellet distribution remain as even as possible, an average pellet diameter of no more than 0.5 mm is required, yielding a superficial gas velocity of, at most, 6.6 m/s. To maintain uniform vertical particle distributions with these pellet sizes and gas velocities, the core height is forced to be a minimum of 5.0 m, derived from transport disengagement height correlations in traditional fluidized beds.

The variation of all the system parameters from those values given above is also considered, and the subsequent effect on the system determined. Included is the need to increase the diameter of the vertical tubes by approximately 26% from bottom to top in order

to compensate for the temperature rise of the helium gas as it heats up (the helium also serves as coolant for the reactor) during its passage through the core. Without this adjustment, the gas velocity near the top of the core would exceed the particles' terminal velocity and fluidization uniformity would be degraded significantly.

This preliminary study of the suspension considerations for a PSR reveals that such a system is quite feasible. However, much of the analysis relies on extrapolation from existing fluidized bed technology and needs to be further tested both analytically and experimentally before true feasibility can be assessed. Should this next level of investigation also show promise, coupled with a PSR's desirable fail-safe LOCA property, this system would be worthy of further consideration for future means of safe, reliable, power production.



CA9700562

Fuel Pellet Dynamics in a Fluidized Bed Reactor Core

G. Rose, Department of Engineering Physics, McMaster University

Abstract

The feasibility of the Pellet Suspension Reactor (PSR) core is tested via numerical simulation. Parameters tested include the overall temperature distribution of the core as well as energy spectra and collision frequency of the micropellets. Optimal operating conditions are then inferred from the results of these tests.

**PELLET ENTRAPMENT IN LOCA SCENERIO FOR THE PSR REACTOR**

W. Fundamenski
Dept. Eng. Phys., McMaster U.
Feb. 5, 1993

Abstract:

A conceptual design of a pellet entrapment system for the PSR reactor is presented, which is capable of removing the excess heat in a passive manner, such that pellet stability is retained ($T_{\max} < 0.8 T_{\text{melt}}$). After loss of coolant (He), the fuel pellets pour out of their vertical tubes and onto a smooth, inverted metal cone sheathed by a water blanket, thus forming a packed bed. The max. heat flux ($\sim 10 \text{ kW/m}^2$) is comparatively small (cf. boiling crisis at $\sim 1 \text{ MW/m}^2$). Effective bed conductivity (50% packing, $0.1 \text{ mm} < r_p < 1 \text{ mm}$) was calculated by the modified SZB model, which includes radiative correction and Knudsen effects, and compared with empirical data. The slanting surfaces and free convection allow for passive cooling as long as an external water reservoir with marginal head is available. First years decay heat $\sim 10^{14} \text{ J}$, would require $\sim 10^4 \text{ m}^3$ of water.



FISSION PRODUCT MANAGEMENT AND FUEL REPROCESSING IN A PELLET SUSPENDED REACTOR

**Simon E. Day
Department of Engineering Physics
McMaster University
Hamilton, Ontario
L8S 4L7**

The Pellet Suspended Reactor (PSR) was designed with the feature of being inherently safe when faced with a loss of coolant accident or exposure to the environment. In order to meet the criteria for the latter the radioactive inventory usually associated with a fission reactor core had to be dealt with. The presence of on-line fuel reprocessing makes this possible.

The main component of the reprocessing unit is a plasma torch which has been proposed for use in general waste management. This plasma, which is powered by a small fraction of the output power from the fission reactor, can effectively break down the used fuel pellets into their constituent atoms thus enabling separation of highly toxic waste components from relatively benign material and that which can be reused in fuel manufacturing. The possibility of the high efficiency of this system makes it an attractive alternative to the expensive and difficult chemical processes presently in use.